RL-78-039

Rutherford Laboratory
CHILTON, DIDCOT, OXON, OX11 0QX

RL-78-039

Science Research Council
Central Laser Facility

Annual Report to the Laser Facility Committee 1978

LASER DIVISION
REPORT NO LD/78/04
RUTHERFORD LABORATORY

SCIENCE RESEARCH COUNCIL CENTRAL LASER FACILITY

ANNUAL REPORT TO THE LASER FACILITY COMMITTEE, 1978

Preface

The report covers work done at the Central Laser Facility, Rutherford Laboratory, up to 31 March 1978. The report is in three main sections namely Facility Development, Single beam Interaction studies and Two beam compression studies. This structure reflects the organisational arrangements adopted at the start of the facility's programme, with Mr T P Hughes (Essex University) and Dr M H Key (Queen's University, Belfast) acting as co-ordinators for the single and double beam programmes respectively. The development of the facility has been primarily an in-house activity.

Since this is the first of what is planned to be a series of annual reports it seems appropriate to give a brief historical background. The project, which was intended from the outset to provide facilities for use by University and other scientists, received Governmental financial approval in October 1975. Accommodation in the Rutherford Laboratory became available in April 1976 and installation of the Nd:glass laser begain in the late summer of that year. The first experiments using the single beam "driver" section of the laser, rated at 100 Gw for 100 ps duration pulses, began in December 1976. In April 1977 the final disc amplifiers (see section 1) became operational and two beam compression of gas filled microballoon targets was first achieved on 28 April. Since that date there have been alternate periods of single and two beam running interleaved with periods for laser maintenance and development (see Table 301, section 3).

Though, as indicated above, Mr Hughes and Dr Key have been primarily responsible for co-ordination of the plasma physics programme, detailed proposals for both experiments and relevant diagnostic instrumentation have originated primarily in groups of University and other scientists set up for this purpose. These groups have been convened by Dr J D Kilkenny of Imperial College (Optical and Magnetic measurements), Dr B C Fawcett of the Appleton Laboratory (X-ray and VUV spectroscopy), Dr T A Hall of Essex University (Optical Spectroscopy), Dr H T Miles of Swansea University (Particle Emission studies), Dr R J Dewhurst of Hull University (Gas Breakdown) and Dr N J Peacock of Culham Laboratory (X-ray Lasers and Harmonic Generation). In addition, theoretical and computational support has been the responsibility of Professor M G Haines of Imperial College. The smooth running of the project owes a great deal to the work of the group convenors and programme co-ordinators.

Sections 2 and 3 of this report reflect the above group structure. However, as the programme developed over the year under review it was appreciated that the initial group structure was not ideal. The groups cited above were based essentially on common techniques rather than common scientific objectives. While this was appropriate in the initial, setting up, phase the group structure and arrangements for allocation of time on the facility were modified in March of this year. The membership of the new groups is given in an Appendix to this report, together with the membership of the newly formed Glass Laser Scientific Programme and Scheduling Committee which has responsibility for allocating time on the facility within the programme approved by the Laser Facility Committee. The new group structure was formally adopted on 31 March and will, therefore, determine the structure of next year's annual report, It is, however, worth noting that the number of active participants in the programme has doubled in the past year and the number of institutions involved has increased from 16 to 20 (including the Rutherford Laboratory itself).

A F Gibson
General Editor

Section 1 T H E D E V E L O P M E N T O F T H E F A C I L I T Y

Section Editor: P R Williams

1.0 INTRODUCTION

1.1 GLASS LASER PHYSICS AND DEVELOPMENT

1.1.1 Experience & modification to the existing laser system
1.1.2 A tunable Nd laser system
1.1.3 Phosphate glass
1.1.4 Laser diagnostics
1.1.5 Laser performance
1.1.6 Optical quality of the laser
1.1.7 Double pass operation of the laser

1.2 PERFORMANCE AND RELIABILITY OF THE GLASS LASER

1.3 COMPUTER CONTROL

1.4 TARGET FABRICATION

1.5 TARGET AREA

1.5.1 Alignment and Focusing
1.5.2 Timing of the two beams for simultaneous arrival at the target

1.6 OPTICAL DESIGN

1.7 GAS LASER DEVELOPMENT

FIGURES

1.0 INTRODUCTION

The year under review has seen extensive developments in the Glass Laser facility and the start of the gas laser development programme. By April 1977 the 100 Gw single beam laser had been operational for four months during which time preliminary single beam experiments had been started. During April the two high power disc amplifiers were commissioned. The performance of these components exceeded their specification by nearly 50%, installation and commissioning was on schedule and it was possible to carry out the first two beam compression of a glass microballoon in late April.

The laser and experimental area occupy a large laboratory building approximately 10 m by 30 m. As the work of the facility developed during the year it quickly became apparent that as the complexity of the experimental equipment increased the space allocated for experimental equipment was inadequate. For this reason it was decided to approximately double the area available for the laser and experiments by constructing an extension to the existing suite of laboratories. This extension was completed in February 1978 adding a further 250 m^2 of area.

The central component in the gas laser development programme is the 1.5 MV electron beam generator which is being constructed in a separate large laboratory. The laboratory was fully equipped during the year and construction of the generator was well advanced.

The patternof operation of the glass laser during the years has been to interleave periods of two beam compression experiments with single beam operation for interaction physics experiments. Both classes of experiment have been carried out in the target chamber that was designed in 1976 by Facility engineers. The extended laboratory now makes it possible to have two experimental areas, each with its own target chamber: one dedicated to compression experiments, the other for single beam interaction studies. Although these plans will be implemented in 1978/79, design work on a new compression chamber is in an advanced state. The existing target chamber will continue to be used for single beam experiments. The new target chamber will initially be used for two beam experiments but it is designed to be compatible with future plans to increase the number of interacting beams to six. The proposed layout of the six beam laser is shown in figure 101.

1.1 GLASS LASER PHYSICS AND DEVELOPMENT

The laser is situated in a temperature, dust, humidity and vibration controlled environment. This helps both to maintain good reproducibility in power and alignment of the output beam and to prevent contamination and hence decrease optical damage levels to all optical surfaces in the laser beam.

As initially installed (figure 102) the laser consisted of an oscillator, 13 amplifiers and several other components for beam control, laser protection and target protection. This installation formed the basis on which steady improvement has been made during the year. A description of the main components follows.

(a) Oscillator and pulse selector

The oscillator, consisting of a Nd:YAG rod, saturable dye cell and etalon output reflector generates a short series of 'modelocked' pulses each of which has the required pulse duration. A fast optical gate, making use of the Pockels effect, selects one pulse from the train and together with a second similar unit reduces the background pulse level to less than 10^{-5} of the main pulse. The pre-pulse level must not damage the experimental target. This selected pulse is projected down the amplifier chain extracting energy as it proceeds and gradually expanding to keep the power density below damage levels. Two types of amplifiers are used.

(b) Rod amplifiers

These are rods of Neodymium doped glass, pumped optically by a set of linear flashtubes wrapped around the rod and themselves surrounded by a diffusing reflector. Pumping efficiency and rod gain coefficients fall with increasing rod diameter making it profitable to use disc amplifiers at beam sizes greater than approximately 100 mm.

(c) Disc amplifiers

These are similar in operation to the rod amplifiers but with the rod replaced by a series of discs in zigzag formation at Brewster's angle to the laser beam. Pump light now passes through the faces of the discs (as compared with the edge of the rod) resulting in higher gain coefficients and better uniformity of the gain distribution.

The faces of the amplifier discs have to withstand very high flash-light loading as well as the laser beam itself. Hence cleanliness of these components is critical and they are protected even from the clean environment of the laser room.

Other beam components are:

(d) Spatial Filter

These components generate a Fraunhofer diffraction pattern and select its central lobe thus ensuring that the beam projected into the amplifier chain is diffraction limited with a very smooth and reproducible beam intensity profile.

(e) Apodiser

A cell containing an absorbing liquid between specially profiled windows operates on the beam to generate an intensity profile which will extract maximum energy from the amplifiers without significant deterioration of this profile due to diffraction at the edge of components and due to transmission through an air path of approximately 30 m.

(f) Saturable dye cell

A cell contains an absorbing dye which bleaches under the action of high beam intensity. The effect is to preferentially attenuate all beams except that of the main pulse, since these beams are all of lower intensity. Thus the dye cell affords protection to the target against pre-pulses and amplified spontaneous emission, and to the early laser components against target reflections.

(g) Vacuum Spatial Filter

Any beam defects such as spatial intensity modulations result in a larger beam focus. The vacuum spatial filter focuses the beam through an aperture which clips the focal spot back to the size characteristic of a good beam. This aperture is a filter which cuts out high spatial frequency noise. This noise is a principal contributory factor to non-linear beam break up.

(h) Faraday Isolator

A Faraday rotator (giving 45° rotation of the plane of polarization) between multilayer dielectric polarizers acts as an optical diode. Light reflected in either polarization by the target is stopped by the isolator and prevented from being amplified back down the laser system to power levels which would cause optical damage to early components. The backward transmission of Faraday isolators is approximately 1% making it necessary to have several isolators to protect the complete laser system.

Towards the end of the year, the configuration of the laser was changed to incorporate double pass amplification in one disc ampliflier. The light emerging from the disc amplifier is retro-reflected by a 100% reflecting plane mirror and further amplified. The emergent beam is reflected from the input dielectric polariser following two 45° rotations of the plane of polarisation in the two passes through the Faraday rotators. Using this technique a beam power of 560 Gw has been obtained in a 100 ps pulse and regular single beam operation at 400 Gw has been possible. During 1978/79 both beams will operate in this double beam configuration.

It is planned to replace the silicate glass in the laser by phosphate glass during 1978/79. This change has the merit of reducing the non-linear optical effects degrading the beam quality at a given power or allowing the laser to be operated at higher powers with the same beam quality. For short pulses the available power on the target is approximately doubled by the use of phosphate glass. In order to assess the performance of the laser amplifiers when used with phosphate glass a tunable Nd:YAG ocillator has been purchased from JK Lasers Ltd. This allows gain measurements at 1.052 μm and 1.064 μm to be made as required.

Effective use of the glass laser in the plasma physics programme demands that pulses of a prescribed power and energy should be delivered on demand. The energy delivered to the target is the product of the energy delivered by the oscillator pulse generator and the gain of the succeeding amplifiers. Effective operation of the laser is therefore wholly dependent on the stability and reliability of the pulse generator. During the year modifications have been made to the pulse generator that have resulted in a significant improvement in reliability and stability.

Users of the facility have become increasingly concerned with the distribution of energy within the focal spot of the laser. It is known that thermal effects, distortion and stress birefringence, and static abberations are the main contributors to defects in the far field distribution. Studies have been made of beam propagation under various operating and cooling conditions in order to minimise focal spot abberations. Details of these modifications and measurements are given in the subsections which follow.

1.1.1 Experience and modification to the existing laser system

Figure 102 is a diagram of the laser system. The following sections record operating experience and any resulting modifications to the various components of the system.

(a) Oscillator

The oscillator has performed very reliably and no problems have occurred due to misalignment or damage to oscillator components. Cleanliness of the saturable dye caused some deterioration of reliability of oscillator performance and has led us to convert to a flowing dye system with a suitable filter. This has operated satisfactorily with a marked improvement in oscillator performance. Oscillator performance repeatability, measured as the fraction of shots on which the oscillator did not give a pulse train consisting of double pulses or no pulse train at all, has been 93% for target shots. This is an excellent figure for a passive mode-locked oscillator of this type. The oscillator head has so far been fired approximately 3 million times with no attention.

(b) Modifications to the pulse generator for single pulse selection

Operating experience in 1977 revealed recurrent problems with the pulse generator. Major modifications were undertaken in early 1978 to improve the reliability of single pulse selection, prepulse rejection, and the energy of the single selected pulse injected into the main amplifier chain.

Figure 103 shows the original layout of the passively modelocked master oscillator (MO), the YAG preamplifier (PA), the first 16mm glass rod amplifier (A1) and the two pulse selection units PS1 and PS2. There are two separate switch-out units simply to increase the contrast ratio between the main selected pulse and the unwanted preceding members of the modelocked oscillator pulse train. Each unit gives a rejection of between 10^{-3} and 10^{-4}. Figure 104 shows schematically the original circuit arrangement for driving the pulse selection unit, each of which comprises two Pockels cells (electrically in parallel but optically in series) between crossed polarisers. The modified component layout is shown in Figure 105, and the new circuit configuration in Figure 106.

The unreliable gating of the original circuit stemmed from the use of a separate krytron to trigger each switch-out unit and it was exacerbated by the slow overall electrical characteristics of the units which gave triangular rather than "top hat" optical gating profiles. Each triangular gate had an <u>independent</u> timing jitter of about ± 3ns with respect to the modelocked train, which led to an unacceptably high shot to shot variance of selected pulse energy and prepulse extinction ratio. This jitter originated predominantly in the Krytrons. As well as independent jitter, the two units displayed independent electronic drift, so that the timing of the gates needed periodic readjustment, often as frequently as twice a day.

These problems were largely overcome using the new circuitry.
The important logical step between the two is that, since the time of flight of pulse between PS1 and PS2 is absolutely fixed by the optical path length, the electrical delay between the two should also be absolute-

ly fixed, completely eliminating relative jitter between the two units. This was achieved by using only one master Krytron high voltage switch to control both units, with the relative timing absolutely fixed by the difference between the cable lengths from the Krytron to each unit. The difficulty in this approach was the current handling limit of the Krytron which precluded simple "doubling up" of the original arrangement. The use of 75 ohm cable on the longer run to PS2 kept the current low enough for reasonable Krytron lifetimes.

The shapes of the optical gate pulses, especially at PS1, were improved by the new circuit, as care was taken to keep stray inductances as low as possible.

The remaining problem of timing jitter between the pulse selector pair and the modelocked train has not proved to be serious, especially when using carefully selected Krytrons. The pulse selector units now cut out an entire single pulse with virtually 100% reliability, and the transmission of the preceding members of the pulse train is down to the oscillator inter-pulse noise level for 90% of all shots. The Krytrons last several months and timing readjustment is only required once a week. However development work is proceeding on another circuit which uses avalanche transistor chains only to drive the Pockels cells, and whose jitter should be as low as a few hundred picoseconds.

Having achieved reliable gating the energy available in the single switched out pulse was still rather low. In the original layout (Fig 103) the usable gains of the 16mm rod amplifier A1 and the preamplifier PA were severely limited by damage and non linear propagation in the Pockels cells of PS2 which followed them. When the order of PS2 and A1 was reversed, as in Figure 105, much higher gains could be used to help compensate for the high reflection losses of the switch-out units, and the usable single pulse energy was increased by up to a factor of three. After theoretical and experimental results had established that the amplified spontaneous emission level was still tolerable at the target, the new configuration was adopted as standard.

(c) Apodiser

Some problems have been experienced with the apodiser due to a gradual deterioration of the liquid. It appears that the absorber liquid attacks the anodised aluminium body causing particulate contamination of the liquid and hence an increasing component of scattered light in the transmitted beam. Liquid changes are required at approximately monthly intervals. An apodiser constructed from different materials should solve this problem.

(d) Rod Amplifier Heads

Having solved problems with flashlamp breakages by more effective mechanical decoupling of amplifier heads, they have operated with high reliability. Shot counts on heads range from 11,700 for the ϕ16 mm head to 4,000 for the ϕ76 mm head giving a total of 823,000 flashlamp firings. Average shot life per lamp, apart from catastrophic failures, has been approximately 100,000 shots.

(e) Disc Amplifier Heads

These heads have been extremely reliable. No lamp failures have occurred in 20,000 lamp firings. Information on disc deterioration is given in a later section but has not resulted in appreciable deterioration of the beam incident on target.

(f) Laser Alignment

Final adjustment of alignment has been carried out and checked using low energy shots onto high speed polaroid undeveloped negative material and observing edge fringing effects caused by previous components. Checks are made every day during experimental runs and minor adjustments are required perhaps two or three times a week. Critical points in the system are (i) the spatial filter pinhole and (ii) the turning mirror which injects the beam into the ϕ25 mm and subsequent rods.

Observation, using a cw beam at 1.06 μm, of far field images of the output beam from the laser show that short term alignment stability is approximately 25 μ radians equivalent to 3 μm on target. This is largely due to air movement in the laser room and will be reduced when beam pipes are installed.

1.1.2 A tunable Nd:laser system

A small Nd:laser system, for use as a laser development off-line test-bed facility, was received from the manufacturer, J K Lasers Limited, in March 1978. It consists of a wavelength tunable Nd:YAG oscillator, followed by a pulse selector unit and a 16 mm Nd:glass rod amplifier.

The oscillator uses three Brewster angle prisms to fold the resonator path through $\sim 180^{\circ}$. Tuning the rear laser mirror in the prisms' dispersion plane allows selective oscillation on any one of the four main lines of Nd in YAG, namely 1.074, 1.064 , 1.061 and 1.052 μm. The ability to operate at 1.052 μm makes the new oscillator a valuable tool for examining the gain of future generations of laser glasses near their peak gain wavelength, as well as for developing a new phosphate-glass compatible master oscillator. Evaluations of active and active-passive mode locking techniques are also planned.

The 1.064, 1.074 and 1.052μm lines have been extensively studied. Reliable passive modelocking has been achieved on all three. A spectrometer was used to ensure that the oscillator output was in all cases on a single line and that no spurious output on the strong 1.064 μm line was present when the laser was tuned to one of the weaker lines.

The pulse selector consists of a single Pockels cell, activated by a laser-triggered spark gap, between crossed Glan Taylor prisms. In operation it has proved less reliable and more difficult to set up than the modified electronically activated pulse selectors described below. It can satisfactorily isolate single pulses, although all measurements made so far with this system have used the whole modelocked pulse train.

The 16mm rod amplifier is pumped by four linear flashlamps in a ceramic cavity. It has been used to test a sample of Owens-Illinois EV2 phosphate glass, and measurements on a Kigre Inc. Q88 sample are currently underway. A gross gain of greater than sixty has been recorded at λ = 1.052 m for the EV2 rod which has a pumped length of only 20cm. This is in dramatic contrast to the 16mm x 20cm silicate glass rod amplifier in use on the main laser system whose maximum gross gain is about 10.

1.1.3 Phosphate Glass

(a) General Considerations

The present intention is to convert from silicate to phosphate glass in the laser system. Comparative performance figures for phosphate glass as against silicate glass from other laboratories vary widely but can be summed up as follows:

(i) Gain

The expected increase in gain coefficient under similar pumping conditions varies by a factor of from 1.5 to 2.2 depending on the supplier and particular batch tested.

(ii) Non linearity

The non linear index is reduced by from 20% to 30%

(iii) Maximum amplifier size

Measurements on disc amplifiers using current edge coatings indicate a maximum beam diameter with phosphate of about 10 cm before being limited in gain by parasitic oscillations.

Thus we conclude that the Rutherford laser is ideally suited to phosphate glass since not only does the high gain and low non linear index enable high output powers to be reached for a given non linear (B) integral but the high gain enables a reduction in the number of amplifiers and consequently an improvement in the beam quality.

Using performance figures from other laboratories it is apparent that the system will be limited by non linear beam break up and damage to the target chamber optics.

If we specify a maximum B-integral of 2 for this optic (BK7 and approximately 5 cm thick), possible peak power is 1.5 Tw/beam. At 100 ps pulse duration the energy per beam is 150 joules and energy density is 2 joules cm^{-2}, well below damage levels for good quality optics and coatings.

It is expected, following these considerations, to be able, with phosphate glass, to achieve a level of 1 Tw per beam and have a reasonable safety margin.

Present uncertainties are the wide diversity of measured gain coefficients for phosphate glass and in particular its performance in our 10.8 cm disc amplifiers.

(b) Phosphate Glass Gain Measurements

A programme was initiated in early 1978 to evaluate commerically available phosphate laser glasses with a view to determining the most suitable type to use for the upgrade of the main laser system. So far, the gross gain has been measured at $\lambda = 1.052$ μm and 1.064 μm for:

(i) a 16 mm by 230 mm Owens-Illinois EV2 phosphate glass rod

(ii) a pair of Kigre Q88 phosphate discs in the 108 mm disc amplifier head

The experimental arrangement is shown in figure 107. The beam from the tunable oscillator (described in section 1.1.2) was expanded before being passed through the test amplifier.
Beam expansion not only defined the test volume in the sample, but also kept the energy density to a tolerable level at the amplifier output. The maximum output energy density used was about 400 mJ/cm^2 for the 16 mm rod at maximum gain. Part of the oscillator beam (about 30%) was sampled by calorimeter E_1 to monitor oscillator shot to shot variations. The remainder was passed through the test sample in the amplifier and was then directed by two dielectric coated mirrors onto the second calorimeter, E_2. This monitored the gross gain as the ratio of pumped to unpumped signal for normalised input pulse. The two dielectric mirrors acted as a filter to discriminate against amplifier flashlamp light arriving at E_2, which was further reduced by use of the iris at A.

Figure 108 shows the variation of gross gain versus capacitor bank input energy for the 16 mm diameter EV2 phosphate glass rod, for both the 1.052 micron and 1.064 micron probe wavelengths. The doping of the rod was 2.5 atomic percent and the results were taken with a 9 mm diameter probe beam travelling along the rod axis. The experimental ratio of the gain coefficients, $[\alpha(1.052\ \mu m)/\alpha(1.064\ \mu m)]$ was 1.51 ± 0.04. The peak value of the gain coefficient was nearly 19%/cm, corresponding to a gross gain of over sixty from the rod, and the gain was still increasing at the voltage limit of the capacitor bank. This looks extremely promising for future applications. As a comparison the 16 mm rod amplifier of the Quantel laser system, using silicate glass at 1.064 μm, has a gain of around ten and an even higher gain should be derived from the phosphate glass rod if its aperture were filled, since the rather high doping concentration would be expected to give a significantly higher gain off-axis.

Figure 109 shows the variation of gross gain versus capacitor bank input energy for the two Q88 discs in the 108 mm diameter disc amplifier head. As a comparison the data for the present ED2 silicate glass discs, taken during the system acceptance testing, are also plotted but 500 shots had been fired between the ED2 tests and the Q88 tests. Any flashlamp or other system deterioration would tend to bias the comparison in favour of the ED2 glass. The range along the x-axis is somewhat limited, since the disc amplifier heads can only be operated at bank voltages between 16 and 20 kV. Also the scatter in the data is rather high because the gross gains measured in a single pass-through the discs, around 1.5 to 1.8, were rather low. The doping concentration of the Q88 discs was 2.2%. The probe beam was 10 mm in diameter and directed down the axis of the disc amplifier.

The most obvious feature of the results is the much lower gain coefficient attained in the disc amplifier configuration compared with the rod amplifier. The average recorded value of $[\alpha(Q88, \lambda = 1.052)/\alpha(Q88, \lambda = 1.064)] = 1.35 \pm 0.1$, is in very good agreement with the manufacturer's published data. The maximum value of the gain coefficient observed on axis in the disc amplifier was $\alpha_{max}(Q88, \lambda = 1.052) = 8.3\%/cm$ (the mean of the values at 20kV). For the full amplifier complement of six discs this corresponds to an on-axis gross gain of 5.9. However, the gross gain when the whole amplifier aperture is used should be up to 25% higher than this - a 13% higher gross gain was observed near the edge of the clear aperture. These figures are to be compared with values of $\alpha_{max}(ED2, \lambda = 1.064\ \mu m) = 7\%/cm$ and a maximum amplifier gross gain of 4.4 for the present silicate glass discs.

A commonly quoted figure of merit for amplifier discs is αD, the product of the small signal gain coefficient and the length of the disc's long axis. The Q88 phosphate discs reached $(\alpha D)_{max} = 1.65$ while the ED2 silicate discs reached $(\alpha D)_{max} = 1.4$. If the performance of the phosphate glass discs was limited by parasitic oscillations, this would correspond to a reflective recoupling of 5.3% at the edge cladding for the 'critical angle' highest gain mode. However, the low value of $(\alpha D)_{max}$, the higher gain off axis, and the fact that α was still rising fairly steeply with the bank energy are indications that the disc amplifier performance was not limited by parasitic oscillations.

A problem in the phosphate based laser glasses which is not a feature of the silicate glasses arises from their relatively high water affinity. Great care is required during manufacture to avoid water absorption which results in quenching of the energy storage in the glass. It was suspected, therefore, that the relatively low observed gain in the disc amplifier experiment was due to water contamination in the glass. In order to check this hypothesis the optical transmission of a disc was measured at $\sim 2.3\ \mu m$ where the attenuation is a sensitive function of water contamination. Preliminary measurements indicated that an excessive water content was the most likely cause of the observed low gain.

1.1.4 Laser Diagnostics

Figure 110 shows a current layout of diagnostics in use on the laser system. The individual items are detailed below.

(a) Oscillator and Pulse selector

The operation of these is monitored by two fast vacuum photodiodes which observe (i) the pulse train from the oscillator as rejected by the pulse selector and (ii) the switched-out pulse. These signals are added with a relative time delay and directly observed on a Tektronix 7912 transient recorder. This recording gives an assurance that the oscillator is giving a good pulse train, that the pulse selector is selecting all of the peak pulse in the train and that no other pulses having energy above a few percent of the main pulse are transmitted.

(b) Prepulse level

A prepulse monitor consisting of two fast silicon PIN photodiodes has been installed to test the beam immediately after the saturable absorber dye cell. In this position it provides an accurate record of the prepulse level incident on target, since the rest of the system is essentially linear.

The fraction of the beam reflected from the uncoated wedged end of the 64 mm rod amplifier is focused down onto the two photodiodes PD1 and PD2, as shown in figure 111. The optical path onto PD1, which is set up to be very sensitive, is carefully shielded with blackened tubing to avoid spurious signals from stray light. The signals from both photodiodes travel to the control room, with 20 ns of additional cable delay inserted into the PD1 channel, where they are added and recorded on a Tektronix 7912 transient digitiser. The digitiser reads out directly into the

GEC 4080 computer which displays the prepulse data on a VDU screen and provides a hard copy as a permanent record of each shot.

Figure 112 is a sketch of the form of the output data from the prepulse monitor, illustrating how it operates.

The prepulse performance of the laser has been highly satisfactory since the modifications to the pulse selector unit were made (see section 1.1.1) On average only about one shot in 15 has been a 'reject' on prepulse grounds. The great majority of these rejects have been due to the oscillator interpulse noise transmitted by the opening of the optical shutters of the pulse selector units, rather than the preceding member(s) of the mode locked pulse train transmitted by any actual malfunction of the pulse selectors. The gated oscillator interpulse noise is a statistical phenomenon associated with the passive mode locking, and as such it is difficult to control directly beyond ensuring optimal setting up of the oscillator voltage and mode locking dye. Its effects could be moderated by the use of additional saturable absorbers external to the oscillator.

(c) Beam Energy

Several beam energy monitors are used as shown in figure 110 . The present points of monitoring are:

(i) Input to the first ϕ25 mm rod amplifiers
(ii) Output of the second ϕ45 mm rod amplifiers
(iii) Output of the rod driver system
(iv) Final output of the two beams

The monitors are Holgate's units using silicon photodiodes and are coupled to an integrating and peak hold circuit. These monitors are insensitive to changes in incident beam angle, position and intensity distribution and are accurate to a few percent once positioned and calibrated.

Accuracy drops to about 10% if calibration is required to hold following a change of position of the monitor. Calibration is carried out against an absorbing glass disc calorimeter (supplied by Laser Instrumentation).

(d) Beam Intensity Profiles

Photographic recording on 1Z emulsion has been used for near field and far field profiles as indicated in figure 113. Recordings of both are made simultaneously in both laser output beams. The near field camera records the distribution in a plane equivalent to that of the entrance window of the target chamber. The far field camera records ten different planes in a selected region near the beam focus, the selected region depending on the requirements of the experimental programme.

An infra-red TV camera can be switched in to view the far field images at 1.06 μm using the cw Nd:YAG alignement laser. Thus it is possible, for example, to monitor distortions due to dynamic thermal effects in the laser amplifiers.

A video disc recorder together with a further two infra-red plumbicons have been purchased and will be used to eliminate photographic processes in the beam diagnostics.

(e) Back reflection

Back reflection intensities in the laser are at their highest at two points in the system, (i) at the output of the final Faraday isolator, (ii) at the output of the first Faraday isolator FR1. The energy at FR1 is monitored using the Holgate's detector (see figure 110) and to check that no serious hot spots occur in this back reflected beam polaroid negative burnpaper is used to look at the beams rejected by the polarizer of FR1. Similar burn paper at the final Faraday rotator is a good indication as to whether or not the back intensity is too high there.

1.1.5 Laser Performance

(a) Beam Profile

Figure 114 gives examples of near and far field images recorded during single and two beam experiments. The near field images are monitored primarily to detect the onset of hot spots in the beam and hence define the limits of operation of the laser. Figure 115 gives an example of the intensity profile across the beam showing approximately 3:1 intensity variations. The peak intensity can be allowed to reach three times the average as this will lead to a peak energy density of 1.3 J/cm^2 at 1/3 Tw per beam in 100 ps and a peak B-integral in the focusing lenses of approximately 1.

Figure 116 gives the best focus intensity distribution taken from a far field picture during a single beam run. Best achievable focal spot sizes are within 50% of diffraction limit. This achievable performance is generally degraded by thermal distortion in the amplifiers and by airflow effects along the 30 m beam path.

Figure 117 shows an example of a degraded profile. It should be remembered that microballoon experiments do not focus the beam on to the target surface. Incident planes are perhaps 50 μm inside focus. Figure 118 shows a beam picture in this plane. Distortions do not, of course, affect the distribution in this plane as severely as that in the focal plane.

As a quantitative check on the far field photography, measurements have been made of the fraction of energy transmitted by various size pinholes set in the plane of best focus. Figure 119 shows an example of this data for the rod system. Considerable distortion was present in these measurements due to the high repetition rate used. This is evident if comparison is made with the 1Z far field recordings described above.

A sequence of beam profiles recorded at different points in the laser are shown in figure 120. Low energy profiles are shown together with high energy profiles. In particular these profiles show the growth of small scale self focusing before the vacuum spatial filter, the elimination of the fine structure by the vacuum spatial filter and the growth of the remaining larger structure down to the output of the system. Figure 120 shows beam profiles at two points in the system showing quantitative modulation values. These profiles also demonstrate demonstrate that (i) the final beam profile is very flat thus enabling a high fill factor at the final amplifiers and (ii) that as high as possible a fill factor is achieved without serious Fresnel diffraction modulation at the edge of the beam due to cut off at the final amplifiers. Further implications of these near field profiles are discussed in a later section.

(b) Amplified Spontaneous Emission (ASE)

The energy transmitted by a pinhole in the plane of best focus of a lens and having a size equivalent to that of the target is a measure of the energy incident on the target. A sensitive photodetector placed behind a pinhole in this way enabled the ASE energy on target to be measured. The measurements compared well with calculated estimates. The ASE level was varied by changing the concentration of dye in the saturable dye cell until the aluminised microballoon target was no longer disturbed before the main pulse arrived. This ASE energy was estimated to be $\sim$ 100 μJ. Dye cell small signal transmission was 10% and main pulse transmission approximately 70%.

(c) Back Reflection

The laser system is designed with several Faraday isolators and a saturable dye cell such that the back reflected energy is at no point higher than the forward going power with 30% reflection back into the disc modules or final rod amplifiers. This design is based on a 100:1 extinction ratio for the Faraday isolators. All Faraday isolators exceed this performance and, further, plasma generated by the forward going pulse in the aperture of the vacuum spatial filter results in a considerable attenuation to the back reflection by this component. Safety margins are consequently high at the oscillator and have enabled us, for example, to transpose the second pulse selector and ϕ16 mm rod to protect the pulse selector from damage by the forward going pulse.

1.1.6 Optical Quality of the Laser

(a) Passive Optical Quality

This has been assessed for the complete system by observation of the far field images in cw Nd:YAG illumination and low power pulsed illumination. Figure 116 shows an image obtained in pulsed illumination. (This was a medium power shot but was very little worse than a low power shot.) Central spot size is larger than diffraction limit by a factor less than 1.5 and the intensity in the side bands is less than that for the Airy distribution. Imperfection of this focus is due to component imperfections and effects of air flow through the beam path. The latter particularly affects the distribution outside the central spot in addition to causing lateral movement of the spot itself. It has been observed that amplifier rods and discs both deteriorate in optical quality with use. Typically, one wavelength of distortion will be observed following several months of operation.

Scatter gives rise to intensity fluctuations on the beam which enhance the non-linear break-up of the beams at high power and so limit the maximum power achievable. Intensity variations due to scatter particles in the apodiser liquid, to a low density of specks on polished optical surfaces and to a higher density of very small specks in multilayer dielectric coatings have been observed.

(b) Dynamic optical quality

Two processes reduce the optical quality of the amplifiers when they are firing

(i) Non-uniform deposition of energy during pumping causes a dynamic optical distortion throughout the pump duration and thereafter until the thermal profile has a chance to relax.

(ii) Cooling processes induce non-uniform thermal profiles and hence optical distortion. These have a long term accumulative effect if cooling is not effective enough between laser shots.

The rods have a principally radial variation in pump distribution and hence this leads mainly to a change in focus position of the laser beam together with some spherical aberration. The rods become slightly negative lenses due to pumping and using our far field multiple image camera we have been able to measure the equivalent focal plane shift at the target for different operating conditions for the laser. For example, this change of focus is $\sim$ 40 μm when driving the rod system fairly hard.

Cooling of the rods also gives a radially varying thermal profile and also gives principally a change of focus for the beams. However, the thermal profile is reversed and the rod becomes slightly positive in power. In principle a zero optical power at the moment of the beam might be achieved by ensuring that the thermal profile due to cooling is exactly compensated by the pump induced profile. This could be achieved in our system by operating with less than two minutes between shots. With necessarily longer cooling times there is a net negative focusing effect.

In addition to the change of curvature of the beam there is also an appreciable distortion when pumping the rods. This distortion dies away to become negligible if at least five minutes elapse between shots. At this repetition rate or slower, no accumulative effects occur and the instantaneous distortion is acceptable particularly if the disc modules, which have given much higher distortion, are in use.

The discs have a near uniform distribution of pump intensity over the beam cross section and develop very little distortion during the pumping pulse.

Long term effects can be severe. Several modes of operation of the discs have been investigated to determine which mode enables the disc to operate repeatedly without significant distortion. Observation of the multiple image far field distributions, as seen using our cw Nd:YAG alignment laser coupled to an infra-red viewer or infra-red TV system provided the information for this investigation.

Observations suggested that:

(i) At least one hour was required before approximate steady state was reached.

(ii) Steady state before and after a shot were not necessarily the same and neither was necessarily the same as the best achievable spot profiles.

(iii) Changes in disc cooling process significantly affected the steady state profiles.

Improved spot distributions were achieved by not using fast flow cooling after a shot. However, there was still found to be an accumulative effect over several shots at one hourly intervals. Investigations are continuing.

1.1.7 Double pass operation

Figure 121 shows the layout of double pass operation of the disc modules.

Double passing increases the output power by increasing the gain at the highest beam area (B integral inversely related to beam area). The requirement to maintain a constant B-integral in the change to double passing results in an output greater than single pass power and less than single pass power x gain of disc amplifier (G). Putting in the appropriate numbers with G = 3.5, expected output power increases by a factor $\approx$ 2.5 and power required from the Quantel system is reduced by factor $\simeq$ 1.4. Operating limits under single pass operation $\simeq$ 15J per beam, therefore operating limits under double pass operation $\simeq$ 37.5 J per beam. At this level average ouptput energy $\simeq$ 0.5 J/cm^2. This level should not give high risk of damage to the Faraday isolator or target optics.

Back reflection must be considered in this mode of operation since we have a 100% mirror in the beam previously injected into the target chamber. Thus the system is equivalent to 100% back reflection of 70% of single beam power. This is equivalent to 15% back reflection at the output of the rod driver section which is well below the safe limit. Back reflection from the target poses no problem since it is reduced by a factor 100 at the Faraday isolator before passing back through the disc module.

Both single and two beam experiments have been carried out using the double pass disc amplifier layout. Single beam operation can achieve higher powers since the B-integral of the rod driver section is reduced by a factor 2, and in excess of 0.5 Tw is obtained. Two beam operation is limited to ∿ 0.35 Tw or 35 J per beam.

1.2 PERFORMANCE AND RELIABILITY OF THE GLASS LASER

During the year under review the laser has been operated in three separate modes.

I Rod amplifiers only to provide a single beam for interaction studies

II Rod amplifiers plus one disc amplifier to provide a higher power single beam for interaction studies.

III Complete system, rod amplifiers plus both disc amplifiers to provide two high power beams for compression studies - some running without discs occurred in these periods.

In mode II towards the end of the year the disc amplifier was used in double pass allowing a maximum single beam power of 560 Gw to be achieved in a test shot and routine operation at 400 Gw to be normally available. No double pass two beam operation took place before 1 April 1978.

The histograms which follow present the running record of the laser for each mode of operation. Total power versus number of shots for each mode is presented for the year (figures 122, 123 and 124). The variation in operating power is not in itself an indication of unreliability of the laser but represents in most cases the varying requirements of the experimental programme. In each figure the 'target shots' are separately identified from the setting up, calibration and laser development shots. The more difficult double beam operation made it necessary to devote many laser shots to setting up and calibration and characterisation of the laser (figure 124). In order to provide $\sim$ 250 double beam targets shots, $\sim$ 430 shots, mainly without using the disc amplifiers, were used for setting up and laser engineering purposes.

A total of 1048 laser shots were delivered to targets during the year and 533 shots were used during plasma physics scheduled time for calibration, setting up and engineering purposes.

Thirty eight weeks of the year were scheduled for plasma physics experiments and fourteen weeks were devoted to facility development and engineering. 82% of laser shots directed at targets were succesful in delivering energy to the target. Of the 18% unsuccessful shots ∿ 7% failed as a result of pulse generator failure, no pulse or a double pulse, ∿ 7% failed as a result of problems wiht the single pulse selector and ∿ 4% arose from electrical and other faults.

1.3 COMPUTER CONTROL

A GEC 4080 computer is used for laser control and monitoring. It is also beginning to play a role in a data processing facility. The computer is interfaced to the laser using CAMAC. The present configuration comprises a system crate with a branch driver connected to two additional crates one of which serves the experimental area. Details of the system are shown in figure 125.

The laser consists of two sections constructed by different manufacturers and was not designed for computer control. The laser is run in different configurations depending on the number of beams required and the desired output energy. Each mode of operation requires different switch settings and charging sequences and the computer has been arranged to control the laser taking this into consideration. The required mode of operation is entered on a keyboard and the laser operation is started using a single push-button. The computer checks switch settings and ensures that interlock chains are complete before starting the charging sequence. When the end of charge condition has been detected the capacitor voltages are read, and the OK to fire signal, correctly synchronised with the oscillator pulses, is sent to the laser. After a shot, a number of energy monitors are read using the same DVM and associated multiplexer as is used for checking capacitor voltages. A print out of all acquired data can be produced for data logging. The energy monitors use Holgate heads which produce a fast rising pulse of amplitude proportional to light energy. A peak hold circuit has been developed with a sufficiently long decay constant to allow the DVM to acquire data without significant loss in accuracy. Special attention has been paid in the design to exclude flash light from the delector using both optical and electrical filtering. Two Tektronix R7912 waveform digitisers are available and these are used to monitor the pulse train from the oscillator and to assess the amount of pre-pulse present. The digitised data is reproduced on the graphics terminal where hard copy may be obtained.

Two 12 channel Lecroy ADC units are in use for recording data from experiments. Each channel consists of a charge sensitive detector and analogue to digital converter. One unit acquires data from X-ray and light diodes while the other is connected to a combined scintillator-photomultiplier for determining neutron yields from D-T filled microballoon implosions. A programme has been written to facilitate calibration of the neutron yield equipment. A special diode detector has been built for determining the output energy of the laser at harmonics of the fundamental frequency generated by frequency doubling crystals. Photographic experimental data, derived from oscilloscope traces, may be digitised using the Tektronix graphics tablet and processed in the computer for display on the graphics terminal. Alternatively the data can be transmitted to the IBM 360/195, using the data link, if more sophisticated processing than can be provided locally is required.

In general, commercially available CAMAC units have been used to connect to the equipment but where, for reasons of non-availability or economy, this has not been practical special units have been developed. In order to ensure that flash tubes in the main amplifiers are undamaged prior to a shot (ie as the result of the previous shot) a pre-ionisation lamp check (PILC) is carried out. A low energy discharge is generated in all the flash lamps and the corresponding current detected. The data is transmiteed to the CAMAC PILC unit where a "lamp OK" signal is generated and available to the computer if the current pulse is greater than a pre-set threshold. The unit is designed for both manual and computer operation and incorporates a LED display giving a pass-fail indication. The unit also monitors the tubes during a main flash. A prototype waveform digitiser has been built using a charge coupled device. The CCD allows an analogue signal to be sampled 100 times at intervals of 10 ns giving a 10 μs acquisition period. Data is read from the CCD at a slower rate to provide time for analogue to digital conversion (12 bits) and data storage. The CAMAC unit has 10 basic inputs arranged in pairs which may be linked to double the sampling rate. The unit was intended for acquiring signals from charge collector probes but can be used for other purposes.

Laser development is a continuing process and the latest proposal for a six beam system, with an additional separate single beam and involving two target chambers, will require a considerable extension and sophistication of the computer control if reliability and flexibility of operation are to be assured. Possibly a computer assisted beam alignement system will need to be developed if the present manual techniques prove to be too time consuming. Development of a beam profile viewing and measuring system is in progress. This will be capable of observing six beams simultaneously using television cameras and a video disc recorder allowing eight laser shots to be recorded. As an extension of this a computer interface will be developed capable of digitising the stored data. Raw data can be transmitted to the IBM 360/195 for archiving. Programmes for producing beam profiles, contour plots or generating a beam 'quality factor' will need to be developed. Design of a two dimensional optical multichannel analyser (OMA) interface is in progress. Initially the OMA will be coupled to a streak camera allowing time and space resolved data to be digitised without the use of an intermediate photographic stage thus making shot to shot processing of data feasible.

1.4 TARGET FABRICATION

During the year the target preparation group have been concerned with the fabrication and supply of two main types of target. Foil targets have been produced for single beam energy transport investigation experiments and various hollow glass microballoon targets have been supplied for the double beam compression experiments. Most effort has been directed to the latter work.

Foil targets have been of two types. Single layer foils of cellulose nitrate and polystyrene of thickness around 0.1 μm have been produced by casting techniques for laser beam burn through type experiments. In order to produce clean dust free films it has been found essential to perform the casting process in the class 100 clean room. Multilayer foil targets with thicknesses up to 10 μm have been produced by vacuum evaporation techniques on thin mylar substrates for fast electron investigation experiments. The most complex target fabricated has contained six layers consisting of: 0.1 μm Al, 1.0 μm SiO, 4 μm NaCl, 3.5 μm mylar substrate, 3 μm KBr and 4 μm CaF_2.

All compression experiments performed during the year were of the 'exploding pusher' type requiring 75 μm diameter, thin walled, gas-filled glass microsphere targets. Throughout the year techniques have been developed and equipment built in order to process and handle these minute objects. Raw microspheres in various grades are purchased in bulk, and initially precision-sieved to the desired size range in an ultrasonically agitated alcohol bath. The grossly non-uniform spheres are then crushed by hydraulic pressure and the survivors separated from the debris by floatation. Gas filling is accomplished by diffusion through the thin (1 μm) walls of the microspheres at elevated temperature and pressure. So far, filling runs have been carried out using hydrogen, deuterium, neon, argon and various mixtures of deuterium and neon. Filled spheres are examined individually under an interference microscope in order to select those which are perfectly uniform and to accurately measure their wall thickness (0.20 nm). Fig 126 shows two typical microspheres as observed under the interference microscope, one being obviously non-uniform and the other being satisfactory. The selected targets are picked up using a vacuum pipette and transferred to a rig where they are glued to the end of a 5 μm diameter carbon fibre attached to a mounting stalk. Finally, before transfer to the target chamber, a thin (20 nm) layer of aluminium is evaporated onto the sphere in order to make it highly reflective and easier to position in the focal spots of the two laser beams. Fig 127 shows a finished, coated, mounted target ready for transfer to the target chamber. Between April 1977, when compression experiments commenced, and the end of the year, about 200 finished, mounted targets were delivered to the experimentalists. Effort is now being devoted to streamlining the processes involved in producing targets in anticipation of a rapidly increasing demand.

The future compression programme will call for alternative types of target, such as solid spheres, and consequently some time has been spent on learning how to produce these. Two methods have been used. For low melting-point materials, particle spheroidisation techniques have been developed and applied successfully to the manufacture of polyethylene targets. For high melting-point materials the centrifugal shot-casting technique developed by the Chemistry Division at Harwell has been used and samples of beryllium, boron, boron chloride, magnesium and zinc spheres have been obtained.

1.5 TARGET AREA

All laser-matter interaction experiments are carried out in the target area whose basic layout is shown in figure 128. The beams are brought to the target chamber (figure 129) where they are focused by two 100 mm f/1 Soro lenses. The lenses and the target platform can be adjusted while the chamber is evacuated. Small fractions of the beams taken out at splitters are used for alignment and focusing as described in more detail below. A small fraction of the oscillator output is brought to an array of diodes in the target room to give trigger pulses and timing references to electronic equipment. Optical probe beams consist of a harmonic beam (which may be Raman shifted) derived from the main laser and a 1 J beam from a Q-switched ruby laser supplied by Imperial College.

In most cases it has been found convenient to adapt the optical paths for different experiments to bring light to equipment in more or less fixed positions rather than move spectrometers and streak cameras round the room.

The laboratory is a multi-user facility with a large number of different types of experiments being carried out in rapid succession. Often, two or three groups will be making independent measurements at the same time, or some will be setting up while others take data.

1.5.1 Alignment and focusing

The alignment and focusing of the main beam onto target, for both single and double beam experiments, is accomplished using the optical system shown in figure 130 . It consists of four major sub systems:

(a) Low magnification imaging in visible light of the target plane, viewed along the main beam direction through the main focusing lenses, for rough positioning of microballoon targets.

Illumination is provided by a filtered lamp behind one of the main beam turning mirrors, and the final image is produced on a TV camera.

(b) A visual microscope viewing the target plane edge-on at right angles to the beam axis, for initial rough positioning of micro-balloon and also plane targets near the beam focal planes.

(c) An infra red (1.06 μm) telemicroscope imaging the target plane at high magnification (≃ 400) for fine focusing onto plane targets and fine aligment and focusing onto microballoon targets: the focal plane telemicroscope (FPTM).

(d) A 1.06μm lens plane telemicroscope (LPTM) viewing the plane of the main focusing lenses for ultra-fine alignment and focusing onto microballoon targets.

The two telemicroscopes are illuminated by the cw Nd:YAG alignment laser. This is introduced into the main laser path at an early point (between the second switch out unit and the first spatial filter) and runs through the rest of the chain including the two spatial filters. It therefore provides a good low power replica of the main beam for alignment purposes except for a small focusing correction which has to be made to account for thermal lensing in the amplifier rods on a main beam shot. This correction has now been fairly accurately determined by photography of the main beam focus and by interaction experiments where the target was scanned through the focus, to be $\delta f = + 75$ (±25) μm. That is, the high power main beam pulse focus of the Soro lenses is about 75 microns further from the lens than the low power alignment laser focus. The figure is quite high because of the preponderance of rod amplifiers in the laser system.

Both telemicroscopes observe the radiation backreflected from the cw alignment laser into the same main beam focusing lens. The conventional

FPTM is focused to observe the spatial distribution of intensity in the target plane but the new LPTM is focused so as to observe the angular distribution of the backscatter from the target by imaging the plane of the main focusing lens. To see why this is of interest, consider the microballoon as a small spherical mirror near the point focus of a perfect lens. If the lateral alignment is perfect and the beam is focused to either the centre or the wall of the spherical reflector, the reflected rays retrace the incident rays and a 'point focus' will be observed on the FPTM. However, if the beam is focused to a point near the half radius of the microballoon (on the lens side) the back reflection follows a very narrow (∿ half a balloon radius) collimated return path from the target to the lens. If the lens has no hole in it, this radiation will converge to the back focus and will then blow up and be lost to, or at least out of focus for, the conventional FPTM. (In fact our Soro lenses have central holes, but the lateral alignment accuracy necessary for collimated retroreflection through them, about 2 μm, is beyond the ability of the present mechanical drives: so the above arguments are valid.) Thus the strong narrowing of the reflected angular distribution, very characteristic of accurate focusing near R/2, cannot be observed by the conventional FPTM type telemicroscope focused in the target plane at the focus of the main beam lens but the LPTM, directly observing the angular distribution of reflected radiation at the lens plane will pick up this behaviour very clearly. Also, if the arguments are extended to include lateral target misalignment, it can be shown that the LPTM will be much more sensitive to small target positioning errors than the conventional FPTM.

Although the present Soro main lenses produce highly aberrated focii of ∿ 30 μm diameter, it was still thought worthwhile to set up and try out the angular distribution LPTM, if only in preparation for the installation of the much higher quality new doublet lenses (see section 1.6) which do not have a central hole. But even with the Soro lenses the LPTM turned out to be a more sensitive tool for ultra-fine focusing and alignment of microballoons than the conventional FPTM. In practice the highly aberrated focal spot smears out the idealised behaviour described above. On the FPTM a very characteristic, easily recognised minimum spot size with symmetric 'flares' around it is observed when the microballoon target is in accurate transverse alignment and with its outer wall towards the back of the 'focal cylinder' of the lens. If the balloon is driven slightly closer to the lens, substantial angular narrowing is observed on the LPTM, with the reflected intensity extending to about one third of the lens radius. The finesse of the focusing, before noticeable degradation of the best pattern is seen, is sharper on the LPTM but also the lateral positioning finesse is markedly sharper on the LPTM than the FPTM. This is to be expected since the LPTM shows clearly when the retroreflected distribution has moved only a small fraction of the lens radius whereas the FPTM only sees image degradation by loss of intensity when the retroreflected beam has actually started to walk right off of the lens aperture.

The practice of applying a very thin ($\sim$ 200 Å) aluminium coating to the microballoon targets, to facilitate alignment and focusing by retro-reflection, has been continued.

Alignment and focusing onto microballoon targets is now performed according to the following sequence. The new microballoon is replaced and positioned so that its image is on the 'cross hairs sight' on the TV monitor of the visible light monitoring system (a). Focal direction adjustments can be referenced to the visual microscope (b) if necessary, but positioning within the depth of focus of (a) is normally sufficient. Then using the cw Nd:YAG laser, the microballoon and/or lens positions are adjusted to give a strong, minimum size, symmetrical retroreflected spot on the FPTM. Then the retroreflected angular distribution is observed on the LPTM and adjustments are made to minimise its extent and centre it on the lens aperture. The procedure is repeated for the other beam so that now the cw beam on each side is accurately focused near the target wall. It remains only to adjust the focusing for the thermal lensing correction, and the desired microballoon illumination configuration (polar or equatorial focus, etc).

For plane targets the procedure is much simpler. After initial target positioning only the East beam of the FPTM is used to obtain the minimum size of the retroreflected image spot and then the thermal lensing correction is made.

The main remaining problem on alignment and focusing has been the very limited accuracy which can be achieved with the lens and target movements due to the mechanical drive couplings to outside the chamber. This will be overcome by the use of electrical drives in the new six beam chamber.

1.5.2 Timing of the two beams for simultaneous arrival at the target

For successful laser compression one seeks to illuminate the target with a good approximation to spherical symmetry. Such symmetry as is achieved would obviously be wasted unless the two beams are accurately synchronised to arrive simultaneously on either side of the target. The tolerance level is of the order of 5-10 psec simultaneity for 100 psec pulses, which corresponds to a path equalisation of the two laser beams to within a few mm.

To achieve synchronisation, two of the main beam turning mirrors, M_1 and M_2 in figure 128 were mounted on precision slides such that the path length of the East beam could be accurately altered. A test target of triangular cross-section was placed in the chamber in the correct target position (aligned and focused as in section 1.5.1) such that each beam saw a target face at 45^o incidence. A specularly reflected beam out from each side of the target was collected by the viewing lens L_3. The target plane was re-imaged by relay optics onto the slit of the S1 streak camera giving two separate spots on the slit, one corresponding to each side of the target. The streak camera was sensitive enough to record reflections from the target of the pulses derived from the Quantel oscillator alone, giving a high data acquisition rate (one shot every 3 seconds). By using the streak camera at 25 ps/mm and making successive fine adjustments to the M_1 and M_2 slides, pulse synchronisation was achieved to within about 5 psec (the time resolution of the streak camera).

1.6 OPTICAL DESIGN

For all the experiments described in the preceding sections, the laser output was focussed on to the targets by commercial lenses with a numerical aperture of f/1. The lenses were aspheric singlets manufactured of a high refractive index glass and had a smallest focal spot size of ∿ 50μm. These lenses, although they have allowed the first year's programme to go ahead, are not considered to be satisfactory for long-term use. In particular, the optical aberrations are unacceptably high and the high index glass is too prone to suffer from self focusing damage arising from coupling of the high non-linear refractive index with the small scale intensity fluctuations in the beams. The singlet lens also suffers from the fact that it cannot be insensitive to operating wavelength and can only be used at λ = 1.06μm precluding the use of the second harmonic ∿ 530nm of the laser for target interaction experiments.

W T Welford and D J Nicholas have designed a new f/1 focussing lens for use at the facility. This lens is a doublet and has the manufacturing advantages that each of the two elements can be figured using visible light and that the aspheric deviation from the mean sphere is small. The lens offers the operating benefits of being constructed of lower refractive index glass (BK7), it gives a minimum focal spot of < 5μm and can be optimised to operate over a wide wavelength range by choosing an appropriate separation between the elements. A further important property of the new design is that 'ghost images' caused by reflections at the surfaces are all arranged to be outside the lens material. At the high powers ∿ 500GW at which these lenses are operated the energy in these ghost images can be sufficient to damage the glass.

Two prototype lenses have been manufactured to this new design. Measurements confirm that the design performance can be met in a practical lens and full power tests will be made to confirm the damage resistance of the lens early in 1978/79. A photograph of the first prototype is reproduced in figure 131.

Theoretical studies (1) have been made of the use of multiple beams for target irradiation particular reference being made to optimising the uniformity of illumination with a minimum number of beams. The result of these studies has been the decision to proceed in 1978/79 with a six-beam irradiation configuration using six f/1 lenses of the new design.

Ref. 1 D J Nicholas, R G Evans, Rutherford Laboratory Report RL-78-017/A.

1.7 GAS LASER DEVELOPMENT

The work of the gas laser development programme at the Rutherford Laboratory is aimed at evaluating the potential of new gas laser systems as future drivers for laser-matter interaction experiments. The main work of this programme will be carried out using a high power electron-beam machine which is presently under construction at the Rutherford Laboratory. This electron-beam-excited laser facility (ELF) will be used to investigate the characteristics of candidate high power gas lasers and will also be available for use by University scientists. Figure 132 is an artist's impression of what the ELF machine will look like in its final form.

ELF consists of a 15 Ω oil filled co-axial Blumlein which will be pulse charged by a twelve stage oil-immersed Marx generator which has an erected capacitance of approximately 42 nF. The output characteristics of the machine will be as follows: diode voltage, 1.5 MV; diode current, 60 KA; electron-beam pulse length, 50 nsec. Initially the machine will be fitted with a fine grain graphite cathode, configured to produce a 60 KA rectangular electron beam of dimensions (5 x 50) cm^2. This electron-beam configuration has been chosen for the excitation of large volume rare-gas halide lasers to be used in the first laser experiments.

The general design of the ELF machine was supplied to the Rutherford Laboratory by the high voltage research group at the Atomic Weapons Research Establishment (AWRE) at Aldermaston. The detailed design work and production of machine drawings has been carried out by Rutherford Laboratory personnel working in close collaboration with the AWRE group. Most of the fabrication work on the ELF machine was contracted out to local engineering companies and by the end of March 1978 the majority of the components had been delivered to the Rutherford Laboratory and assembly work was underway.

Initial physics experiments will concentrate on investigation of the recently discovered atomic selenium laser. In this system excited state selenium is produced by the photolysis of carbonyl selenide (OCSe):

$$OCSe + h\nu(uv) \rightarrow Se(^1S_o) + CO$$

followed by lasing in the selenium atom:

$$Se(^1S_o) \rightarrow Se(^3P_1) + h\nu_{laser}$$

In this system lasing occurs at 488 nm. In the Rutherford Laboratory experiments the excited selenium atoms will be produced by photolysis of carbonyl selenide (OCSe) or carbon sulphoselenide (SCSe) gas by an electron beam pumped rare gas halide laser. ArF will be used to photolyse OCSe and photolysis of SCSe will be attempted using ArF and KrCl lasers.

Apparatus is presently being constructed to produce OCSe and SCSe by reacting C and CS_2 respectively with Se. In addition, oven controlled, microwave discharge, selenium lamps have been developed and tested which will be used to monitor ground state and excited state selenium concentrations in the photolysis cell by ultraviolet absorption spectrometry. Finally a rare gas halide laser cell is being designed which will fit on the ELF machine and will produce an elongated output beam which will be capable of photolysing a long path (50-100 cm) OCSe and SCSe cell. A rare gas halide laser pulse energy of 10 to 50 J is expected which should be sufficient to photolyse large enough quantities of OCSe or SCSe for laser action in selenium to be achieved.

This section of the report was prepared by J E Boon, P Gottfeldt, I N Ross, P T Rumsby, W T Toner, M S White, P R Williams of the Rutherford Laboratory on behalf of the Facility Development Group of the Scientific Programme and Scheduling Committee. The assistance of many other members of the Rutherford Laboratory Laser Division is gratefully acknowledged.

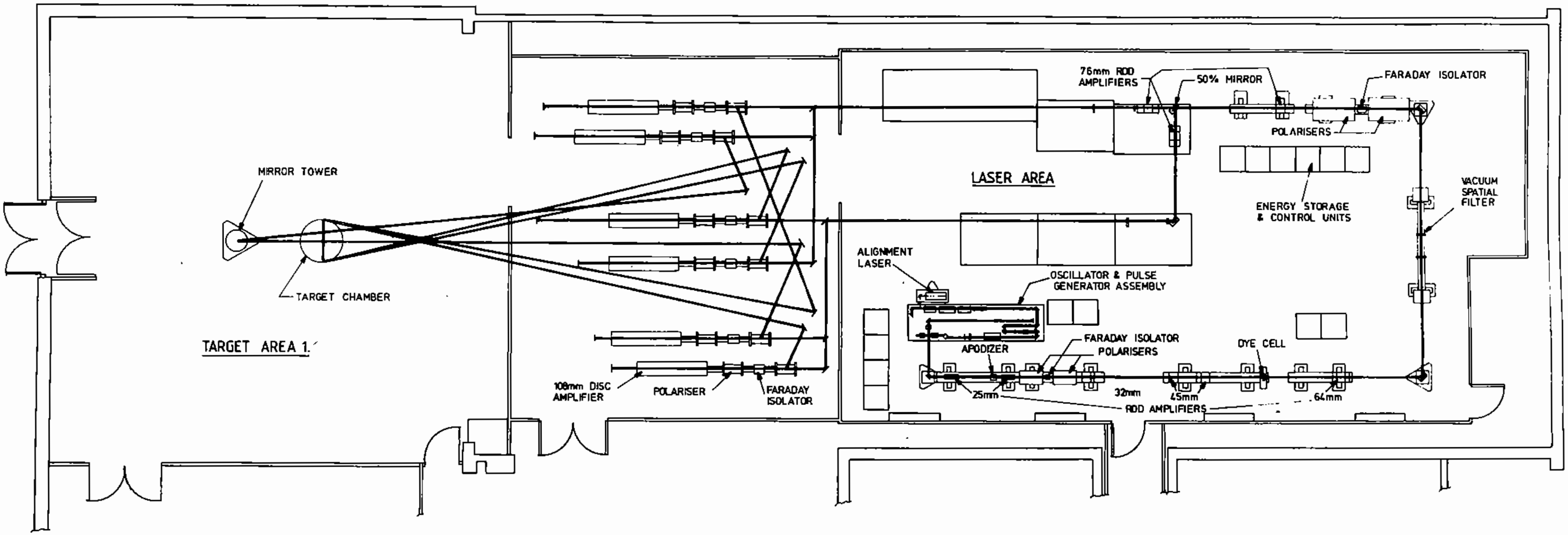

6 BEAM Nd: GLASS LASER SYSTEM.

FIG. 101

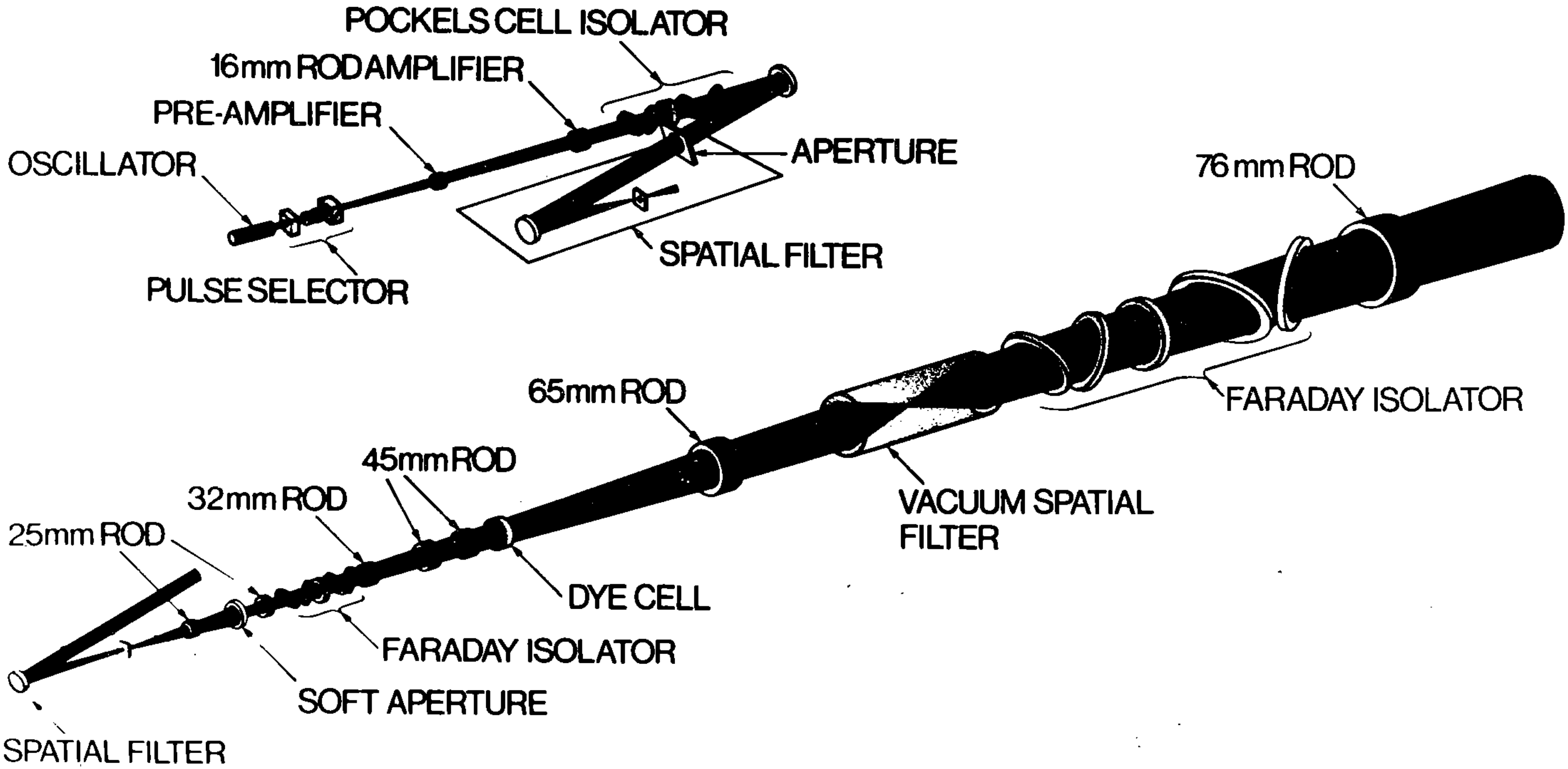
POCKELS CELL ISOLATOR
16mm ROD AMPLIFIER
PRE-AMPLIFIER
OSCILLATOR
APERTURE
76 mm ROD
SPATIAL FILTER
PULSE SELECTOR
FARADAY ISOLATOR
65mm ROD
45mm ROD
32mm ROD
25mm ROD
VACUUM SPATIAL FILTER
DYE CELL
FARADAY ISOLATOR
SOFT APERTURE
SPATIAL FILTER

FIG, 102

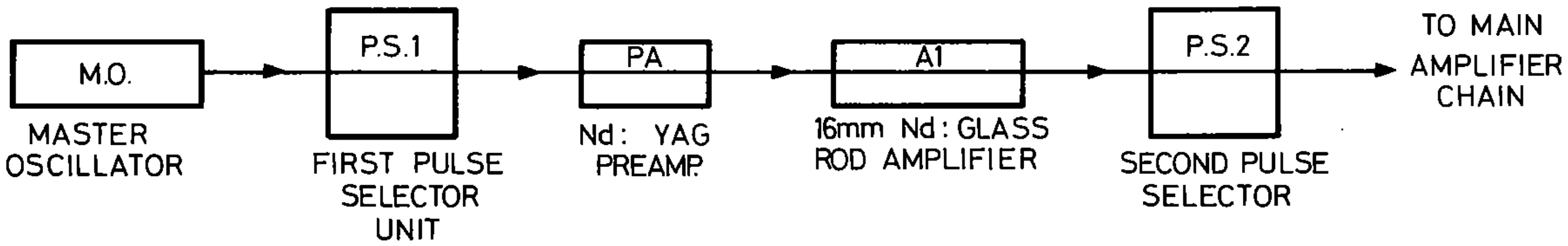

FIGURE 103 ORIGINAL LAYOUT OF QUANTEL PULSE GENERATOR COMPONENTS

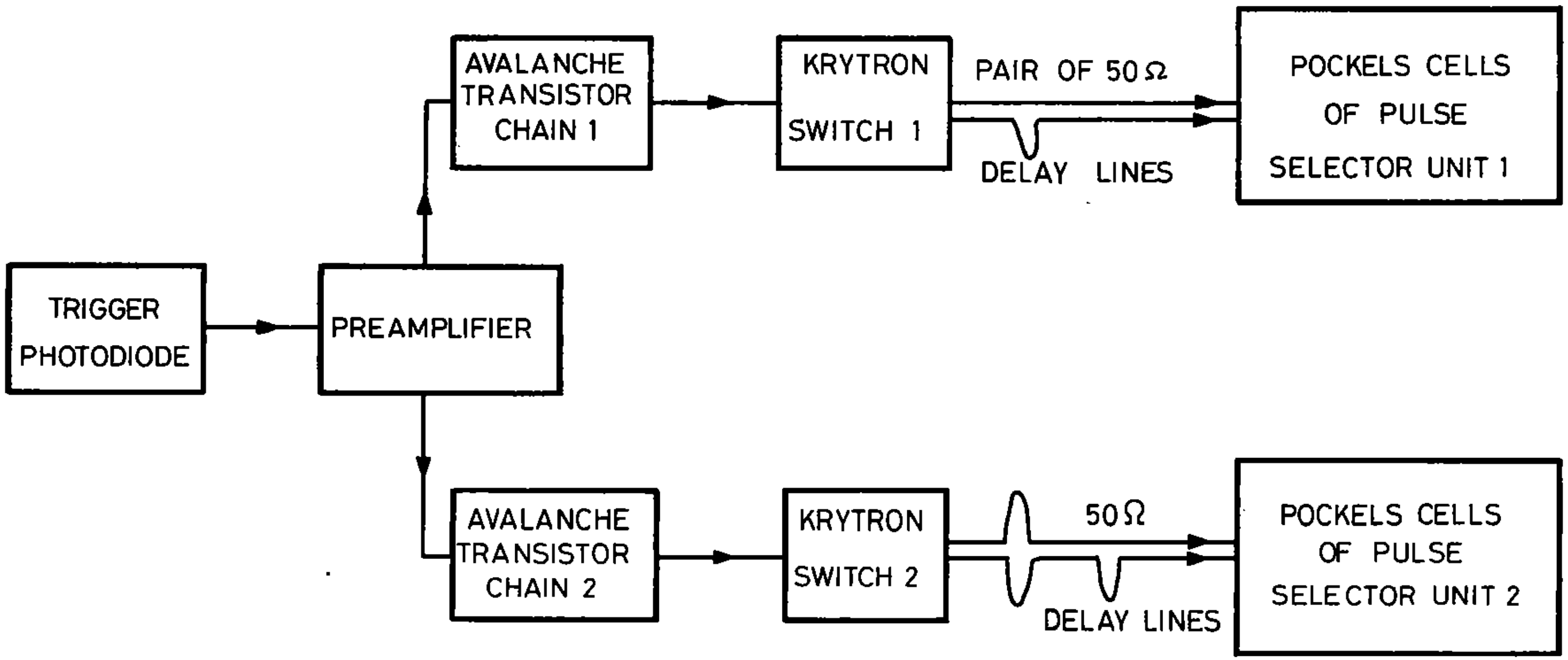

FIGURE 104 SCHEMATIC OF ORIGINAL QUANTEL DRIVING CIRCUIT FOR THE PULSE SELECTOR UNITS

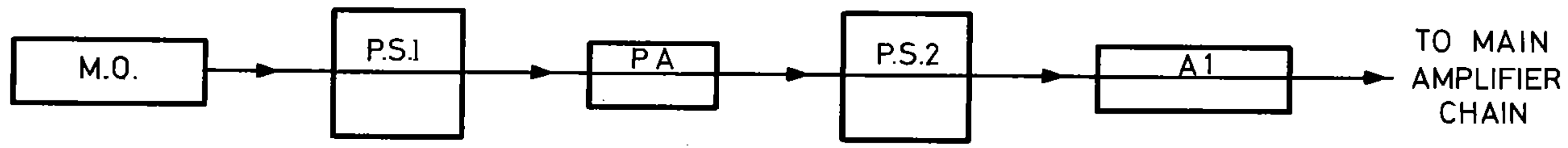

FIGURE 105 MODIFIED LAYOUT OF QUANTEL PULSE GENERATOR COMPONENTS WITH AMPLIFIER AND SECOND PULSE SELECTOR REVERSED

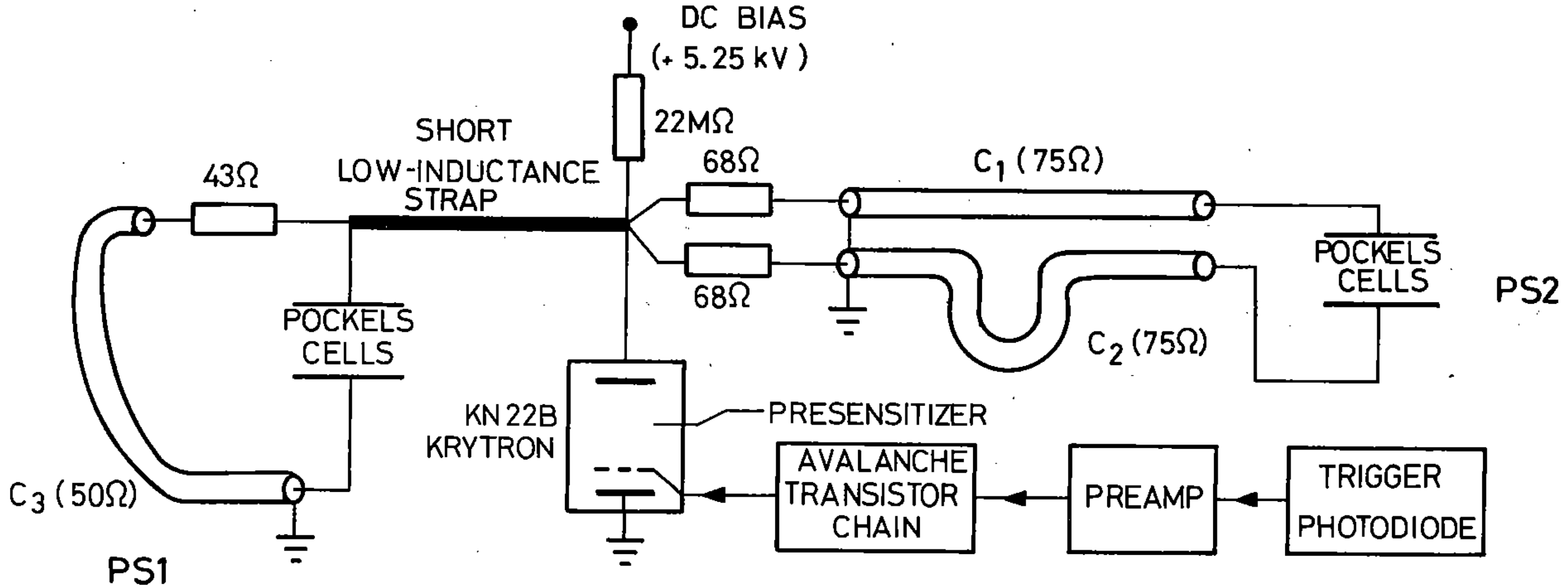

FIGURE 106 NEW PULSE SELECTOR DRIVING CIRCUIT

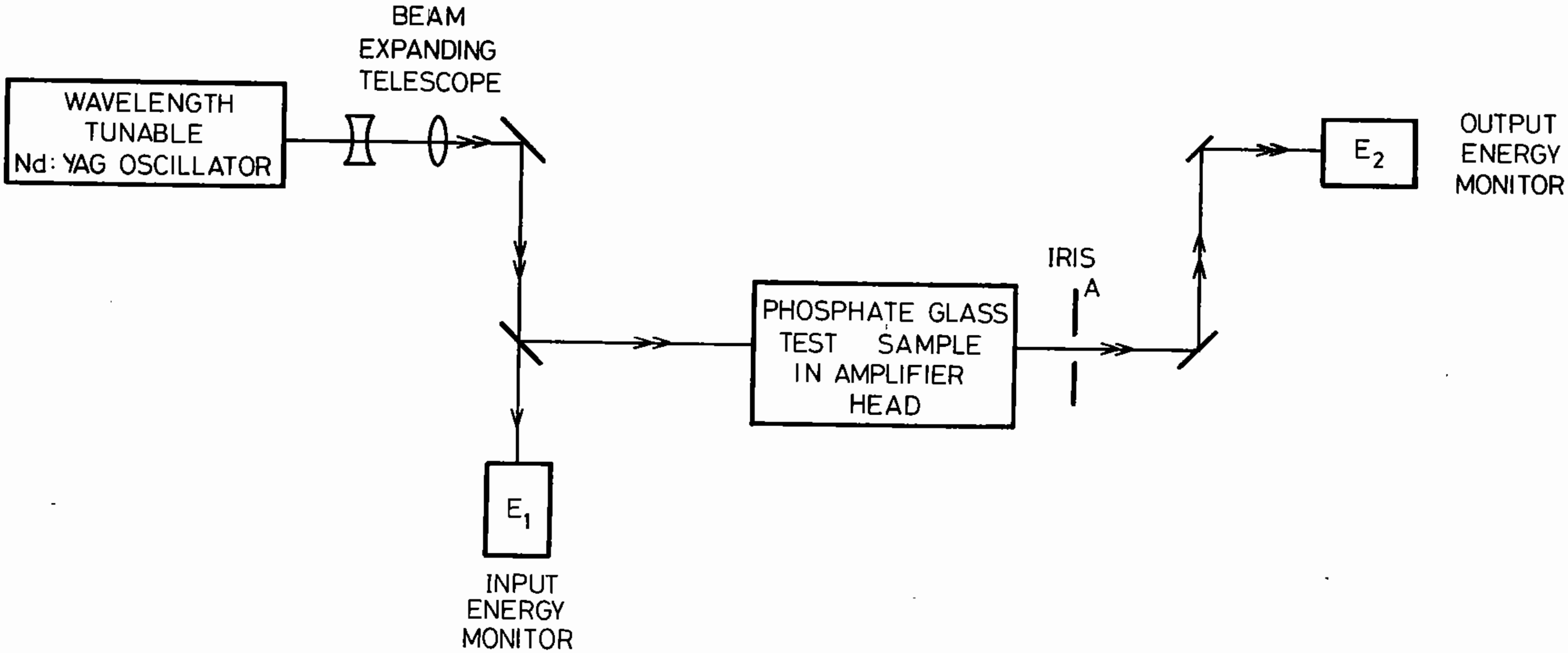

FIGURE 107 EXPERIMENTAL ARRANGEMENT FOR GAIN MEASUREMENTS ON PHOSPHATE GLASS AMPLIFIERS

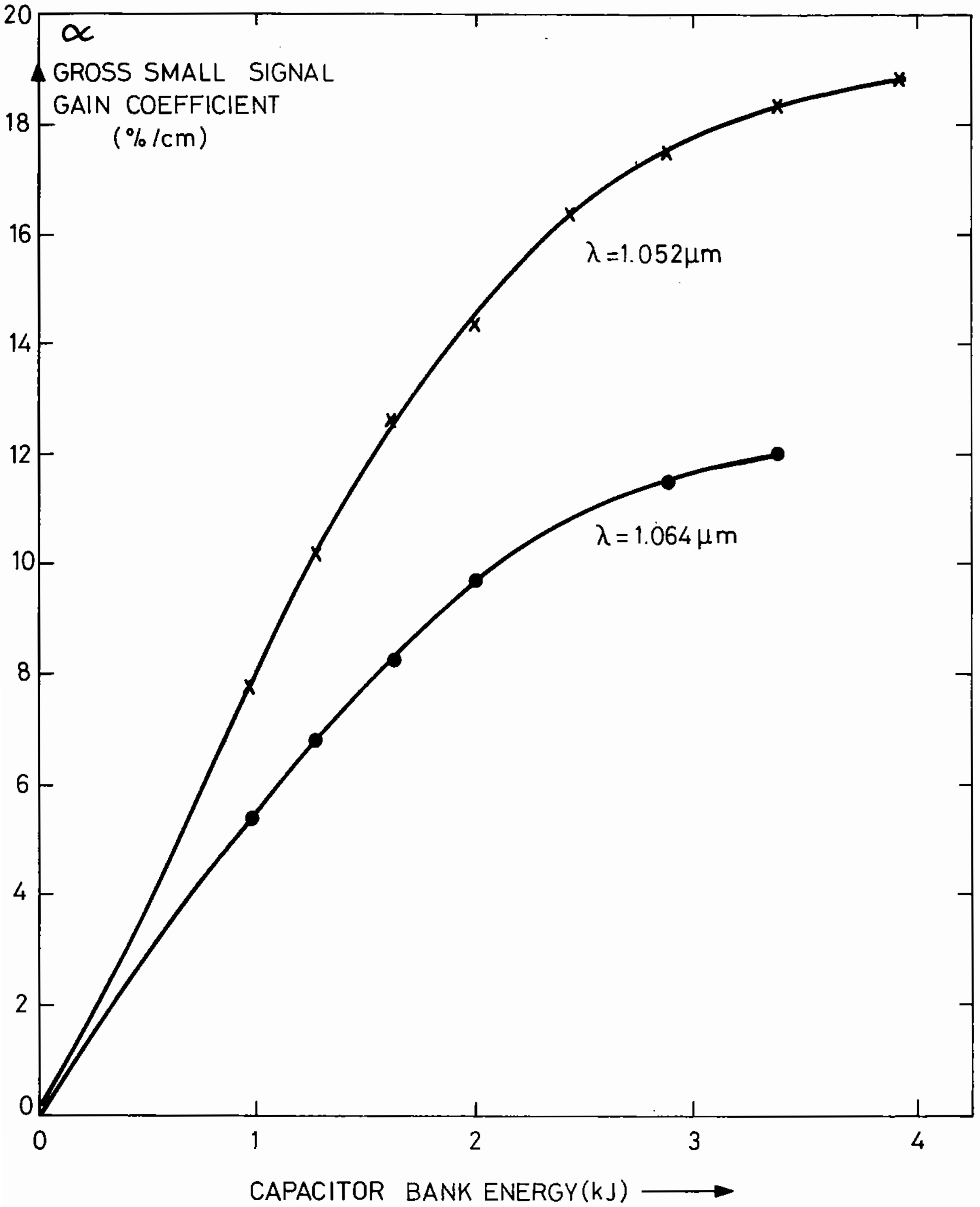

FIGURE 108. SMALL SIGNAL GAIN versus INPUT ENERGY FOR EV2 PHOSPHATE ROD IN 16mm HEAD

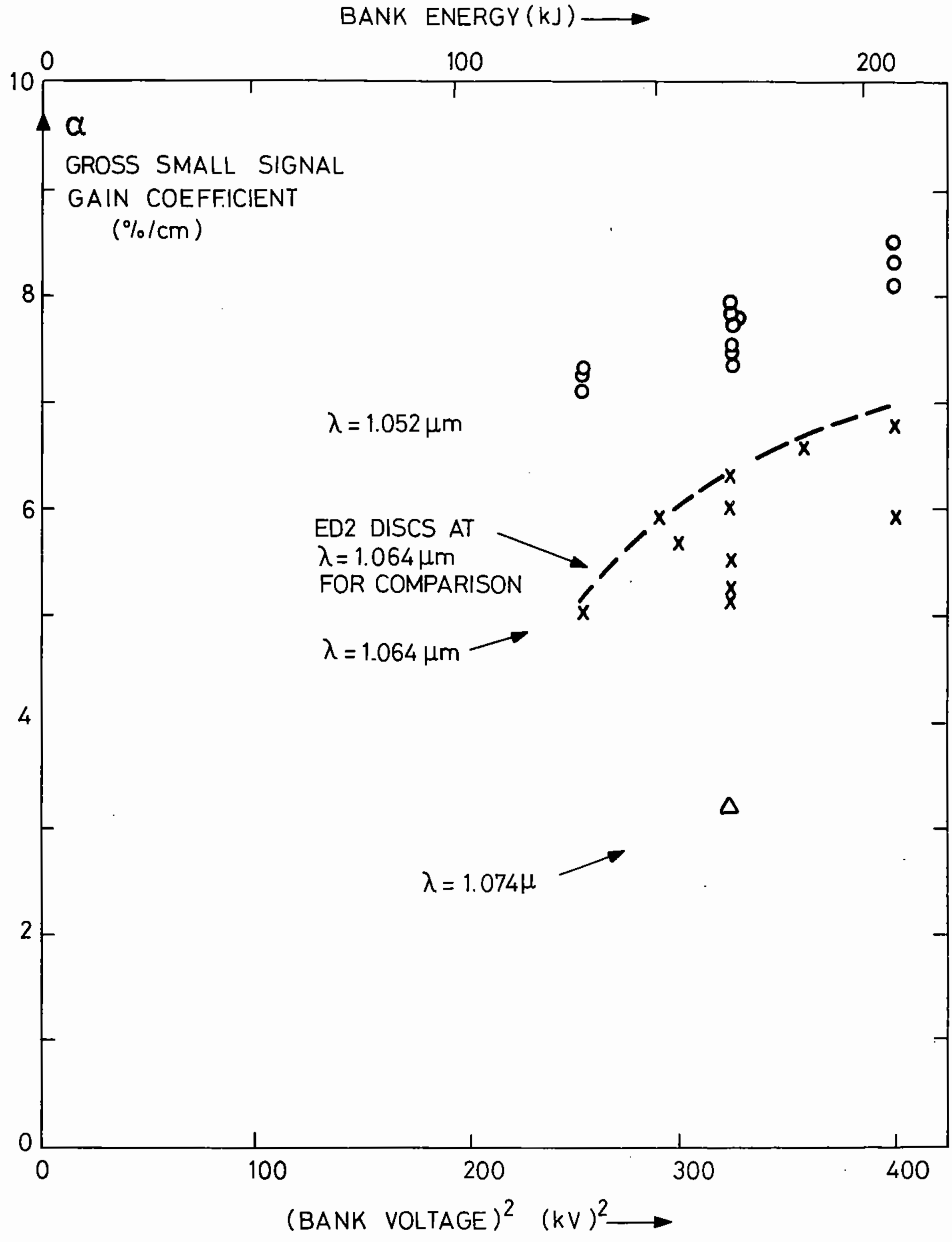

FIGURE 109. GAIN OF PAIR OF Q88 PHOSPHATE DISCS AS A FUNCTION OF BANK ENERGY AT λ = 1.052, 1.064, AND 1.074 μm

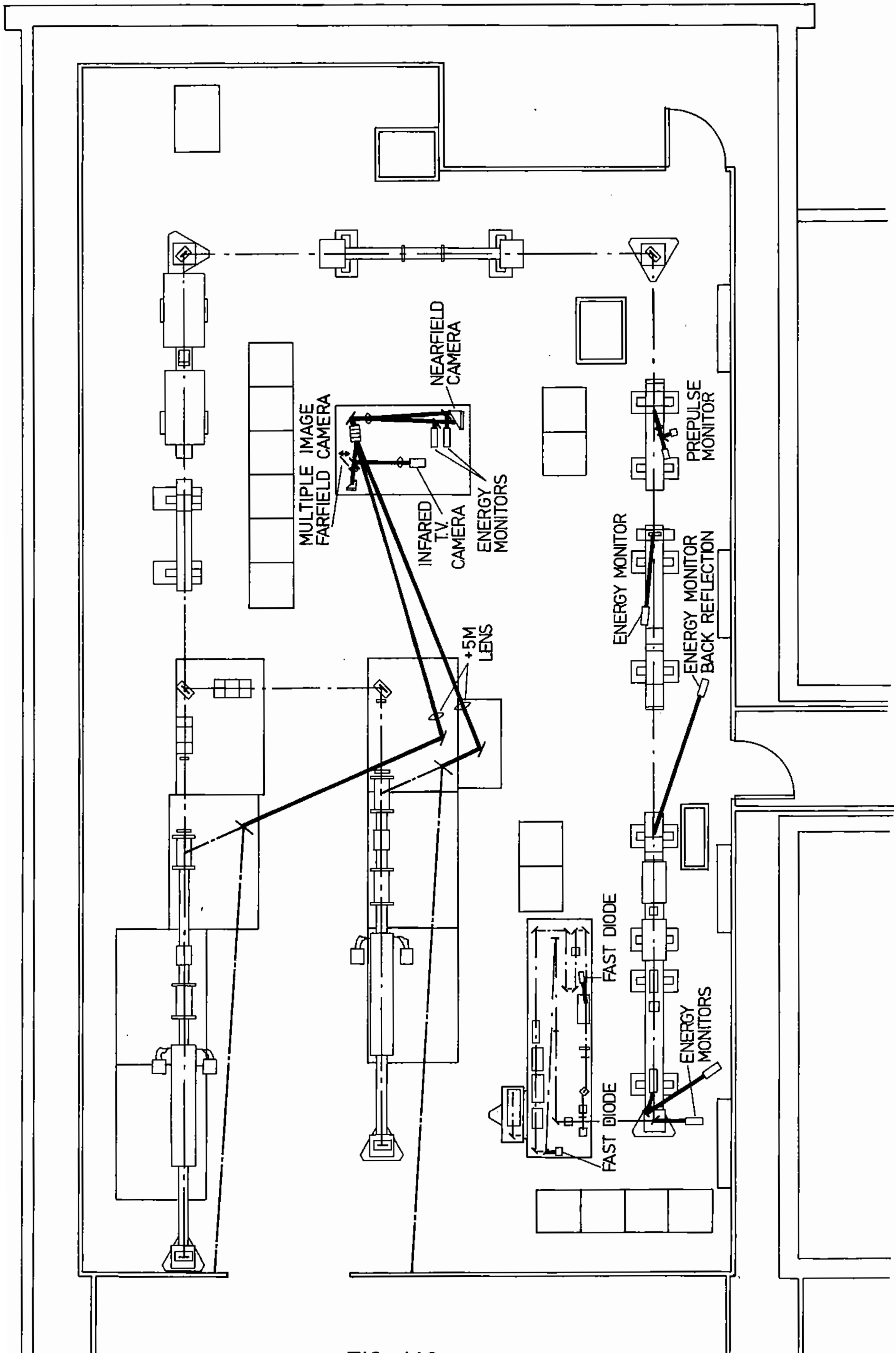
NEARFIELD CAMERA
MULTIPLE IMAGE FARFIELD CAMERA
INFARED T.V. CAMERA
ENERGY MONITORS
+5M LENS
PREPULSE MONITOR
ENERGY MONITOR
ENERGY MONITOR BACK REFLECTION
FAST DIODE
FAST DIODE
ENERGY MONITORS

FIG. 110

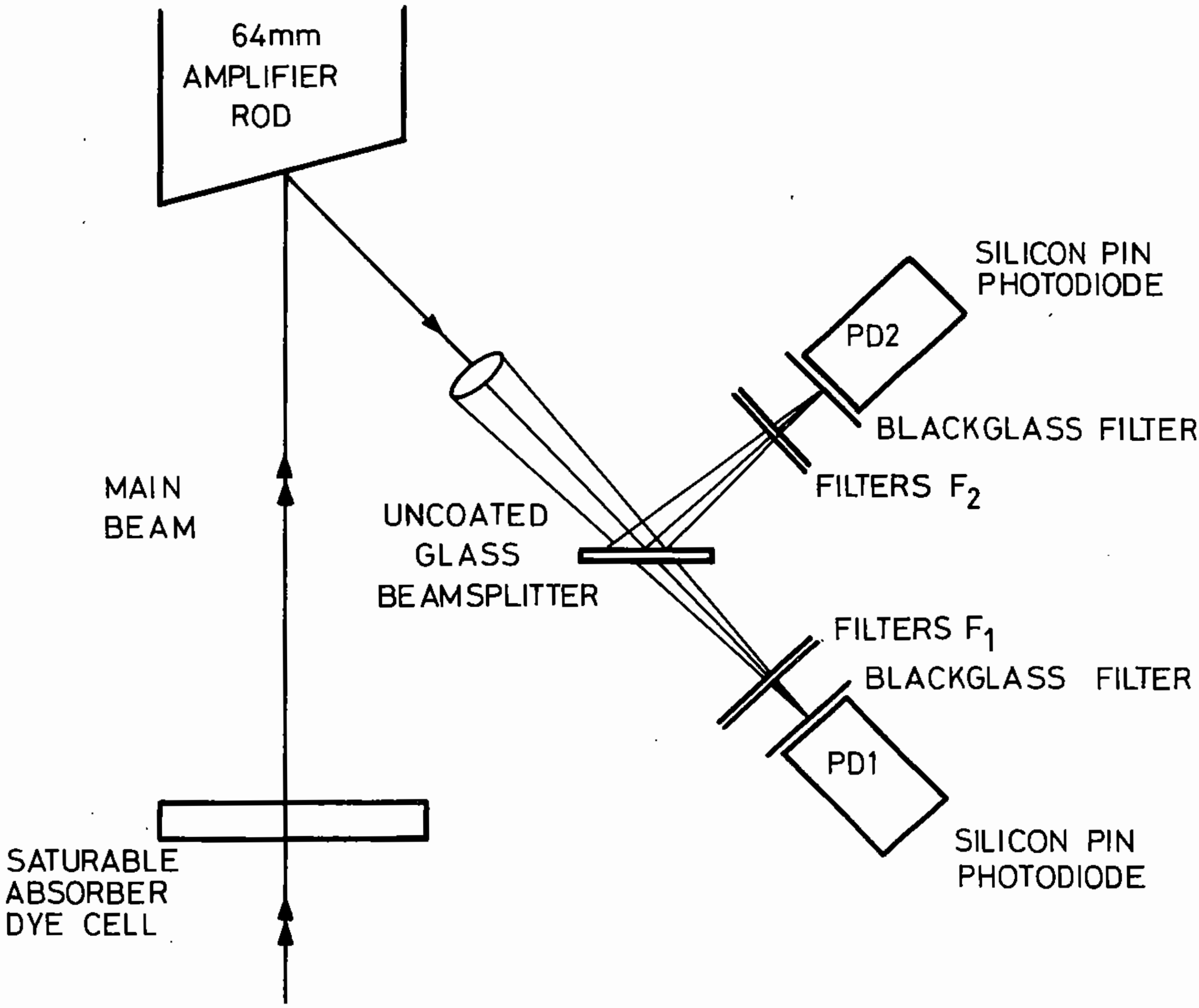

FIGURE 111 .OPTICAL LAYOUT OF THE PREPULSE MONITOR

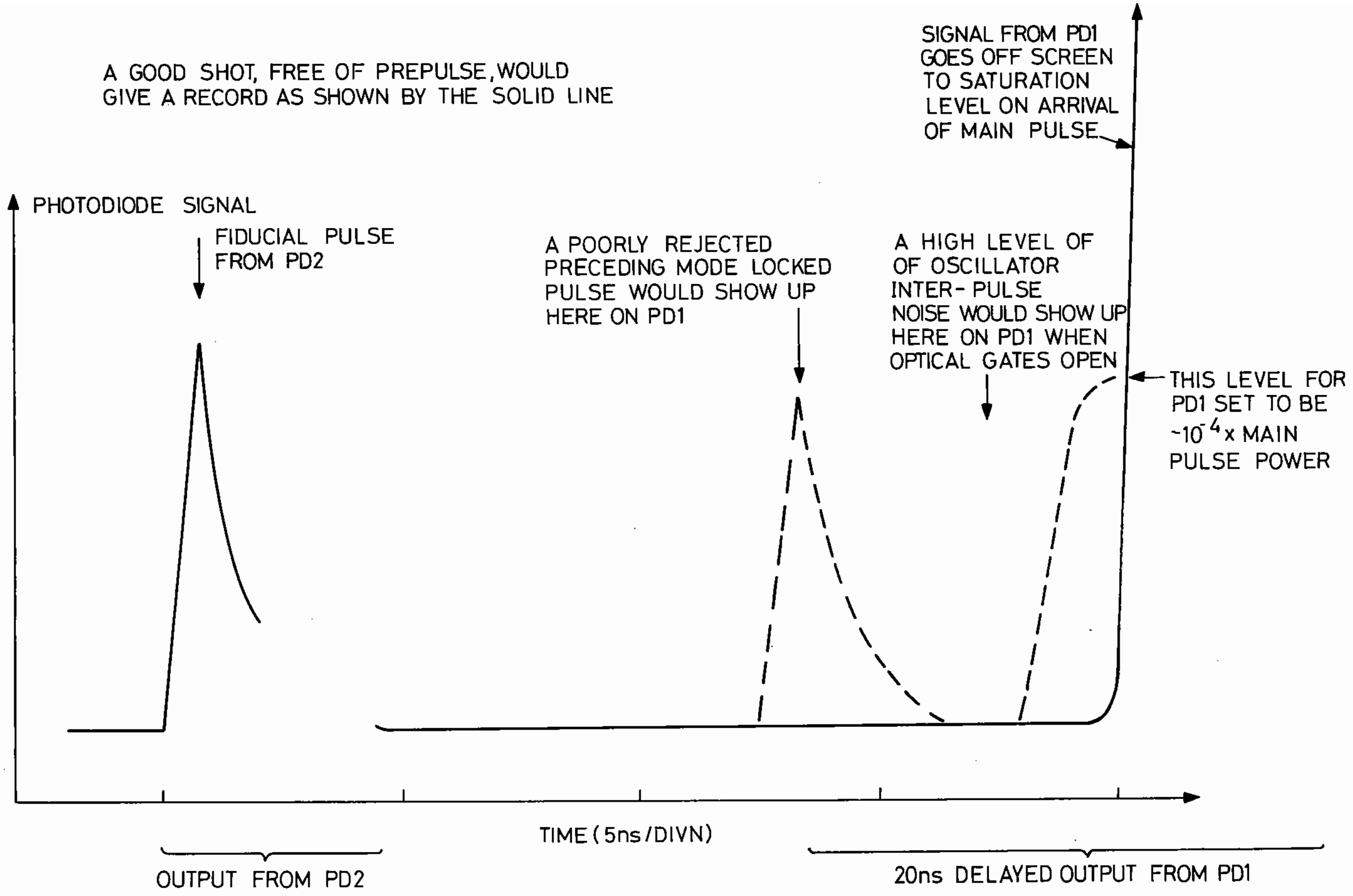

FIGURE 112. SKETCH OF THE MAIN FEATURES OF A PREPULSE MONITOR RECORD

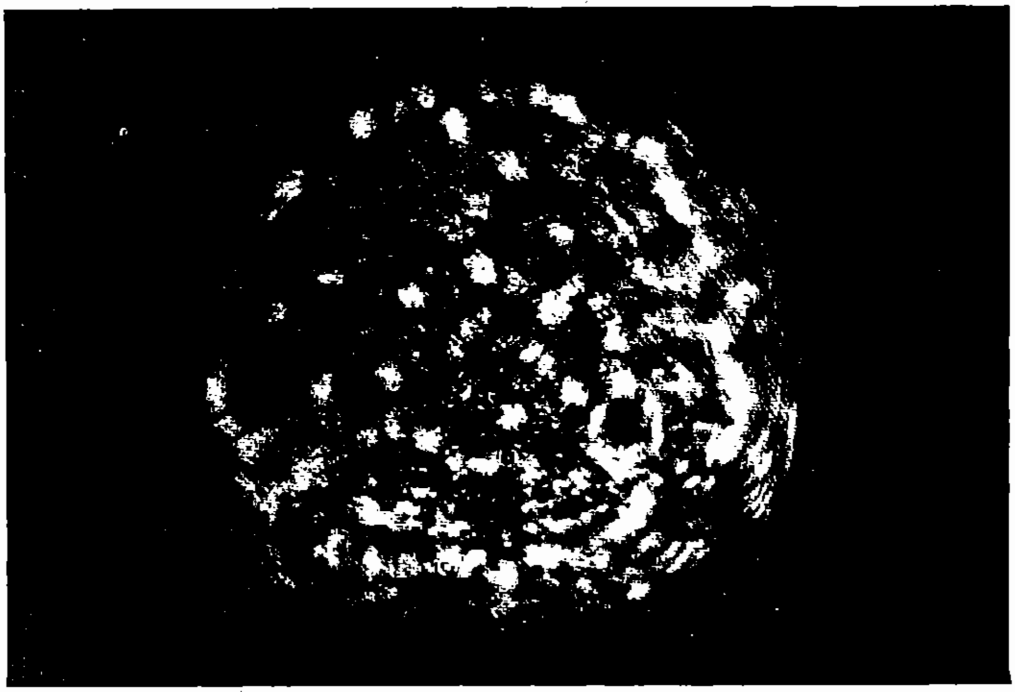

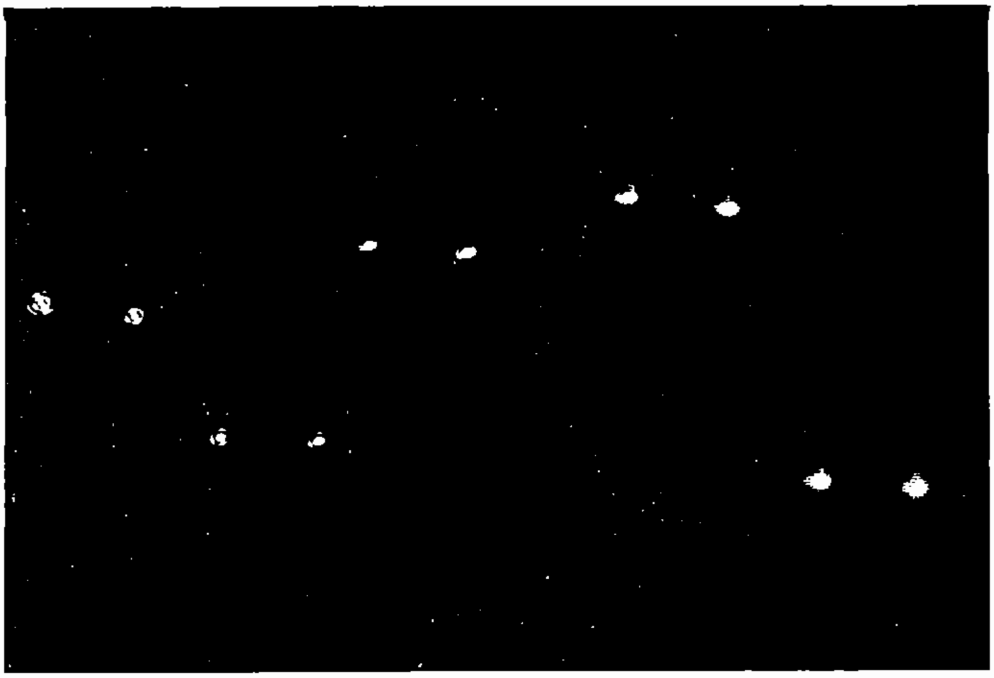

FIG. 113

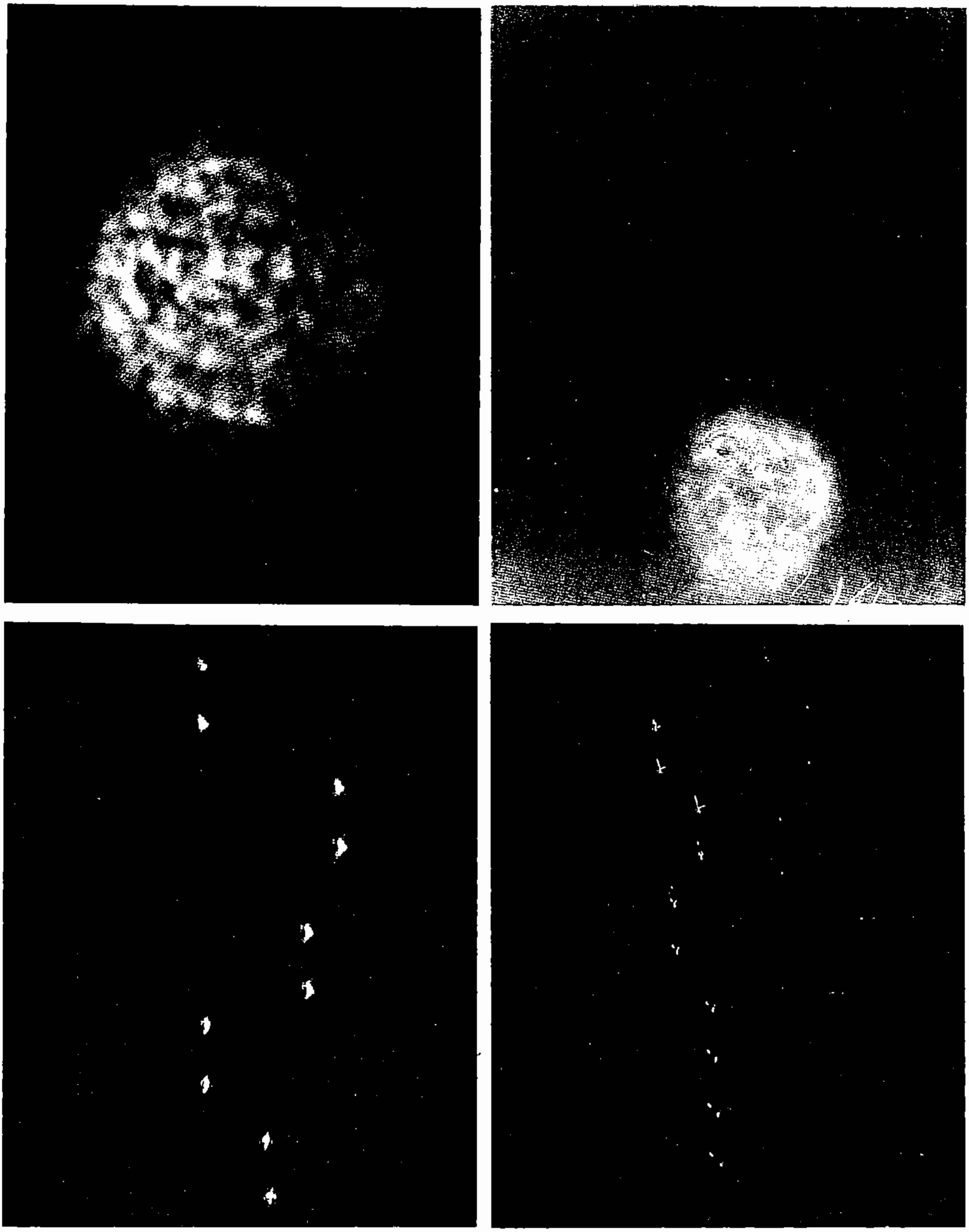

FIG. 114

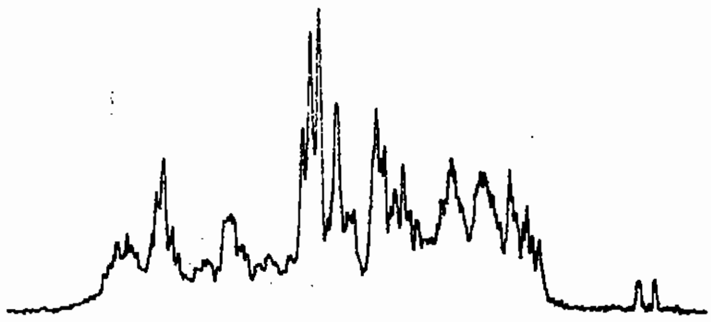

FIG. 115

FIG. 116

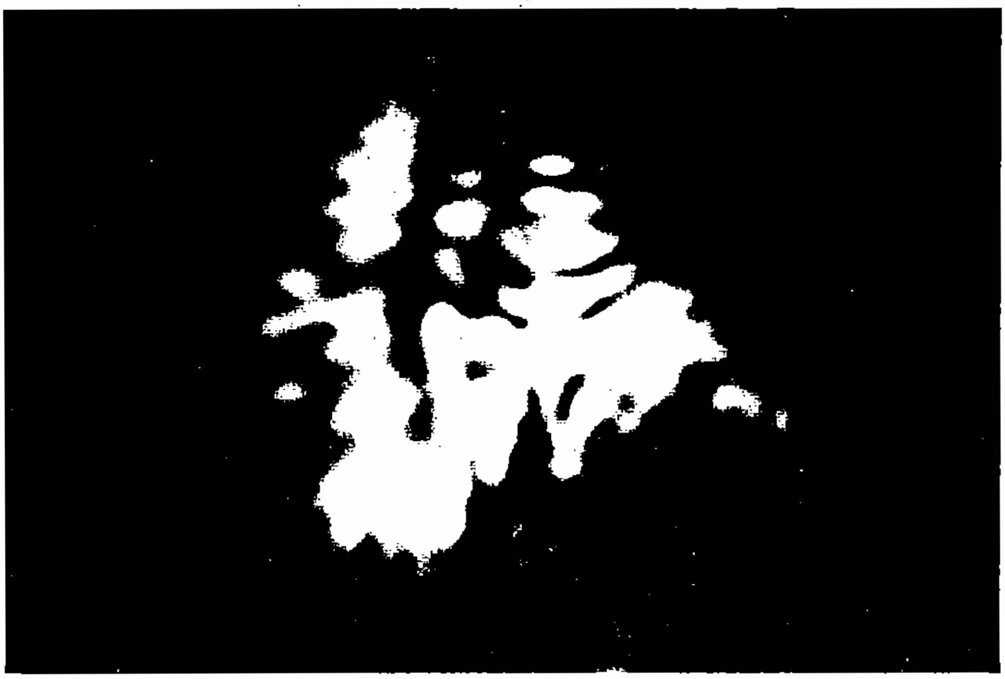

FIG. 117

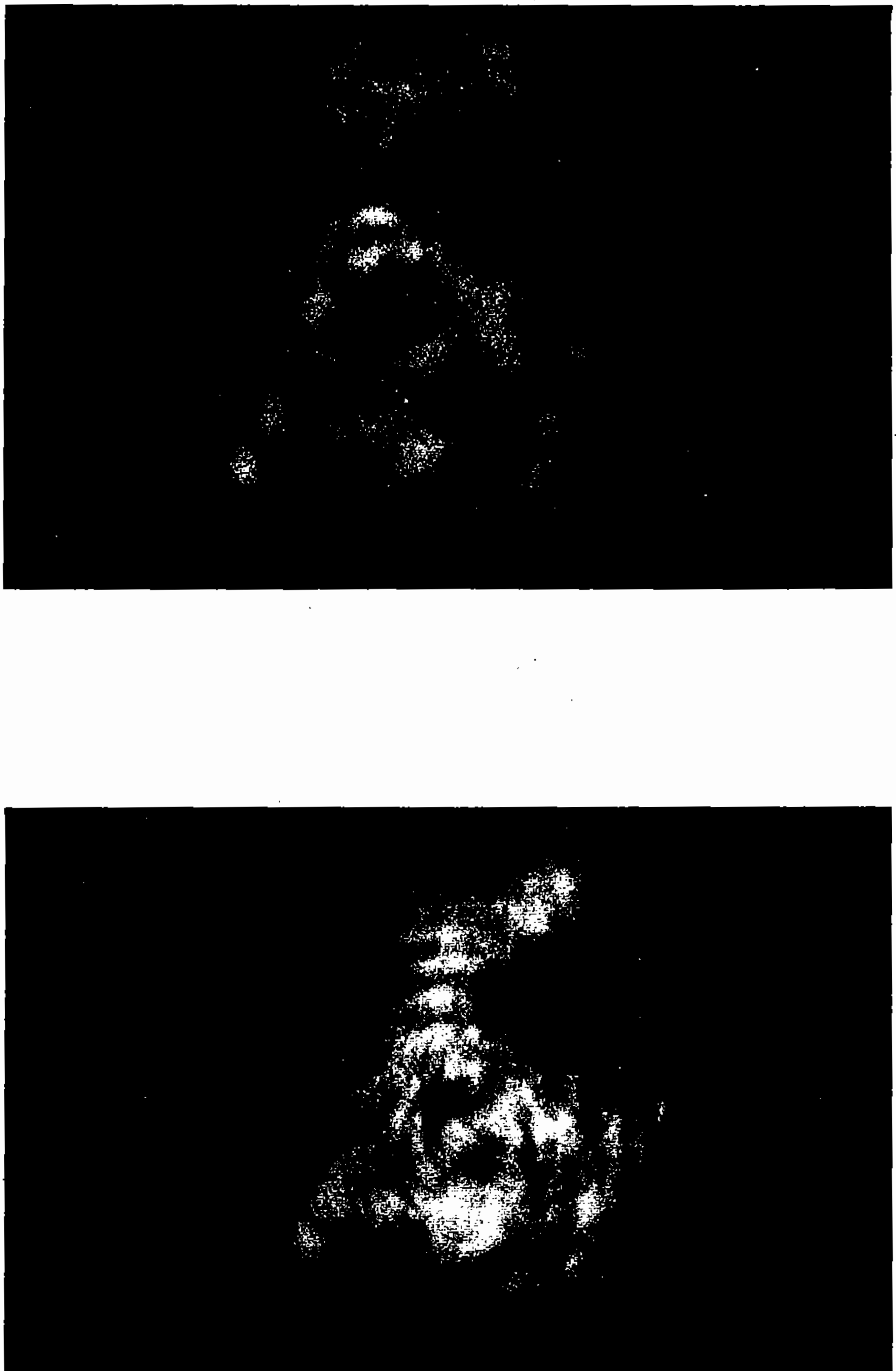

FIG. 118

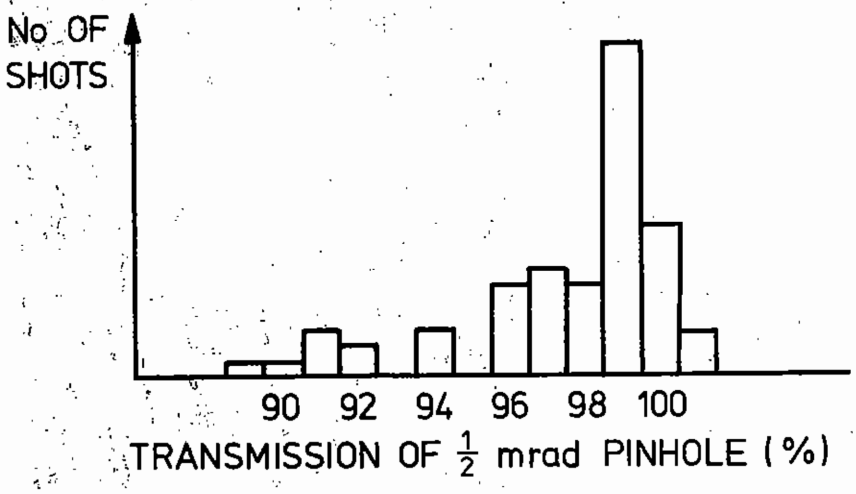

LASER DIVERGENCE

FIG. 119

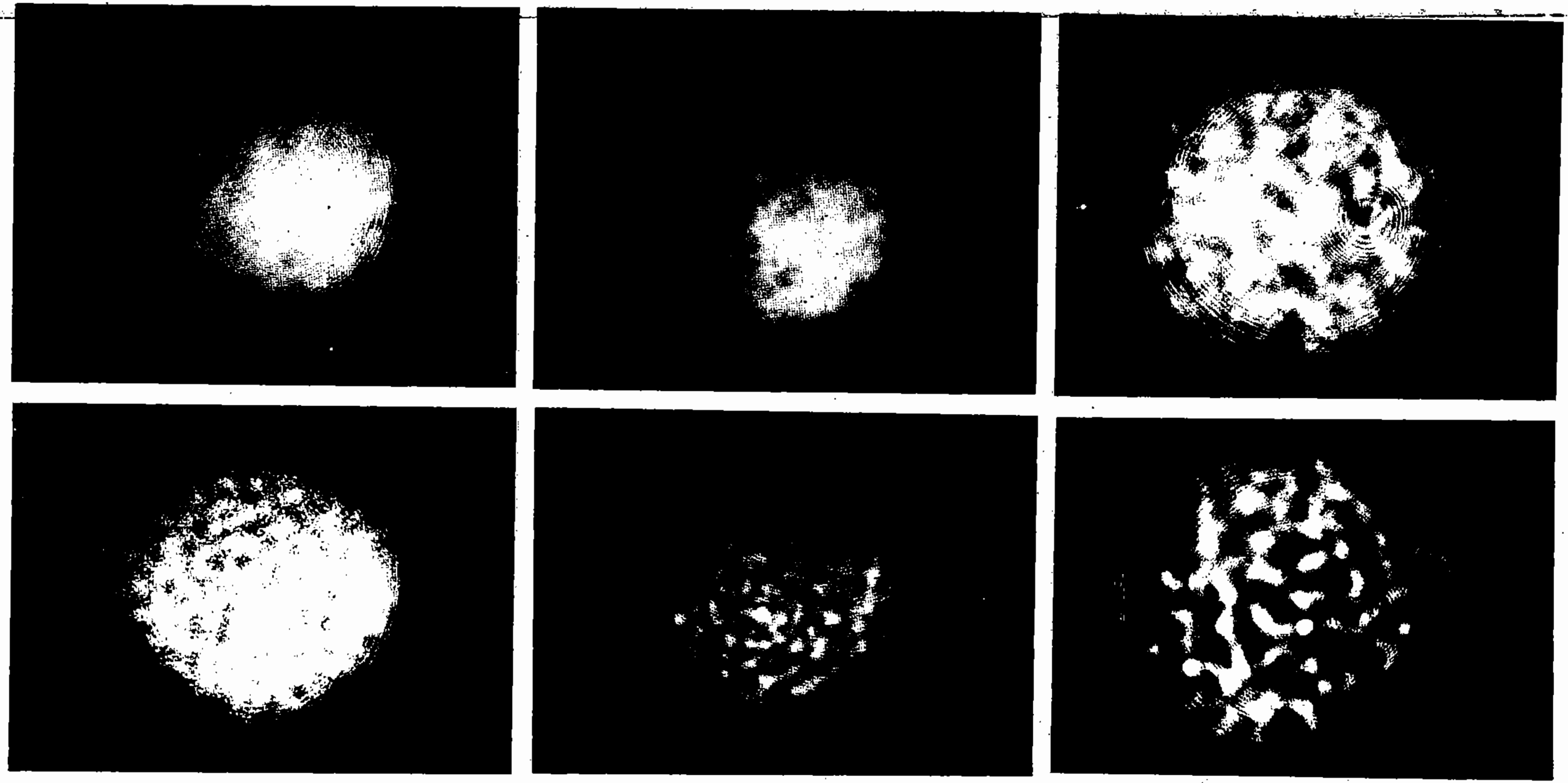

FIG. 120

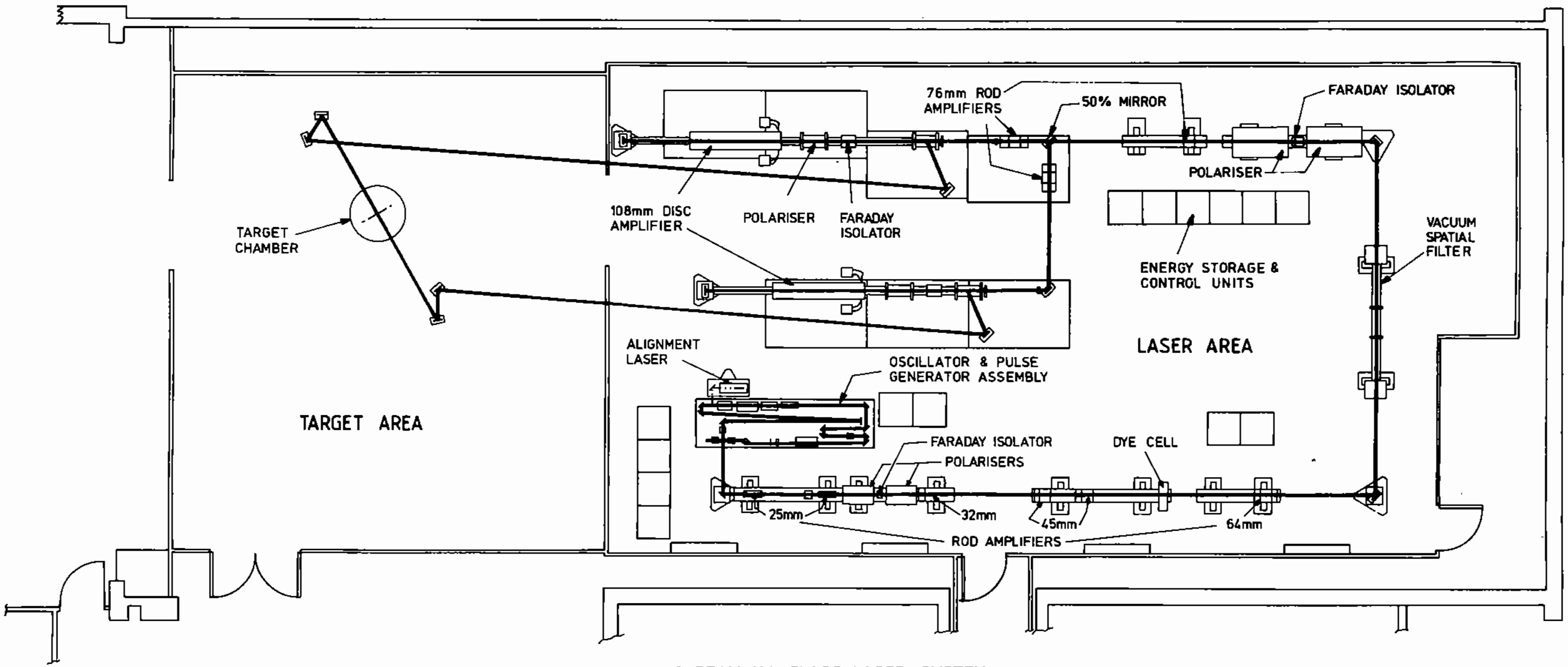

2 BEAM Nd: GLASS LASER SYSTEM.

FIG. 121

MODE I. Single beam - rod amplifier only.

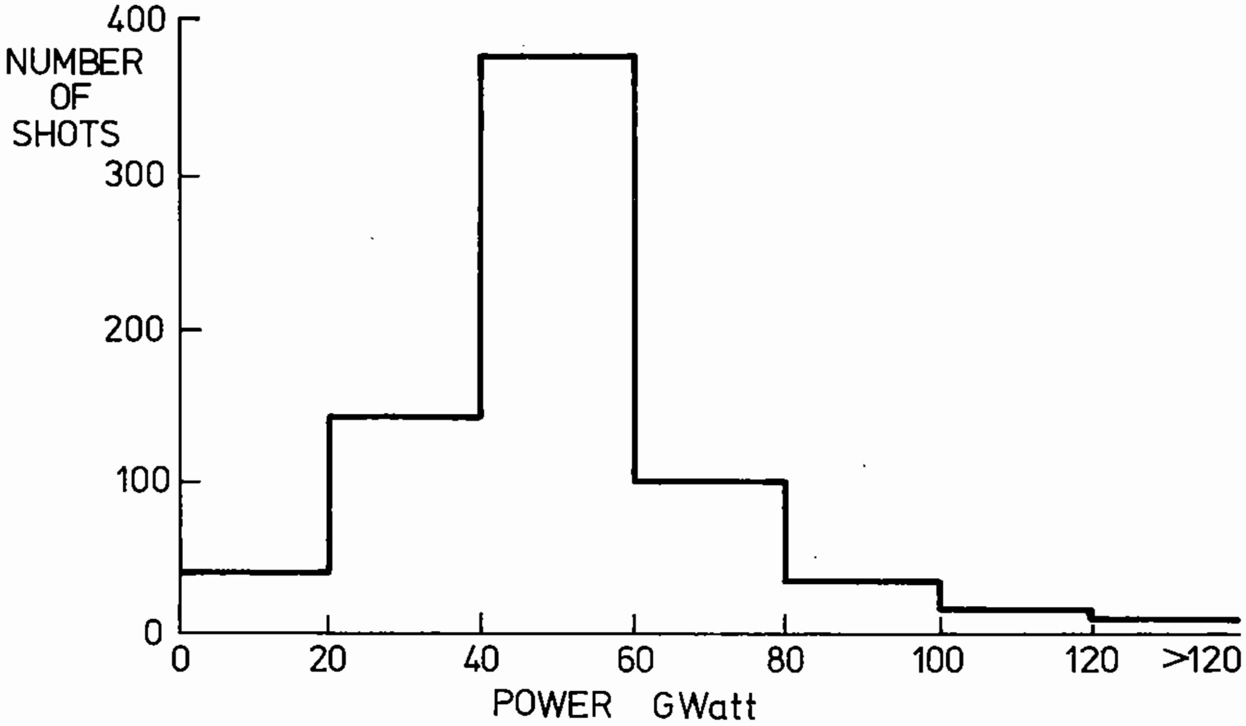

TOTAL SCHEDULED TIME	13 WEEKS
TOTAL NUMBER OF TARGET SHOTS	723
SETTING UP AND CALIBRATION SHOTS	179
NON USABLE TARGET SHOTS	127
TARGET OPERATING EFFICIENCY	82 %

FIG. 122

MODE II. Single beam – rod amplifier + one disc amplifier.

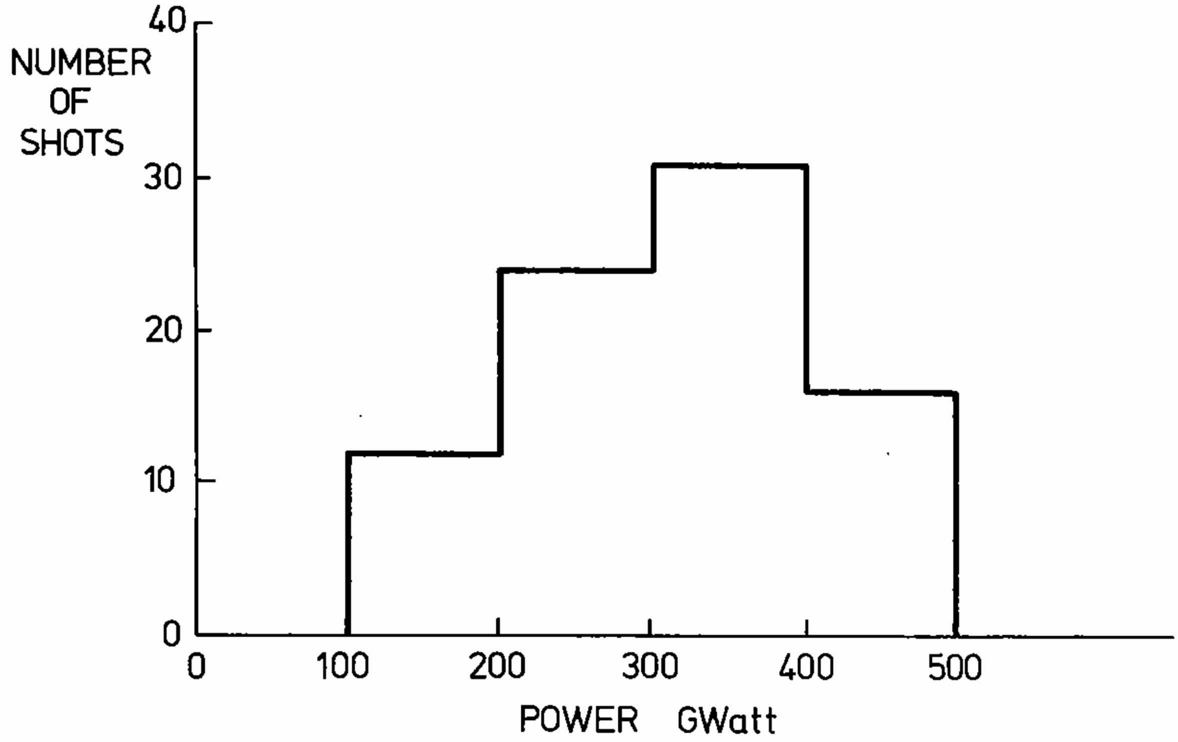

TOTAL SCHEDULED TIME	5 WEEKS
TOTAL NUMBER OF TARGET SHOTS	83
SETTING UP AND CALIBRATION SHOTS	22
NON USABLE TARGET SHOTS	12
TARGET OPERATING EFFICIENCY	85 %

FIG. 123

MODE III Double beam

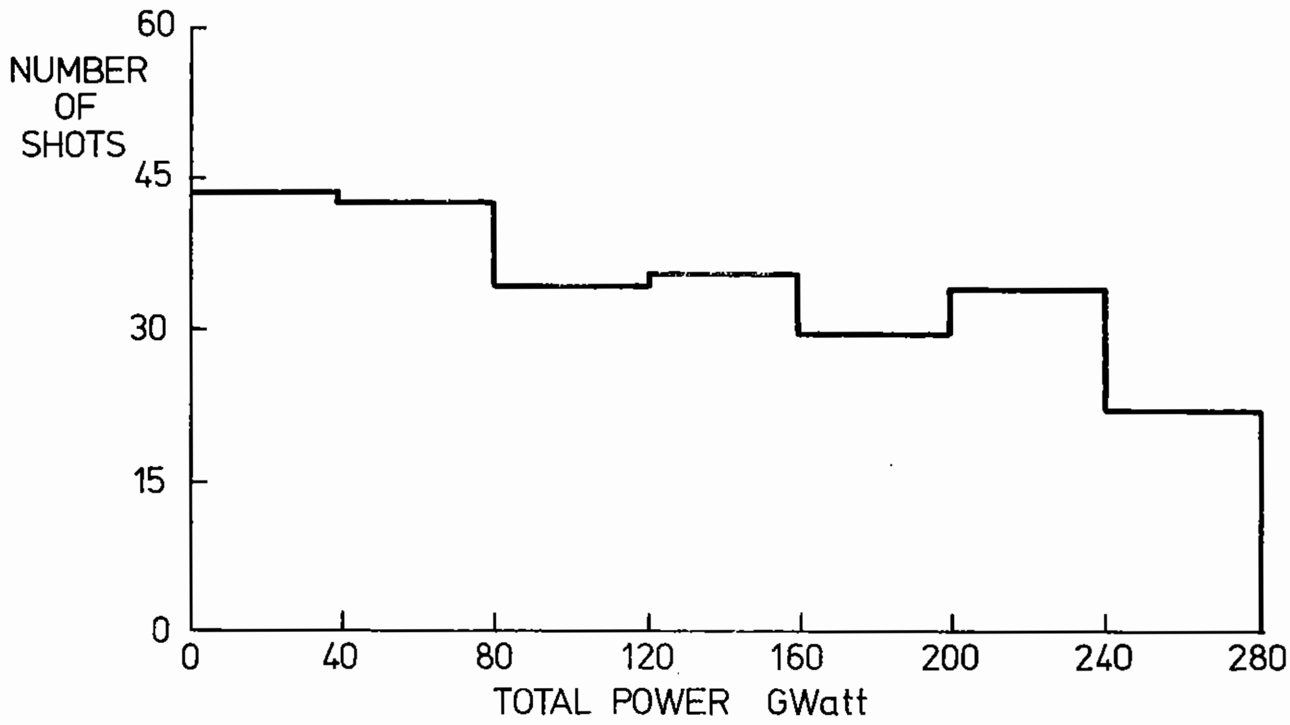

TOTAL SCHEDULED TIME	20 WEEKS
TOTAL NUMBER OF TARGET SHOTS	242
* SETTING UP AND CALIBRATION SHOTS	52 with discs
" " " " "	280 without discs
NON USABLE TARGET SHOTS	50
TARGET OPERATING EFFICIENCY	80 %

* This record includes time spent in adjustment and calibration of the laser for two beam operation.

FIG. 124

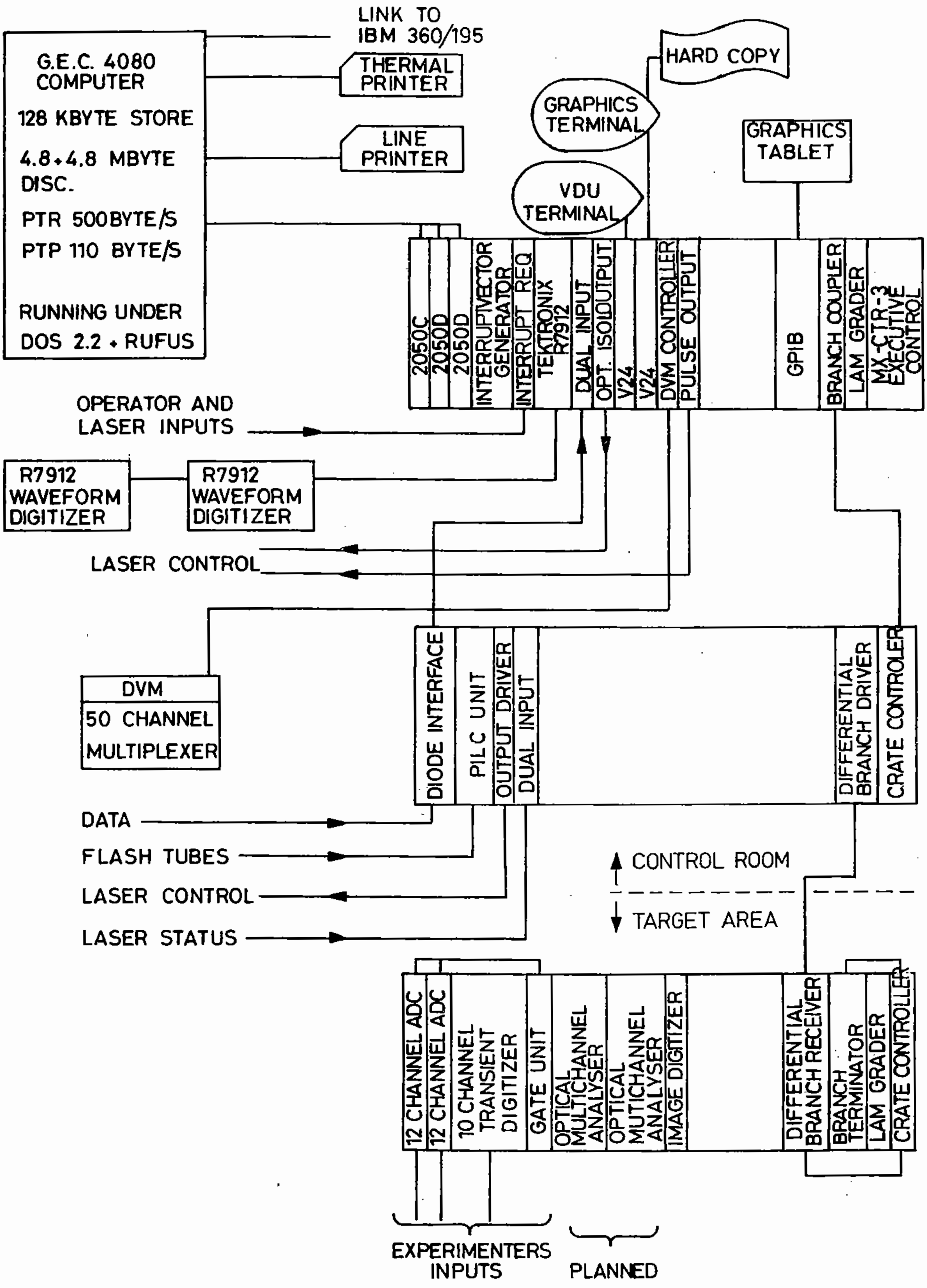

LASER COMPUTER CONTROL AND DATA ACQUISITION

FIG. 125

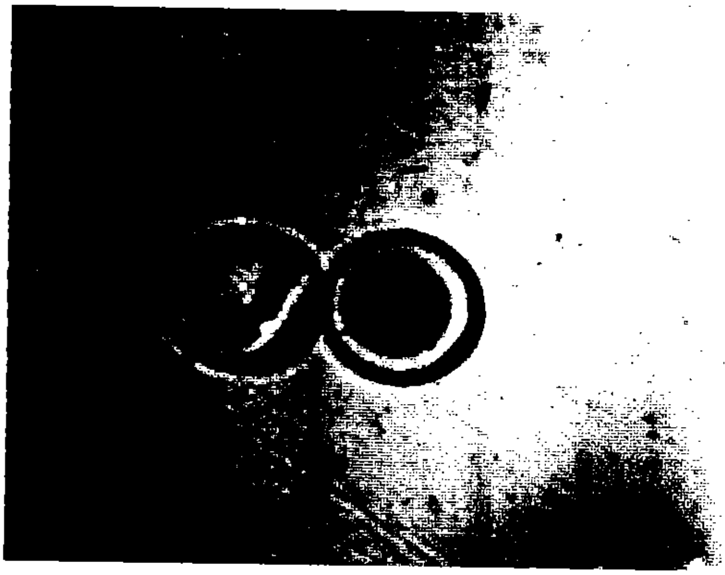

FIG. 126

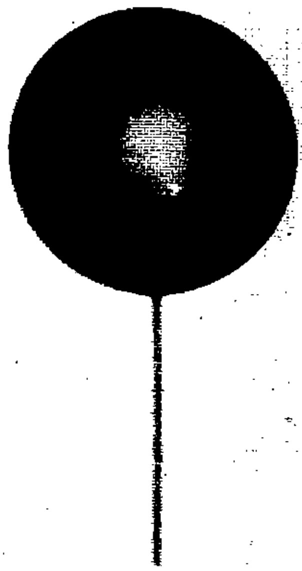

FIG. 127

RUTHERFORD

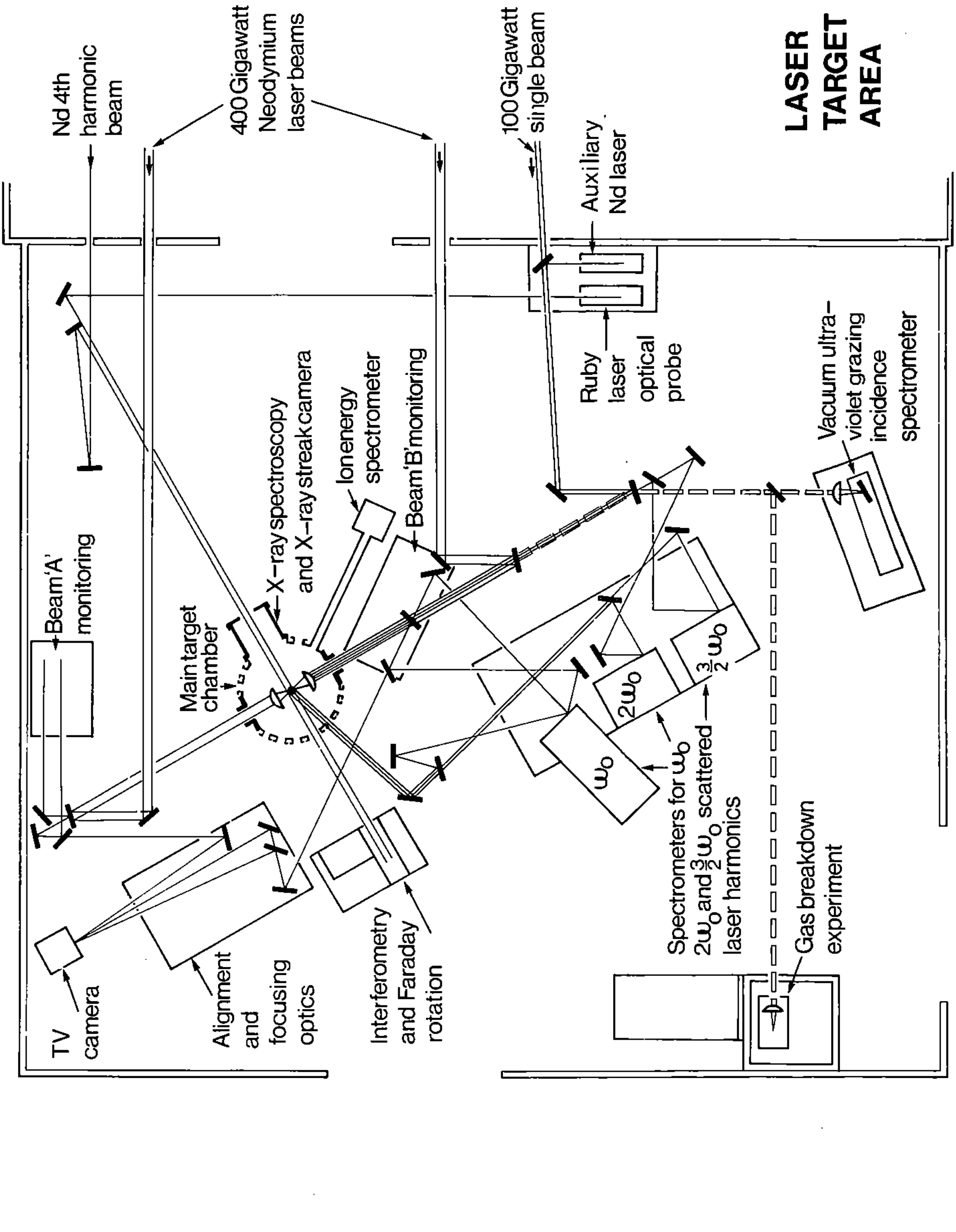

FIG. 128

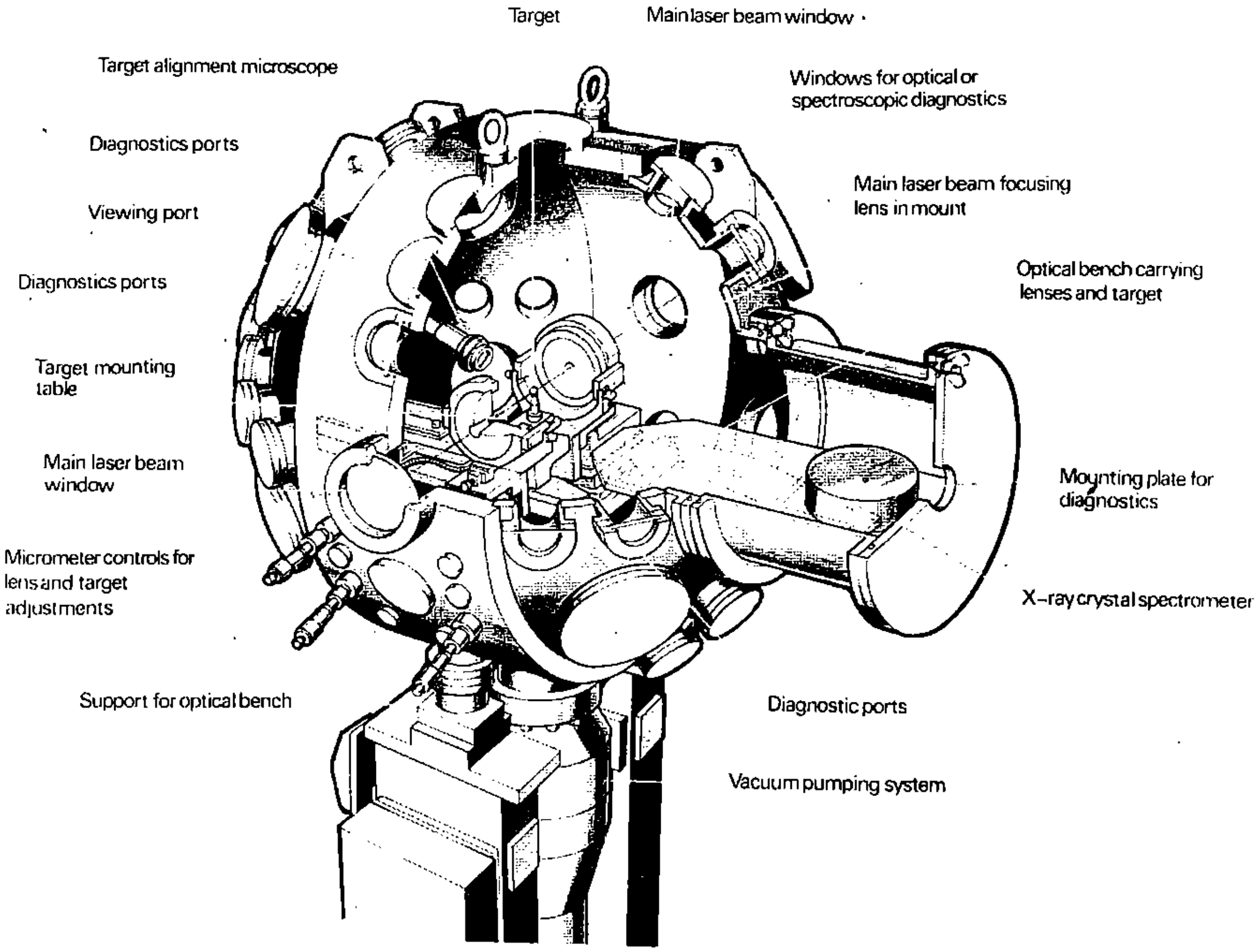
Target
Main laser beam window
Target alignment microscope
Windows for optical or spectroscopic diagnostics
Diagnostics ports
Main laser beam focusing lens in mount
Viewing port
Optical bench carrying lenses and target
Diagnostics ports
Target mounting table
Main laser beam window
Mounting plate for diagnostics
Micrometer controls for lens and target adjustments
X-ray crystal spectrometer
Support for optical bench
Diagnostic ports
Vacuum pumping system

FIG. 129

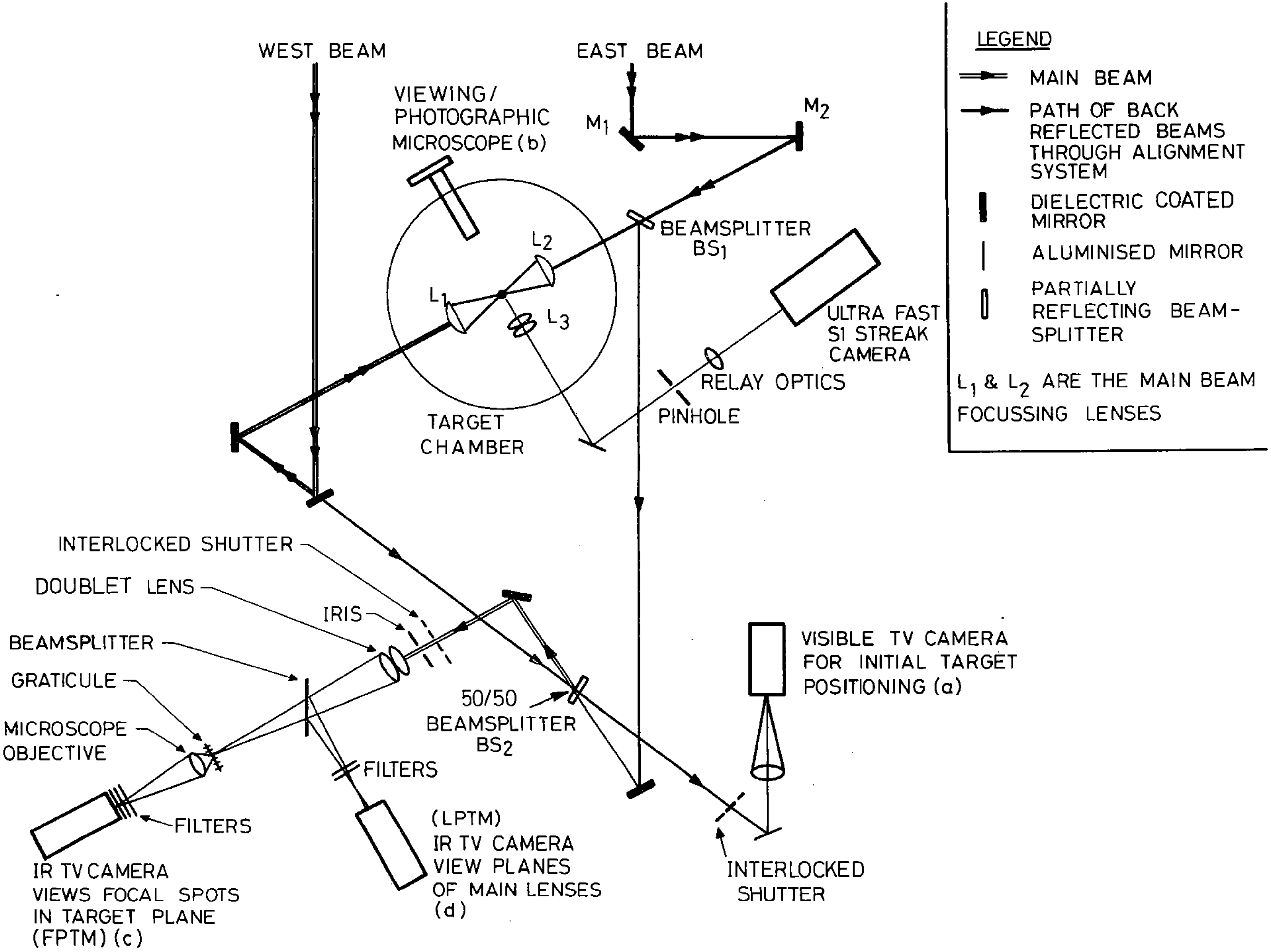
LEGEND
MAIN BEAM
PATH OF BACK REFLECTED BEAMS THROUGH ALIGNMENT SYSTEM
DIELECTRIC COATED MIRROR
ALUMINISED MIRROR
PARTIALLY REFLECTING BEAM-SPLITTER
L_1 & L_2 ARE THE MAIN BEAM FOCUSSING LENSES
WEST BEAM
EAST BEAM
VIEWING/ PHOTOGRAPHIC MICROSCOPE (b)
M_1
M_2
BEAMSPLITTER BS_1
L_1
L_2
L_3
ULTRA FAST S1 STREAK CAMERA
RELAY OPTICS
PINHOLE
TARGET CHAMBER
INTERLOCKED SHUTTER
DOUBLET LENS
IRIS
BEAMSPLITTER
GRATICULE
MICROSCOPE OBJECTIVE
50/50 BEAMSPLITTER BS_2
VISIBLE TV CAMERA FOR INITIAL TARGET POSITIONING (a)
FILTERS
FILTERS
(LPTM) IR TV CAMERA VIEW PLANES OF MAIN LENSES (d)
IR TV CAMERA VIEWS FOCAL SPOTS IN TARGET PLANE (FPTM) (c)
INTERLOCKED SHUTTER

FIG. 130

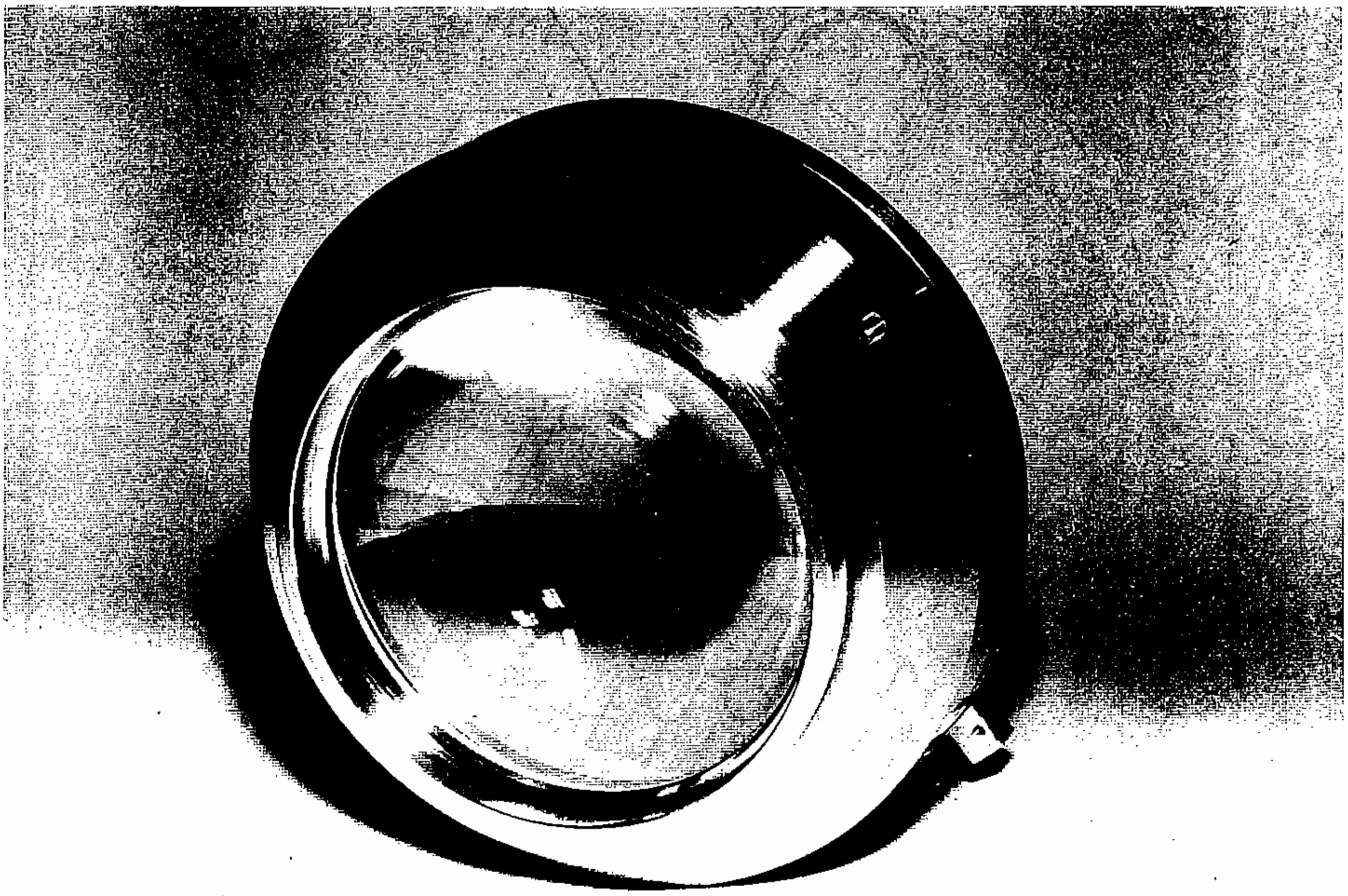

FIG. 131

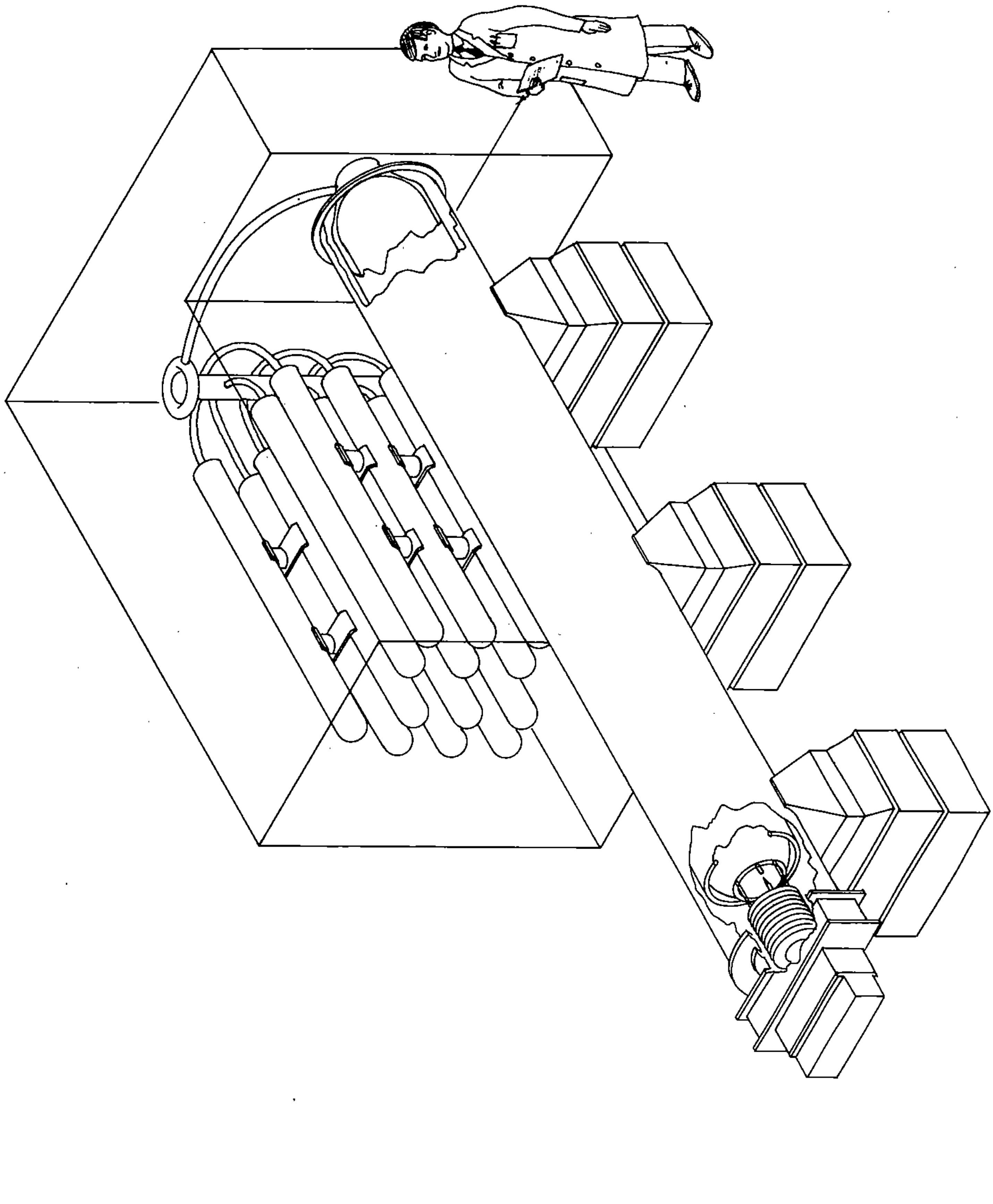

FIG. 132

Section 2 S I N G L E B E A M I N T E R A C T I O N S T U D I E S

Section Editor: T P Hughes

2.0 INTRODUCTION AND SUMMARY

2.1 OPTICAL AND MAGNETIC MEASUREMENTS

2.1.1 Measurement of megagauss magnetic fields in laser produced plasmas

2.1.2 Measurement of the time history of holes burnt in thin foils by high power lasers

2.2 X-RAY AND VUV SPECTROSCOPY

2.2.1 Crystal spectroscopy

2.2.2 Time-resolved X-ray spectroscopy

2.2.3 Grazing incidence spectroscopy

2.2.4 Observations with filtered X-ray diodes

2.3 OPTICAL EMISSION STUDIES

2.4 PARTICLE EMISSION MEASUREMENTS

2.4.1 Charge collector probes

2.4.2 Ion charge analysis

2.5 GAS BREAKDOWN OBSERVATIONS

2.6 RELATED THEORETICAL AND COMPUTATIONAL STUDIES

2.6.1 Imperial College

2.6.2 University College of North Wales, Bangor

2.6.3 Glasgow University

2.6.4 St Andrew's University

REFERENCES

FIGURES

2.0 INTRODUCTION AND SUMMARY

In April 1976 a proposal for a Single Beam Experimental Programme was accepted by the Laser Facility Steering Committee. The annual report presented in April 1977 described progress in preparing equipment, and some preliminary experiments carried out with the Quantel laser in the first few months of operation. During the year covered by the present report, it has been possible to build on the foundations laid previously: the scientific programme of single beam experiments has made substantial progress and several important results have been obtained. The work of the Experimental Groups is summarised below: detailed reports are given in sections 2.1 to 2.6. Contributions to the single beam experiments and the related theoretical work reported here have been made by workers from nine UK University groups and from the Astrophysical Research Division of the SRC Appleton Laboratory, with members of the Rutherford Laboratory Laser Division staff.

(a) Optical and Magnetic Measurements

Clear evidence has been obtained, from simultaneous Faraday rotation and interferometric observations, for the occurrence of megagauss magnetic fields in plasmas generated from 1 mm aluminium wire targets. The experiments used the Raman-shifted second harmonic of the neodymium laser pulse for the probe beam, and achieved 30 ps temporal and 1.5 μm spatial resolution with a minimum detectable field of 100 kG. With microballoon targets, no measurable field was observed.

The time history of holes burnt in thin foil targets was investigated using a wide variety of diagnostics and the observations were compared with simulations with both the 1D MEDUSA and the 2D LASERB codes. Evidence was obtained for severe inhibitionof thermal transport, to a greater extent that could be ascribed to magnetic field effects.

(b) X-ray and VUV Spectroscopy

X-ray crystal spectra with excellent resolution have been obtained from a wide variety of target materials. Some of the results have already been analysed and have proved valuable in astrophysics. Helium-like spectra and nearby satellite lines have been recorded for elements between Al and Ti. These are important for plasma diagnostics because in principle they may be used to determine the electron density and temperature. Time resolution is essential for this purpose and this has now been achieved to 20 ps using an X-ray streak camera. With an aluminium target it was found that the satellite lines appeared only for a time equal to the laser pulse duration whereas the helium-like resonance and intercombination lines were emitted for about 1 ns. The influence of opacity remains to be determined before reliable interpretation in terms of plasma parameters is possible.

Grazing incidence spectroscopy in the region 130 to 180 Å using a small rocket instrument revealed very strong continuous radiation. It is apparent that better results will be obtained in the region from 10 to 100 Å and a versatile new instrument has been ordered with a 5 m radius for this purpose.

(c) Optical Emission Studies

The angular distribution of laser light scattered from solid targets was determined with an array of pin diodes. The target was moved axially relative to the lens and it was found that the diffusely scattered energy was greatest when the laser beam was best focused, being approximately equally divided between polarizations parallel and perpendicular to that of the incident light. Defocusing reduced the proportion of parallel-polarized scattered light.

Backscattered laser harmonics were studied spectroscopically. The second harmonic region was found to have a broad, asymmetric spectrum biased towards the red from $2\omega_o$ and sometimes extending over more than 100 Å. A fine spectral structure was observed which has been interpreted as being due to the occurrence of large amplitude ion acoustic waves. The spectral breadth was greatest at optimum focus. The $(3/2)\omega_o$ regions was also recorded: the spectrum here was again broad but it was very irreproducible, the envelope sometimes having a single maximum and sometimes two.

(d) Particle Emission Measurements

A new ion analyser has been commissioned which has shown that the fastest ions observed are protons from target surface contamination. Measurements made on highly stripped ions were found to be strongly dependent on the pressure in the target chamber.

A novel pyroelectric ion detector has been tried out and may prove to be useful in a modified form.

(e) Gas Breakdown Observations

Spectroscopic observations in the near ultra-violet region were made of laser induced gas breakdown in neon between 50 and 7380 torr. Lines of Ne I to Ne IV were recorded. The results were consistent with inverse bremsstrahlung absorption of laser light at high pressures but at low pressures the spectra were too weak for any conclusions to be drawn. In future experiments at low pressures charged particles will be collected in a DC field with time of flight measurements for M/Z.

(f) Related Theoretical and Computational Studies

The use of the MEDUSA and LASERB codes in interpreting optical and magnetic measurements has already been mentioned in (a) above.

Additional computations were made with the 2D CASTOR code incorporating the TRIP atomic physics package, which predicted a reversal of the spontaneously generated magnetic field, due to a decreasing electron density gradient between the absorption region and the ablating surface.

Theoretical studies have been made of several parametric interactions and of resonance absorption, and the results are currently being compared with particle simulation codes EMPIRE ($1\frac{1}{2}$D) and E214 (1D). Codes with $2\frac{1}{2}$D and 2D are being developed.

The effects of magnetic fields and the influence of rippling of the critical density surface on resonance absorption have also been investigated theoretically. The former may not be very important but rippling can greatly increase the absorption of light at near normal incidence.

2.1 OPTICAL AND MAGNETIC MEASUREMENTS

2.1.1 Measurement of Megagauss Magnetic Fields in Laser Produced Plasmas

The generation of spontaneous magnetic fields in laser produced plasmas due to thermoelectric effects (201,202), absorption (203) and target discontinuities (204), have been theoretically predicted and imply substantial modifications to plasma transport properties. Measurements of thermoelectric (205) and resonance absorption (205,206) generated field profiles have been made in microwave-plasma interactions and the existence of thermoelectric fields in laser produced plasmas has been shown by Faraday rotation (207). These measurements have now been extended to measurement of magnetic field profiles in laser produced plasmas obtained by simultaneous Faraday rotation and interferometric measurements with good spatial and temporal resolution.

The experimental arrangement is shown in figure 201. The target was irradiated through an f/1.0 lens with a single beam of the Rutherford Neodymium Glass Laser. The pulse length was 100 ps and the energy varied over the range 5 to 40 J. The focal spot diameter was measured to be 30 μm giving irradiances up to 2 x 10^{16} Wcm^{-2}. A portion of the main beam was split off to form the probe beam. This beam was frequency doubled in an angle tuned KD*P crystal and after passing through a variable optical delay was frequency shifted to 6329 Å by stimulated Raman scattering in ethanol (208). The probe pulse energy was 500 μJ in 30 ps and was timed to arrive at the target 60 ps late relative to the main pulse to an accuracy of 15 ps as measured by a streak camera. The focal spot region was imaged by an f/1.4, x10 microscope objective and relay lens with 50x overall magnification and 1.5 μm resolution. Part of the image beam was split off into a folded wavefront interferometer and the remainder was polarisation analysed using a Wollaston prism set orthogonal to the probe beam polarisation. Images were recorded on Polaroid 57 and Kodak 2485 film. A small percentage of 1.06 μm light was imaged on the film to provide a focal spot position reference for comparing images.

Three types of target were used for these studies. These were:

(i) 1 mm diameter aluminium wires

(ii) Small 40 μm diameter empty glass microballoons

(iii) 250 μm diameter polythene fibres with step discontinuities in Z formed by overplating 1000 Å thick bands of aluminium.

These latter targets should be particularly sensitive to discontinuity generated magnetic field (204) measurements since the probe beam is collinear with the magnetic field over a relatively large distance.

Typical results of the Faraday rotated components for an aluminium wire target are shown in figure 202(a). The probe beam polarisation is rotated to the right, viewing along the beam, when travelling parallel to B, and figure 202(b), taken with the polariser rotated by 10^{o}, shows the toroidal nature of the field which is consistent with the direction of thermo-electric fields generated from an axial density and radial temperature gradient. There is evidence on a few shots for a double structure in the axial field profile, with one component in the opposite direction to the conventional thermoelectric fields. This will be discussed in more detail in relation to the measured density profile below.

Faraday rotation and interferometric data is inverted by an integral inversion routine that performs a least squares fit to the data of the relevant integral of a parameterised test function by a combined Newton-Raphson/steepest descent method. For the magnetic field inversion axial symmetry is assumed: the rotation ϕ is given by:

$$\phi\ (y) = \int_y^{\infty} \frac{n_e \ B\cos\ r\ dr}{\sqrt{r^2 - y^2}} = \int_y^{\infty} \frac{n_e \ By\ dr}{\sqrt{r^2 - y^2}}$$

The programme is also used to invert the Abel equation for density profiles. The radial and axial density and field profiles are shown in figure 203 and figure 204 respectively for a shot on an aluminium wire target. The field reaches a maximum value of 1.8 MG at a radius of 17.5 μm which is in good agreement with the HWHM focal spot radius of 15 μm. The axial profile at the peak field shows a double humped structure associated with a reversal of the density gradient. Although information is not available for the direction of rotation of the two components on this shot, it is reasonable to assume that the inner field is reversed due to the reversal of the density gradient. Density gradient reversals have been reported by other workers at similar values of $I\lambda^2$ (209). A simple saturation mechanism for the field has been considered by Max (210) and gives a saturated field magnitude of:

$$B = 3.3 \left(\frac{Te}{1keV}\right)^{\frac{1}{2}} \frac{10\mu}{L} \left(\frac{A}{Z+1}\right)^{\frac{1}{2}} = 1.2 \text{ MG}$$

which is in reasonable agreement with the measured field, taking L to be the mean of the density and focal spot scale lengths.

The measurements carried out on small microballoon targets showed no evidence of magnetic fields within the system sensitivity of 100 kG, a result in agreement with measurements made elsewhere (211). It is expected that on small targets whose diameter is of the order of the focal spot size, the symmetry of the spherical expansion will result in small source terms for magnetic fields.

Conversely, targets with a step discontinuity in Z across the focal region are expected to give rise to large linear magnetic fields along the line of the discontinuity due to the density jump crossed with the axial temperature gradient. However, measurements on targets with a polythene (Z eff = 3) and aluminium (Z = 13) discontinuity showed no evidence of discontinuity fields, and additionally showed a reduction of an order of magnitude in thermoelectric fields. Furthermore, no evidence was obtained for a discontinuity from the interferometric data (figure 205) a result which is consistent with predictions of the MEDUSA code for the profile of the blowoff plasma for materials of different Z.

2.1.2 Measurement of the Time History of Holes Burnt in Thin Foils by High Power Lasers

Thin foil experiments have in the past provided valuable clues to laser-plasma phenomena. The transmission of thin foils (212) and the ion emission (213) have been interpreted as evidence of inhibition of thermal conduction. Recently a one-dimensional simulation with ponderomotive force but without fast electrons (214) has modified the conclusion of these earlier results.

During the period under review new measurements were obtained of the time history of burnthrough and backscattered light when high power neodymium laser pulses are incident on thin polystyrene foils. Simultaneously, the transmission of a ruby probem beam at 0.69 μm was measured. A 0.15 μm foil becomes transparent to the 1 μm laser about half way through a 100 ps pulse but, in contrast with simulations, the transmission is low after burnthrough. The transmission of the ruby probe beam can be measured after the neodymium laser pulse but the size of the burnthrough hole is no bigger than the size of the focused laser beam. This is not predicted by a two-dimensional simulation, even with magetic field inhibition of the heat flux. To explain the hole size a flux limit in addition to the magnetic field inhibition is needed. Other observations can be interpreted as being due to the small size of the hole. The transmitted light is severely refracted because of diffraction as the beam is transmitted through the small hole. Ion probe data show that the fast ions come from a region of the foil only 40 μm in diameter.

A 5J, 100 ps output of the neodymium laser was focused onto thin polystyrene foils to a focal spot of size 30 μm x 16 μm, giving a peak irradiance of $4. 10^{15}$ Wcm^{-2}. The 7 cm beam underfilled a 10 cm, f/1 aspheric lens. The polystyrene (CH_2) targets were of thickness 0.08 μm to 0.34 μm and were placed in an evacuated (10^{-4} torr) target vessel prior to irradiation. A large number of diagnostics, some of which were new, were employed. These are listed below.

(a) The 1.06 μm light burning through the foil was collected by a second, identical aspheric lens. Some of this light was used to image the plane of the second lens onto film. This provided time-integrated information of the angular distribution of the burn-through light in the collection cone of the second lens. Similar pictures were obtained for light backscattered into the focusing lens.

(b) A further fraction of the burnthrough light was used to image the target plane at the S1 photocathode of a streak camera. This provided temporal and spatial information on the burnthrough light with 10 μm, 12 ps resolution. A similar arrangement relayed the backscattered 1 μm light onto the same streak camera. The intensity response and streak speed linearity were subsequently calibrated with a dye laser.

During the thin foil experiments a small fraction of the incident pulse was also relayed to the S1 camera to give the incident power and also a time origin for interpretation of the burnthrough and backscatter streaks.

(c) Light scattered outside the collection cone of the two aspheric lenses was sampled by a photodiode array. Each p-i-n diode was calibrated against a calorimeter using pulses from the oscillator of the neodymium laser.

(d) A ruby laser probe beam, directed antiparallel to the 1 μm beam, backlighted the foil target. The main focusing aspheric lens was used to image the target plane in 0.69 μm light at the S20 photocathode of a second streak camera. Thus the temporal and spatial variations in transmission of the probe beam were measured, with 10 μm, 25 ps resolution.

The Q-switched ruby laser gave a 1J, 20 nsec output which was essentially constant on the timescale of the experiment. Some mode-beating was present in the ruby laser ouput.

During the thin foil experiments, a small fraction of the incident 1 μm pulse was split off, frequency doubled and relayed to the S20 streak camera as a time-marker.

(e) Ion probes were used and provided time resolved information on the rate of arrival of ions of given mass and energy.

(f) Additional diagnostics included calorimetry, far-field monitors and occasionally magnetic probes situated 10 mm from the target.

The observations may be summarised as follows:

(a) The beam diameter of the 1 μm pulse is 6 cm and does not fill the 10 cm aperture of the aspheric focusing lens. This enables the time-integrated lens pictures to monitor the increase in angular spread of the 1 μm beam caused by the plasma after burnthrough. A large angular spread is observed with some energy being refracted outside the collection cone of the second lens. The distribution is not always azimuthally symmetric (figure 206): the increase in angle of the beam emerging from the target is ∿ 10%. This is approximately the same as the diffraction angle $\delta\theta = \lambda/d$ for a parallel 1 μm beam passing through a 20 μm hole.

(b) The S1 streaks show burnthrough occurring about half way through the incident pulse for 0.14 μm foils, later for thicker foils, earlier for thinner foils. For 0.14 μm foils the transmission remains low (∿ 20%) even after burnthrough (figure 207). The backscattered 1.06 μm light occurs predominantly early in the incident pulse but is still finite after burnthrough. This may be due to stimulated Brillouin backscatter or to burnthrough occurring only at isolated points in the critical surface.

Little spatial structure was observed: the burnthrough pulse was occasionally broader immediately after the onset of transmission. This may be due to refraction effects.

The burnthrough of thick foils (0.34 μm) allows the observation of the incident pulse before the foil becomes overdense. For a typical incident pulse, opacity sets in at ∿ 0.1 Gw power level.

A number of shots gave rise to early burnthrough and these correlate fairly well with the presence of significant prepulses, ie

$$E > 10^{-5} E_{LAS}$$

(c) The p-i-n diode array and the photographs of the aspheric lenses gave a scattered light distribution peaked strongly in the axial directions but with some energy falling outside the lenses. For the burnthrough light, less than 10% of the energy was scattered outside of the second aspheric lens.

(d) The S20 streaks of the foils with ruby backlighting (figure 207) show:

(i) the cut-off of the ruby light due to ionization about 200 ps before the peak of the incident pulse, a little later in the outer regions of the focal spot;

(ii) plasma emission. This may be the spectral wing of the $(3/2)\omega_o$ emission at around the peak of the incident pulse. During this time, the transmission of the ruby beam is unknown;

(iii) the presence of transmitted ruby light immediately after the plasma emission, with diameter 25 μm. Refraction effects give rise to a cusp shape which, at later times at least, gives a measure of the hole diameter. After 1 ns, the burnthrough hole has a diameter of ∿ 100 μm.

The transmission of ruby light immediately after the plasma emission is ∿ 30%. The plasma emission was observed on shots when the ruby was not operated. The emission has the same spatial extent as the focal spot and typically a doubly peaked time dependence.

(e) Ion probes show that fast and slow ions are emitted in plumes of angle $\sim 20^{o}$ about the target normals. Assuming an $M/Z = 1.75$, fast ions ($v > 10^{8}$ cm sec^{-1}) carry 50 - 60% of the total energy but account for only 7% of the total mass. The mass recovered as fast ions was two times larger at the front than at the back of the foil. In total 200 pgm was recovered in fast ions corresponding to a hole diameter of 42 μm. Total fast and slow ion mass was 3 ngm corresponding to a foil diameter of 170 μm. Data is shown in figure 208.

(f) Carefully screened magnetic probes show that magnetic fields are present and are of opposite sign each side of the foil (figure 209). If these fields are thermoelectrically generated, they will be in opposite azimuthal directions each side of the foil and in the same direction as the fields observed ($\nabla T \times \nabla n$).

In order to interpret these observations they have been compared with two different simulations:

(a) The one-dimensional, Lagrangian code MEDUSA was used to model the thin foil experiments. Inverse bremsstrahlung, ponderomotive force and fast electrons were included. Numerical experiments were performed during which the flux limit and the fractional absorption were varied together with an ad hoc reduction in the thermal conductivity $K = \alpha K_{Spitzer}$. Typical results are shown in figure 210.

The burnthrough time is earlier than observed experimentally by $\sim$ 40 ps and variations in the flux limit do not change this by more than 5 ps. The same is true for variations in α. Removing the ponderomotive force increases the burnthrough time to $\sim$ 30 ps before the peak of the incident pulse.

When burnthrough occurs the plasma is approximately isothermal.

(b) A two-dimensional simulation using LASERB was also used to model the thin foil experiments. Simulations have been performed with and without magnetic inhibition of the heat flux, and with additional heat flux inhibition. There is no atomic physics included and no ponderomotive force.

Results for magnetic field inhibition are shown in figure 211. In this figure the laser is incident in negative z direction. The magnetic field restricts the radial extent of the hot plasma. However, the magnetic field is small in the mid-plane of the foil (figure 212) and so here the $1/(1+\omega^2\tau^2)$ inhibition is small. The normalised radial heat flux is shown in figure 213 and a large radial heat flux occurs in the centre. As a result of this, the size of the hole becomes quite large. Figure 214 shows the size of the hole as a function of time. Even with $\omega\tau$ inhibition it is still larger than observed experimentally with the ruby streaks.

A few runs with a reduced thermal conductivity have been performed and this does reduce the hole size. Numerical problems have so far prevented this simulation from running further.

A transmission can be obtained from the simulations. Effectively, 100% transmission is predicted as soon as the plasma density drops below $0.9n_c$. Thus the transmission should rise to nearly 100% about 10 ps after burnthrough.

LASERB has also been used to predict the angular scattering of the transmitted light. In the geometric optics approximation, the angular spread of the transmitted light is unchanged because with $\omega\tau$ inhibition only, the hole in the plasma rapidly becomes very large. The ion probe signals can also be obtained and these are shown in figure 215, calculated for probes 66 cm from the foil.

The observed burnthrough time is later than predicted by both codes. Possibly this is due to the omission of atomic effects. It is interesting that the burnthrough time does not depend on the flux limit.

The transmission after burnthrough is still low. This could be due to turbulence. The effective collision frequency in the presence of turbulence is (215):

$$\nu^*/\omega_{pe} = 0.5 \left|\frac{\Delta n}{n_{cr}}\right|^2$$

for $n > n_{cr}/2$. For example, a 0.15 μm polystyrence foil if fully stripped would become 100 μm thick for a top hat density distribution at $n_{cr}/2$. The wave attenuation length

$$d \sim 2cn_{cr}/\nu^* n$$

Thus if $n = n_{cr}/2$, then $d = 4\left|\frac{n}{\Delta n}\right|^2$ μm

We observe a 20% power transmission which implies a $\Delta n/n \sim 18\%$. Manheimer (216) gives a value for the thermal conduction coefficient in the presence of ion turbulence which may be written:

$$\frac{K_{an}}{K_{c\ell}} = \frac{1}{\gamma^2 n\, \lambda_{De}^3} \left(\frac{n}{\Delta n}\right)^2 \frac{\ln\Lambda}{320\pi\delta\varepsilon}$$

where $K_{c\ell}$ is the Spitzer (217) thermal conduction coefficient and δ and ε are his factors for a non-Loretzian gas. With $T_e \sim 1$ keV and $n_e \sim 10^{21}$ cm^{-3} this reduces to:

$$\frac{K_{an}}{K_{c\ell}} = 4.12\ 10^{-5} \left(\frac{n}{\Delta n}\right)^2$$

$$= 1.3\ 10^{-3}$$

Such a low value of the lateral heat flow would not be consistent with the observed hole size (figure 214).

The backscattering light even after burnthrough could be due to a back-scattering instability or scattering off the edges of the hole.

In summary, then, we have three new pieces of experimental information showing that the radial extent of a hole burnt in a thin foil is small. Namely, there is a large angular spread to the transmitted light, the mass of the fast ions corresponds to only a 40 μm diameter hole and ruby backlighting streaks show a 20 μm diameter hole.

Comparison with simulations shows that ωτ inhibition is insufficient to account for this size and that extra heat flux inhibition is necessary.

Moreover, the transmission of thin foils is low, indicating a high turbulence level causing anomalous absorption.

J D Kilkenny (Convenor), D R Gray, J Murdoch (Imperial College); O Willi (Oxford); R Illingworth(Strathclyde); E Wooding (Royal Holloway College); A Raven, P T Rumsby, W T Toner, M S White (Rutherford Laboratory).

2.2 X-RAY AND VUV SPECTROSCOPY

2.2.1 Crystal Spectroscopy

(a) Neon sequence spectra

This work extends earlier work at Queen's University, Belfast, to higher Z ions between 38 Sr and 45 Rh using more powerful though shorter laser pulses. The spectrometer was a curved PET crystal instrument recording photographically on Kodirex film. Figure 216 shows lines in the neon-like strontium spectrum. Here the ground configuration is $2p^6\ ^1S_o$, so there is only a single ground state and the spectrum is relatively simple. In LS coupling three (2-3) transitions to the ground state are expected with $\Delta\ell = +1$(2p-3d) and two with $\Delta\ell = -1$(2p-3s). In addition, inner shell transitions are expected (2s-3b). Satellites to the ground state transitions 2p-3d are also observed, which have been ascribed with the aid of atomic structure calculations by Dr R D Cowan of Los Alamos to the presence of one or two additional electrons and may thus be described as inner shell transitions in Na- and Mg-like ions, $2p^6 3s$-$2p^5 3d3s$ and $2p^6 3s^2$-$2p^5 3d3s^2$ respectively. The satellites to the 2p-3s transitions may be due to an additional 3s or 3p electron.

The 2p-4d transition is also present, with satellites which have not been observed previously.

Figure 217 shows part of the spectrum of molybdenum (Z=42), together with calibrating lines of helium-like sulphur. In addition to the neon-like lines of Mo XXXIII and the satellites mentioned above, strong satellite bands are present due to inner shell transitions in less highly charged ions (3 to 6 satellite electrons).

New classifications in the neon sequence ions Sr XXIX and Rb XXVIII have resulted from this work and the observations in Mo XXXIII are in good agreement with earlier work by Boiko et al. of the Lebedev Institute (218). The results are of interest in studies of the solar corona. Isoelectronic extrapolation to lines of Fe XVII and their satellites suggests that a feature observed at 15.208 Å consists of the Fe XVI $2p^6 3s-2p^5 3d3s$ satellites to the neon-like Fe XVII 2p-3d line at 15.260 Å.

(b) Spectra of Fe XVII to XXIII

The spectra of Fe XVII to XXIII were recorded, using a DeBroglie crystal spectrometer with an RAP crystal bent to a 4 cm radius, between 8 and 22 Å.

The observations were analysed with the aid of theoretical calculations of energy levels and oscillator strengths and the results have been published (219, 220).

(c) Helium sequence spectra

Because of their relative simplicity the helium-like spectra have been studied intensively both theoretically and experimentally and are of considerable astrophysical interest.

The relative spectral line intensities from 2 and 3 electron ion species have been proposed as possible diagnostics for laser produced plasma density and temperature measurements (221). Prominent features in the spectrum are the appearance of satellite lines, arising from $1s^2\ n\ell \rightarrow 1s\ 2p\ n\ell$ transitions in Li-like ions, and the He-like intercombination line $1s^2\ {}^1S_o \rightarrow 1s\ 2p\ {}^3P_1$ on the long wavelength side of the He-like ion resonance transition $1s^2\ {}^1S_o \rightarrow 1s2p\ {}^1P_1$, (222). The intensity ratios of satellite to resonance lines have been shown to be temperature dependent, whereas the intercombination line intensity is density dependent.

At the Rutherford Laboratory the helium-like spectra Al XII, Si XIII, S XV, Cl XVI, K XVIII and Ti XXI have all been recorded in the X-ray region with good resolution, using curved crystal spectrometers with ADP, PET and germanium crystals. In addition to the usual window foil, a thicker filter foil was placed over half the aperture for some exposures to check the calibration of the emulsion.

Figure 218 shows a microdensitometer trace of the aluminium spectrum. The broadening of the higher series members suggests an electron density in the region of 10^{21} cm^{-3} on the basis of simple Holtsmark theory (223) but the time and space variation of the emission has not been taken into account. A similar result is obtained from the silicon spectrum (figure 219). The highest Z ion for which the helium-like spectrum has so far been recorded at the Rutherford Laboratory is Ti XXI. The microdensitometer trace (figure 220) shows the resonance line (w in Gabriel's notation (224)), the intercombination line (y) and the K_α doublet, which is resolved. The Li-like Ti XX and the Be-like Ti XIX inner shell transition satellites are also observed.

The spectra referred to above are time and space integrated and it is possible that with 100 ps pulses the intensities of these lines may behave very differently in time and in space. Taking the apparent ratio of the resonance to the intercombination line intensity in the case of aluminium, ignoring these uncertainties and also neglecting any effects of optical opacity (225), an electron density of about 5×10^{20} cm^{-3} is obtained. From the relative intensities of satellite lines an electron temperature of around 300 eV may be deduced in the same spirit, with evidence that the plasma is ionizing rather than recombining. Time and space resolved measurements are needed (see below) to improve the reliability of temperature and density measurements. The values of n_e and T_e given above are both almost certainly too low.

2.2.2 Time-resolved X-ray Spectroscopy

This work takes advantage of an X-ray streak camera with ∿ 20 ps time resolution to look at the time dependence of the plasma density and temperature (226,227) using the helium-like lines and their satellites referred to above.

A flat TℓAP crystal (2d = 25.75 Å) was used to disperse the X-ray radiation from a laser plasma onto the photocathode of an X-ray streak camera used in transmission mode. The crystal was free to move along the perpendicular bisector of a line joining the plasma and the cathode centre and hence allowed selection of the wavelength incident on the cathode. The cathode had an 8 μm Be substrate coated with a few hundred Å of gold and strong VUV radiation was stopped by an additional 25 μm Be filter in front of the crystal. The target used was 2000 Å of Al coated onto a glass substrate and laser pulses of 20-40 J in 100 ps were focused with a 12 cm f/1 Soro lens. An X-ray pinhole camera, a temperature measuring X-ray diode array and a single shot space resolving X-ray spectrometer (228) with a PET crystal were used simultaneously on each shot to provide additional information.

The experiment was set up to look at the He-like resonance line of Al at 7.75 Å and the intensity of the line emission was optimised by defocusing the lens by ∿ 300 μm. Streaks were obtained with time resolutions of ∿ 150 ns and $\lesssim$ 50 ps by adjusting an aperture slit in front of the crystal and streak speeds of ∿ 1 ns/cm were used. Sweep speed calibration was possible when the laser oscillator malfunctioned and generated a double mode-locked train whereby two pulses were gated and each generated an emitting plasma.

A preliminary analysis of the results (figure 221) shows that the satellite lines are emitted for a time equal to the pulse duration (∿ 100 ps) whereas the intercombination and resonance lines are still visible at ∿ 1 ns. An apparent dip in the resonance line intensity at ∿ 100 ps suggests that the line is seen both in the early ionisation and later in the recombination phase. A deflection of the lines in time, which is most marked in the intercombination line, suggests that the radiation is emitted from a plasma zone moving out from the target surface and an expansion velocity estimate is possible ($\sim 5 \times 10^7$ cm/sec).

A complete reduction of the data is in progress but potential usefulness of the technique as a diagnostic will depend on whether opacity effects in the resonance line intensity can be understood (225). An atomic physics package including radiation transfer used with a fluid code such as the 1D MEDUSA code will be necessary for this purpose.

2.2.3 Grazing Incidence Spectroscopy

Observations of Fe and Mn spectra obtained with the 2m Gabriel spectrograph on loan from the Appleton Laboratory were analysed. Lines of n = 2-2 transitions in the spectra of Fe XVIII to XXIII and Mn XVII to XXII are shown in figure 222 together with isoelectronic transitions in Ca, Sc and Ti recorded previously at the Appleton Laboratory. The presence of Fe XXIV lines near 10 Å (on both grating and crystal spectra) indicates qualitatively the high electron temperatures achieved in the laser-produced plasma. The spectral data thus obtained are important for the interpretation of solar flare spectra.

A small grazing incidence spectrograph designed for rocket use and covering the spectral range between 130 Å and 800 Å has been used in the main target chamber with a variety of targets. Spectra of silicon, aluminium and elements in the period between titanium and iron were recorded. A high level of bremsstrahlung or recombination continuum was present on all the spectra and only on the silicon and aluminium spectra were spectral lines more intense than the continuum. In addition, evidence of considerable absorption was found on the spectra of the transition elements presumably due to cool plasma near the plane target surface. The aluminium and silicon spectral lines in this wavelength region were of ionisation stages below the eleventh. Spectral lines from higher stages in this spectral region were too faint to observe above the continuum levels but have previously been observed with the 2 m vacuum spectrograph at wavelengths shorter than those covered by the rocket instrument. The width of the film in the rocket instrument plateholder does not permit the imaging of the plasma as a function of distance from the target surface as in the case of the other instrument. It was evident from these observations that the grazing incidence experiments would more profitably be conducted in future using an instrument aligned to record spectra from 10 Å to 100 Å and also an instrument which permits imaging of the plasma across the width of the plate-holder. A 5 m instrument has been ordered which will meet these requirements. When it is required to work at longer wavelengths it may be necessary to use wire targets or spherical targets instead of plane targets to avoid absorption. These absorption effects are much more severe with 100 ps laser pulses than with nanosecond laser pulses.

2.2.4 Observations with Filtered X-ray Diodes

Two arrays of four Quantrad diodes with different foil filters were used to monitor X-ray emission from the plasma. The results were similar in general to those obtained elsewhere. However, it is possible that parts of the observed signals were due to:

(a) fast electrons penetrating the filter foil,
(b) X-ray generated in the foil by electrons,
(c) fluorescence of the foil,
(d) X-rays not from the plasma.

An experiment was carried out to test these possibilities by placing a collimating tube with a small entrance aperture and a 1200 gauss magnet in front of one of the diodes. The effect was to reduce the signal by an order of magnitude. The design of the diode arrays was therefore modified to provide collimation and prevent fast electrons from reaching the filter foils, which were placed at a greater distance from the diodes. Similar precautions were also taken with X-ray crystal spectrometers, thus reducing the level of fogging encountered on the film.

A further array of filtered X-ray diodes using scintillators and photomultipliers was designed and will be available soon to extend the high-energy range of observations of X-ray spectra.

B C Fawcett (Convenor), A Ridgeley (Appleton Laboratory); R J Hutcheon (Leicester); M H Key, C L S Lewis, J A Lunney, A Moore (Belfast); T A Hall, T P Hughes, P L Salter (Essex); R K Thareja (Strathclyde).

2.3 OPTICAL EMISSION STUDIES

The high laser irradiances in laser produced plasmas give rise to many non-linear processes. Several of these processes manifest themselves in characteristic harmonic spectra emitted from the plasma near the laser wavelength and its harmonics. No single diagnostic can distinguish between the different mechanisms and the best approach to understanding the interactions is to correlate several different measurements. During the past year several diagnostics have been commissioned and some preliminary results have been obtained. On some of the diagnostics, however, some development work still needs to be done.

An array of twelve silicon PIN photodiodes, behind 400 Å bandwidth interference filters centred at λ = 1.06 µm, was divided between the horizontal (P), vertical (S) and 45^{o} planes to measure the angular distribution of laser radiation scattered from 4 J, horizontally polarized pulses incident on a thick polystyrene target. Each diode was carefully screened electrically and its integrated output was recorded.

Measurements were made of the scattered light distribution for four different axial positions of the target surface relative to the focal plane of the laser beam between $\delta z = 0$ (the position of the focus of the cw YAG alignment laser) and $\delta z = +200$ µm further away from the lens. Thermal lensing in the amplifiers following the vacuum spatial filter is believed to shift the focal plane of the main beam to a position δz_o in the range + 50 µm < δz_o + 100 µm.

Figure 223 shows a polar diagram of the angular energy distributions in the P and S planes for a target at $\delta z = 0$. Nearly all the scattered light is contained in a 60^{o} half-angle cone around the laser beam axis. This was the case for all axial positions of the target. However, the ratio of the scattered light energies in the P and S planes varied significantly with focus, as did the total diffuse scattered energy (TSE) outside the cone of the lens (figure 224). With the target surface at $\delta z = 50$ µm, near the main beam focus, the TSE was a maximum, and the scattered energies in the P and S planes were approximately equal. A change in the target position in either direction reduced the TSE and resulted in markedly less scattering in the plane of polarization of the laser light. This result may be interpreted as evidence for a polarization dependent absorption mechanism, such as resonant absorption. The approximately equal scattering into the P and S planes when the target surface is near the main beam focus could be due to the minimization of angles of incidence in the (spherically aberrated) focus, and the generally greater diffuse scattering here could be evidence for break up or rippling of the critical density surface.

Spectroscopic observations have been made of the light collected by the main beam focusing lens from plasmas produced from thick polystyrene targets. Three grating spectrometers received backscattered laser light (ω_L) and the $2\omega_L$ and $(3/2)\omega_L$ harmonics via beam splitters and relay optics. Films and plates used to record the spectra were calibrated using the back scattered light to avoid any problems due to reciprocity failure. Photodiodes in the target chamber monitored the scattered ω_L and $2\omega_L$ radiation. A calorimeter measured the energy at ω_L retroreflected through the main beam lens. The near field patterns of $2\omega_L$ and $(3/2)\omega_L$ emission were recorded by conventional cameras behind 50 Å bandwidth interference filters. Figure 225 shows a typical $2\omega_L$ spectrum and the corresponding densitometer trace. The laser energy was 6.9 J in a 100 ps pulse. The spectrum is asymmetric, extending mainly towards longer wavelengths with a sharper cut-off on the short wavelength side of the unperturbed $2\omega_L$ line. In some cases the total breadth recorded is more than 100 Å. A spatially varying fine structure is observed in the spectrum and, though considerable care was taken in focusing the optical relay system, it is not yet clear whether the spatial structure is due to the source or to the optics. A regular fine spectral structure appears in many spectrograms on the long wavelength side of $2\omega_L$. The interval between maxima is generally in the range 0.7 to 1.5 Å. Sequences of as many as 18 regularly spaced maxima have been measured. Two or more sequences with significantly different spacings may occur in different regions of the same spectrogram. A possible explanation of this phenomenon may be due to the excitation of ion acoustic waves.

The $2\omega_L$ spectrum was recorded for a range of laser pulse energies and for a number of different axial positions of the target surface. As the target surface was moved away from the lens, starting at the focal plane of the cw YAG laser ($\delta z = 0$), the full spectral width at half-intensity of the emission increased from 12 Å to a maximum of 20 Å at $\delta z = 100$ μm (corresponding approximately to the expected focal plane of the main laser pulse) and then fell to 5 Å at $\delta z = 300$ μm (figure 226). The spectral width seems to be independent of laser pulse energy between 2 and 7 J and these results are averages from several shots with pulse energies in this range. The absence of variation with input energy suggests either that the spectral breadth depends only on the geometrical structure of the focused beam in the energy range studied or that the irradiance on the target does not increase with energy due to deteriorating beam quality. The target position for maximum spectral breadth is approximately the same as that which yields maximum X-ray emission.

The $(3/2)\omega_L$ spectrum was recorded for a single focusing position with $\delta z = +\ 50$ μm. The spectrum varied greatly from shot to shot and no correlation has been found with other paramaters. Figure 227 shows spectra from two shots of similar energy, 4.4 and 4.1 J. The separation of the two peaks has been interpreted by Avrov et al.(229) as a measure of the electron temperature. In the present experiment separations were observed in the range 50 to 250 Å, corresponding on this basis to temperatures in the range 1 to 5 keV, but the X-ray diode signals indicated a roughly constant temperature of about 700 eV in all cases. In contrast to the observation of Avrov et al, the blue peak is stronger than the red. As with the $2\omega_L$ spectra, the imaging of the target surface is poor but in the $(3/2)\omega_L$ spectra the spatial resolution is sufficient to show that most of this radiation comes from small localised regions of the plasma. In general the spectra suggest that the emitting regions are hotter than the surrounding plasma and offer indirect evidence consistent with the occurrence of large internal magnetic fields.

Some attempts were made to observe the $2\omega_L$ emission with a streak camera situated behind the spectrograph. The results from these experiments are as yet inconclusive.

T A Hall (Convenor), E Fabrikesi, T P Hughes (Essex); P D Carter,
S Majumdar, S Sim (Royal Holloway College); M S White (Rutherford Laboratory).

2.4 PARTICLE EMISSION MEASUREMENTS

2.4.1 Charge collector probes

Data collection from the array of Faraday cup collector probes in the target chamber is now a routine operation and occurs whenever experiments require information on the ion emission. Throughout the year the probes have been operated both as an indicator of the quality of laser shots and also to obtain quantitative data.

An experiment to determine empirically the optimum focal position of the main lens is an example of the former mode of operation. The fast ion signal was observed as the lens target separation was changed leading to the conclusion that the fastest ions were generated at a lens position which also gave the greatest scattered laser light level. This position was consequently assumed to be that at which the greatest intensity occurred.

The normal probe array, together with the two miniature detectors which observe the emission through the holes in the lenses, were used to gather quantitative data on the total ion emission energy from thin ($\simeq$ 0.15 μm) foil polystyrene targets. Results obtained showed that for foils of this thickness (which burn through during the laser pulse) the ion emission plumes have roughly the same spectrum and distribution both front and back. Expansion occurred normal to the target surface with half maximum full width angular distributions of about 20° for both fast and slow ions. Integration over the distribution gave values for the total energy collected in ion expansion energy from which values of laser energy absorption between 10 and 18% were deduced.

On laser shots when prepulses ($> 10^{-4}$) occurred the ion energy spectra were considerably softened. This result is consistent with similar observations made by other laboratories and suggests that significant changes in the interaction mechanisms occur. The effect of prepulses on the absorption processes deserves considerable further study.

2.4.2 Ion Charge Analysis

A single-channel electrostatic ion analyser has been constructed (figure 228) in order to determine the ionic composition of the expanding plasma. This device has been commissioned using plane beryllium, polythene and other heavier targets and results have shown that the fastest ions observed ($V > 4 \times 10^{8}$ cm/sec) consist predominantly of protons originating from a thin ($\sim$ 50 nm) hydrocarbon contamination layer on the surface.

Quantitative measurements of the energy distributions of the various species were attempted but significant results were only obtained for protons and for singly charged ions. Results obtained for highly stripped species were found to be significantly modified by the effects of charge exchange collisions occurring along the 0.88 m flight path to the analyser. The equipment has now been modified in order to reduce the pressure along this path to better than 10^{-5} torr to overcome such problems.

Preliminary attempts were made to time resolve the ion energy flux using a novel probe consisting of a fast ion pyroelectric detector situated behind a thin aluminium foil. Such a device is sensitive only to the fast ions which penetrate the foil. Comparison of the observed energy arrival rate (intensity) to that deduced from the signal produced by an adjacent Faraday cup probe should give an indication of the instantaneous M/Z value of the expanding ions.

Tests showed that the detector was not sufficiently sensitive and that ion energy loss in the foil (0.75 μm thick) was rather large. A new, more sensitive, detector has now been obtained upon which a thin layer ($\sim$100 nm) of aluminium will be deposited. This device has a somewhat faster response and consequently the next series of tests will be performed with it mounted closer to the target giving rise to a greatly increased ion energy arrival rate.

P T Rumsby (Convenor)(Rutherford Laboratory); T Goldsack (Imperial College).

2.5 GAS BREAKDOWN OPERATIONS

In the early part of the year, the stainless-steel gas breakdown chamber was commissioned. The accompanying vacuum system reached a pressure of 6×10^{-8} torr and the entire system had a three hour pump down time to 5×10^{-7} torr. Further features of the system were discussed in the 1976/77 Progress Report.

In July, an investigation was carried out into laser-induced breakdown in neon, studying the visible and near ultraviolet radiation from plasmas formed by 100 ps laser pulses focused into the gas at room temperature. Peak irradiance at the focus of the 120 mm lens was about 10^{15} w/cm^2. Spectroscopic observations (figure 229) were made at pressures of 50, 760, 7380 torr using a Hilger medium quartz spectrograph. At 760 torr, eight shots were required for a good exposure. Lines of Ne I, II, III, IV were identified, with Ne I and II dominant in the outer regions of the breakdown volume.

To produce Ne IV atoms, more than 126 eV of energy must be supplied to each ground state atom. At low pressures and with short laser pulse durations (ie $p\tau \lesssim 10^{-7}$ torr s) the initial plasma is unlikely to be formed by inverse bremsstrahlung processes but instead by multiphoton ionisation. Our experimental evidence showed that there was subsequent heating of the plasma during the time of the laser pulse.

It is well known that heating of electrons by the process of multiphoton inverse bremmstrahlung becomes important if $2e^2E_o^2 / m\omega^2 >> h\omega$, where E_o is the radiation electric field with frequency ω and e, m are the charge and mass of an electron respectively. For a neodymium laser the conditions corresponds to a laser intensity of $I >> 10^{12}$ w.cm^2. In this regime it can be shown (230-232) that the rate of energy absorption decreases as the irradiance increases and in the strong field limit becomes proportional to $I^{-\frac{1}{2}}$. The rate of change of kinetic energy of free electrons is given by:

$$\frac{d\varepsilon}{dt} = \frac{e^2E_o^2}{2m\omega^2}\ \nu_{eff}$$

where in the high field case, $\nu_{eff} = \dfrac{8\pi^3NZ^2e m\omega^3}{E_o^3}$

Thus when the average irradiance I = 1 x 10^{15} w.cm^2, say, τ = 100 ps, and the gas pressure is 760 torr, $\int_o^\tau \frac{d\varepsilon}{dt} \simeq 850$ eV. We conclude that inverse bremsstrahlung provides an adequate explanation of the presence of Ne IV lines without invoking any other heating process.

An attempt was made to study laser absorption processes at lower pressures. At 50 torr, twenty laser shots were required for a weak spectroscopic plate exposure. Ne I, II and III were identified. Since the resultant spectrum was weak after so many laser shots, it was concluded that the diagnostic technique in its present form had reached the limit of its usefulness and no conclusion on laser absorption processes could be made.

It is therefore proposed that in order to study laser absorption in gases at low pressure and very high radiation fields, future diagnostics should include particle detectors. The gas breakdown cell is being modified to include two electrodes providing a small uniform DC field across the focal region of the lens. Positive ions produced at the focus will be collected at the cathode and the ion current will be monitored using the low noise high bandwidth amplifiers developed at Swansea. M/Z will be determined by time of flight at pressures in the range 10^{-4} - 10^{-2} torr.

R J Dewhurst (Convenor)(Hull).

2.6 RELATED THEORETICAL AND COMPUTATIONAL STUDIES

Introduction

A particular interest of several of the theory groups has been to explore the effects of the generation of magnetic fields due to the $\nabla n \times \nabla T$ source term. Hot rings and fast ion production have been produced under non-uniform irradiation of targets. Several two-dimensional codes are available to study these effects. Analytic studies of resonance absorption, including the enhancement on a rippled surface, have been carried out. But non-linear effects of the laser-plasma interaction can only be satisfactorily modelled with particle-in-cell computer models. Two one-dimensional codes have been developed; an electromagnetic and relativistic code with particle velocity followed in two dimensions, and an electrostatic code which is combined with an analytic formulation of the electromagnetic wave. The former is limited to normal incidence only, whilst the latter models resonance absorption at arbitrary angles. Both codes restrict plasma and ion-acoustic waves to one dimension, but demonstrate ponderomotive force steepening of the density gradient and fast electron production.

2.6.1 Imperial College

(a) Electrostatic 1D Particle Code E214

The 1D particle code has been used for the study of resonance absorption and fast particle production in the case of a thin slab. Ponderomotive force steepening of the density profile as well as fast electrons have been found. Standard cases are now being compared with the $1\frac{1}{2}$D electromagnetic code at Bangor.

We are now contemplating the development of a 2D particle-code with which to perform modelling of scattering instabilities for use as a check on our relatively inexpensive 1D code and to extend the modelling to Brillouin and Raman backscatter as well as resonance absorption by means of a semi-analytical treatment. This will enable a greater parametric range to be explored.

(b) Resonance absorption in a magnetic field

Following the study on the resonant absorption of p-polarised e.m. waves incident obliquely on an inhomogeneous plasma, an attempt was made to investigate the problem of resonance absorption in the case of normal-incidence in the presence of a constant magnetic field perpendicular to the plane of incidence. However, it has recently been brought to our attention that part of the paper by R B White and F F Chen (Plasma Phys 16 565 1974) is devoted to this same problem. Although this paper deals with a cold plasma, our study suggests that the results are approximately valid for plasmas with temperatures up to $\sim$ 10 keV. In particular, it follows that in the presence of a magnetic field of $\sim$ 0.3 MG (as recently measured) absorption of radiation by this effect can be no more than $\simeq$ 3% at normal incidence.

2.6.2 University College of North Wales, Bangor

Over the period covered by this report the work of the group at the University College of North Wales, Bangor, has concentrated on the development of a particle code and on theoretical studies and computer simulations of harmonic generation in laser plasma interactions. In the first half of the year much time was taken up with further development of the $1\frac{1}{2}$D electromagnetic particle simulation code EMPIRE and with checking output from the code against published results from computer experiments elsewhere. These proved wholly satisfactory.

During the past six months our effort has been directed to problems concerned with harmonic generation. A number of competing processes - Raman scattering, two-plasmon decay at quarter-critical density and parametric decay amongst others - result in the generation of harmonics of the laser frequency ω_o within the plasma. The various processes are characterised by different growth rates, frequency shifts and by different relative amplitudes of the harmonics. Since the generation of harmonics is a low energy transfer process by comparison with the initial parametric process, it follows that the behaviour of the harmonics bears a simple relationship to this process. We chose to examine the Raman mechanism by virtue of the fact that, unlike the two-plasmon decay process, it may be simulated using the $1\frac{1}{2}$D code. A theoretical model in which an electron plasma wave at the quarter-critical density couples successively with the backscattered harmonic at $n\omega_o/2$ ($n = 1, 2, 3. ...$) to produce a harmonic at $(n + 1)\omega_o/2$ has been developed. The growth rates of the harmonics bear a simple relationship to the Raman growth rate in a homogeneous plasma. Scaling laws for the relative harmonic amplitudes have been obtained. The Raman instability is modified significantly - and eventually saturated - by strong particle trapping. This non-linear phase has been investigated in a series of computer experiments using the EMPIRE code. Comparisons of the frequency shifts and non-linear growth rates obtained with those from a non-linear theory are in progress.

Harmonics may additionally be generated in the presence of a magnetic field $\underline{B}$ by virtue of the fact that the $\underline{v} \times \underline{B}$ force drives large amplitude electron oscillations near the critical density in inhomogeneous plasmas. Theoretical work has produce expressions for the relative harmonic amplitude and simulations of this mechanism using the computer code are in progress.

2.6.3 Glasgow University

Two dimensional numerical results have been obtained for laser produced carbon plasmas evolving through the formation of the critical surface. These results show a novel reversal of the spontaneously generated magnetic field. The laser pulse is taken to be normal unfocused irradiation of high intensity (> 10^{15} w/cm^2) from a Nd:glass laser (100 ps FWHM pulse length, 100 J energy, Gaussian in time and radius with half-width 25 μm), on a plane solid carbon target. The importance of B reversal is that it introduces a heat conduction path along B = 0 other than that along the axis of the beam.

Simulations were carried out using the 2D CASTOR flux code (234) modified by a time dependent atomic physics model TRIP (235) which includes three-body recombination (necessary in dense plasma) as well as radiation recombination and collisional ionisation required to simulate ionisation in low density plasmas. The time dependence and three-body recombination are instrumental in predicting a decreasing electron density gradient between the laser absorption region and the ablating surface. It is due to combination of this negative gradient $\frac{\partial n_e}{\partial z}$ in conjunction with the usual negative $\frac{\partial T_e}{\partial r}$ that $\frac{\partial B}{\partial t}$ is negative and can result in anomalous field reversal.

2.6.4 St Andrew's University

An analytical formulation has been made of the resonant absorption of laser light at a rippled critical surface. When laser light is incident on a plasma, density variations perpendicular to the main density gradient may develop, producing a rippling of the critical surface. It has been shown that such ripples can lead to resonant absorption of normally incident radiation and the magnitude of the absorption coefficient has been estimated.

M G Haines (Convenor), B Hafizi, J D Kilkenny (Imperial College); H C Barr, T J M Boyd, G A Gardner, L R T Gardner, W T Hewitt, G Humphreys-Jones (Bangor); E W Laing, W P S Tan (Glasgow); R A Cairns (St Andrews).

REFERENCES

201. J A Stamper et al. Phys. Rev. Lett. 35, 663 (1975)

202. D G Colombant, N K Winsor, Phys. Rev. Lett. 38, 697 (1977)

203. J J Thomson, C E Max, K Estabrook, Phys. Rev. Lett. 35, 663 (1975)

204. D A Tidman, Phys. Rev. Lett. 32, 1179 (1974)

205. A Raven, P T Rumsby, Phys. Lett. 60A, 42 (1977)

206. W F Di Vergilio et al. Phys. Rev. Lett. 38, 541 (1977)

207. J A Stamper, B H Ripin, Phys. Rev. Lett. 34, 138 (1975)
J A Stamper, E A McLean and B H Ripin, NRL Report No. 3758 (1978)

208. R S Adrain, E G Arthurs, W Sibbett, Optics Communications 15, 290 (1975)

209. H Azechi et al. Phys. Rev. Lett 39, 1144 (1977)
R Fedosejevs et al. Phys. Rev. Letts. 39, 932 (1977)

210. C E Max, W M Manheimer, J J Thomson, Phys. Fluids, 21, 128 (1978)

211. E Storm, private communication.

212. R C Malone, R L McGory, R L Morse. Phys. Rev. Lett. 34 721 (1975)

213. J S Pearlman, J P Anthes. Appl. Phys. Lett. 27, 581 (1975)

214. D Henderson, LASL Report

215 R J Faehl, W L Kruer. Phys. Fluids. 20, 55 (1977)

216. W M Manheimer. Phys. Fluids 20, 265 (1977)

217. L Spitzer. Physics of fully ionized gases. (Interscience, 1956)

218. V A Boiko, et al. Lebedev Preprint No. 20 (1976)

219. G E Bromage, et al. J.O.S.A. (in press) 1978.

220. G E Bromage, et al. Culham Report CLM-R170 (1977)

221. C P Bhalla, A H Gabriel, L P Presynakov. Mon. Nat. R. Astr. Soc., 172, 359 (1975)

222. U Feldman, G A Doschek, D H Nagel, R D Cowan, R R Whitlock. Astrophysical Journal, 192 , 213 (1974)

223. H R Griem, H J Kunze, Phys. Rev. Lett. 23, 1279 (1969)

224. A H Gabriel, Mon. Nat. Roy. Astro. Soc. 160, 99 (1972)

225. J C Weisheit, et al. J Q Spec. and Rad. Transfer 16. 659 (1976)

226. D J Bradley, A G Roddie, W Sibbett, M H Key, M J Lamb, C L S Lewis, P Sachsenmaier. Opt. Comm. 15, 231 (1975)

227. M H Key, M J Lamb, C L S Lewis, P Sachsenmaier. Opt. Comm. 19, 383 (1976)

228. J G Lunney, M J Lamb, R K Thareja, L Cooke, A K Roy, C L S Lewis. XI European Conf. on Laser Interaction with Matter, Oxford (1977)

229. A I Avrov, et al. J.E.T.P. Letts. 24, 262 (1976)

230. J F Seely, E G Harris, Phys. Rev. A. 7. 3. 1064-1067, 1973

231. T P Hughes, Plasmas and Laser Light, publ. Adam Hilger, 1975

232. G J Pert, J. Phys. A. 9. 3. 463-471, 1976

233. Yu P Raizer, Sov. Phys. Usp. 8, 650-673, 1966

234. J P Christiansen, N K Winsor, J Magill, J P Boris "Castor, a 2-D Laser Target MOdel" Culham Laboratory CPN 4/76

235. J Magill, J. Phys. D: Appl. Phys. 10, 2257 (1977)

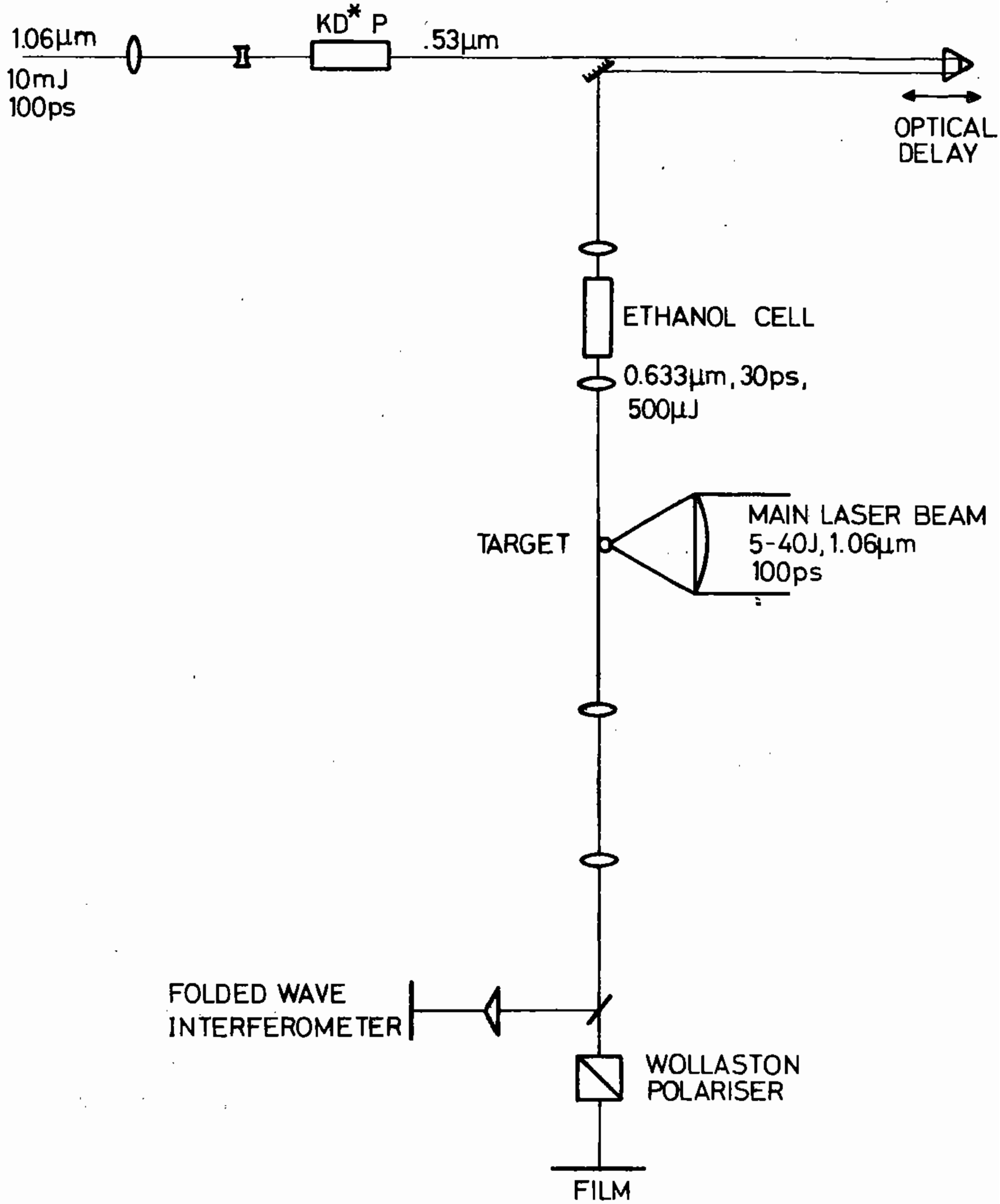

FIG. 201 EXPERIMENTAL ARRANGEMENT OF PROBE BEAM SYSTEM

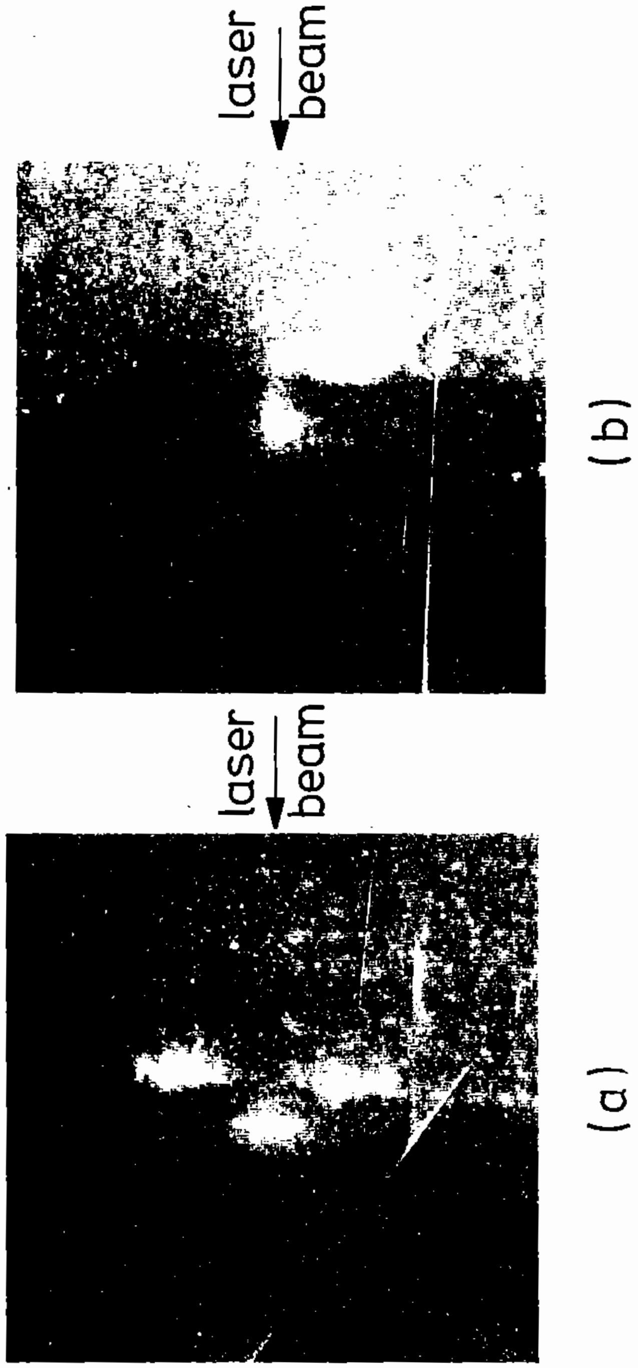

FIG. 202 A. FARADAY ROTATION PHOTOGRAPHS WITH CROSSED POLARISERS. THE CENTRAL SPOT MARKS THE POSITION OF THE FOCUS. E = 9.3J. TIME IS 60PS AFTER THE PEAK OF THE MAIN PULSE.

B. FARADAY ROTATION PHOTOGRAPH WITH POLARISER ANGLED AT 10^{o} SHOWING TOROIDAL NATURE OF THE FIELD. E = 9.4J. TIME AS IN (A).

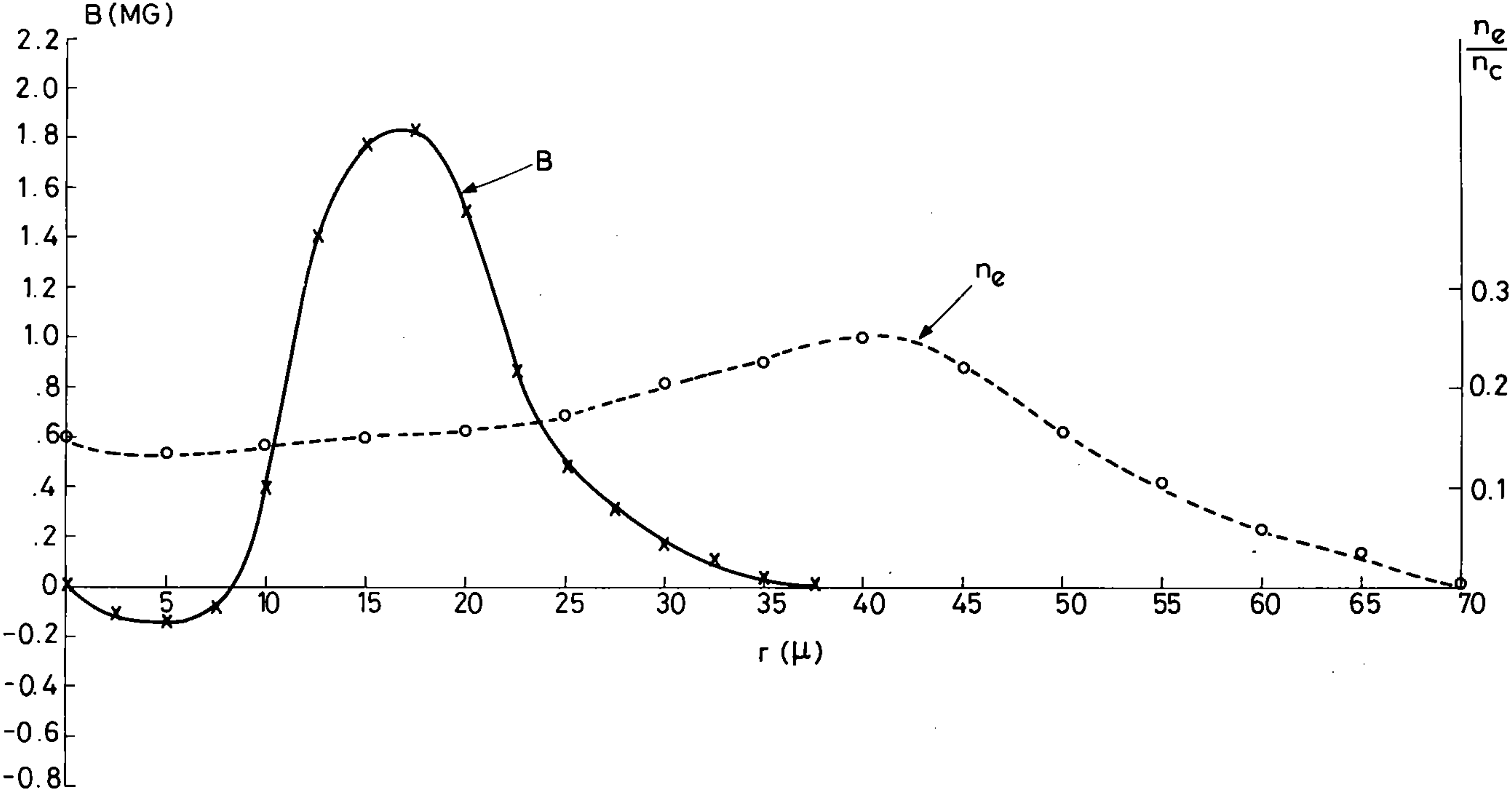

FIG. 203 RADIAL FIELD AND DENSITY PROFILES AT

$Z = 12.5\mu$. $E = 20.4J$. TIME AS IN FIG. 202.

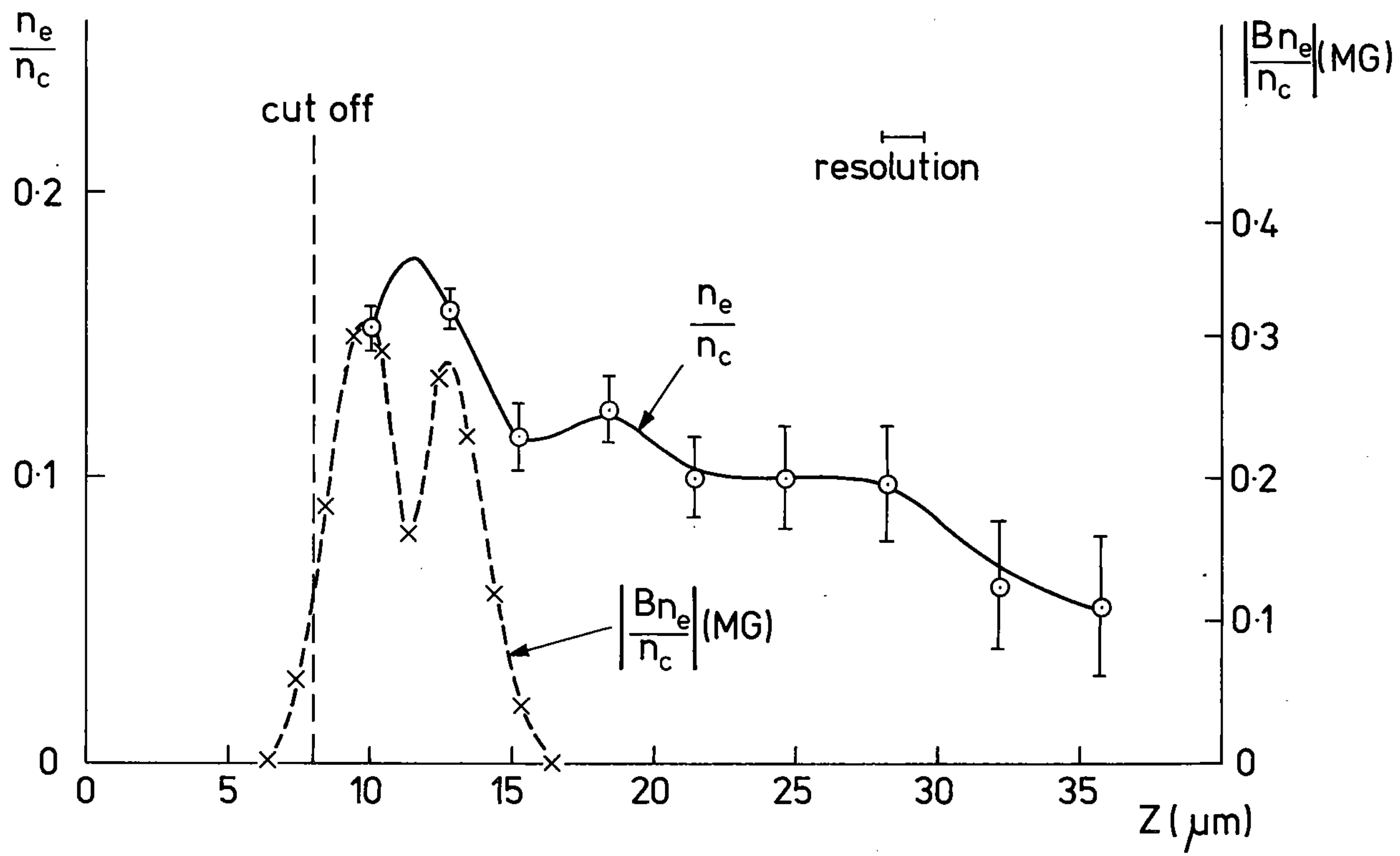

FIG. 204 AXIAL FIELD (---) AND DENSITY (——) PROFILES AT R = 15_{μ} FOR THE SAME SHOT AS FIG. 203.

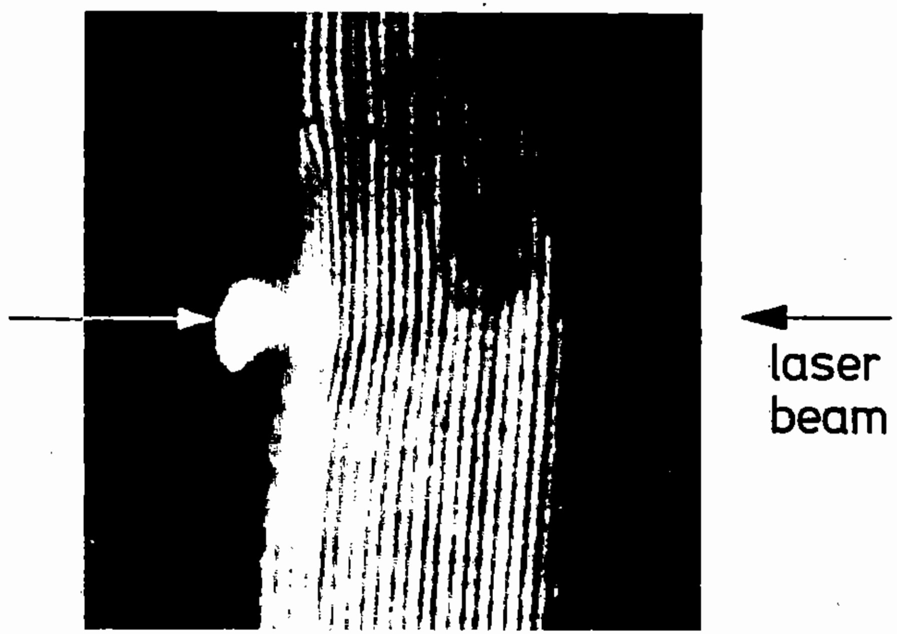

FIG. 205 INTERFEROGRAM OF Z DISCONTINUITY TARGET. ARROW MARKS THE POSITION OF THE ORIGINAL DISCONTINUITY BETWEEN ALUMINIUM AND POLYTHENE. E = 23.6J. TIME AS IN FIG. 202.

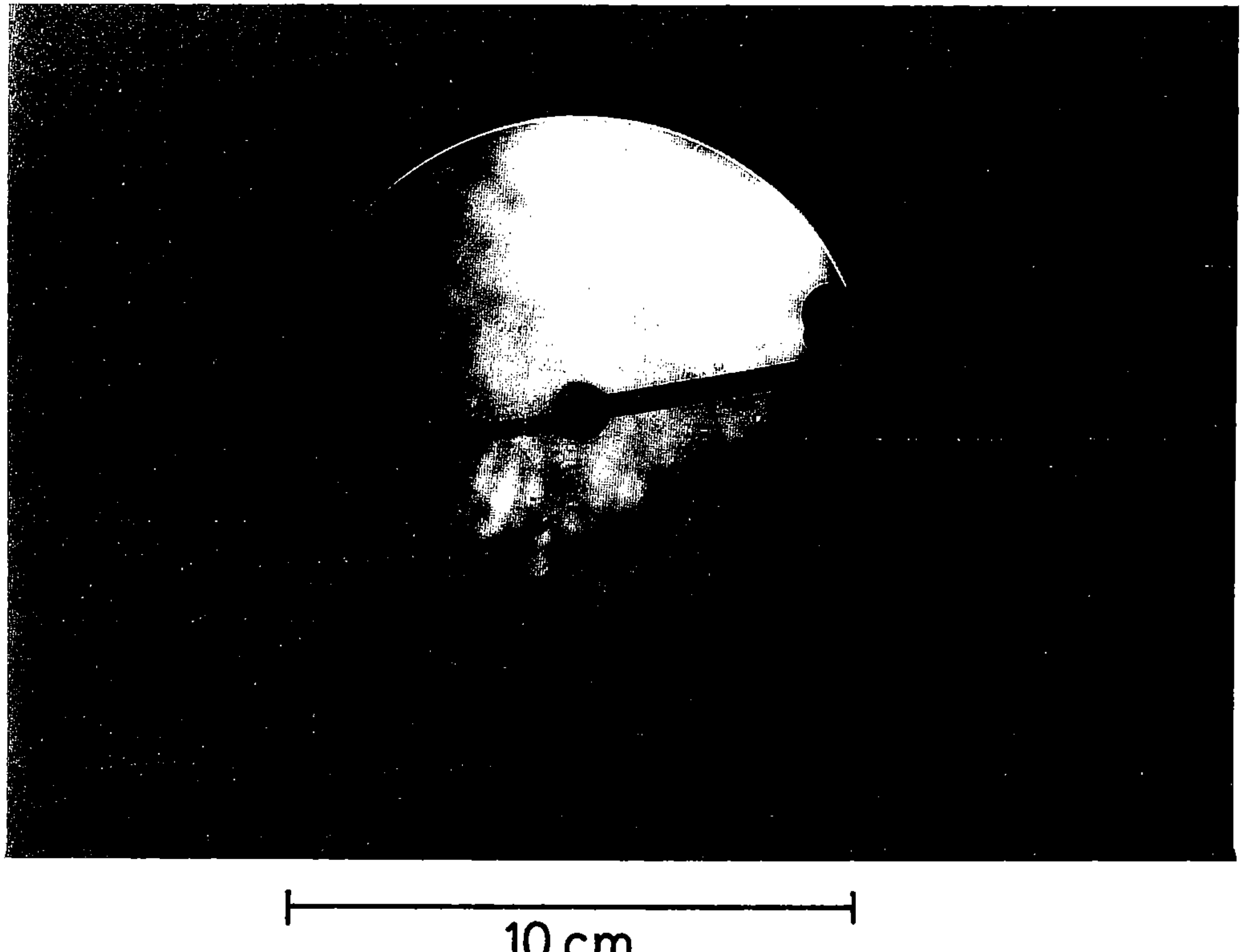

FIG. 206 INTENSITY DISTRIBUTION IN BACK COLLECTION LENS.

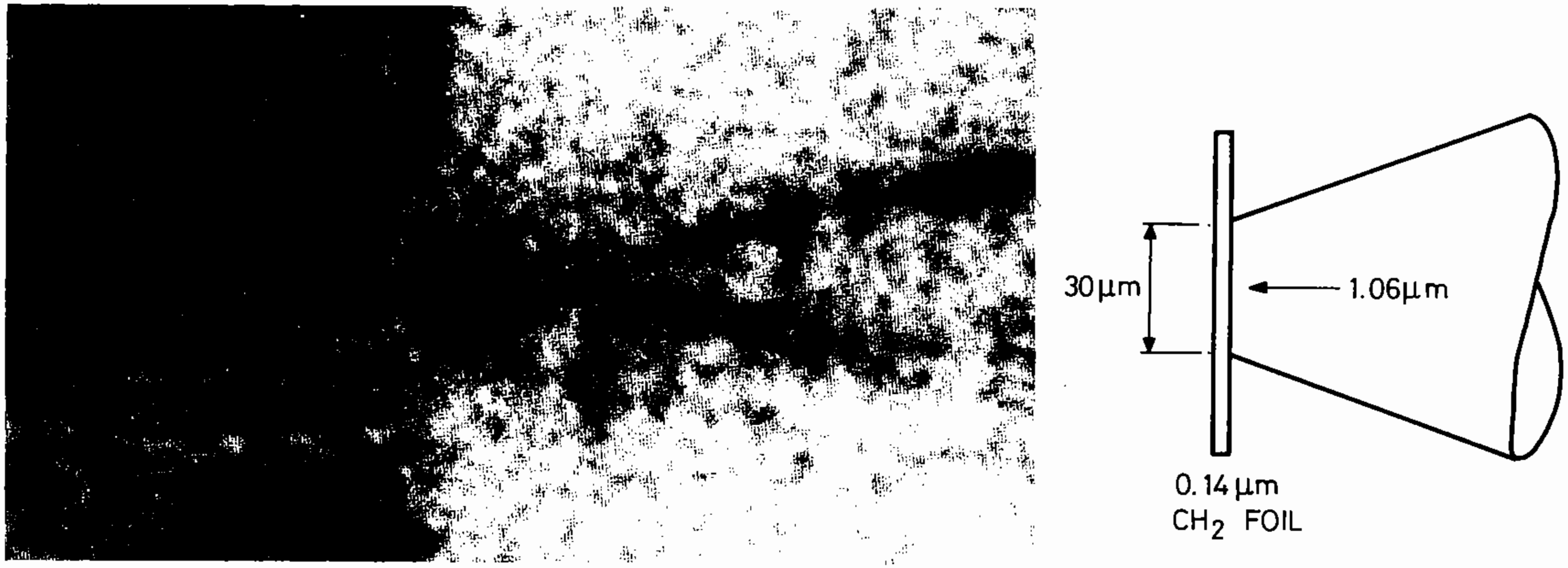

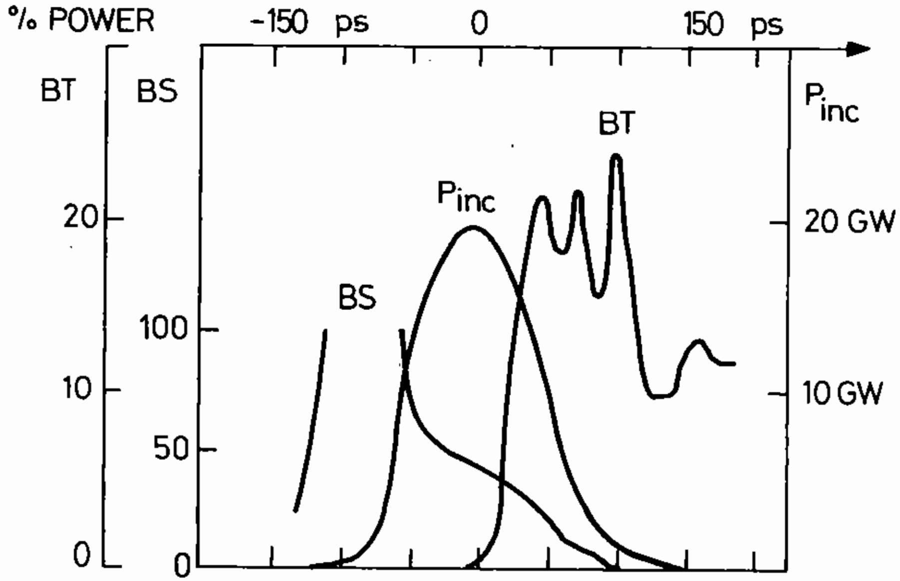

SHOT 020278/008

E_{inc} = 2.1 J

E_{BT} = 6 % E_{inc}

E_{BS} = 30.95 % E_{inc}

FIG. 207 STREAK CAMERA DATA

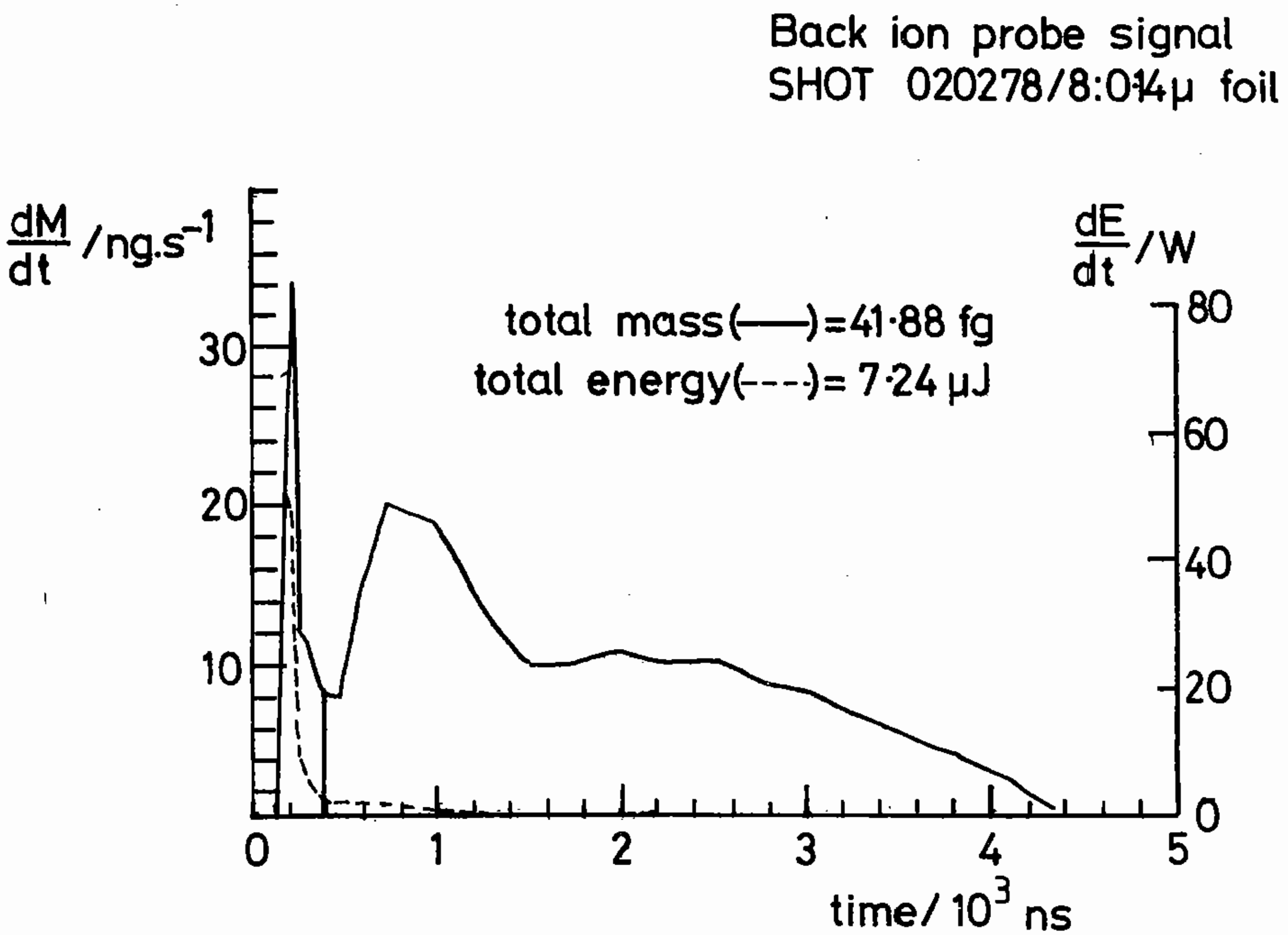

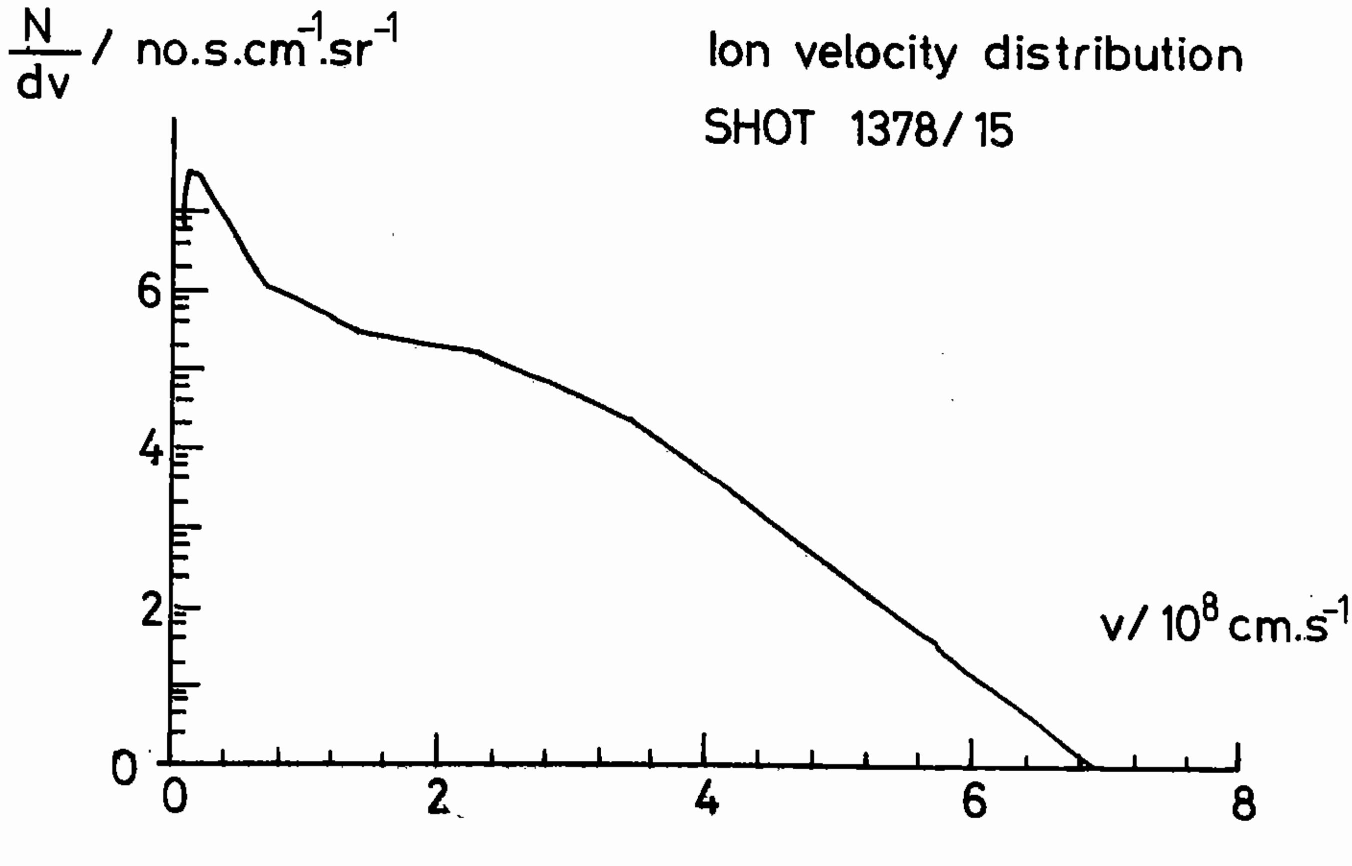

FIG. 208 Ion probe data

magnetic field

SHOT 34 (23-3)

0·09 μm foil

0·5 gauss

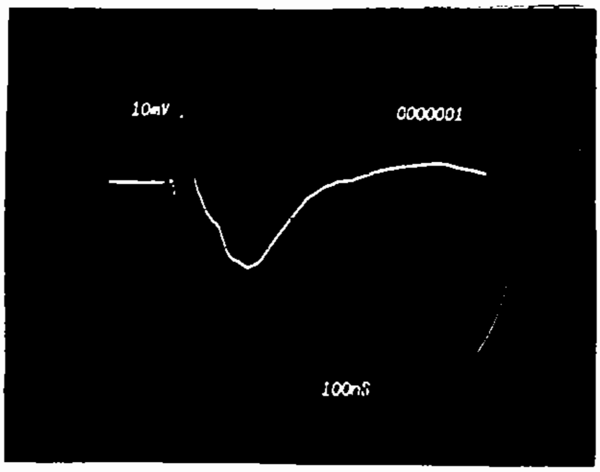

500 nsec

[R/I.C.]

probe - target separation: 13mm

FIG. 209 MAGNETIC PROBE SIGNAL

MEDUSA SIMULATION OF THIN FOIL BURNTHROUGH

Incident pulse: 100ps FWHM, $P_{max} = 5.10^{15}\ W.cm^{-2}$

Foil: 0·18 μm thick CH_2 at z=100μm [at t=0

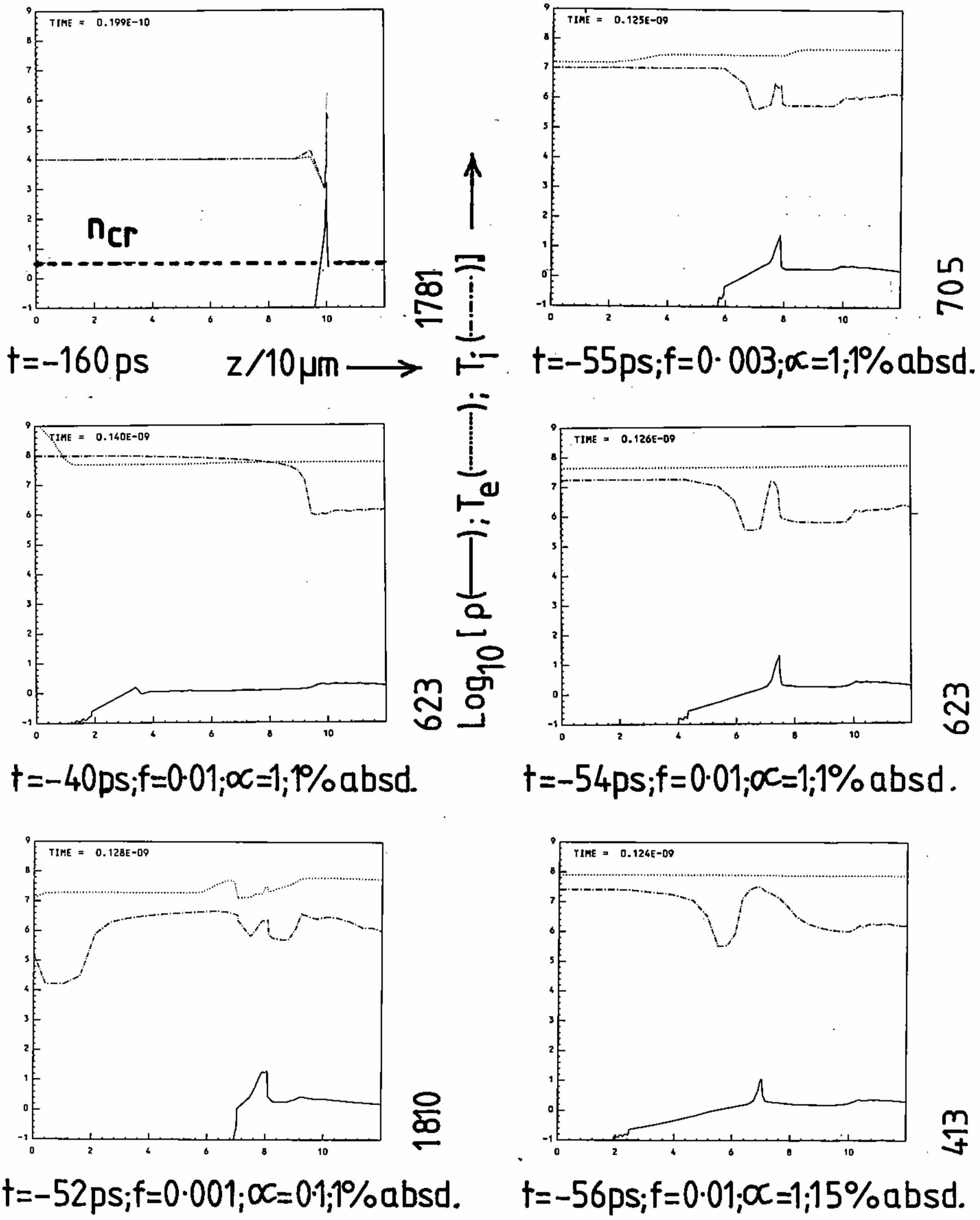

FIG. 210 MEDUSA SIMULATIONS

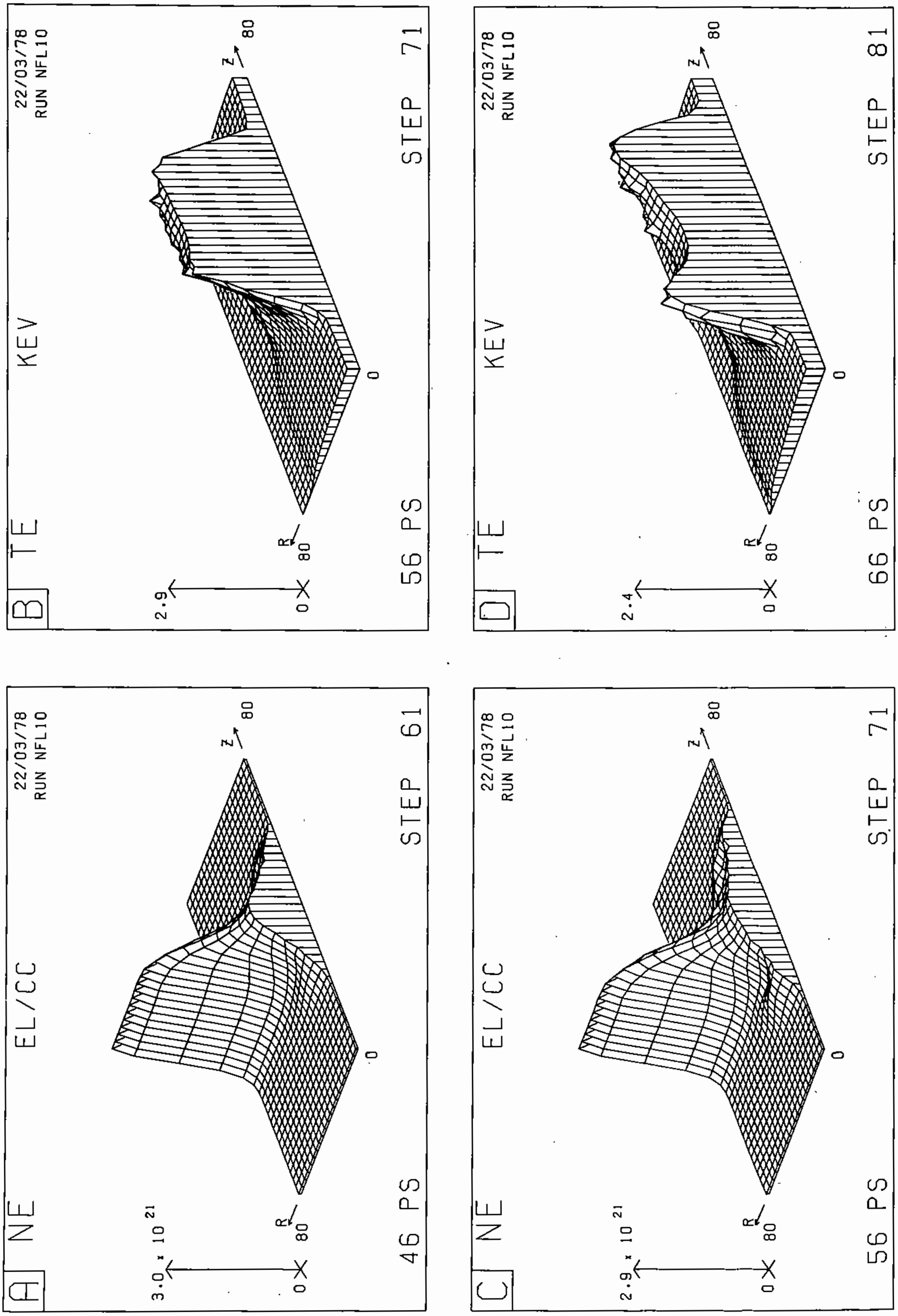

FIG. 211 LASERB SIMULATION WITH $\omega\tau$ INHIBITION

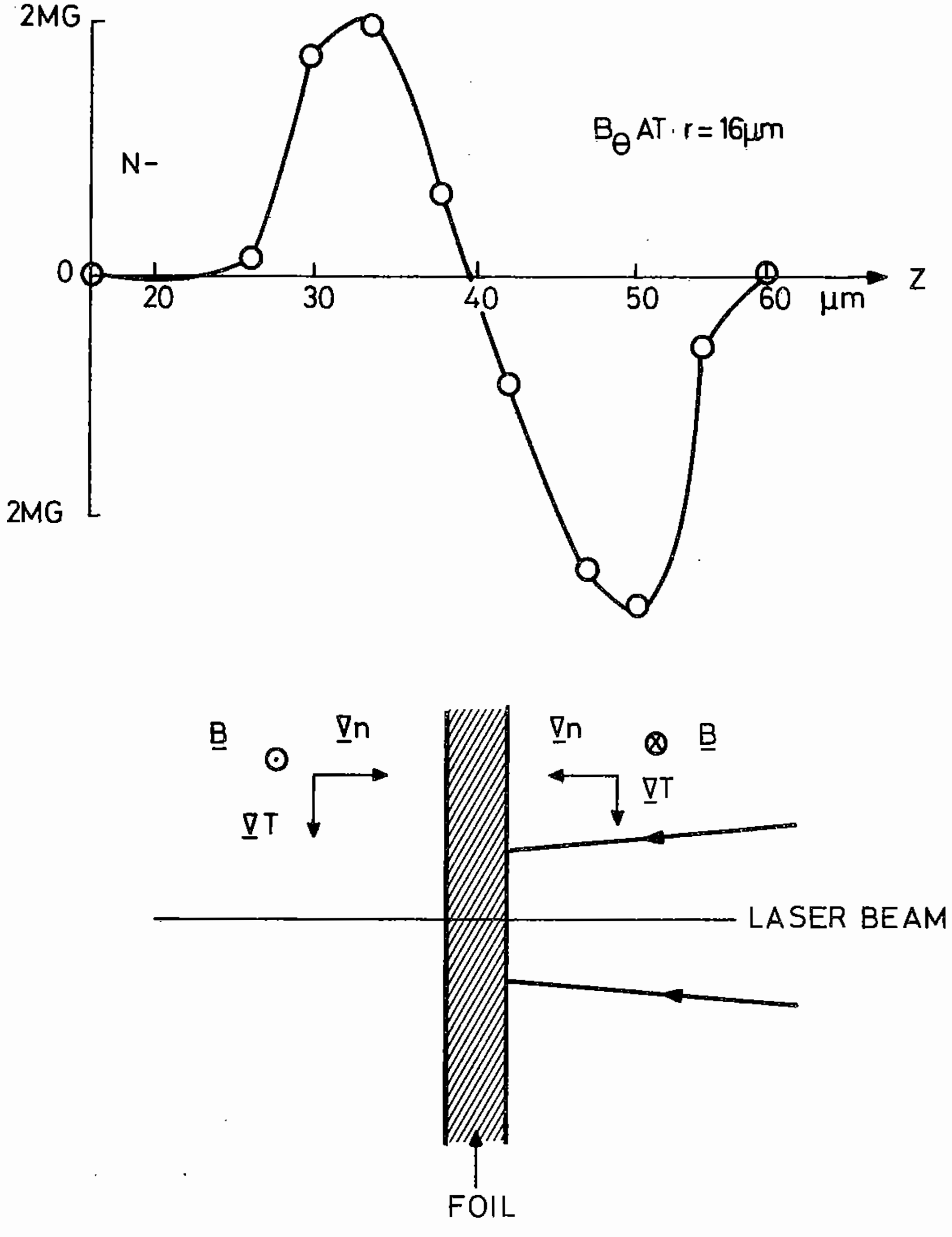

FIG. 212 LASERB PREDICTION OF MAGNETIC FIELD

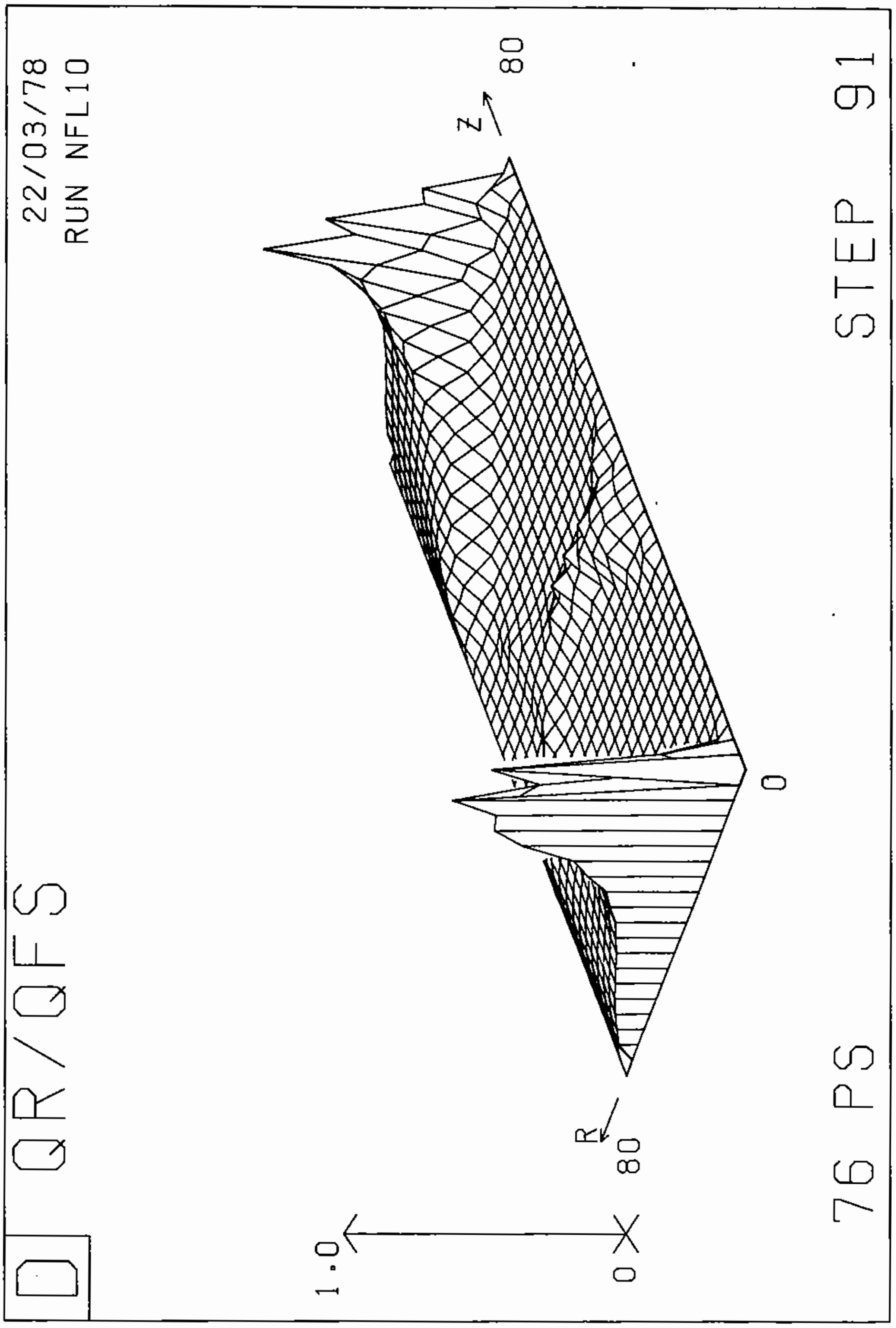

FIG. 213 LASERB: RADIAL HEAT FLUX AS A FRACTION OF THE FREE STREAMING LIMIT

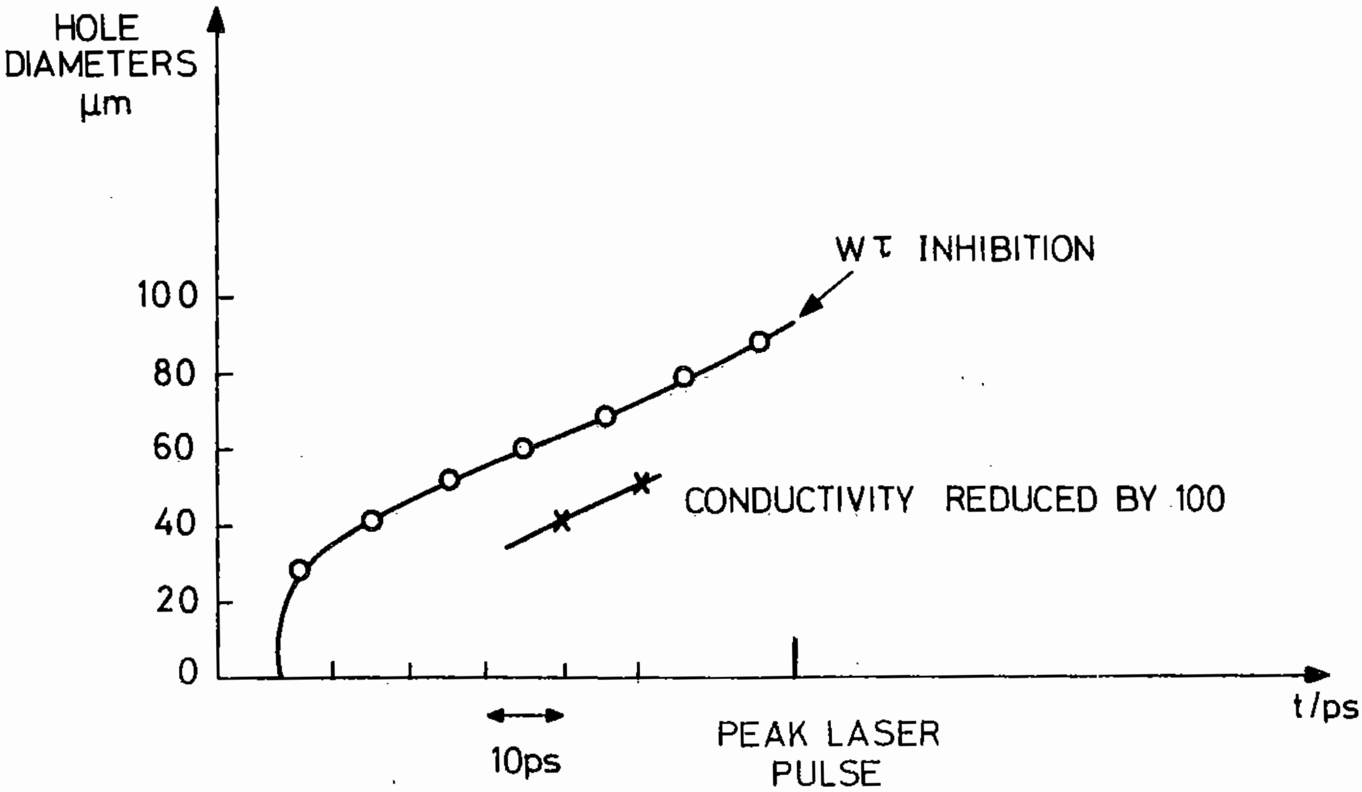

FIG. 214 LASERB PREDICTION OF HOLE DIAMETER.
1J ABSORBED IN 12µM RADIUS SPOT.
120PS PULSE LENGTH. 0.15µM FOIL THICKNESS.

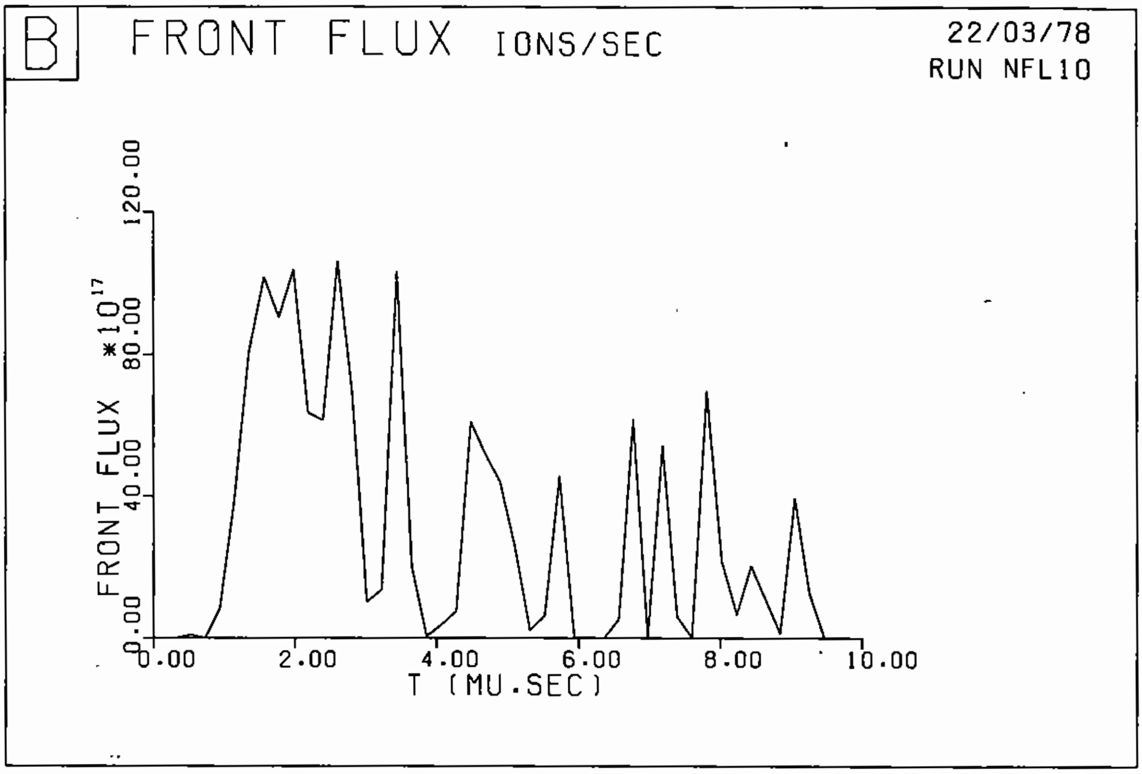

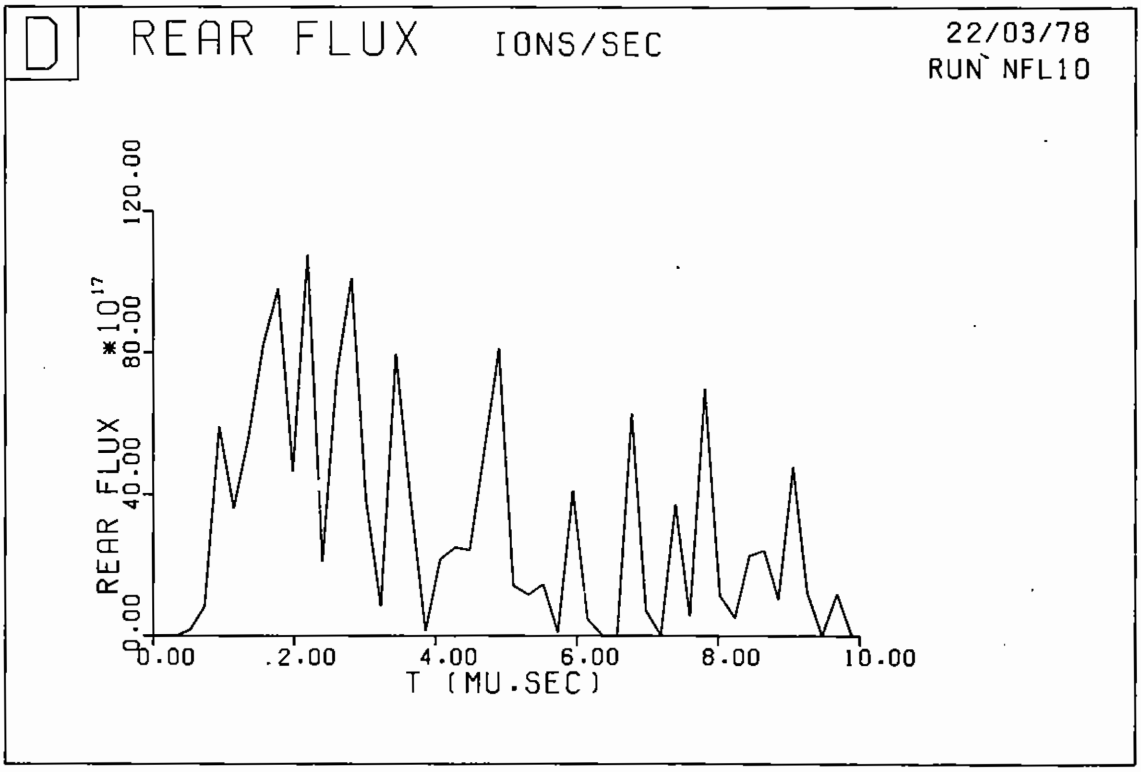

FIG. 215 LASERB: ION EMISSION

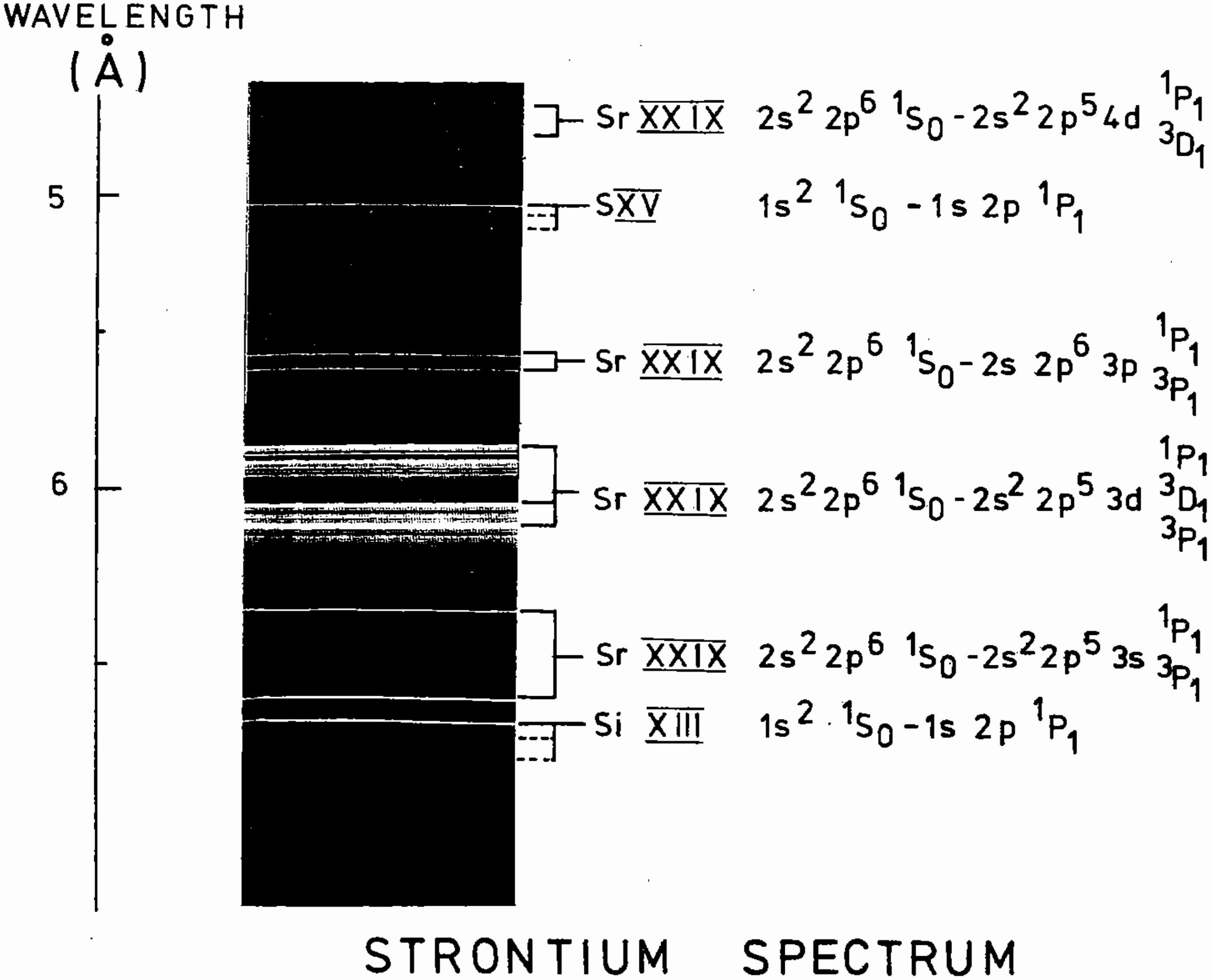

FIG. 216 NEON-LIKE X-RAY SPECTRUM OF STRONTIUM, SHOWING SATELLITE LINES.

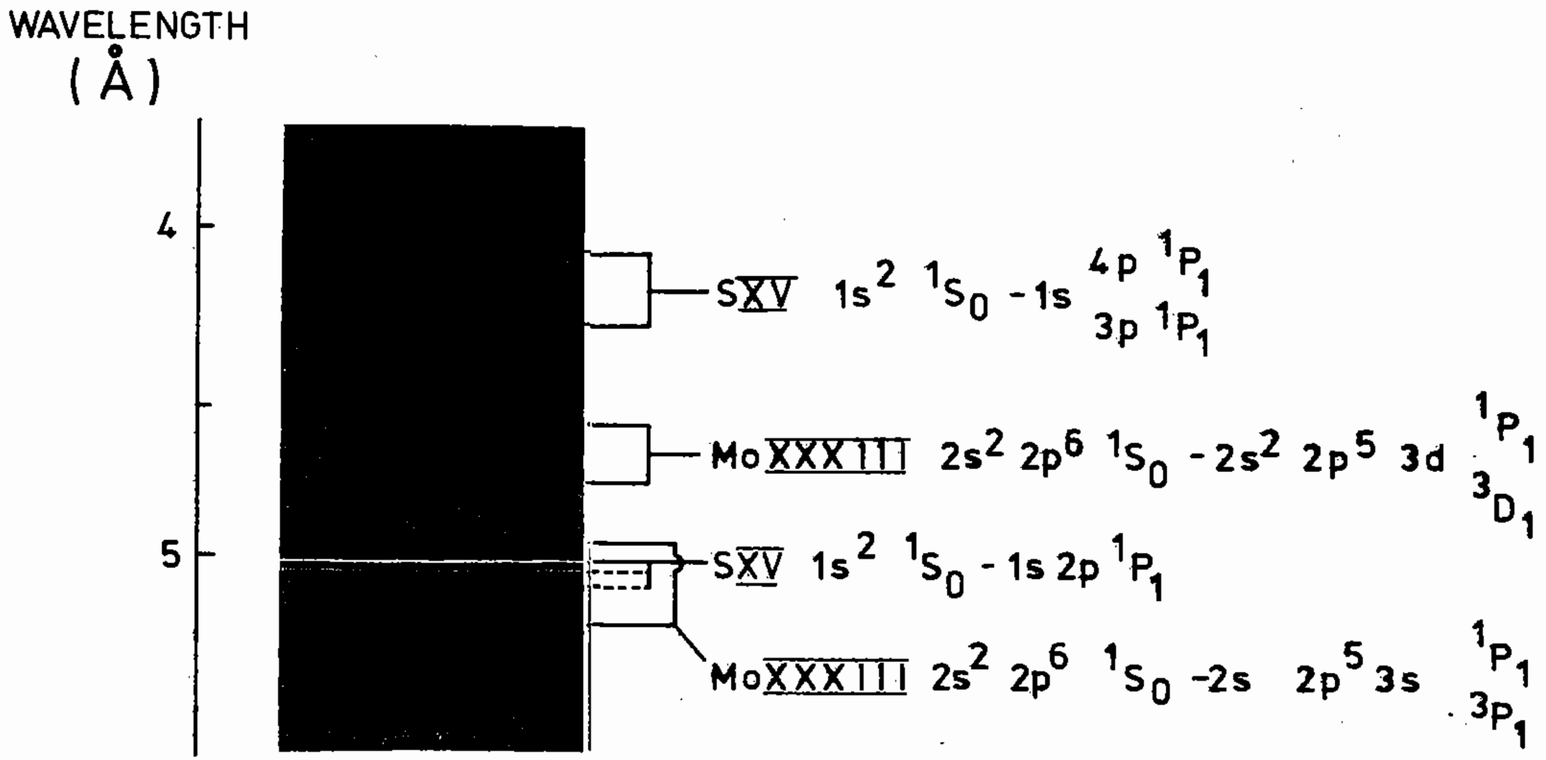

MOLYBDENUM SPECTRUM

FIG. 217 NEON-LIKE X-RAY SPECTRUM OF MOLYBDENUM, WITH SATELLITE LINES AND HELIUM-LIKE SULPHUR LINES

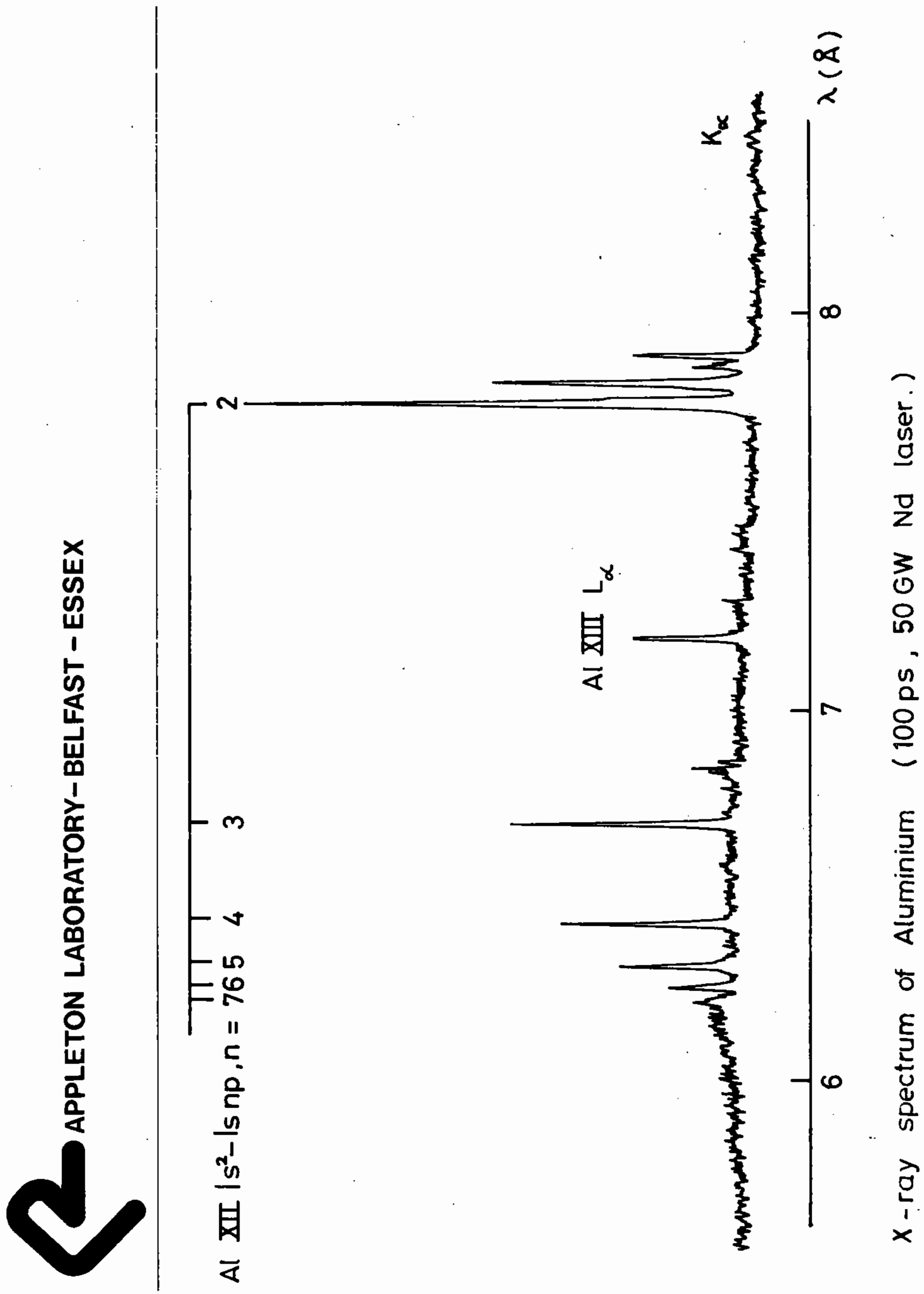

FIG. 218 X-RAY SPECTRUM OF ALUMINIUM, SHOWING HE- AND H- LIKE LINES AND SATELLITES

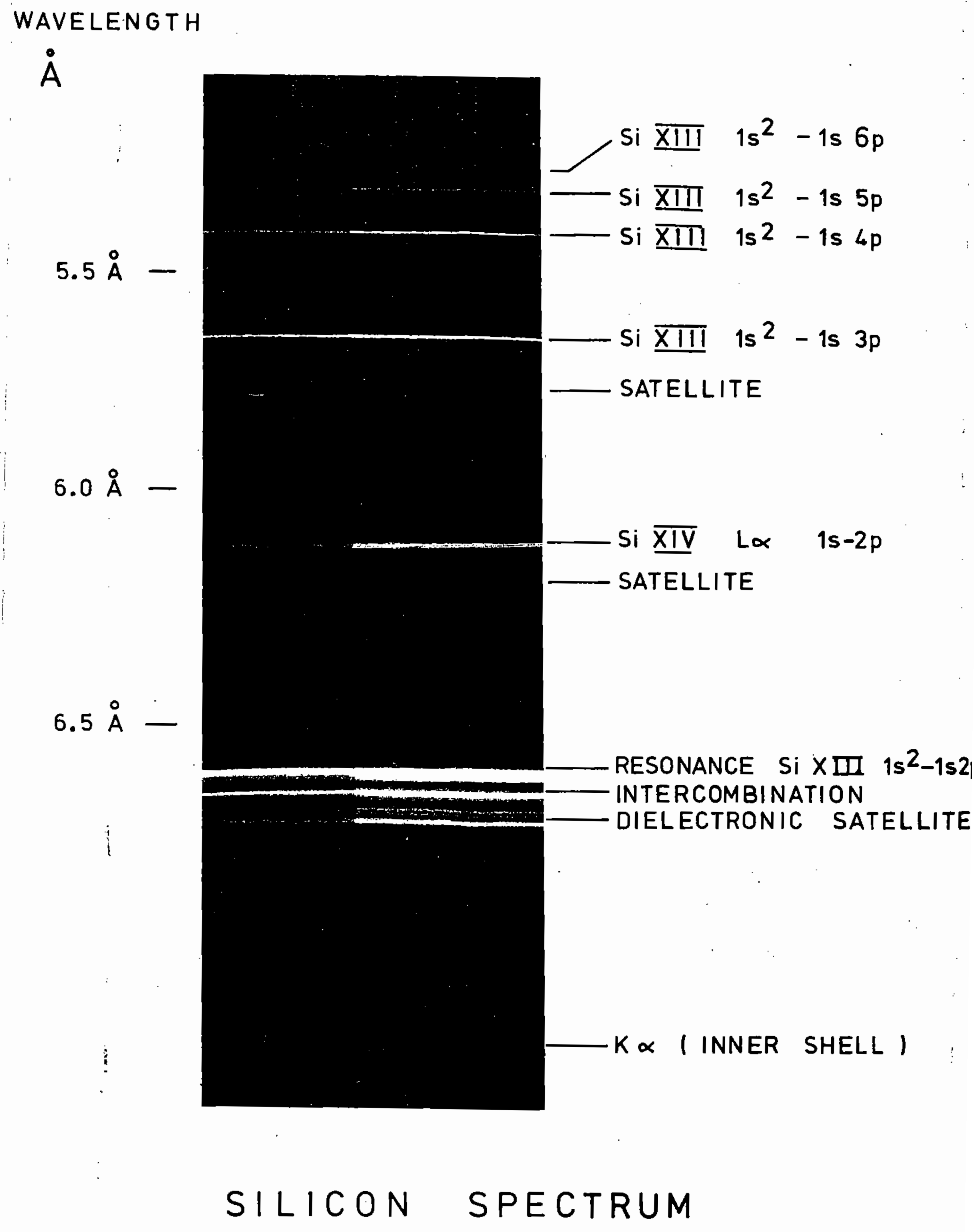

FIG. 219 X-RAY SPECTRUM OF SILICON, SHOWING HE-LIKE LINES AND SATELLITES

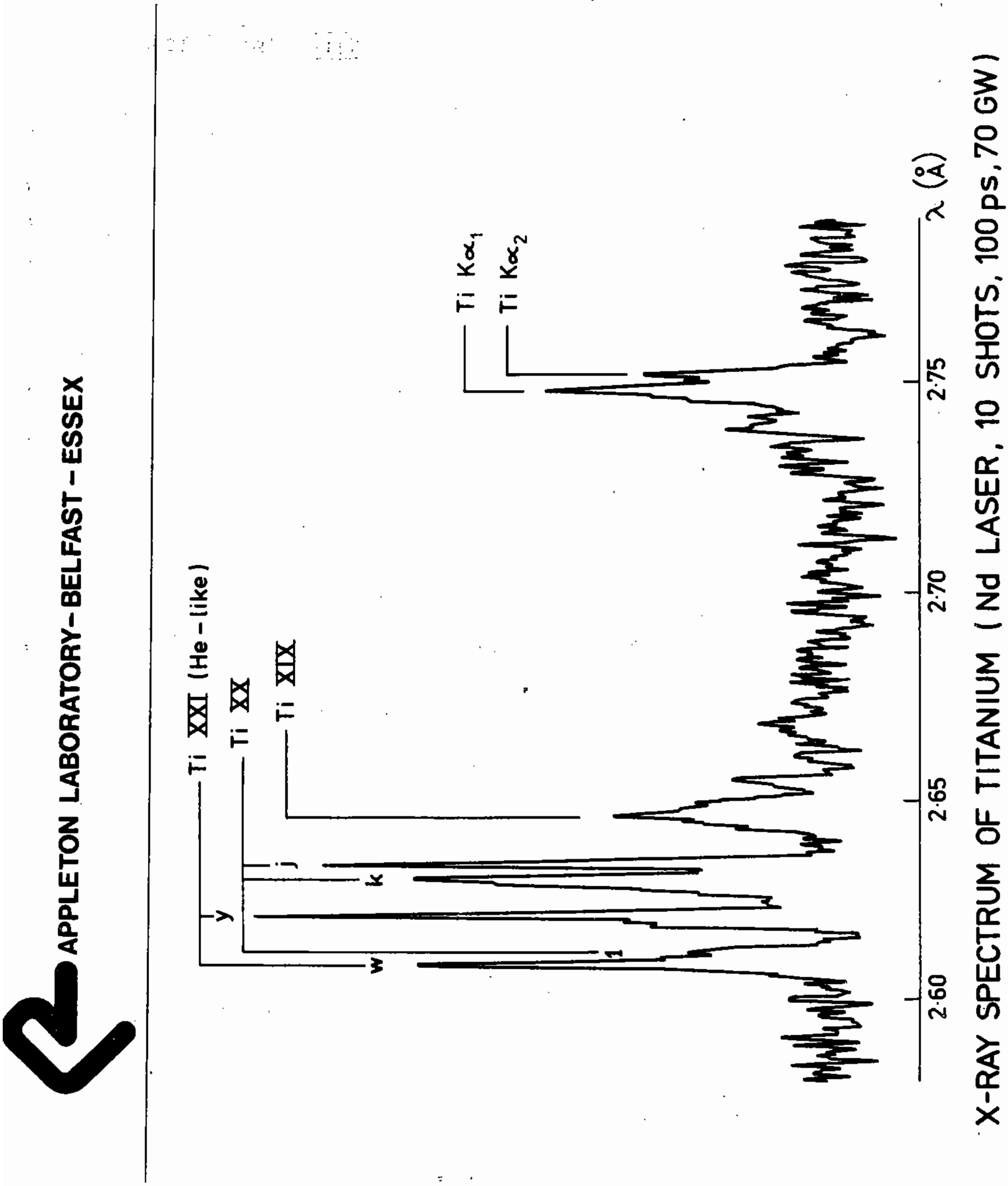

FIG. 220 X-RAY SPECTRUM OF TITANIUM, SHOWING HE-LIKE LINES AND SATELLITES

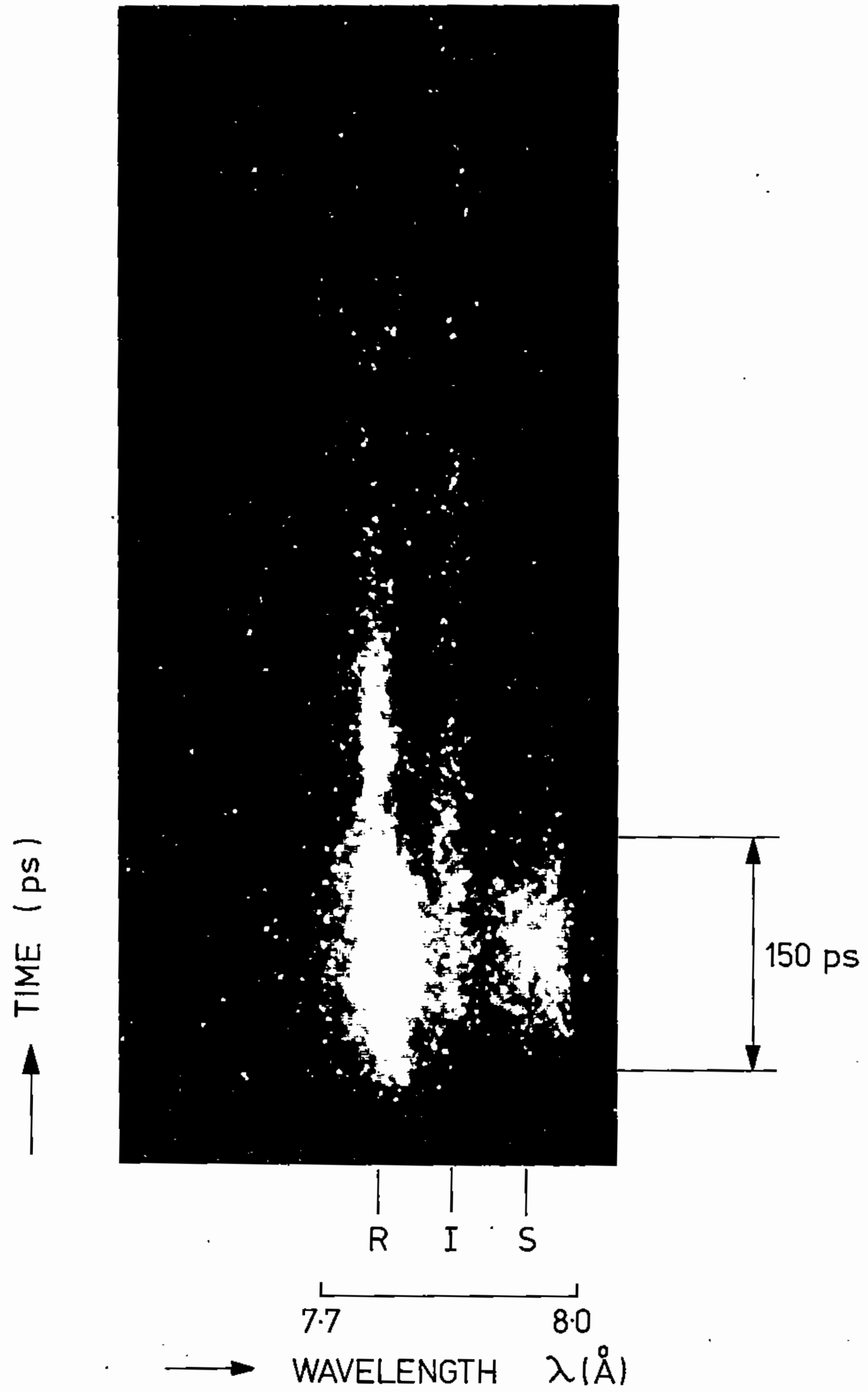

R. RESONANCE $1s^2\ ^1S_0 - 1s\ 2p\ ^1P_1$

I. INTERCOMBINATION $1s^2\ ^1S_0 - 1s\ 2p\ 3P_1$

S. DI-ELECTRONIC SATELLITES $1s^2 nl - 1s\ 2pnl$

FIG. 221 TIME-RESOLVED X-RAY SPECTRUM OF ALUMINIUM

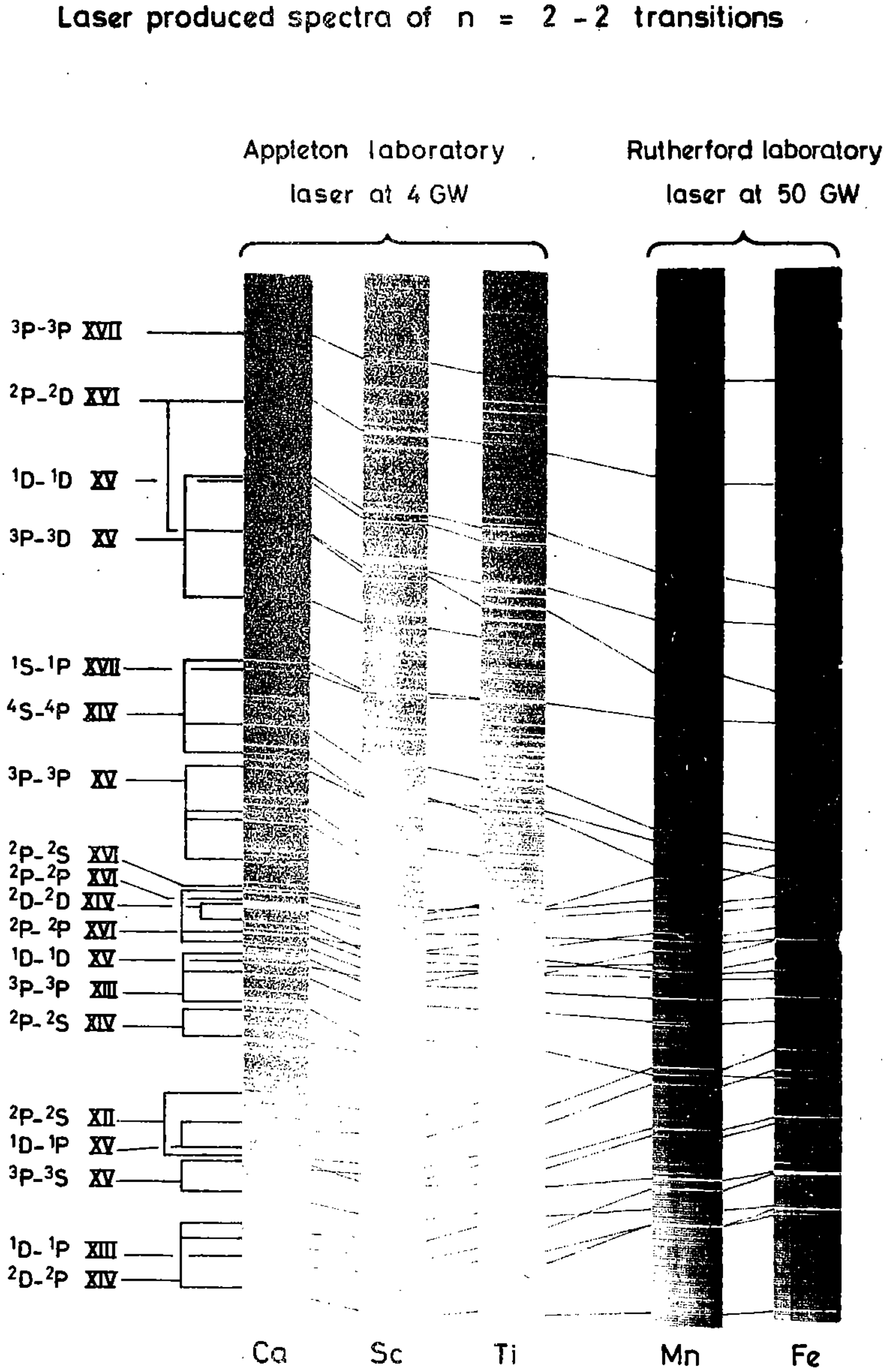

FIG. 222 LASER-PRODUCED VUV SPECTRA OF N = 2-2 TRANSITIONS IN CA, SC, TI, MN AND FE.

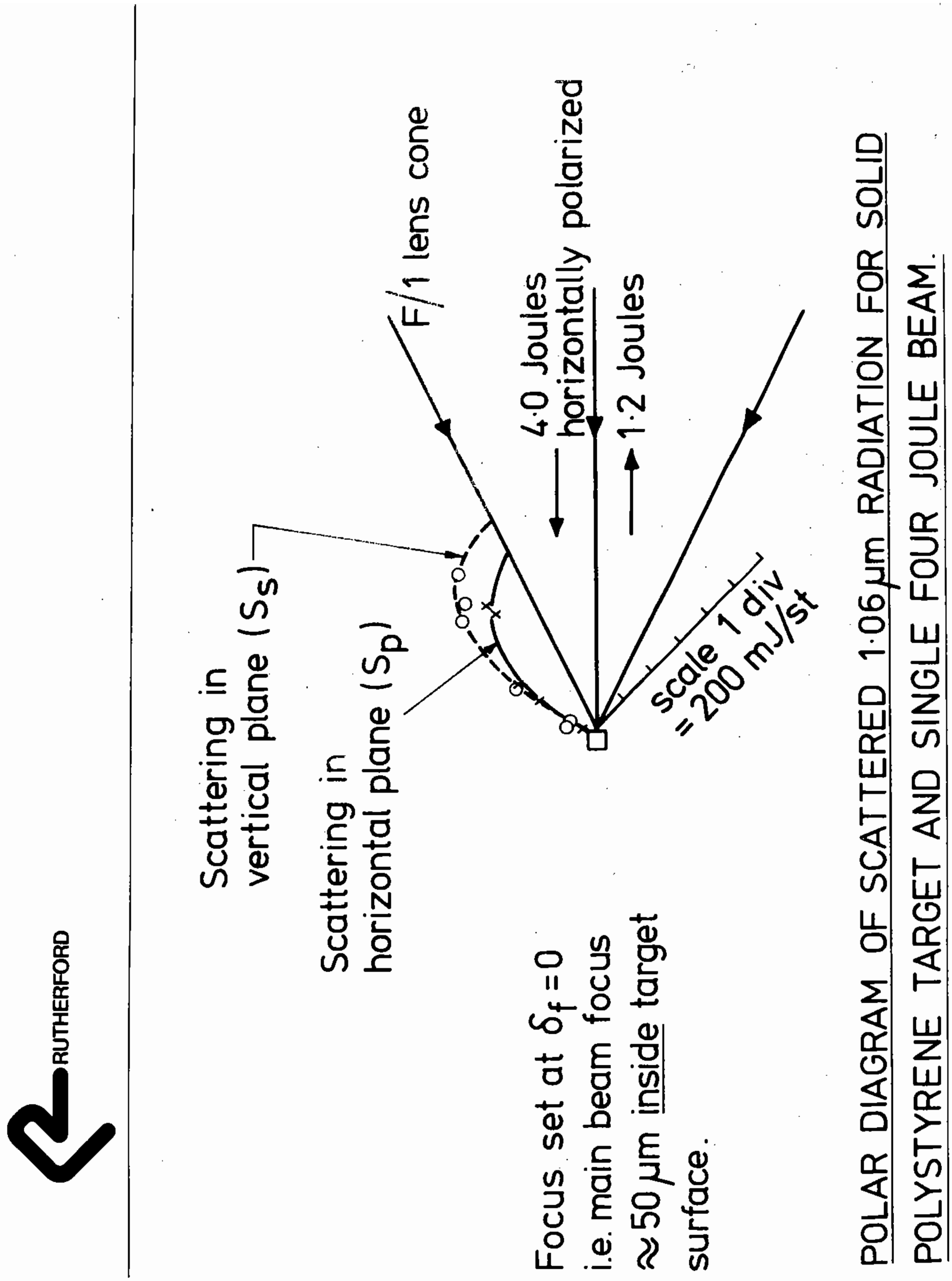

FIG. 223 ANGULAR DISTRIBUTION OF LASER LIGHT SCATTERED FORM A POLYSTYRENE TARGET

Ratio of (scattered light integrated over the P plane of incidence / that for S plane) as a funtion of focussing

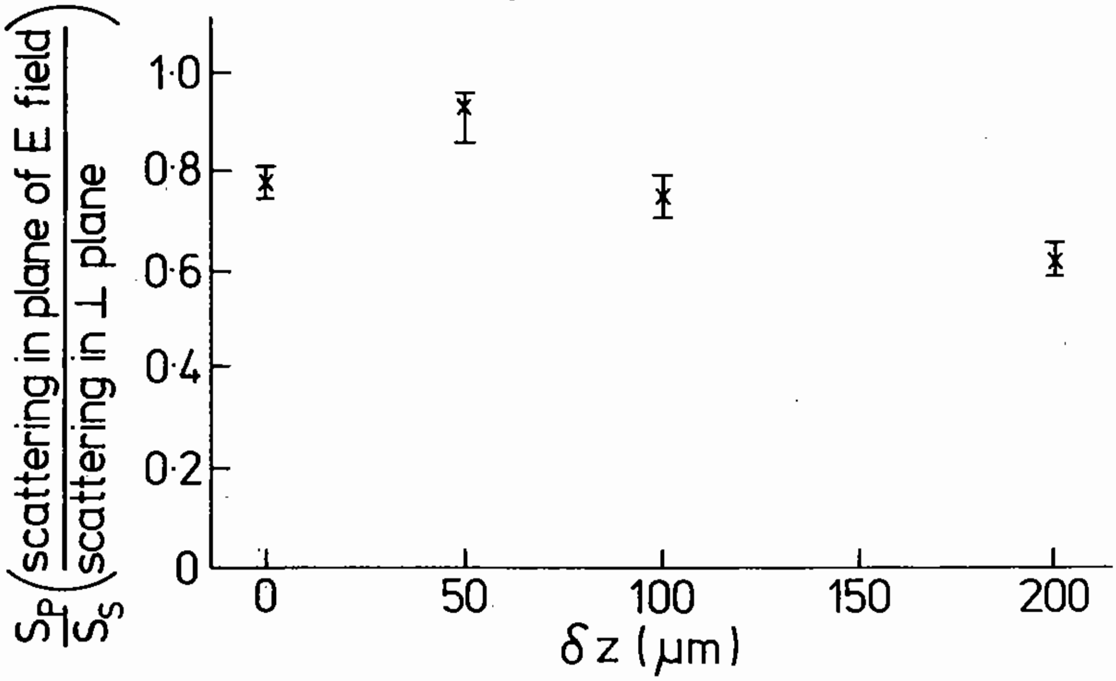

Normalised total diffuse scattered energy as a function of focussing. For 4 Joules of laser energy onto a solid polystyrene target.

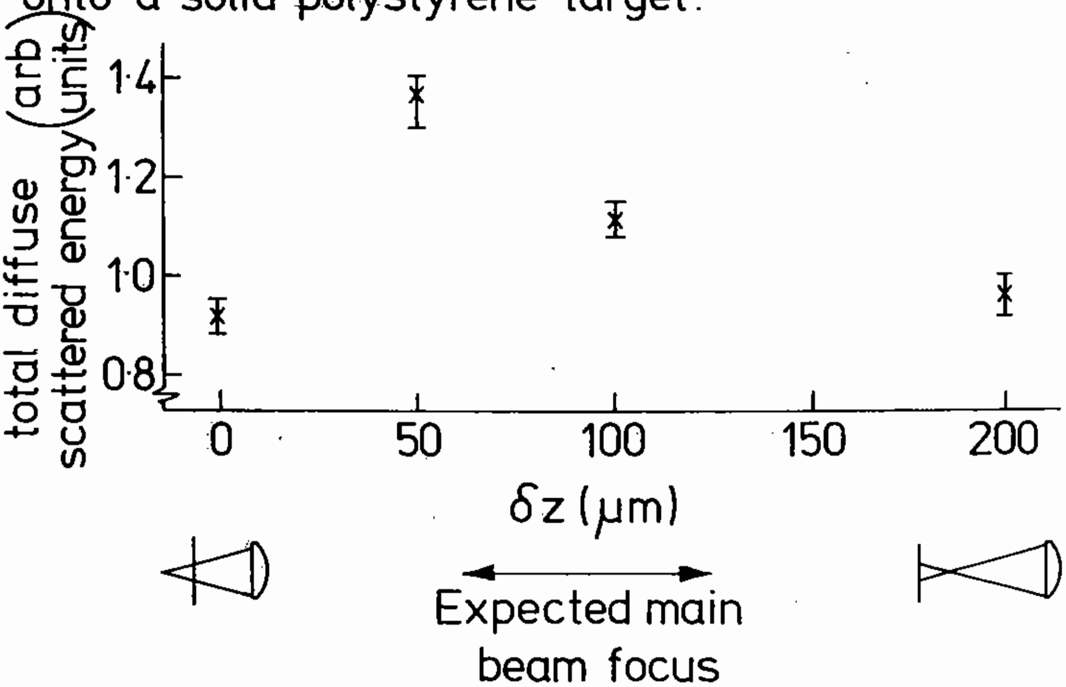

FIG. 224 VARIATION OF SCATTERED LASER LIGHT INTENSITY WITH FOCUS (POLYSTYRENE TARGET)

ESSEX - ROYAL HOLLOWAY

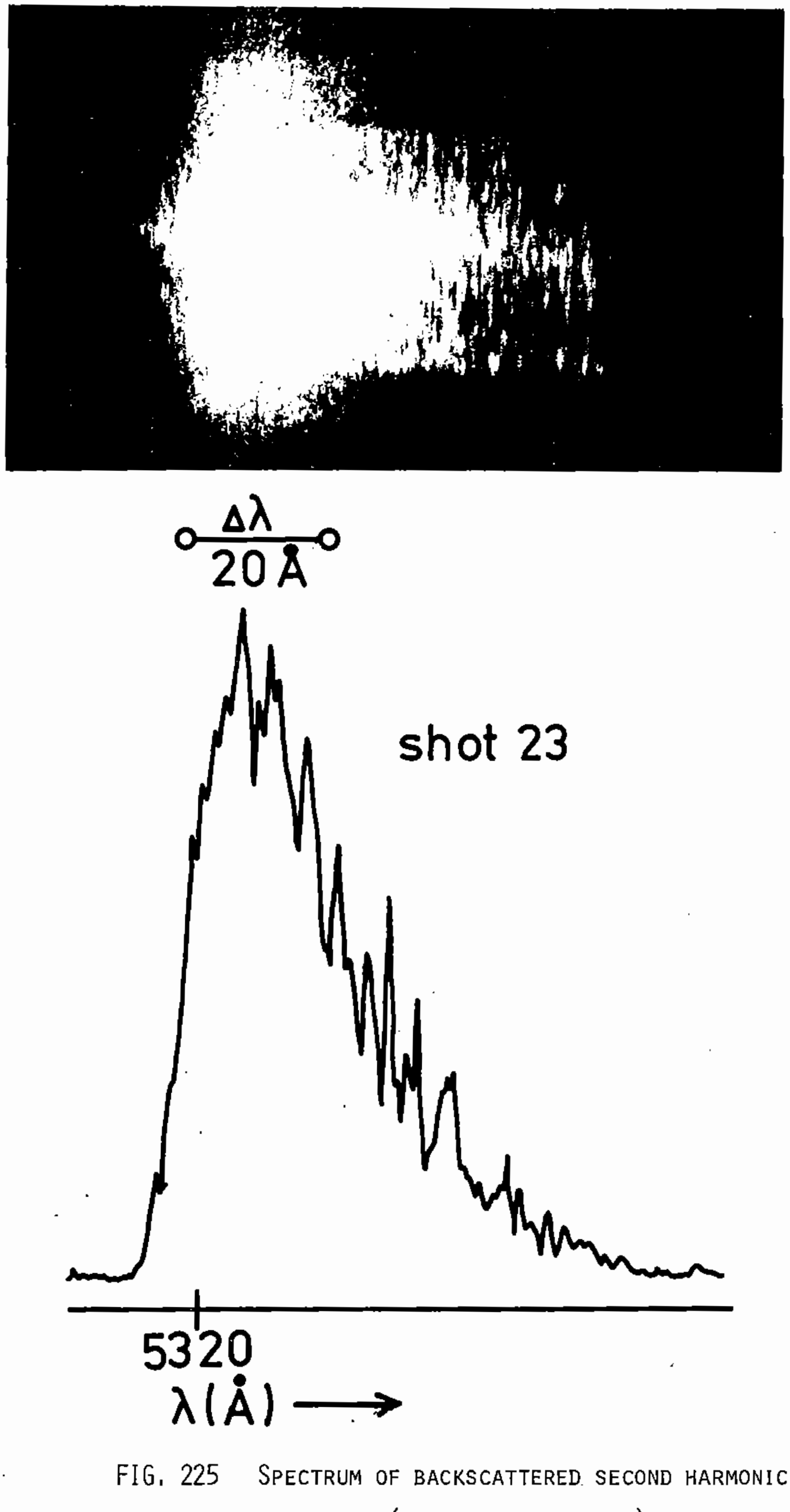

FIG. 225 SPECTRUM OF BACKSCATTERED SECOND HARMONIC RADIATION (POLYSTYRENE TARGET)

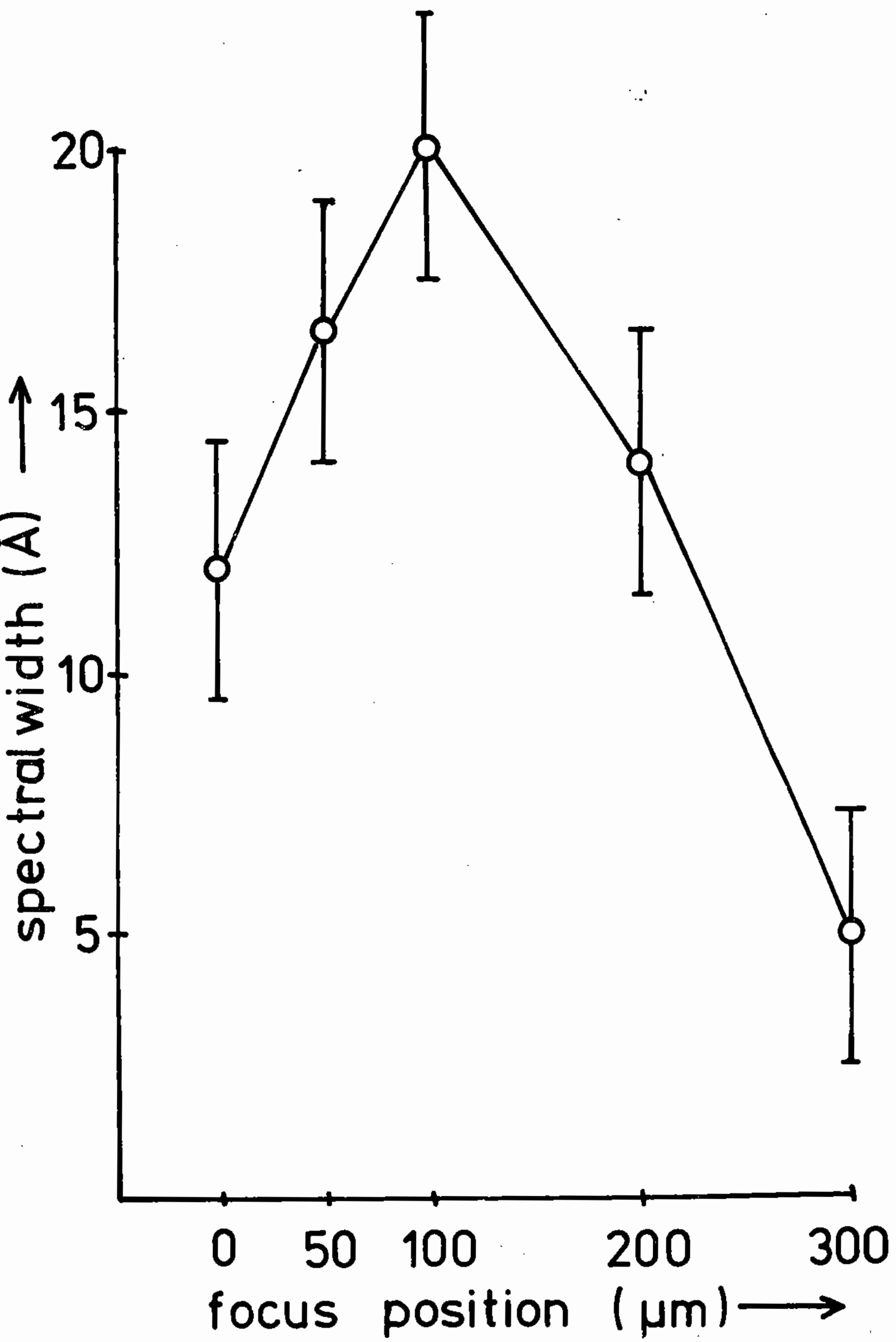

FIG. 226 VARIATION OF SECOND HARMONIC SPECTRAL WIDTH WITH FOCUS (POLYSTYRENE TARGET)

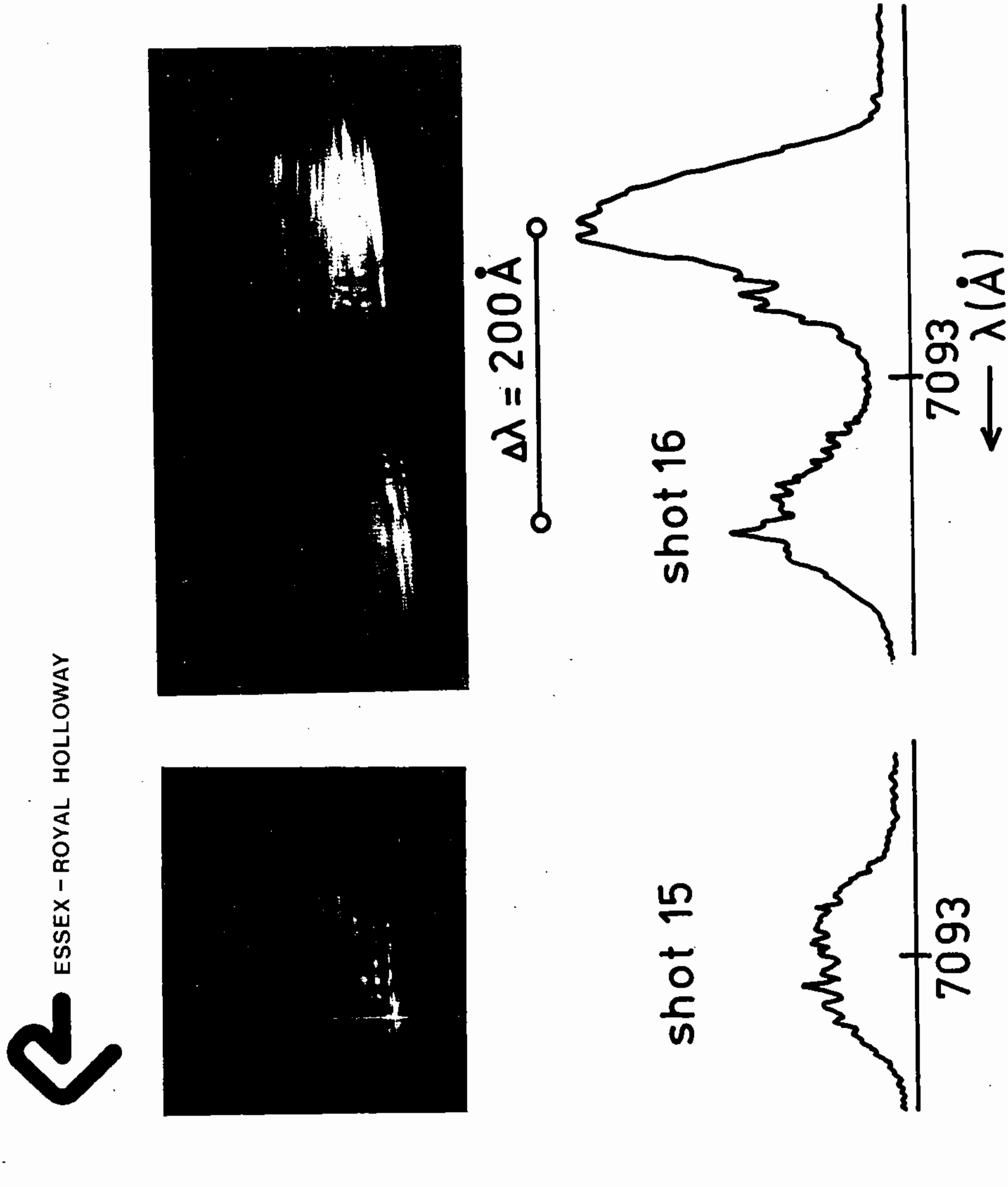

FIG. 227 SPECTRA OF BACKSCATTERED $^3/_2$ HARMONIC FROM TWO SIMILAR PULSES (POLYSTYRENE TARGET)

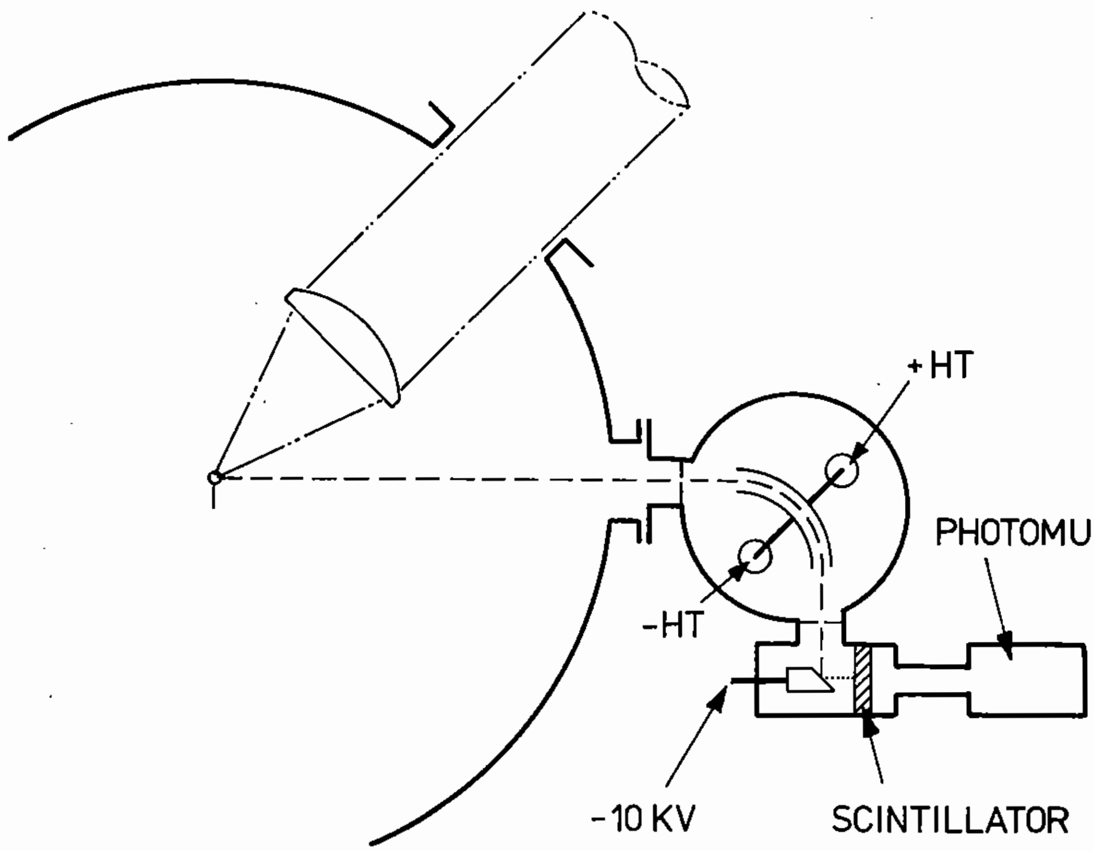

FIG. 228 ELECTROSTATIC ION ANALYSER

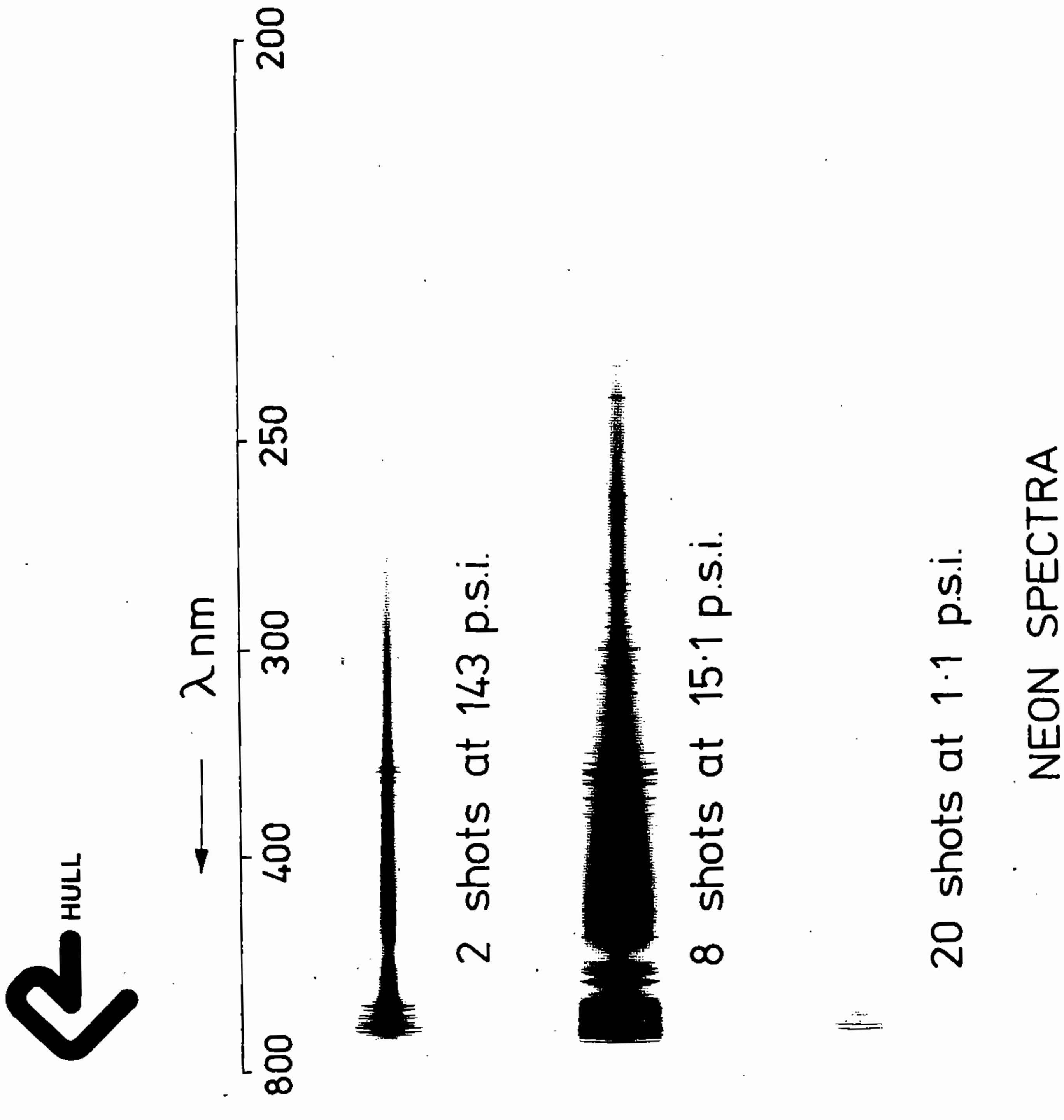

FIG. 229 SPECTRA RECORDED FROM NEON BREAKDOWN PLASMAS AT VARIOUS PRESSURES (QUARTZ SPECTROGRAPH)

Section 3 TWO BEAM COMPRESSION STUDIES

Section Editor: M H Key

3.0 FOREWORD AND SUMMARY

- 3.0.1 The Experimental Scientific Programme
- 3.0.2 Theory

3.1 VACUUM ULTRA VIOLET AND X-RAY SPECTROSCOPY

- 3.1.1 Experimental Conditions
- 3.1.2 X-ray images
- 3.1.3 X-ray continuum measurements
- 3.1.4 Space resolved plasma parameters and scaling behaviour for exploding pusher compression
- 3.1.5 Direct observation of implosion dynamics
- 3.1.6 Study of transport inhibition
- 3.1.7 Test for shell disintegration
- 3.1.8 Production and diagnosis of dense cool implosion plasma

3.2 OPTICAL SPECTROSCOPY

3.3 PARTICLE EMISSION STUDIES

- 3.3.1 Charge Collector Probes
- 3.3.2 Ion charge state Analysers
- 3.3.3 Neutron measurements
- 3.3.4 Alpha particle detection

3.4 OPTICAL AND MAGNETIC MEASUREMENTS

- 3.4.1 Ruby backlighting of microballoon implosions
- 3.4.2 Interferometric measurements

3.5 THEORY AND COMPUTATIONAL MODELLING

- 3.5.1 Development of MEDUSA at the Rutherford Laboratory
- 3.5.2 Applications of MEDUSA and incorporation of atomic physics codes
- 3.5.3 Sensitivity of MEDUSA to assumptions about the equation of state
- 3.5.4 The two dimensional simulation LASER B
- 3.5.5 Code development at Hull
- 3.5.6 Fusion product interaactions with dense plasmas
- 3.5.7 Equation of state for a partially degenerate plasma
- 3.5.8 Spectral line shapes, line formation and radiation transport

REFERENCES

TABLES

FIGURES

3.0 FOREWORD AND SUMMARY

This report describes the progress that has been made up to April 1978 in the programme for the study of laser compression of matter adopted by the Laser Facility Committee on 6 October 1976.

The work has been in three main areas, namely the experimental scientific programme, the supporting theoretical work and the development of the experimental facilities for plasma physics experiments and target production. The facilities are described elsewhere in section 1 while the first two areas are covered here.

There was a large measure of overlap of both the people involved and the apparatus used with the parallel programme of single beam experiments described in section 2. The experimental work has in fact been conducted on a time sharing basis using the same target chamber and diagnostic facilities. Table 1 shows an approximate time table illustrating this time sharing and summarising the time allocation and objectives of the main experiments.

3.0.1 The experimental scientific programme

The objectives of the first phase of the scientific programme have remained largely as initially proposed. Emphasis was placed at first on development of technical and diagnostic capability to conduct implosion experiments using the two beam laser with f/1 lens focusing of opposed laser beams on spherical targets, see figure 129. The preparatory efforts culminated in the first microballoon implosion on 28 April 1977 which was also the first in Western Europe and yielded data from a variety of diagnostic systems including the characteristic X-ray image of the type shown in figure 301.

The targets chosen for the first phase of scientific investigation were gas filled thin walled glass microballoons with typically 0.8 μm wall thickness and 80 μm diameter. The implosion of such targets, by 20 J of laser energy delivered in 100 picoseconds, which was available initially from the laser, created implosion core plasmas of moderate density ($\sim 10^{23}$ electrons cm^{-3} or 0.3 gcm^{-3}), rather high temperature ($\sim$ 0.7 keV) and therefore pressure $\sim 2 \times 10^{8}$ bar.

Such implosions have been termed 'exploding pusher implosions' because hot electrons created where the laser light is absorbed by the plasma have range similar to the glass shell thickness. This results in heating throughout the shell followed by its explosive expansion. The inward moving half of the shell material converges upon and finally stagnates against the already preheated fill gas. The associated conversion of kinetic energy of implosion to thermal energy determines the implosion plasma parameters.

Exploding pusher implosions give implosion core densities that do not increase with increasing laser power for a given target, while the temperature increases approximately linearly with laser power. They therefore allow the creation of rather high temperatures and study of inertially confined thermonuclear fusion. For this reason there has been extensive study of such targets internationally in laser fusion programmes. It is clear, however, that attainment of very high compressed densities, essential both in realising efficient burn in thermonuclear fusion targets and in creating laboratory plasmas at densities and pressures much higher than has been possible to date, requires ablative implosions with adiabatic compression. That implies targets in which the hot electron range is insufficient to penetrate the wall and preheat the material to be compressed while the time variation of ablation pressure outside the target is tailored to minimise non-adiabatic shock wave heating. Such implosions will need very uniform spherical irradiation, and targets with a high degree of sphericity and surface smoothness to avoid instabilities of the implosion. They also need longer duration laser pulses and pulse shaping. All these requirements present experimental problems and therefore this work began with the simpler 'exploding pusher' implosions. Moreover, exploding pusher implosions are convenient for the study of energy absorption and transport in spherical geometry. They allow development of quantitative understanding of, for example: inhibition of heat transport by cold electrons, the range and intensity of preheating by hot electrons, the effect of fast ions on momentum transfer to the implosion by the ablation process and important checks on the validity of computer hydrodynamic models.

A logical progression from the exploding pusher implosions towards ablative implosions is possible by increasing the target wall thickness and such transitional experiments are now being started. An inevitable consequence of increasing the target mass at constant laser power is a reduction of implosion core temperature and loss of convenient diagnostic information in the form of X-ray and fusion particle emission. Development of X-ray shadowgraphy diagnostic techniques for dense cool implosion cores has therefore been a recent objective. The immediate goal of these lines of development is to study ablative implosions of thick walled targets with long laser pulses in a six beam f/1 focusing geometry using the new target area and laser facilities described in section 1 and planned for operation by the end of 1978.

In the experimental programme to date the strategy in common with other workers has been to look for either new or better diagnostic data chosen to be sensitive to particular processes of interest. These data when compared with theoretical and particularly computational modelling (the latter is discussed in section 3.5 below) may then lead to quantitative conclusions about the chosen processes. The importance of a close relationship between experimental and computational work is evident in this situation. A more detailed account of the experimental work is given in the experimental group reports in sections 3.1 to 3.4 but the main features are summarised below.

The first implosion studies which began in April 1977 provided a base of information allowing corroboration of observations elsewhere and correlation with other work. Ion collectors showed three current peaks corresponding to fast ions due to the hot electrons, to ablation plasma ions, and to implosion plasma ions (figure 302). The data also gave a measure of the absorbed energy (Table 2) and the fast ion velocity spectrum (figure 304), the latter being relatable to the hot electron temperature. Scattered laser light monitored by an array of silicon diodes and calorimeters gave a second measure of the absorbed energy (Table 3), the polar distribution of scattered light, and evidence of the S:P absorption and scattering asymmetry associated with resonance absorption (figure 306). Hard X-ray continuum monitoring showed the hot and cold electron bremsstrahlung spectra and gave the hot electron temperature (figure 307). X-ray pinhole camera images showed the effect of varying the focusing on the target microsphere and gave a routine check of the accuracy of alignment and quality of implosion (figure 301). The physics experiments were of two main types: those to study coronal phenomena such as absorption scattering and those to study the implosion.

In the corona physics experiments, effort was directed initially to investigation of harmonic emission from the corona at $2\omega_o$ and $(3/2)\omega_o$. Harmonic spectra, figures 308 and 309 were recorded with spatial resolution and images of the target in the two harmonic emissions showed the spatial structure of the harmonic emission regions (figure 310). Streak photography of the $2\omega_o$ emission regions measured the outward movement of the critical density surface during target irradiation. Preliminary results with $2\omega_o$ shadowgraphy and magnetic probes were also obtained. The harmonic spectra have been considered in relation to still tentative theoretical models proposed in the literature and the data give some evidence of the inadequacy of these current models. The harmonic images have shown one new and unexpected feature in that $(3/2)\omega_o$ emission is observed to emanate from localised points of size less than the few microns resolution of the recording optics. This poses intriguing questions as to the mechanism generating the $(3/2)\omega_o$ harmonic.

By June 1977 significant new results were being obtained by space resolved X-ray spectroscopy with an instrument designed to give 7 micron spatial resolution and typically 2000:1 spectral resolution by X-ray crystal diffraction. This device yielded the first reported single shot spectra of both high intensity, sufficient to record continua as well as lines, and high resolution, sufficient to measure line widths (figure 311). The targets were filled with neon gas so that the compressed gas emission spectrum could be distinguished from that due to the imploded glass.

Data analysis yielded the first simultaneous measurements of the electron temperature and density in the three main emission zones of the implosion plasma, namely the outer glass shell plasma, the imploded glass tamper plasma and the compressed gas plasma. The data are significant in that sensitive comparisons with hydrodynamic computer codes are made possible as discussed below. The spectroscopic studies were subsequently extended to include targets filled with neon doped D_2, Argon and D_2+T_2 (figures 312 and 313). The latter were used to determine ion temperature from the yield of neutrons and α particles (figure 314). A rather detailed comparison of experimental data and computer calculations was then possible (eg Table 10). Information on the respective roles of hot and cold electrons in heat transport and on scaling of compression ratio with gas fill density was obtained.

Development of X-ray streak camera techniques had been in progress for some time in UK Universities and led to a 10 picosecond resolution commercial camera system, figure 315, being set up to study implosions. Whole image streaking and the high sensitivity of the camera system gave a clear record of the behaviour of the ablation plasma at the irradiated poles of the target relative to the implosion core, as shown in figure 316. The comparison of implosions of unfilled and gas filled targets showed that the former developed an X-ray emitting core much earlier in time. This may be interpreted as an implosion of fast ions travelling at velocities > 10^8 cm^{-1} due to hot electrons from the corona plasma penetrating the thin walled target and accelerating ions from its inner surface.

Transport inhibition in the axial direction with spherical targets was studied by X-ray spectroscopic measurement of burn-through by the thermal front on microballoon targets coated with thin layers of aluminium. With 100 picosecond pulse irradiation at 3 x 10^{15} watts cm^{-2} about 1000 Å of aluminium was sufficient to suppress Si XIII emission relative to that of Al XII indicating severely inhibited heat transport (figure 317). In a corollary of the same experiment with Al layered targets evidence of shell break up was obtained from the appearance of Al XII emission in the implosion core (figure 318).

More recent optical studies of corona physics included the use of a Raman shifted second harmonic pulsed probe beam for Faraday rotation, shadowgraphy and interferometry. Faraday rotation data on megagauss thermoelectric magnetic field generation on plane targets is discussed in section 2.1. Application of the same methods to microballoon targets showed reduced magnetic fields of < 0.1 Mgauss. Interferometry with an f/1.4 objective lens allowed density profile determination for densities greater than critical and showed preliminary evidence of profile steepening. The composition of the fast ion flux from the corona, about which there has been controversy, was studied with an E/Z electrostatic analyser and protons were found to be a major constituent due presumably to adsorbed hydrocarbon impurities on the target surface.

The need for a capability in diagnosing compressions which do not create high temperatures and which cannot therefore be studied from the emission of X-rays or fusion products was referred to above. A first step in this direction was made when pulsed X-ray shadowgraphy was used to show the stages of development of a cool dense implosion created by 5J, 100 picosecond irradiation of 87 bar neon-filled glass microballoons. The pulsed

X-ray source was an auxilliary plasma formed on a solid brass target close to the implosion event as shown in figure 319 . Intense 1.5 keV X-ray emission due mainly to resonance radiation from neon-like ions of Cu and Zn occurred during the 100 picosecond irradiation of the brass target. An X-ray pinhole camera recorded an image of the implosion viewed against the background emission from the auxilliary plasma. The background plasma was formed after a variable delay so that the dense zone of the implosion was seen as a region of absorption as illustrated in figure 320. Preliminary analysis of the data has indicated a twenty to thirty times volumetric compression of the 87 bar neon and a core density of about 2 gcm^{-3}. This was the first reported use of X-ray shadowgraphy to study implosions and the high density plasma observed is possibly the highest directly measured density in laser driven implosion studies.

The progress of the experimental programme was reviewed at the Gordon Conference on laser interaction with matter in August 1977, at the 11th European Conference on laser interaction with matter at Oxford in September 1977 and at the Topical Meeting on Inertial Confinement Fusion at San Diego, USA, in February 1978 (301,302) and a number of individual publications and conference papers have been generated.

3.0.2 Theory

This is described in detail in the report of the theory group, section 3.5. The main feature of the theoretical work related to implosion studies has been the development of hydrodynamic codes and their application in planning experiments and interpreting results. There has also been work on line broadening calculations for X-ray lines emitted by high Z ions and more basic work on the equation of state of high density matter and thermonuclear reactions in high density plasma.

The one dimensional Lagrangian MEDUSA code has been the most used of the hydrodynamic codes. It was taken in its published form and developed in various ways. At Oxford University the sensitivity of compression calculations to equations of state was investigated and at the University of Glasgow it was adapted to include the atomic physics of high Z materials. In work at Rutherford Laboratory it was used to examine the effects of pulse shaping on compression, to describe X-ray continuum emission and absorption and to examine the effects of hot electron pre-heating and cold electron transport inhibition.

Recently a 1D Lagrangian code developed at the University of Hull, incorporating atomic physics and radiation transfer for resonance lines emission, has been added to those available and should provide a much better basis for interpretation of spectral line emission. A 2D Lagrangian code from the University of Hull is also being developed for longer term use.

There have been several instances where computational work has interacted strongly with the experimental programme. The experimental measurement of compressed core density and temperature when compared with MEDUSA modelling lead to the conclusion that hot electron energy transport dominated the implosion dynamics. With no hot electrons simulation of the experiments showed an ablatively driven implosion with the heat wave not penetrating the imploding wall and with core densities that were an order of magnitude above experimental results. Introduction of a variable fraction of hot electrons of temperature determined from the experimental hot electron X-ray bremsstrahlung spectrum caused a change to 'exploding pusher' behaviour, and a reduction of implosion core densities. Variation of a cold electron transport flux limiter on the other hand was found to make very little change to the predicted results.

X-ray streak camera observations of implosion time have been related to MEDUSA calculations indicating that the local energy per unit area on the irradiated poles of the shell rather than the average energy per unit surface area of the target determines the implosion time. The magnitude of cold electron transport inhibition necessary to explain the 'burn through' of Al layers on glass microballoon targets has been assessed by comparison with calculations using MEDUSA. Planning and interpretation of experiments involving X-ray shadowgraphy of dense cool implosions was also conducted in this way. Most recently the planning of future experiments on ablatively driven implosions is being approached through computer simulations.

There is a need for improved modelling of hot electron transport, radiation transfer, and atomic physics in the 1D codes and for 2D modelling capability in connection with ablatively driven implosions. These are current areas of development.

3.1 VACUUM ULTRA VIOLET AND X-RAY SPECTROSCOPY

The work of the group has included both diagnostic system developments and experimental studies. The experimental studies of microballoon implosions have involved hard X-ray continuum spectral measurements, X-ray pinhole photography, space resolved X-ray spectroscopy, X-ray streak photography and spectroscopy, and X-ray shadowgraphy.

3.1.1 Experimental Conditions

The experiments have been conducted with the apparatus shown schematically in figure 321. Two 11 cm diameter laser beams were focused by f/1 aspheric lenses on to opposite sides of glass microballoon targets of typically 70 μm diameter and 1.0 μm wall thickness. The targets were gas filled with D_2, D_2+T_2, Ne+D_2 mixtures or Argon. They had a 30 nm aluminium coating to facilitate alignment by imaging via the focusing lenses of CW YAG laser light retroreflected from the target. The laser power was typically 100 gigawatts in each beam incident on the target and the pulse duration 100 picoseconds. Measurement of the laser beam divergence and the focal spot size produced by the f/1 lenses indicated that the spot size was mainly determined by lens aberrations. Half the energy was inside a 30 μm diameter circle. The total B integral for the laser was 3 and small scale beam break up was attenuated by spatial filtering at the mid point of the chain, so that non-linear effects in the focus were small.

The flux density on target was greatest ($\sim 10^{16}$ watt/cm^{-2}) with polar focusing (focal plane at the target surface). A displacement of the focal plane by two diameters of the target to a point beyond the target gave the most uniform illumination but reduced the flux density to $\sim 10^{15}$ watts/cm^{-2}.

3.1.2 X-ray images

X-ray pinhole photography of implosions is undertaken with a two channel camera giving images through filters of typically 1.4 and 2.5 keV cut off energy via 3 μm and 12 μm pinholes respectively. Examples of such images are shown in figure 301 where the focusing on the microballoon is varied. X-ray images of improved resolution are obtainable with Kirkpatrick Baez grazing incidence X-ray microscopes and a 10x magnification system using 5 m radius of curvature mirros has recently come into operation (figure). Design studies for a higher magnification, higher resolution and higher intensity Wolter type axisymmetric microscope are underway.

X-ray image recording using phosphers optically coupled to high gain image intensifiers has also recently been successfully developed.

3.1.3 X-ray continuum measurements

X-ray continuum measurements using two filtered diode array sets are now routine. Two diode arrays are permanently installed in the target chamber so that electron temperatures can be measured for each laser shot. The two diode arrays are designed to minimise the effects of fast electrons on the filter foils and also hard X-ray fluorescence, since it was shown that these effects could contribute significantly to the measured signals. Each array consists of four X-ray diodes mounted behind absorber foils. Two of the foils have fairly low cut-off energies (3.5 keV and 5.2 keV) so that a measure of the thermal electron temperature can be made, and two have high cut-off energies (12.4 keV and 33 keV) to obtain an estimate of the hot electron temperature T_{HOT}. Reliable measurements of the thermal electron temperature can be made since the accuracy available is good ($\gtrsim$ 10%). However, the hot electron temperature cannot be measured as accurately due to the poorer signal levels. Typical temperatures obtained for 10 J incident laser energy in two beams with a microballoon targets are 800 eV ± 100 eV for the thermal electron temperature and a hot electron temperature of 5 keV to 8 keV. Even though greater accuracies can be obtained using an analogue to digital converter for a direct measure of the charge, the signal levels for hard X-rays (E > 30 keV) is still low. To overcome this problem an X-ray scintillator array has been designed and constructed to operate at X-ray energies up to 100 keV and this will provide greater sensitivies for hard X-rays and more reliable measurements of the hot electron temperature.

3.1.4 Space-resolved plasma parameters and scaling behaviour for exploding pusher compression

(a) General

Measurements have been made of space resolved X-ray spectra and of neutron α particle yield from implosions of gas filled microballoons. These have yielded values for the electron number density and temperature of the compressed gas, the imploded glass and the outer glass shell plasmas as well as values for the ion temperature in the implosion core.

The instrument (Figures 322 and 323) used for the space resolved X-ray spectroscopy is of interest since it has given the first reported single shot measurements of absolute X-ray line intensities, continuum spectra and line widths in the three plasma zones referred to above. The design is based on obtaining the maximum intensity in the spectrum consistent with adequate spatial spectral resolution. The spatial resolution was set by the width of the slit which was 5 or 10 microns and thus the spatial resolution varied over the spectral range from 6 to 7.4 microns (for the 5 micron slit). The spectral range was determined by the range of angles of incidence on the crystal and was 8.2Å to 2.7Å for a PET crystal and 24Å to 8Å for a TlAP crystal. The spectral resolution depended on source size and varied from 1000 to 4500 over the spectral range for a 15 μ (implosion core) source. The slit to plasma distance was 6 mm giving 3 x to 7 x magnification on the space resolution axis and a high brightness spectrum. The instrument had fixed slits formed in 25 micron copper substrates by a photo etching process. The spectrometer slit was covered by a metal foil filter (1.5 micron Al or 25 micron Be for the TlAP and PET crystals respectively). The instrument was absolutely calibrated in the sense that the integrated reflection coefficients for the crystals were measured as a function of wavelength with better than 1% accuracy using facilities developed in the UK for X-ray astronomy (302). The absolute response of Kodirex film as a function of wavelength and angle of incidence for standard development procedures was also known (303). Thus recorded film densities were transformed to absolute space resolved but time integrated emission from the plasma with an accuracy limited by the Kodirex film response date.

Results obtained were of the form illustrated schematically in figure 324. The spectrometer was oriented with its slit in the plane perpendicular to the laser beam axis so that the spatial resolution axis was along the laser beam axis at the target. The spectrum then showed three spatial zones of emission, namely the two irradiated poles of the spherical target and the implosion core.

In the initial work 8.5 bar Neon filled targets were studied in detail (301). The investigation has since continued with further objectives including:

(i) variation of the gas fill density to examine compression ratio scaling

(ii) Use of 5% Neon doping in D_2 gas filled targets having the same gas fill density as $D_2 + T_2$ filled targets. This allowed density determination for the $D_2 + T_2$ implosions.

(iii) Use of Argon-filled targets to assess the feasibility of recording Ar XVII emission. The shorter wavelength of Argon XVII emission, relative to Ne IX, is more suitable for indicating plasma parameters in denser implosions.

Examples of short sections of the spectra are shown in figures 311, 312 and 313 for targets with gas fills of 8.5 bar Neon, 11 bar D_2 + 5% Neon and 0.3 bar Argon respectively.

The complete spectra for several gas fills and with either PET or TℓAP crystal dispersion have been analysed by densitometry. Absolute intensity and spectral line shapes were obtained from densitometry on the spectral axis, along either the implosion core or the glass shell plasma emission regions. Spatial dimensions of the emission zones at wavelengths of interest were obtained from densitometry on the space resolution axis.

The spectral analysis will not be discussed in detail here as it has been described elsewhere (301,304). The methods used to determine electron number density and temperature are summarised in Tables 4 and 5.

The calculation of Stark broadened line widths used in determining density from the Ne IX $1^1S_o - 3^1P_1$ and Si XIII $1^1S_o - 3^1P_1$ lines involved some new work which is briefly described here. Electron impact and ion microfield broadening was treated. The microfield included screening treated by methods developed from the work of Hooper (305). The computer code involved was developed by Richards (306). Data on the relevant energy levels in Si XIII and Ne IX were supplied by Bromage from an atomic structure computer model (307).

There was an advantage in basing density determination on Helium-like ion line widths since these scale approximately linearly with density compared to the $(\text{density})^{2/3}$ scaling of Lyman series line widths. In either case, however, the Stark profiles had to be modified to allow for optical opacity. As a first approximation this was done here by assuming a homogeneous plasma with ground state ion densities determined from the ionization ratios indicated in Table 5 and with line-of-sight depth measured from the space resolved spectra.

Examples of fitting a theoretical profile to experimental results are shwon in figures 325 and 326. The figures show the original Stark profile as well as the self-absorbed profiles.

Application of the various spectroscopic diagnostic methods allowed alternative estimates of the same parameters as shown in Tables 6,7,8, for the three spatial zones in 8.5 bar Neon filled targets.* Generally

---

* Some values in Tables 6 to 8 have been changed from those in reference 302 where preliminary data analysis had not included all appropriate factors (eg opacity corrections to line shapes).

one method was preferred for accuracy and the others gave a check. Temperatures were best obtained from continuum slopes and densities from line widths. (Temperatures from ionization ratios were unreliable because of uncertainty about ionization and recombination rates.)

The more recent experiments have been analysed in a similar fashion to that described above. All the data in the form of best values for parameters can then be considered in relation to theoretical models.

(b) The role of 'hot' electrons - Table 9

The implosion was modelled assuming the total energy incident to be uniformly distributed over the sphere. Calculations with F = 0, (no hot electrons), predicted high densities in the compressed gas, $\sim$ 12 gcm^{-3}, which was 52 times more than the experimental value of 0.23 gcm^{-3}. The implosion was ablative in character with a cold dense shell of increasingly compressed wall material being driven inwards by the ablation pressure as shown in figure 327.

If the laser energy was assumed instead to create hot electrons at the critical density, (F = 1), the long range electrons in the $kT_e \sim 10$ keV Maxwellian, thus generated, heated the glass shell ahead of the ablation front. This caused 'exploding pusher' behaviour (308) with initially a decrease in glass shell density but an increase in thickness as shown in figure 327. Convergence at the centre finally created a sharp increase in density in the strongly preheated core material. The final density was much reduced relative to the case F = 0 because preheating caused a high temperature for the final phase of compression. The predicted density was 1.3 gcm^{-3}. This was still over 5x greater than the experimental value but strongly suggestedthat the energy absorbed at the critical density went initially into hot electrons. Elaborate multi-group diffusion treatment of the hot electron transport is able to predict values of density very close to the above experimental values 308.

Experimental evidence for the existence of hot electrons is found in the spectral slope of X-ray Bremsstrahlung emission at energies above 10 keV. Data recorded with X-ray diodes with filter cut off energies of 12 keV and 33 keV implied a hot electron temperature of 6.3±0.7 keV in the present experiments. The ratio of this temperature to the background temperature in the glass shell plasma (table 8) was about 8. The existence of this hot electron temperature is well documented. The present observations suggest that the absorbed laser energy must, in the first instance, go almost entirely into creating hot electrons.

(c) Scaling of compression ratio - Table 10

The data obtained make it possible to examine over a limited parameter range the scaling of compression ratio with gas density. Table 7 shows the experimental core densities and compression ratios. The values of radius, wall thickness, initial gas density and laser energy are also shown for the particular target shots.

A semi-empirical scaling law due to Storm et al (308) suggests that the compression ratio C depends on wall thickness Δr, target radius r and initial gas fill density ρ_0 gcm^{-3} as follows:

$$C = \frac{8.6}{\rho_0} \left(\frac{\Delta r}{r}\right) \qquad (1)$$

Examination of Table 10 shows that the semi-empirical scaling was rather consistent with the experimental data. It is interesting to note in addition that the predictions of the sophisticated LASNEX code were quoted (308) as agreeing with equation (1) if the constant was increased by a factor 1.5 . The MEDUSA prediction, as noted in the previous section, consistently overestimated the compression ratio as shown in Table 10. MEDUSA data did, however, agree with experiment in predicting an increase in compression ratio to give essentially constant compressed density as the Neon gas fill was changed from 8.5 to 2.5 bar.

It may be concluded that over the limited range of this investigation the scaling law equation (1) gives a good description of the compression ratio for the gas fill.

(d) Implosion core temperature - Table 11

It was found that both the compressed gas and the X-ray emitting imploded glass had the same electron temperature within the accuracy limits of measurement. The table shows electron temperatures in 8.5 bar Neon, 11 bar D_2 + 5% Neon and 10 bar $D_2 + T_2$. (In the latter case only the glass temperature could be measured.) The gas fill density variation was a factor of 3.5 while the electron temperature was essentially unchanged, indicating little or no dependence of electron temperature on gas fill density.

Calculations with MEDUSA gave temperatures within a factor of 2 of the experimental values as shown in Table 11. This correspondence was much closer than was found for density as discussed in the previous section. It is worth noting that the observed temperatures were also very close to the values obtained from the ratio (Absorbed laser energy)/(number of electrons and ions in the target).

Ion temperature was measured only for the $D_2 + T_2$ filled target. The yield of neutrons was measured with an absolutely calibrated scintillator detector and the yield figure was checked against the α particle yield determined by counting α tracks in cellulose nitrate. The implosion compression ratio was assumed to be the same as that measured directly for a similar target with the same fill density of D_2 + 5% Neon.

The ion temperature T_i was then determined from a self-similar model of the compression leading to the expression (309),

$$N_{DT} = 4\ p^2\ r^4\ C^{2/3}\ F_{DT}(T_i C) \qquad (2)$$

where $F_{DT}(T_i C)$ is a temperature-dependent function calculated in reference (309), C is the compression ratio, r the shell radius in microns and p the fill pressure in bars. N_{DT} is the neutron yield.

The ion temperature was found to be 1.5 times higher than the electron temperature and this was in agreement within the measurement errors with the MEDUSA simulation result in Table 11.

(e) The imploded glass - Table 12

The experimental data showed the gas and glass temperatures to be equal within the measuring errors, Tables 6 and 7. The densities were also very similar, with the glass being 1.4 x denser than the gas. This difference was not much larger than the measurement error. There was a clear discrepancy with MEDUSA in that the calculations typically overestimated the compressed density by a factor of about 5 but showed the right kind of variation with target parameters. However the predictions indicated 4x greater density and 4x less electron temperature for glass relative to the gas. This relative difference was not seen experimentally and the question arises as to why this was so.

There must have been a much more efficient thermal contact between gas and glass than that included in the modelling. MEDUSA computed Spitzer conductivity and preheating by hot electrons as described above. This was insufficient to explain the observations.

Other possibilities for a more efficient thermal exchange are an alternative hot electron preheat treatment or turbulent mixing at the interface due to fluid instability. Further investigation of this discrepancy is planned.

(f) The glass shell plasma - Table 8

The parameters of the glass shell plasma in Table 8 were space and time averaged over the strong density and temperature gradients of the ablation front and characterized the zone of maximum X-ray emission. A back-up diagnostic was the X-ray continuum slope between 3.5 and 5.2 keV from filtered X-ray diodes which gave Te $\sim$ 800 ± 100 eV.

MEDUSA modelling showed the parameters of the emission to be sensitive to assumptions about transport inhibition.

With no hot electrons (F=0) and inhibition of conductivity by a factor f, reduction of the Spitzer conductivity and the free streaming limit, the 'burn through' depth was consistent with the burn through experiment with f = 10 and most emission came from a very sharp temperature front where $T_e \sim 600$ eV and $N_e \sim 2 \times 10^{22}$. More severe inhibition gave higher temperature and density at the emission zone and less burn through.

Inclusion of hot electrons, F=1, gave the observed burn through if $f \sim 300$ x as shown in figure 317 but the heat front was much less sharp due to energy deposition by the fast electrons and most emission occurred from a region of 2×10^{22} density but only 200 eV temperature.

On physical grounds it seems reasonable that the few slow electrons of the 'hot' electron distribution should not be allowed to affect the transport of energy by slow electrons in the 'cold' distribution, so that turning off 'hot' electron transport in examining the ablation plasma is probably a reasonable approximation. This leads to the conclusion that the observed parameters of the ablation zone plasma are consistent with the predicted parameters from modelling with 10x inhibition of heat conduction and no treatment of hot electrons.

(g) Argon XVII emission

Figure 313 shows the emission of Ar XVII $1^1S_o - 2^1P_1$ and its associated intercombination and dielectronic satellite lines. The emission is spatially resolved and came from a compression core size which, after correction for the spatial resolution of the instrument, was about 10μm. This is consistent with ∿ 350x compression of the 0.33 bar Argon to 0.2 g cm^{-3} as predicted by the compression factor scaling law discussed above. The line broadening in this emission has not yet been analysed but is clearly spectrally resolved.

No other Argon emission lines were observed in this experiment but with more energy on target and higher implosion core temperature this would be possible. (The target was a 69 micron diameter, 0.83 micron wall microballoon and the laser energy on target was 19 J.)

The > 3 keV X-ray energy of the line radiation allows it to penetrate dense material with less absorption than Neon emission with advantages for dense core diagnostics.

3.1.5 Direct observation of implosion dynamics by X-ray streak photography

A UK-developed X-ray streak camera system, figures 315 and 328, recorded the time and space development of the structure of the implosion as seen in broad band X-ray emission.

The experimental system is shown in figure 328. The streak camera was used with normal incidence on a transmission photocathode. It had a 9 micron Beryllium photocathode substrate on which a 150 Å layer of gold was deposited to form the photoemitting surface. The streak tube was evacuated by the pumping system of the experimental chamber to less than 7×10^{-5} Torr. An 8μm pinhole, 1.5 cm from the target, produced an 11x magnified image of the target on the rear surface of the photocathode. The system was used with either no filter on the pinhole, giving a 1 keV cut off energy due to the photocathode substrate or with a 2.5×10^{-3} cm Beryllium filter giving 1.4 keV cut off energy. The streak axis was chosen to be perpendicular to the axis of the two opposed laser beams focused on the microballoon and the axis of observation was also perpendicular to the laser beam axes.

Figure 329 illustrates the static X-ray image seen by the pinhole camera and also by the streak camera. The focusing has been chosen to be 'polar' so that the emission of X-rays at the irradiated poles is concentrated within a focal spot of ∿ 40 micron diameter. This form of illumination was chosen to allow whole image streaking without a slit which gives greater sensitivity to the emission from the poles relative to that from the implosion core.

The result of streaking the whole image at 1.4×10^{9} cm sec^{-1} is shown in the lower image in figure 329 . The time resolution in the streak is $\Delta t = \Delta x/v$ and was therefore poorer for the wider polar emission than for the implosion core. From the static image it was concluded that $\Delta t =$ 23 psec in the core and 60 psec in the polar plasma. The streak photograph and densitometry in figure 330 show very clearly that, after correction for the instrumental resolution, the polar plasma emits for 130 psec at > half intensity, which was essentially the duration of the laser pulse. There was a delay to peak emission from the implosion core of 110 psec and the implosion core emitted for 120 psec at > half peak intensity. This streak picture was taken with 1 keV filtering and it is seen that the polar plasma remains static in space.

Changing to 1.4 keV filtering, figure 331 , shows two new features. The polar plasma moved outward during the laser pulse and the implosion core emission duration was shorter (83 ps). Similar outward movement was also seen in second harmonic emission zone streak photographs discussed in section 3.2.

Comparing a gas filled target implosion with an 'empty' target containing ~ 2 Torr residual $CO_2 + SO_2$ (figure 316) showed strikingly that emission from the implosion core began much earlier in the case of the empty target. The shaded zone on the densitometer tracings in figure 330 emphasises this. In fact the emission occured so promptly that the velocity of implosion causing it was beyond the limit of measurement; ie $> 10^8$ cm sec^{-1}. Also there was a steady build up in the intensity of emission from the core up to the time of the 'normal' implosion peak. The interpretation of this observation is considered below.

Implosion records were obtained over a range of values of laser energy/ shell mass. The range covered was not as large as the instrumentation could handle but nevertheless it is interesting to examine the variation of the delay between the laser peak intensity (assumed to occur at the peak of X-ray emission from the poles) and the peak emission from the implosion core. This is called 'implosion time' and plotted in figure 332 as a function of 'specific energy' which is the local energy per unit area divided by the shell mass per unit area at the poles.

The reason for choosing the local specific energy rather than the energy/ shell mass arose from comparisons with the MEDUSA calculations. MEDUSA is a 1D code and cannot therefore explicitly treat non uniform illumination of the target. When comparisons with MEDUSA were made assuming the total energy from the laser to be uniformly deposited in the shell the result was a poor fit to the experiments with predicted implosion times being too long despite inclusion of hot electron transport by methods discussed above.

On the other hand, ignoring the total energy and calculating an implosion with the same energy per unit area as that incident in the polar focal spots produced a reasonable match with the experiment as shown in figure 332. It may be inferred from this that the implosion time is influenced by the local energy per unit area. This is consistent with the observation noted in section 1 that with polar illumination the imploding plasma was not spherically symmetric, with the compression on the polar axis being more rapid that on the transverse axis. The hot electron energy transport does not therefore eliminate sensitivity to local variations of intensity in 'exploding pusher' implosions.

Computation with MEDUSA of the time variation of X-ray recombination radiation from the core and corona plasma, fig 333 produced a qualitative match with the experimental data in figure 330. There was, however, a rather shorter duration of emission predicted for the core and a greater intensity of core relative to corona. This is connected, probably, with MEDUSA's over estimate of the compression ratio noted in detailed studies in section 3.5.

It is perhaps worth comment that the data on 'implosion time' in figure 332 cannot be directly interpreted to give an 'implosion velocity' since the relatively low temperature high density exploding shell material is not observed in these measurements but rather the separate ablation plasma and compression core plasma. The time during the laser pulse when the shell begins to explode is presumably variable becoming earlier with higher power.

The observation of prompt emission from the implosion core in the case of empty microballoons was interesting and novel. The mechanism was thought to be a sufficient fast ion emission from the rear surface of the microballoon to create central pressures comparable with those in the 'normal' implosion with a gas fill. This hypothesis admits of some simple tests.

The 'normal' gas filled target implosion shown in fig 316 created, as shown in section 3.1.4, peak electron number density $\sim 5 \times 10^{22}$ cm^{-3}. If densities of this order were produced in the hypothetical fast ion implosion the density of ions in the implosion core would be $\frac{f}{z} \times 5 \times 10^{22}$, where z is the average charge on the ions and f is the fraction of the 'normal' density. The ions must have imploded at velocity $\sim 10^{8}$ cm s^{-1} so assuming mass/charge ratio ~ 2 and an implosion core of 15 μ diameter, the energy carried by the ions was ~ 0.15 f J. The energy absorbed from the laser was ~ 1.5 J. Thus the fast ions would have carried 0.1 f of the laser energy.

It is a familiar result that outward moving fast ions ($v > 10^8$ cm s^{-1}) carry over 50% of the absorbed energy. It therefore appears energetically possible to explain the fast ion implosion if fast ions from the inside surface carry over 5% of the absorbed energy (ie 1/10 of the outward fast ion energy). There is evidence for rear surface fast ion fluxes of this order in plane target experiments (310).

An interesting implication of this observation is that neutrons produced in 'empty' shell implosions with frozen $D_2 + T_2$ on the inner wall may be due to this 'fast ion' implosion process producing high energy collisions at low density rather than to reactions at higher density and lower temperature (311).

3.1.6 Study of transport inhibition from 'burn through' of aluminium layers on spherical targets

There is considerable evidence for inhibition of heat conduction in the ablation front of laser produced plasmas (312,313,314,315). The experiments have generally been with plane targets and it was therefore interesting to examine the situation with microballoon spherical targets.

The experimental technique used was space resolved X-ray spectroscopy with the apparatus shown in figure 322.

The targets were glass microballoons with a variable thickness of Al in the range of 0.05 to 0.3 microns. The total wall thickness (glass + aluminium) was constant at 1 micron. Figure 334 shows schematically a target and its outer wall X-ray spectrum in the region of Si XIII, Si XIV, Al XII and Al XIII resonance line emission.

The objective was to compare the intensity of Aluminium lines with those from the Silicon in the underlying glass as a measure of the penetration of the heat front through the aluminium layer. In order to make simple comparisons with calculations the transitions Si XIII $1\,^1S_0 - 3\,^1P_1$ and Al XII $1\,^1S_0 - 4\,^1P_1$ were studied. These originate on high quantum number levels that are populated in LTE relative to the continuum. The total emission is also not severely modified by opacity effects and the two lines in question are well separated from all others. Comparison with LTE optically thin calculated emission is therefore reasonable. Figure 317 shows the experimentally recorded ratio of the lines as a function of the Al thickness. The cut off in Si intensity occurs for a layer thickness of 0.1 microns. Very weak Si emission was observed at thicknesses 0.2 and 0.3 microns. This is not fully understood and was not rechecked. In particular during the experiment there was a failure of the prepulse monitoring system so the presence of prepulses cannot be ruled out. Alternatively such effects might be produced by instabilities of the ablation surface or localised hot spots in the heating.

It has been common practice to invoke an arbitrary 'flux limit' in describing inhibited thermal transport. The classical flux limit for free streaming heat flow (316) is assumed to be reduced by a factor f and this is used as a variable parameter to fit the observables of an experiment. Alternatively the Spitzer coefficient of conductivity has been arbitrarily scaled down in addition to the same scaling-down of the free streaming flux limit. The justification for such procedures is that simple one-parameter fits to data are obtainable.

In terms of microscopic physical processes it is known that absorption of laser energy generates mainly 'hot' electrons with $kT_H \sim 8\ kT_c$ where T_c is the background plasma temperature in the ablation plasma. The 'hot' electrons themselves transport energy, as do the cold electrons. The main processes that may inhibit the transport are magnet fields (317,318) and ion turbulence (319,320). It is not established however that the way in which the various components of the velocity distribution, termed for convenience 'hot' plus 'cold' electrons, interact with the inhibition processes may reasonably be described by a one parameter inhibition.

Calculations were made with the MEDUSA code with the arbitrary model for transport of energy described earlier in which hot electrons were included (F=1) and the cold electron heat transport had a reduced free streaming limit. The reduction was a variable factor 'f'. With this model the calculations in figure 317 showed values of f of the order of 300 to fit the data (excluding the data points at 0.2 and 0.3 microns).

This experiment is preliminary and more detailed consideration of the use of such simple prescriptions for inhibition is under way. In particular the above model allowed uninhibited transport by the low energy part of the 'hot' electron Maxwellian and this was a significant contribution causing burn-through when large inhibition of cold electron heat conduction was assumed.

Calculations with no 'hot' electrons and a reduction of the free streaming limit and Spitzer conductivity by a factor $\sim$ 10 also predicted the observed amount of burn-through. The latter, while excluding hot electrons which were found to be a major factor in implosion dynamics (Section 3.1.4(d)) may be more realistic since they also excluded the non-physical process where low energy 'hot' electrons could dominate low energy electron heat transport.

3.1.7 Test for shell disintegration during the implosion

A preliminary study was made as a corollary of the experiment on transport inhibition described above which was aimed at examining whether any loss of integrity of layers on a layered spherical target occurred during the implosion. Fluid instabilities of the Rayleigh-Taylor type or strong local variations in implosion velocity could lead to such a layer mixing.

A possible method for such an observation was to look for evidence of Al ions in the X-ray emitting implosion core when the Aluminium was present only as an outer surface coating on the microballoon. Figure 318 shows space resolved spectra of Al XII emission from implosions with 0.1 and 0.2 microns aluminium layers. The vertical axis was space resolved along the axis between the two irradiated poles of the microsphere as described in Section 3.1.4. The horizontal axis was spectrally resolved.

With layer integrity during the implosion, Al XII emission would be strong at the two poles but absent in the implosion core with no local rise in intensity in the centre. Short 271077/083 showed evidence however of a local intensity rise in the implosion core for the dielectronic satellite lines. The target had aluminium as its support stalk as well as on the microballoon surface so it could not be ruled out that the one dimensional spatial resolution was seeing 'central' emission from the support stalk. Short 151277/163 had no aluminizing on the support stalk but still showed evidence of a central emission peak on all lines in the Al XII resonance peak. It follows that the Aluminium emitted X-rays while localised near the centre plane between the two irradiated poles of the microballoon.

The possibilities seem to be:

i) fluid instability shell break-up allowing Al into the implosion core
ii) prepulse damage to the shell allowing Al into the implosion core
iii) effects of spherically non-uniform irradiation.

At the present preliminary stage none of these effects can be given greater weight than the others though the long term aim of the approach is to study possible fluid instabilities.

3.1.8 PRODUCTION AND DIAGNOSIS BY PULSED X-RAY SHADOWGRAPHY OF A DENSE COOL IMPLOSION PLASMA

A very recent and only partially analysed experiment has yielded rather novel results.

There is a general interest in ablatively driven implosions and it is clear that as an initial step these might be achieved without increased laser power with thick-walled shell targets but at the expense of lower implosion velocity and lower implosion plasma temperature. There would then be no emission of fusion reaction products or penetrating X-rays from the implosion core and the problem presents itself as to how to diagnose such a plasma.

As a first step in this direction a scheme was developed for probing the implosion plasma with externally generated X-rays. In order to test the idea it was also necessary to devise an implosion that would produce a dense, cold, non-X-ray-emitting implosion core. Figure 319 shows schematically the system arrived at.

The target was a glass microballoon of 66 micron diameter and 1.3 micron wall thickness filled with Neon at 87 bar pressure, or 70 mg cm^{-3}. The target was imploded in a two beam f/1 lens focusing system with 3J 100 psec pulses in each beam. The focal plane was displaced two diameters behind the irradiated surface in each beam giving maximum spherical uniformity of irradiation and a peak flux density at the irradiated poles of 2×10^{14} watts cm^{-2}. A third beam of 5J in 100 psec, displaced slightly in angle and delayed in time relative to one of the two main beams, was generated by a simple double mirror arrangement. It was focused via one of the main focusing lenses onto the 45^{o} inclined surface of a solid brass (Cu + Zn) target. The microballoon was mounted on a 150 micron carbon fibre stem attached to the same brass rod, see figure 335. The delayed beam angle was adjusted to place its intersection with the brass target behind the microballoon along the orthogonal line of view of an X-ray pinhole camera. The delayed beam was thus out of focus by two balloon diameters and created an area of plasma on the brass target greater than the projected size of the microballoon. The X-ray pinhole camera thus viewed the microballoon against a background of X-ray emission from the brass target as shown schematically in figure 319. It was anticipated that, with appropriate timing and choice of X-ray filtering, the dense core of the implosion would be seen as a sharply defined zone of absorption by the pinhole camera.

The pinhole camera was operated at 4:1 magnification with two 12.5 micron pinholes and Beryllium filters of thickness 5.0×10^{-3} and 1.25×10^{-2} cm giving filter cut off energies of 1.8 keV and 2.4 keV respectively. The spectrum transmitted by these filters from the auxiliary plasma was measured with the calibrated X-ray crystal spectrometer described in section 3.1.4 and is shown in figure 336.

The discussion here will concentrate on the low energy channel data It was found that the intensity of background X-rays was typically 10 times greater than that from the microballoon corona plasma when simultaneous pinhole camera images of the microballoon implosion and the background plasma were compared.

The experiment was started with the time delay for the backlighting plasma set at 350 picoseconds. Figure 337 shows the result. (A measure of the simplicity of the experiment is that this result was the first shot attempted.) The sketch shows the initial microballoon to scale and the much larger zone of background illumination is clearly seen. The shadowgraph image of the imploding target is seen as the light zone in the background illumination. It has good circular symmetry and shows a rise in intensity in the centre which is clearer in the densitometer trace below the picture. This is evidence of a dense shell structure at this stage of the implosion.

A sequence of pictures with varying timing is shown in figure 320 . It is seen that at 250 psec and 350 psec the dense shell structure was clearly present with a small central intensity peak. Peak compression occured at about 460 to 570 psec and was followed by expansion at 670 psec It can also be seen that the minimum intensity in the absorption region does not reach the base line. The reason for this is that the emission from the corona plasma was non-negligible and set the level observed in the centre.

When the irradiation was focused to minimum spot size on the two poles of the target microsphere, the shadowgraphs recorded clearly showed a non-spherical implosion (see figure 338). The dense plasma assumed a two lobed shape and it was clear that the implosion velocity was greatest at the irradiated poles. The shadowgraph quality was poorer in this case because the particular system of focusing used caused a reduced size of the backlighting plasma with minimum focal spot size on the target.

The timing and choice of X-ray filtering depend on understanding the implosion history, the X-ray absorption processes in the imploding plasma and the emission spectrum of the background plasma.

The implosion history was modelled by the MEDUSA computer code which is described more fully in section 3.5. The sequence of events can be considered in relation to the laser pulse. At peak laser power a shock front of about 500 kbar pressure had penetrated about half the shell thickness raising temperature to about 30 eV and fluid velocity to about 2×10^{6} cm s^{-1} behind the shock. At the end of the pulse (70 picoseconds after the peak), the shock had just entered the gas. There was little overall displacement of the glass shell at this stage. The shock in the gas raised the gas temperature to about 40 eV, raised the density by about 4 x and caused an implosion flow velocity. The latter reached values up to 10^{7} cm s^{-1} at the centre when the shock converged about 300 psecs after the laser power maximum. Shock reflection heating gave a local electron temperature peak of about 300 eV but implosion of the wall and surrounding gas continued and the temperature at the centre decreased. At peak compression of the gas-glass interface, about 400 picoseconds after the laser power maximum, the predicted gas densities were 0.5 to 1 gcm^{-3} and electron temperatures were 50 to 100 eV. Radiation cooling and ionization energy were not included in the calculation so some further compression was expected to occur in the experiment.

It was clear from the modelling of the implosion that the 100 psec duration of X-ray emission from the auxiliary plasma was sufficiently short to 'freeze' the motion of the imploding plasma to a level of resolution as good as that of the pinhole camera and that timing in the range 0-600 picoseconds delay was appropriate.

Absorption of X-rays would occur most strongly by photoionization of K shell electrons. In particular, Oxygen in the glass would be in the form of He-like ions from 30 eV < KT_e < 200 eV and similarly Neon for 50 eV < KT_e < 300 eV. The Helium-like ion photoionization thresholds are 739 eV for Oxygen, 1195 eV for Neon and 2437 eV for Silicon, (ignoring depression of ionization potential in dense plasmas). The absorption coefficient for photoionization may be written as:

(1)

$$K\nu = \frac{1.4 \times 10^{-15}}{(h\nu_{eV})^3} N_i \frac{U_{i+1}(T)}{U_i(T)} \frac{X_i^2 \text{ eV}}{X_H \text{ eV}} \xi \quad cm^{-1} \tag{3}$$

for the process $A_i + h\nu \rightleftarrows A_{i+1} + e$, where there are ξ equivalent electrons in the shell being ionized, the ionization potential of A_i is X_i and that of hydrogen X_H, the partition functions for the ions are U_i and U_{i+1}, N_i cm^{-2} is the number density of ions A_i, and $h\nu$ is the photon energy. Equation (3) reduces for the cases of interest to the expressions:

Oxygen $$K_\nu = \frac{3.5 \times 10^3 \ \varepsilon(T) \ \rho \text{ glass}}{(h\nu_{keV})^3} \tag{4}$$

Silicon $$K_\nu = \frac{1.7 \times 10^4 \ \varepsilon(T) \ \rho \text{ glass}}{(h\nu_{keV})^3} \tag{5}$$

Neon $$K_\nu = \frac{1.5 \times 10^4 \ \varepsilon(T) \ \rho \text{ neon}}{(h\nu_{keV})^3} \tag{6}$$

where $\varepsilon(T)$ represents the fraction of the ions of the element that have two or more electrons and ρ is the density in g cm^{-3}. (Where one or more screening electrons are present outside the K shell there will be a shift of the photoionization threshold from the He-like ion value towards the lower energy un-ionized K edge.) At energies below the K shell photoionization threshold and for the high densities of interest here the dominant absorption process would be inverse Bremsstrahlung for which,

$$K_\nu = \frac{3.7 \times 10^8 \ N_e^2 \ Z}{T_e^{\frac{1}{2}} \ \nu^3} \left(1 - \exp \frac{-h\nu}{KT}\right) \quad cm^{-1} \tag{7}$$

for T in ^oK and ν in Hz.

In glass, absorption at energies below the K electron threshold of Si would be due to photoionization of Oxygen so inverse Bremsstrahlung was not of interest. However, below the K electron threshold of Neon, inverse Bremsstrahlung dominates and one can write:

$$K_{\nu} = \frac{1.6 \times 10^{2} \rho^{2}}{T_{eV}^{\frac{1}{2}}(h\nu_{keV})^{3}} \qquad (8)$$

It is clear from equations (4) to (6) that for energies above the circa 1 keV photoionization threshold for Neon K electrons, absorption by Oxygen in the glass and by Neon in the gas fill would be similarly effective for the same density. Below the Neon threshold, but above that for Oxygen, the Oxygen absorption would dominate.

The choice of target element for the auxiliary plasma generating the probe X-rays was governed by the need to have a greater intensity of X-rays from this source than from the corona plasma of the microballoon. It is well known that L shell resonance spectra of elements of $Z \sim 30$ are the most intense sources of 1 keV X-rays in laser produced plasmas (321) and for that reason Cu XX and Zn XXi 2-3 resonance multiplet emission (322) was chosen for the probe radiation.

The data was analysed by first transforming the densitometer tracings to intensity profiles using the non-linear response characteristic of the Kodirex recording film. The emission of the corona plasma was then subtracted using measured emission profiles of the corona plasma alone on the axes YY and XX of figure 320. These were normalised to the intensities at peak absorption in figure 320. (This assumed that the peak absorption was large and would lead to negligible transmission. This assumption was justified in retrospect.) Finally a bell shaped curve derived from separate photography of the auxiliary plasma emission was fitted to the wings of the profiles and the data were reduced to attenuation as a function of position along the axes XX and YY (see fig 339).

The accuracy of the experimental measurement of attenuation decreased with increasing attenuation and meaningful data for opacities up to about three were obtained. It was concluded from the measured spectrum of the probe X-rays that the observed attenuation was due to photo-ionization of K shell electrons in oxygen in the glass and in the Neon gas fill.

The MEDUSA code was modified to predict the transverse attenuation profiles time-integrated over the 100 picosecond probe pulse duration at various times during the implosion. The calculation also explicitly treated the spectral composition of the probe radiation. Figure 339 shows such a computed opacity profile for a time delay of 416 picoseconds corresponding to peak compression. The experimentally measured opacity profile for a time delay of 460 picoseconds is also shown.

There is reasonable agreement between the calculated and measured results with the measured data at opacity 2.0 indicating a 0.8 times smaller compressed core than the calculation. Also the measured data were obtained with a 15 micron resolution pinhole camera so that the observation would have overestimated the $\sim$ 30 micron diameter of the absorption zone by about 4 microns and underestimated the peak absorption. These two factors suggest more compression in the experiment than in the calculation with an experimental volume compression ratio two to three times higher than calculated. If this were the case the gas would have been compressed $\sim$ 25 times to a density 2 g cm^{-3} and a density radius product ρr of $\sim 4 \times 10^{-3}$ g cm^{-2}.

The fact that the calculation ignored radiative cooling and ionization energy in describing the compressed gas leads to the conclusion that more compression should occur than was calculated. The compression is very sensitive to radiation cooling and when bremsstrahlung radiation was included in the calculation without correction for self-absorption the predicted compression ratio was dramatically increased by over 20x. Proper correction for opacity is of course necessary and a more accurate calculation would yield results somewhere between the extremes described.

A second comparison with MEDUSA was made by plotting the recorded dimensions of the absorption zone at opacity ~ 2 against the calculated values at various times as shown in figure 340. There is fair agreement in the time of peak compression. The measured diameter values are approximate since they were not obtained by the full procedure described in relation to figure 339 but were obtained by direct measurement of the densitometer tracings in figure 320.

The feature seen in figure 320 at times 250 and 350 picoseconds prior to the implosion when maximum attenuation occurs in a ring-like zone was also predicted by the MEDUSA calculations and evidences the progress of the compression zone in the implosion towards the centre.

At this preliminary stage in the data analysis it may be concluded that X-ray shadowgraphy offers a new way to study implosions. It records directly the region of peak density in contrast to X-ray emission observations and is of particular value where cool implosion cores with no significant X-ray or fusion product yield are being studied.

The particular implosion studied here has yielded rather high values of density and ρr evidenced by the shadowgraphy results. There are several ways in which this preliminary result can be developed and such development is planned for future work.

B C Fawcett (Convenor), A Richards, A Ridgeley (Appleton Laboratory); L Cooke, M J Lamb, C L S Lewis, J G Lunney, A Moore, J M Ward (Belfast); N J Peacock (Culham Laboratory); T A Hall, T P Hughes, P Salter (Essex); N Tahir (Glasgow); D D Burgess, R Lee, W Sibbett, R J Speer (Imperial College); K D Evans, R J Hutcheon (Leicester); D Brown (Royal Holloway College); M H Key (Rutherford Laboratory); R Thareja (Strathclyde).

3.2 OPTICAL SPECTROSCOPY

Several experimental techniques have been deployed during the last year to study the spatial, spectral and temporal properties of the emission from the plasma at and around $2\omega_L$ and $(3/2)\omega_L$ (where ω_L is the laser frequency). From these studies information can be gained concerning the interaction processes of the laser light with the plasma. Although these processes are related to those observed in the plain target experiments, the change in geometry can have subtle effects. For example, resonance absorption is strongly dependent upon the angle of incidence whereas most other non-linear absorption processes are not. Thus the relative importance of resonance absorption may be significantly different for microballoon illumination, where we have a wide range of angles of incidence, from plane target experiments where the range of angles of incidence is limited by the geometry of the f/1 focusing optics.

Spatial information is gained using an optical system shown in figure 341 which produces four images of the plasma harmonic emission viewed at 90^o to the laser beam axis in the horizontal plane. The images were formed by an f/2 objective with 5 micron resolution and 30x magnification. Interference filters selected 2ω and $(3/2)\omega$ emission and a polarizing prism split the images into vertical and horizontal polarization. The polarization of the two laser beams was orthogonal with both at 45^o to the horizontal plane. An example of the results is shown in figure 310.

The 2ω image shows emission from the two irradiated polar regions of the microballoon with emission extending out beyond the initial target surface. There is an overall background emission with some brighter zones within it. 2ω emission is seen over an area of the target surface similar to that for X-ray emission in the pinhole photographs. The 2ω image was also projected with 60x magnification onto a streak camera slit giving a 300μ x 5μ field of observation along the laser axis in the target plane. The image was streaked at 500 psec cm^{-1} giving 15 psec time resolution and 15 micron spatial resolution. A fraction of the incident light was also brought to the camera slit as a time marker.

An example of the resulting streaked 2ω image is shown in figure 342 and from the slope of the two emission zones in the streak record it can be seen that both polar zones of emission move outwards at 1.7×10^{7} cm sec^{-1}. The results were rather variable in that large variations in relative intensity at the two poles were observed and also variations in absolute and relative velocity of outward motion. However, on average the outward motion was at $1.1 \pm 0.7 \times 10^{7}$ cm sec^{-1}. This is roughly consistent with hydrodynamic computer simulations with the MEDUSA code which is discussed below. The 2ω emission is known to occur at the critical density surface and this is seen in the simulations to move outwards as the plasma ablates.

It had been intended to compare the outward motion of the critical density region with that of the quarter critical density region as a measure of average density gradient by making similar observations on the (3/2)ω emission. However, the nature of the (3/2)ω emission seen in figure 310 precludes this possibility. The emission is seen to occur from localised spots of very high intensity and size less than the resolution limit of the optics as evidenced by diffraction rings seen in the image. The spot positions and numbers varied randomly from shot to shot and the emission spots on figure 310 are seen to be uncorrelated in the two perpendicular polarization images.

Possible mechanisms for these observations have been considered. For microballoon targets, the threshold intensity for $2\omega_{pe}$ decay is expected to be close to the experimental irradiances of 10^{15} W cm^{-2} due to the steep density gradients. This threshold is now above that for a small degree of filamentation to occur in the plasma (as observed by Haas et al (323,324))leading to localised heating of the plasma. This will give rise to the creation of small hot regions of plasma above the threshold for $2\omega_{pe}$ decay giving the observed spectral and spatial distributions. Since the intensity is well above that required for $2\omega_{o}$ production, this filamentation will lead to small regions of brighter $2\omega_{o}$ emission embedded in a uniform background, again in accordance with observations.

The spectra of both (3/2)ω and 2ω emission were recorded by projecting highly magnified images of the target, formed in backscattering through the main focusing lenses, onto the input slits of stigmatic grating spectrometers. The resulting spectra were thus spatially and spectrally resolved. Bright spot emission of (3/2)ω were seen in this way as it was in the images described above. The (3/2)ω spectrum, figure 309 , showed large broadening with symmetrically red and blue shifted maxima and a central minimum at (3/2)ω. This feature has been noted in several experiments and has also been interpreted in terms of a model which relates the peak separation to the local plasma electron temperature (325).

The model assumes that the threshold for the two plasmon decay instability (326) is exceeded and that parametric interaction of laser photons with the resulting plasmons at one quarter critical density leads to the (3/2)ω generation and spectral characteristics. Following this model the observed 100 to 400 Å range of spectral peak separation in the present experiment would imply electron temperatures from 2 to 8 keV. The significance of the numbers thus derived is doubtful, however, first because the nature of the process leading to the localised hot spot emission is unknown, and secondly because it is not independently proven that the above model is applicable.

The 2ω spectrum illustrated in figure 308 is of the general form noted in other experiments with a component at 2ω and a red shifted wing of variable extent with periodic fine structure. The red wing of the 2ω spectrum has also been considered as an indicator of local plasma parameters (327,328) using a model which requires the onset of the parametric decay into a plasmon and a phonon at the critical density, $\omega_L \rightarrow \omega_{pl} + \omega_{ph}$, and parametric interaction of the laser light with the resulting plasmons, $\omega_L + \omega_{pl} \rightarrow \omega_{2\omega}$.
The red shift of the emission is then given by:

$$\Delta\lambda_{A^o} = \left|\frac{Z}{A}\right|^{\frac{1}{2}} \left[20T_e + 7 \times 10^{-15} q(a/\lambda_o)^{2/3}\right]^{\frac{1}{2}}$$

with T_e in keV, q the laser flux density in watt cm^{-2}, 'a' the scale length of the density gradient and λ_o the laser wavelength.

With the present experimental conditions the above model would indicate, assuming $a/\lambda \sim 1$ and $q \sim 3 \times 10^{15}$ watts cm^{-2}, Te ranging from 10 keV to 250 keV, if the 10 to 50 Å shot to shot variable width of the red shifted wing of the 2ω emission is equated to $\Delta\lambda$ above. Clearly such a simple interpretation is physically unrealistic in the present experiments.

In summary, it seems that while there are models relating line width of both $(3/2)\omega$ and 2ω emission to plasma parameters these models need further investigation and refinement before deductions about plasma parameters can be made for experiments in the parameter range involved here.

E Fabrikesi, T A Hall, T P Hughes (Essex); P Carter S Majumdar, S Sim, E Wooding (Royal Holloway College); A Raven (Oxford); M S White, W T Toner (Rutherford Laboratory); J D Kilkenny, J Murdoch (Imperial College).

3.3 PARTICLE EMISSION STUDIES

3.3.1 Charge collector probes

In order to study the properties of the ablated plasma, several biased Faraday cup ion collectors have been constructed and placed at various positions on the target chamber wall (37cm from the plasma). Up to 10 channels of ion current data have been obtained on a single shot. The detectors have been tested for secondary electron emission and fast electron collection by using various types of collector structure and super-imposing transverse magnetic fields and consequently the signals observed are due to ion current only.

The current pulses recorded by each probe show a reproducible three component structure (Fig 302). Velocities at the current peaks for each component are 2×10^8, 5×10^7 and 10^7 cm/sec respectively corresponding to energies for oxygen ions of 320, 20 and 0.8KeV. These three components are assumed to be due to the hot electron plasma created by the absorption process, to the ablating thermal plasma and to the imploded plasma respectively. The first two components are observed with plane target experiments whereas the third slow component is a feature of implosion events alone.

Ion collector data has been analysed to give mass and energy flux rates assuming the ions to have M/Z = 2 (Fig 303). In this case the first ion component typically carries 60% or more of the total energy recovered by the probes but this has only a few percent of the mass. Assuming the fast ions were protons with M/Z = 1 would reduce the fast ion energy fraction to about 40%.

Ion velocity spectra have been obtained from the data which can be compared with a self similar isothermal plasma expansion model to give a value for the temperature of the hot electrons which cause the fast ion emission. The accuracy of this method is such that values of the hot electron temperature between 5 and 15KeV are consistent with the data (Fig 304).

Recently a model has been developed to treat the expansion of a plasma with two electron temperatures (329). Preliminary comparison of the experimental ion velocity spectra with this model are encouraging and suggest that it can be used to determine the values of the hot and cold electron temperatures and densities.

The total energy recovered by the probe array has been compared with the energy incident on the target and has shown that the absorption fraction is rather low at about 10 or 15%. This figure compares well with measurements made of the scattered light using a diode array (table 2).

3.3.2 Ion charge state analysers

It is essential to obtain information on the M/Z values of the various ion components to understand the physical processes occurring in the target corona. Consequently three different types of analyser are being developed.

An electro-dynamic analyser, which is capable of obtaining the energy spectra of several ion species on a single shot, has been constructed and the time varying (t^{-2}) voltage waveforms generated. Maximum observable energies are of order 100KeV and consequently this device will not be suitable for looking at the ablated thermal plasma ($v < 10^8$ cm/sec). Operation of the instrument is scheduled for June 1978.

A Thomson parabola type analyser with cellulose nitrate foil detection system is now being developed to allow complete characterisation of all fast ions ($v > 2 \times 10^8$ cm/sec) on a single microballoon shot.

A single channel 90° electrostatic E/Z analyser has been operational from October 1977 and has been used to carry out preliminary observations of the fast ion charge composition from microballoon targets. Interpretation of the results obtained so far has been complicated by the presence of charge exchange collisons occurring along the 87 cm flight path between the plasma and the analyser, since the background gas pressure was between 10^{-3} and 10^{-4} Torr. Electron capture cross-sections for multiply-charged ions in the 10^{8} - 10^{9} cm/sec velocity range increase rapidly with Z (331) and can reach values of several x $10^{-15}cm^{2}$. For protons and heavy singly-charged ions, capture cross-sections are high at velocities below 10^{8} cm/sec (332). System pressures considerably below 10^{-4} Torr are required to completely overcome such problems.

Fig 305 is a typical trace obtained, with the analyser set to detect the fast ion component, and shows a predominance of protons and heavy ions of low charge state. All highly stripped ions with velocities of a few 10^{8} cm/sec have been degraded to lower Z due to electron capture events. The protons of velocities greater than about 3 x 10^{8} cm/sec suffer negligible capture collisons however and consequently results obtained are meaningful. These show that protons are a major consistuent of the highest velocity ions observed (up to 5 x 10^{8} cm/sec) and probably originate from hydrocarbon contamination of the thin aluminium coating applied to the balloons. The analyser is now being modified in order to reduce the base pressure in the flight path to better than 10^{-5} Torr whereupon the experiments will be repeated.

3.3.3 Neutron measurements

At the beginning of September, microballoons containing a 10 bar deuterium-tritium gas mixture were imploded and the yields of 14 MeV neutrons were measured with a scintillator-photomultiplier detector. The oscilloscope trace for one of these shots is shown in Fig 314 . One can see clearly resolved X-ray and neutron peaks with the correct time separation for the target-detector distance of 72 cm. The time marker signal from a diode illuminated by a fraction of the incident laser beam serves to distinguish neutrons from X-rays when only one pulse is present. A subsequent shot with more X-ray shielding gave only a neutron peak, and, in shots where the target contained no tritium, only X-rays were seen. An absolute calibration was established from the measured response of the detector to cosmic-ray mu-mesons and published data on the deposition of energy in plastic scintillator by 14MeV neutrons. Useful data were obtained from three shots whose yields were: 1.2×10^5, 1.0×10^5 and 1.8×10^5, with a statistical uncertainty about 15% and an overall normalisation uncertainty of about 30%.

This data has been considered in two ways. First it was compared with the self similar implosion/explosion model (309) which indicated an ion temperature at peak compression of 1KeV. Secondly the quantity 'useful specific energy' used in a scaling law analysis of neutron yield from exploding pusher targets (330) was evaluated. This required the experimentally recorded absorption fraction 13 ± 7% and a numerical procedure defined by the authors of the model to evaluate the fraction of the pulse duration given 'useful' absorption. The result was 0.01 ± 0.005 J ng^{-1} specific absorbed energy. The neutron yield recorded is 10 x above the LLL data compilation for 0.01 J ng^{-1} but at the 20% upper bound for the absorbed fraction the neutron yield agrees with the LLL data.

It is planned to develop the detector as a routine ion temperature diagnostic and to extend its sensitivity so that neutrons from the D-D reaction (whose yield is $\sim 10^{-2}$ of the D-T reaction) can also be measured.

3.3.4 Alpha particle detection using cellulose nitrate foils

It is possible to detect fast ions and charged fusion reaction particles by observation of the tracks that they make in cellulose nitrate (CN) foils.

Fast heavy glass ions produce tracks only about 1μm deep whereas the 3.5MeV alpha particles produced by the fusion of D_2 and T_2 pass through about 20μm of CN. Consequently foils 12μm thick exhibit clear hole tracks when irradiated with alpha particles.

12μm thick CN foils have been placed at a distance of 30mm from the target for some shots on which microballoons filled with DT gas were imploded during November 1977. For each shot the number of clear tracks was determined and the total number of alpha particles deduced.

Results have been obtained for thres shots which all show total yields of about 10^4 alpha particles.

Simultaneous neutron measurements using the system described above gave results that agreed to better than 20%.

H Miles (Convenor), M Clement, S Sethuraman (Swansea); T Goldsack (Imperial College); P T Rumsby, W T Toner (Rutherford Laboratory); S Sartang (Westfield College).

3.4 OPTICAL AND MAGNETIC MEASUREMENTS

Two experimental techniques have been used to study the spatial and temporal variation of density in the outer region of irradiated microballoons. A new technique, which has been successfully used, is to backlight the microballoon with a Q switched ruby laser and observe the outward motion of the critical density surface. This technique shows an outward velocity of about 2 x 10^7 cm/s for the critical density surface. Simulation results indicate that this is evidence for inhibition of thermal conduction. Recently interferometric measurement with a Raman shifted $2\omega_o$ probe beam have been made.

3.4.1 Ruby backlighting of microballoon implosions

Microballoon implosions (at typically 5J/beam) were illuminated at 90^o to the incident neodymium laser direction with a 20 ns ruby laser pulse. The target plane was imaged with f/2 optics onto the slit of the S1 streak camera through a ruby interference filter.

Unfortunately, a crucial timing error meant that only two streaks of an implosion were obtained on a slow sweep rate. Figure 343 shows the first streak and a sketch of the streak. It shows the initial fast (in $\sim$ 300 ps) ablation out to $\sim$ 70 μm from the microballoon centre. This gives a velocity of $\sim$ 2 10^7 cms^{-1} in agreement with earlier measurements for the ablation of the $2\omega_o$ emitting regions (see section 3.2). Note that after $\sim$ 500 ps the critical surface (for ruby laser light) moves only $\sim$ 10 μm in $\sim$ 1 ns giving a velocity $\sim$ 10^6 cms^{-1}. The microballoon is not visible before incidence of the main laser pulse due to its transparency.

We are currently working to remove the temporal modulation present in the ruby laser illumination.

3.4.2 Interferometric measurements

Interferometric measurements using the Raman shifted $2\omega_o$ probe (see section 2.1.1) have been carried out on small microballoon (40 μm) and plane targets. Data from these is only partially analysed but shows interesting structure in the density profile, possibly associated with ponderomotive effects at these intensities.

D R Gray, J D Kilkenny, J Murdoch (Imperial College);
A Raven (Oxford); W T Toner (Rutherford Laboratory).

3.5 THEORY AND COMPUTATIONAL MODELLING

Two-Beam Compression Studies

Introduction

The main theoretical work related to compression studies has been the employment of one-dimensional Lagrangian fluid simulations. However the classical plasma physics, which should include the ponderomotive force, has been modified by two additional effects; an inhibition of the energy flux due possibly to turbulence, and the transport and deposition of energy by a small fraction of highly suprathermal electrons created near the critical surface where the laser energy is deposited. These two modifications appear to be essential for obtaining agreement with experiments. The sensitivity of the compressional process to the equation of state and some nuclear transport properties of the highly compressed core have been investigated. Spectral line broadening of dense plasmas has been studied theoretically which will be useful as a diagnostic. As a preliminary investigation into two dimensional phenomena, an Eulerian computer simulation of compression with polar irradiation of a spherical target has been carried out. These theoretical studies are conducted both at the Universities and at the Rutherford Laboratory, but we are moving towards having all computational models available as standard and fully tested programmes on the Rutherford Laboratory computer.

M G Haines
Imperial College

3.5.1 Development of MEDUSA at the Rutherford Laboratory

Theoretical support for the laser compression programme has centered on hydrodynamic modelling of the plasma using the computer code MEDUSA originally written at the Culham Laboratory. This is a one dimensional code and thus is forced to assume perfect spherical symmetry of the target and illuminating optics.

In its original form the code assumed classical heat conduction and made no allowance for the suprathermal electrons created by absorption of laser energy through resonance and parametric processes. These suprathermal electrons dominate the energy transport in thin shell targets ('exploding pushers') and it has been essential to include this non classical energy transport term in order to obtain any reasonable agreement with experiment. The model adopted so far assumes a source of suprathermal electrons in the computational cell including the critical density surface. This source term is to some extent an adjustable parameter but it is constrained by the experimentally measured hot electron 'temperature' measured from X-ray continuum emission. The suprathermal electrons then lose energy by classical electron-electron collisons along straight line paths, assuming that the source term is isotropic.

With the inclusion of the non-classical heat transport and assuming that virtually all the absorbed laser energy appears as suprathermal electrons, MEDUSA gives reasonable agreement with measured plasma parameters such as density and temperature of the imploded plasma and implosion velocity.

At laser power densities greater than 10^{15}watt cm^{-2} the momentum carried by the photons is appreciable and the radiation pressure of the laser beam is a significant term in the total pressure of the plasma. This has been included in MEDUSA using the WKB approximation to solve the electromagnetic wave equations in a non-uniform plasma and has shown the same steepening of the plasma density profile near critical density as has been reported by the groups. It can be shown analytically that supersonic plasma flow through this steepened profile is unstable and this is possibly the cause of oscillations which have been observed in the simulation runs and have previously been ascribed to numerical instability.

In this modified form MEDUSA has been extensively used to model experimental conditions and various X-ray emission and absorption diagnostics have been added as required. For instance the bound-free absorption of Neon and Oxygen are included to model the X-ray backlighting experiment and the 3p - 1s and 4p - 1s transitions of the helium like ions of Aluminium and Silicon are modelled for the thermal transport experiment on Al coated microballoons.

MEDUSA is also being used to plan future experiments which will seek to observe truly ablative compression rather than exploding pusher behaviour. Progress in this direction has already been made with the X-ray backlighting experiment where use of the code made it possible to design a target with a long implosion time and a cool implosion core.

With the thicker wall targets that may be needed for ablative compression experiments it is likely that radiative energy transfer will be important and work in conjunction with the University of Glasgow has proceeded to include radiative transfer in MEDUSA. So far only a single radiation temperature is included but it is intended to extend this to a multi group treatment in the future.

R G Evans, D J Nicholas and L A Walsh

3.5.2 Applications of MEDUSA and incorporation of Atomic Physics Codes

(a) Introduction

We present a survey of work done at Glasgow University. We have introduced modifications in MEDUSA (333) which permit simulation of the compression of gas-filled microspheres, including layered targets. We have also incorporated atomic physics packages CORONA (334) and TRIP (335). Both aspects of our work are described in greater detail below and some typical results are given in an appendix. We first outline the general motivation of our work.

MEDUSA calculates the hydrodynamic and thermodynamic behaviour of a plasma irradiated by an intense laser beam. The plasma is assumed to be a charge neutral mixture of electrons and ions, with fixed degree of ionisation. Although this approximation may be valid for a D-T plasma, in the case of medium Z targets (Z up to 20) important atomic physics effects are neglected. One important aspect is that the degree of ionisation is variable and the mean ionisation may change significantly during the compression and expansion due to microscopic processes taking place in the plasma. In order to account for these atomic processes, we have incorporated into MEDUSA two different atomic physics packages, CORONA and TRIP. The former model assumes equilibrium between collisional ionisation and radiative recombination, and depends only on electron temperature. TRIP, in time-independent form, also includes three-body recombination and thus depends also on electron density. (A time-dependent form of TRIP exists, and is being used in our 2D plane target code CASTOR, but has not yet been used with MEDUSA). The two versions of MEDUSA incorporation CORONA and TRIP are denoted respectively MEDUSAZ and MEDUSAT.

(b) Compression of Microspheres

The standard version of MEDUSA can deal only with solid microspheres. We have modified it to handle hollow shells, gas-filled microspheres and layered targets. In the case of solid spheres, density and temperature are initially uniform, so pressure is also uniform and inward motion of the material is a direct result of compression alone. In the case of hollow shells, it is necessary to assign a minimum residual pressure $\simeq 10^{-6}$ x typical gas pressure. For gas-filled microspheres we adopt essentially the same procedure, except that there is a smaller step-down in pressure $\simeq 10^{-2}$ to 10^{-3} take account of solid-gas transition.

The finite pressure gradient at the solid-gas boundary causes a rapid inward motion of the material. This can be avoided by holding the boundary stationary until the thermal front arrives and ionises the material, and leads to high compression. In fact, thermal transport due to suprathermal electrons and radiation is much faster than that due to thermal electrons, and results in an explosion of the shell (the pusher mode). The inner solid boundary is driven into the gas and compresses it, resulting in shock heating and inhibiting overall compression. It is therefore more realistic to allow free motion of the inner boundary; in some sense this compensates for the neglect of suprathermal electrons and radiative absorption. Both these effects will be introduced later in the code.

(c) Steady State Atomic Physics Models

In many cases of interest, the macroscopic parameters characterising the state of the plasma, such as density and temperature, change slowly in comparison with the rates of relaxation processes leading to thermodynamic equilibrium. The system is then in a state close to thermodynamic equilibrium corresponding to the instantaneous values of the macroscopic variables.

(i) Steady state CORONA model

The plasma is in equilibrium with collisional ionisation balanced with radiative recombination. Since these are both two-body processes, the equilibrium state depends only on electron temperature. The fraction f_μ of atoms μ-times ionised is determined by a relation of the form

$$S_{\mu-1}\, f_{\mu-1} = R_\mu f_\mu \qquad (1)$$

$S_{\mu-1}$ (Te) is the rate coefficient for collisional ionisation of (μ-1) times ionised atoms, while R_μ (T_e) is the recombination rate coefficient for μ-times ionised atoms.

Solution of (1) is trivial, giving

$$f_\mu = \left| \frac{S_o}{R_1}\ \frac{S_1}{R_2} \cdots \frac{S_{\mu-1}}{R_\mu} \right| \quad f_o \qquad (2)$$

where f_o is the fraction of atoms in neutral state. S_μ and R_μ are given in ref 334 . Applying the constraint

$$\sum_\mu f_\mu = 1 \qquad (3)$$

$$f_o = \left| 1 + \sum_\mu \left| \frac{S_o}{R_1}\ \frac{S_1}{R_2} \cdots \frac{S_{\mu-1}}{R_\mu} \right| \right|^{-1} \qquad (4)$$

Using relations

$$\langle\mu\rangle = \sum_\mu \mu\, f_\mu \qquad (5)$$

$$\langle\mu\rangle = \sum_\mu \mu^2\, f_\mu \qquad (6)$$

we evaluate $\langle\mu\rangle$ and $\langle\mu^2\rangle$ as a function of the instantaneous electron temperature, and thereby obtain required plasma variables, eg pressure, specific heat, internal energy, radiation loss.

This model is valid if the electron number density is small enough so that radiative recombination is more important than 3-body recombination. It may therefore be applied in the corona region, but would fail in the superdense core where the density may increase by a factor $\simeq 10^4$ x solid density. A density-dependent model is indicated here.

(ii) Steady state TRIP model

We now include 3-body recombination which leads to an extra term of the form $n_e\ B\mu(T_e)$ in the recombination coefficient $R\mu$. $\langle\mu\rangle$ and $\langle\mu^2\rangle$ now become functions of T_e and n_e.

(iii) Validity of steady state models

We can derive a criterion $\quad n_e \geqslant 10^{18}/\tau \quad m^{-3}$ (7)

where τ is the time (in seconds) over which macroscopic plasma variables change significantly. We find in our results that a small region of plasma in the corona should be treated by a time-dependent model. However, since most of the energy is dumped at the critical density surface this region is more important than the coronal region and a steady state model should be quite satisfactory.

We can also derive a criterion which defines the region in which radiative recombination dominates over 3-body recombination, viz

$$n_e < 10^{22}\ (\kappa T_e)^{7/2} \quad m^{-3}$$

(κT_e is in eV).

We find that the criterion is well satisfied in the coronal region but fails in the superdense core, where it is essential to use the TRIP model, which will of course yield the same results as CORONA when the latter is a valid model.

E W Laing and N A Tahir
University of Glasgow

APPENDIX

We present some results of the compression of a 1 μgm solid carbon microsphere on application of an ideal laser fusion pulse.

$$P(t) = P_o(1 - t/\tau)^{-p}$$

We choose $p = -2$ and $\tau = 1.61 \times 10^{-9}$ s for optimum compression. Three models are considered:

MEDUSA (with Z fixed at value 6), MEDUSAZ and MEDUSAT

Initial pellet parameters

$R_o = 4.92 \times 10^{-5}$ m

$\rho_o = 2 \times 10^{3}$ kg m^{-3}

$c_s = 1.85 \times 10^{4}$ ms^{-1}

Pulse parameters

	MEDUSA	MEDUSAZ	MEDUSAT
Initial power per steradian P_o (watts)	7×10^{8}	2.1×10^{9}	2.1×10^{9}
Total energy per steradian (Joules)	70	70	70

Initial plasma parameters

	MEDUSA	MEDUSAZ	MEDUSAT
plasma pressure (Jm^{-3})	4.12×10^{11}	3.31×10^{11}	1.22×10^{11}
mean Z	6	2.49	0.45
Temperature T_e	6×10^{4}	6×10^{4}	6×10^{4}

Final state

	MEDUSA	MEDUSAZ	MEDUSAT
$(\rho/\rho_o)_{max}$	2.43×10^4	4×10^3	5×10^4
T_i max	8×10^7	1.7×10^7	2×10^7
Radiation loss (J)	~ 5	~ 3.5	~ 5

NOTES

1. The MEDUSAT run is optimised with $P_o = 2.1 \times 10^9$ w/steradian. The same value of P_o has been used in MEDUSAZ for the sake of direct comparison. Consequently the latter results are not optimised and the compression ratio and temperatures are low.

2. The initial power level used in MEDUSA is lower than in MEDUSAT since in the latter we start with a low ionization level while in MEDUSA we have taken fully ionized carbon, (Z = 6). This can easily be taken into account in MEDUSA.

3. The initial ionization levels in the MEDUSAZ and MEDUSAT runs differ substantially, being considerably higher in MEDUSAZ. The reason for this is that in MEDUSAT the ionization level is very low in the high density core, as it should be, whereas in MEDUSAZ the ionization level in the core is determined only by the high core temperature. This is an immediate illustration of the importance of using the TRIP package.

3.5.3 SENSITIVITY OF THE MEDUSA CODE TO ASSUMPTIONS ABOUT THE EQUATION OF STATE AND PRESSURE PROFILE

(a) Equation of State

This report discusses the effect of changing the equation of state used in MEDUSA for a better approximation which includes ion-ion correlation effects at high densities. Departures from ideal gas behaviour of the ions will occur at high densities because the ions will not be uniformly distributed and will show a more or less pronounced lattice structure.

The tendency for the ions to be ordered will be governed by the ratio of the electrostatic to thermal energy.

$$\Gamma = \frac{(Ze)^2}{4akT\pi\varepsilon_o} \; ; \; a = (\tfrac{3}{4}\pi n)^{1/3}$$

There is an extensive literature on this subject and the most reliable calculations are those of Hansen (336) using a Monte Carlo method. Recently De Witt (337) has fitted various functional forms to Hansen's data yielding, for instance the form
$U/nkT = -0.89461\ \Gamma + 0.8165\ \Gamma^{\frac{1}{4}} - 0.5012$ for $1 < \Gamma < 40$.

At high densities the electron gas also becomes non-uniform forming 'quasi-atoms' of nuclei surrounded by an electron cloud with a high probability of finding an electron close to the nucleus. For a partially degenerate electron gas it is possible to calculate the pressure as a function of temperature T and density n using the 'quasi-atom' calculations of Geiger et al (338). In Fig 344 we show the calculated lines of constant p/nkT for hydrogen. In the absence of degeneracy and non-uniformity effects this parameter would be equal to two for ionised hydrogen. In the range of interest for laser fusion, $1 < kT < 10^5$ eV, $10^{15} < n < 10^{25}\,cm^{-3}$, p/nkT varies between about 1.5 and 5.0. Similar calculations for Neon show U/nkT varying between 3 and 40 whereas classically for fully ionized neon p/nkT = 11.

(b) Computations with MEDUSA

The purpose of this work is to test the sensitivity of MEDUSA computations to the assumptions made regarding the equation of state. It was thought that the data given by Brueckner and Jorna (339) concerning compression and fusion output of a solid DT sphere might be recalculated, first with the equation of state incorporated in the programme and then with an altered equation of state.

The data used are shown in the following table

Table

Solid DT sphere: initial radius 1.5 mm

Laser pulse form: two rectangular pulses and a ramp

$6.3.10^{11}$ W from 0 to 5.47 n sec

$6.3.10^{12}$ W from 5.47 to 7.20 n sec

Linear rise from

$6.3.10^{12}$ W at 7.21 n sec to

4.10^{14} W at 7.42 n sec

Initial temperature: 5000 K

The final compression and neutron yield depend very much on the precise time sequence and the pulse shapes and optimisation is carried out by varying the data inserted into the code.

Changing the ion equation of state from the perfect gas model normally used in MEDUSA to the Hansen model reduced the maximum shock wave velocity and the optimum compression could be regained by changing the timing of the laser pulses. The optimised fusion energy yield was 229kJ with the perfect gas equation of state for the ions and 222kJ with the Hansen equation of state. In both cases the Fermi Thomas equation of state was used for the electrons.

MEDUSA has also been used to study adiabatic compression since this is preferred to shock heating in a laser fusion target. In plane geometry Kidder has shown that if the boundary pressure is varied as $p = p_o(1-{}^t/t_o)^{-n}$ with $n = {}^5/_4$ then the compression will be isentropic. Several runs of MEDUSA have been performed, changing the value of the exponent n and observing the departure from adiabatic compression by plotting log p against log ρ at different times. The initial adiabat for a perfect gas is determined by

$$\frac{\partial \log p}{\partial \log \rho} = \gamma = {}^5/_3.$$

Quite large changes in n, by up to 50% cause very little departure from the adiabat. Figure 345 shows results for $n = {}^{15}/_8$ with almost adiabatic compression and n = 5 showing the departure from the adiabat caused by the formation of shock waves.

H Motz and R Bond
University of Oxford

3.5.4 The two dimensional simulation LASER B

LASER B is a two dimensional two temperature Eulerian simulation, with ray tacing included. The two dimensional natûre of the plasma irradition had been investigated by putting a spherical plasma shell onto the 2D meash, and then irradiating it with two focused laser beams, simulating the experiment. The polar regions tends to become hotter than the equator, and this causes a thermoelectric generation of a magnetic field. However, from the simulation the magnetic field tends to be ablated away from the critical density surface, thus reducing the heat flux inhibiting effect of the magnetic field. The temperature difference between the poles and the equator is thus not too large and a reasonably symmetric implosion results. The implosion phase is not modelled well by LASER B because it uses an Eulerian mesh.

The absorption processes used in the simulation are classical inverse Bremsstrahlung plus a 50% energy dump for any rays which enter a region of density greater than 0.8 x the critical density. The latter absorption simulates resonant absorption. With this absorption process the overall absorption is 20%. The angular distribution of the scatter light can be obtained from the ray tracing package. One such ray trace is shown in figure 346, there the focused rays are incident from the right and the hatched region is where the plasma is above critical density. From this ray trace, most of the light is scattered into the equatorial direction. Comparison with the experiment has been hindered by the irreproducibility of the angular distribution of the scattered light.

J D Kilkenny
Imperial College

3.5.5 Code Development at Hull

The following codes developed at Hull have been either transferred to the Rutherford Laboratory, or it is planned to do so in the near future.

1. 1D Lagrangian - a general MEDUSA type code, including all MEDUSA features. This code further includes a detailed rate equation treatment of ionisation processes using algorithms developed at Hull (340), together with radiative transport of specified lines by multi-group S_N (341). These latter features allow one to predict the detailed line structure observed spectroscopically.

2. 2D Lagrangian - basis 2D Lagrangian code including two temperatures, thermal conduction, laser absorption. Thermal conduction is treated by 9-point ICCG (342).

3. 2D Eulerian. This code involves a detailed treatment of the self-generated magnetic field within the M.H.D. approximation (343). New algorithms have been developed to treat these terms completely using the complete set of transport terms. Diffusion effects are treated by an asymmetric matrix version of ICCG.

Further development of these codes is envisaged. At present the radiation/ionisation balance in the 1D code is explicit. An implicit treatment using the virtual scattering method is planned, but not implemented. Furthermore a multi-group S_N treatment of hot electron transport has been written, but is not yet included in the code.

3.5.6 Fusion Product Interactions with dense Plasmas

The work has been concerned largely with developing a formula for studying the interaction of charged particles produced by fusion in laser-compressed near-degenerate plasmas. The new physics in this work rests largely in the use of manybody field theory to describe the plasma in a multi-component form rather than as a sum of single component plasmas. For example it is now possible to consider fluctuations in total charge density rather than fluctuations in electron or ion densities separately. Thus the Coulomb shielding between a positive test particle and the ion population is described largely in terms of the electron density, as one would expect from simple physics considerations, rather than by the ion density alone.

T D Beynon
Birmingham University

3.5.7 Equation of state for a partially degenerate plasma

The methods of thermodynamic quantum field theory have been used to obtain the equation of state and other thermodynamic properties of a plasma. Electrons may be partially degenerate while ions are treated classically and restricted to charge number Z = 1 or 2. Results have been obtained for densities in the range 10^{26}-10^{34} m^{-3} and for temperatures of 10^5-10^8 K.

The important non-dimensional parameters for these effects are:

$$\Gamma_e = e^2 n_e^{1/3}/4\pi\varepsilon_o \kappa T,$$

$$\Gamma_i = Z^2 e^2 n_i^{1/3}/4\pi\varepsilon_o \kappa T = Z^{5/3}\Gamma_e$$

if $n_e = Zn_i$ and $\Lambda = \left|\frac{\kappa T}{\varepsilon_F}\right|^{3/2}$, with obvious notation. In the range of interest, ions will always behave classically.

We first calculate the equation of state of an electron gas, with ions forming a neutralising background. This is a useful model for a metal, but less so at the high temperatures we are considering. However we use it as a convenient first step in calculating the equation of state for the full plasma. Results agree with other recent work (344) and indicate a maximum departure from the ideal gas pressure (classical and quantum) of around 15-20% around $n = 10^{30}$ and $T = 10^5$.

We then consider the equation of state of a plasma containing ions of charge Ze. Use of first-order perturbation theory restricts the region of densities and temperatures such that $\Gamma_i < 1$. We have considered only Z = 1 or 2, comparing our results with those found using the Fermi-Thomas method (338). Good agreement is obtained in the partially and highly degenerate regions. However, in the classical limit the Fermi-Thomas theory predicts a much larger correction than our results, which reduce to the Debye-Hückel case, unlike the Fermi-Thomas theory.

The main objective of this work has still to be achieved, namely, to relax the restrictions on Γ_i. One way is to calculate to higher orders in perturbation theory, but this is unlikely to achieve the value of $\Gamma_i > 100$ predicted by Hansen et al. (345) in numerical simulation studies to be the region where a phase-transition to an ordered ion lattice occurs. Further analytic studies are in progress.

J W Johnston, J Cumming and E W Laing

3.5.8 Spectral Line Shapes, Line Formation, and Radiation Transport

(a) Introduction and General Survey

In the past 12 months substantial new results have been obtained on line-broadening and radiative transfer processes in dense laser compressed plasmas. The problem of spectral line formation for multiply ionized emitters in a dense or ultra-dense plasma presents a number of fundamental difficulties not normally encountered in orthodox treatments of pressure broadening and radiative transport. Foremost amongst these are basic statistical mechanical problems resulting from the strong interaction between the charged emitter and its local environment (see below) which have a close relationship with work in other areas of the theory of dense matter. The study of spectral line shapes (and intensities) in laser-compressed plasmas is therefore both an important diagnostic (as already stressed by several recent reviews by Peacock, Vinagradov and Boiko) and also offers a means of studying some quite basic physical problems of much wider fundamental importance.

Work on such problems began in April 1977. Broadly speaking, the line formation problem can be discussed in three stages, the line-shape itself, the consequent transport of the resultant radiation in a time and space varying plasma, and (ultimately) the coupling of energy transport effects due to radiation back into compression codes. Of these, the highest priority has been given to the line-shape problem, since the latter ultimately controls also total line intensities (via the opacity) and because it is in the line-shape that the severest physical (as opposed to computation) problems arise. A new and fully quantum statistical formulation of the line-shape problem has been developed (by R W Lee), capable of treating degeneracy effects as well as phenomena due to the emitter-plasma interaction excluded in all other theories, and has now been coded at I.C. The set of codes making up this package is listed below.

The codes have been used to make a wide variety of line-shape calculations, and substantial new physical effects, important at high densities and excluded from earlier theories, have been predicted, as described in four papers published or in course of publication (346, 347, 348, 349). An experimental investigation of some of these using the Rutherford laser facility has been initiated. With the new line-shape codes fully operational at I.C. for H- and He- like ions, the second stage in studying line formation problems has been initiated via a 1-D model of the transport process in inhomogeneous plasmas and development of this for plasmas of specified n_e and T_e configuration is continuing. The full problem of a simultaneous self-consistent calculation of coupled compression dynamics and radiation transport, however, is regarded (from much evidence from computations of astrophysical and other dense energetic man-made phenomena) as being unrealistic at the present stage. Apart from severe computational problems, much more emphasis is also first needed on the underlying physical processes themselves. Ionization rates (for example) can be altered via degeneracy effects. Also, recent experimental work at I.C. (350) has shown clear and large departues of excitation rates in hydrogen plasmas from accepted values, presently tentatively ascribed to long-range shielding effects. Work is in progress considering the implications of such high density effects on rate processes in laser-compressed plasmas. Also, as an attempt to circumvent the sheer computational problems of simultaneously calculating the radiative transport and the hydrodynamics of the compression, work has begun on attempting to simulate the radiative transport analytically, so that the radiative energy transport can be modelled in the existing MHD codes on a cell by cell basis.

In addition to the new work described above, an older line-shape code written by A G Richards at I.C. circa 1972 has been reactivated at Rutherford (by J M Ward) for use as a general facility. This code is an orthodox formulation of the Griem-

Baranger type theories for ionized emitters incorporating a Hooper type microfield and can be used for quick estimates of parameters such as line-widths. (It should be stressed that the more recent work at I.C. clearly shows that such orthodox treatments, widely used elsewhere, can be in error by very substantial factors both theoretically and experimentally, see reference 346.

(b) Line-Shape Calculations

The new theoretical treatment is described in the 4 papers by R W Lee already referenced. This theory has had as a main aim the proper incorporation of the following effects, all of which are important under the conditions of n_e and T_e relevant in laser-plasmas, and all of which have now been incorporated and studied.

(i) Initial Correlations

The usual approximation that the emitter-perturber density matrix is factorizable can be shown to fail for high charge emitters in dense plasmas.

(ii) Local Polarization

Related to the above, charged emitters strongly polarize the local plasma environment, thus altering the interaction between the optical electrons and the perturbing particles. This polarization depends on the atomic state of the emitting electron and gives rise to new physical effects in the resulting line-shape.

(iii) Degeneracy

The partial degeneracy of the electron gas under some conditions of interest requires a proper quantum-statistical, many-body description of the plasma (in contrast to the binary collision classical-path approximation adopted in most line-shape theories).

(iv) Non-thermal effects

The possibility of enhanced plasmon levels resulting from e.g. fast electron streaming again requires a proper many-body treatment of the line-broadening processes.

(v) Ion dynamic effects and multi-component plasmas

Under conditions of present interest the usual static ion theories often fail. In addition the multi-component nature of the plasma is important, and strong ion-acoustic resonances can arise and cause important modifications to spectral line-shape.

(vi) Bulk motion

The possibility of bulk-plasma motion relative to the emitter in turn reflects back on the theoretical description of the effects described above.

The theoretical basis of the computations and detailed results are given in references (346) to (349). In illustration figure 347 shows computations made for Si XIV Ly-β at 3×10^{23} electrons cm^{-3} and $T_e = 3.10^6\ {}^oK$ compared on a log scale with 'standard' theoretical predictions, the new effects being the large (measurable) asymmetry and shift, as well as changed line-width. (It should be noted that the new theory also explains a major discrepancy between experiment and orthodox theory for H Ly-α, see reference 346 .) Non-thermal effects have also been studied, eg figure 348 shows Si XIV Ly-γ in a plasma with $T_e = 5.10^6\ {}^oK$, $n_e = 9 \times 10^{22}\ cm^{-3}$, plus an additional 'hot' electron source such that 0.1% of the electrons have an elevated temperature of $5 \times 10^7\ {}^oK$. The consequent new features in the experimental profile should be observable with at most modest improvements in experimental resolution if the hot electron component presently proposed in various models of the plasma really exists.

(c) Codes

The main line-shape, and line-shape related, codes presently operational are:

(i) Function

Calculates both real and imaginary parts of the response function for a multi-component plasma (including degeneracy effects).

(ii) Microfield

Calculates orthodox plasma ion microfields at multiply charged test points.

(iii) LAB

Calculates pressure-broadened line profiles of H-like ion species (using results of (i) and (ii) for transitions $n = 1 \rightarrow 2,3,4$ and 5, and $n = 2 \rightarrow 3,4$.

(iv) LHE

Calculates pressure broadening for He-like ions ($1^1S - 3^1P$, 3^1D and $2^1P - 3^1P$, 3^1D).

(v) FIT

Performs slab radiation transport for multiple slabs of different T_e, n_e, slab width and ground state density (uses interactive graphics in fitting to experimental data).

In addition, an 'orthodox' (classical-path binary collision electron broadening, static ion) line-shape code is now available at Rutherford Laboratory under the name RICH. This code has been used in preliminary analysis of transitions in helium-like neon and silicon observed in microballoon implosions discussed elsewhere in this report, prior to a fuller analysis using the results of the quantum statistical code.

R W Lee and D D Burgess (Imperial College); A G Richards and G Bromage (ARD Appleton Laboratory) J M Ward (Rutherford Laboratory).

REFERENCES

301. Key M H et al Rutherford Laboratory Reports RL-77-122/B and RL-78-020

302. Evans K D, Leigh B Space Science Instrumentation 2 105 (1975)

303. Hobby M C and Peacock N J J Phys E 6 854 (1973)

304. Hughes T P Single Beam Interaction Studies at the Rutherford Laboratory, Paper 1.9, 11th European Conference on Laser Interaction with Matter, Oxford September 1977

305. O'Brien J T and Hooper C F Phys Rev A 5 867 (1972)

306. Richards A G (Culham Laboratory) Private communication and J Phys B (to be submitted)

307. Bromage G E (Culham Laboratory) Private communication and J Phys B (to be submitted)

308. Storm E K, Larsen J T A simple scaling model for exploding pusher targets Lawrence Livermore Laboratory Report No UCRL-79788

309. Mayer F J, Johnson R R and Tanner D J Phys Fluid 19 2049 (1976)

310. Lubin M, Goldman L et al, Compression and Transport Studies in Laser Fusion Experiments Paper IV.7, 11th European Conference on Laser Interaction with Matter, Oxford, September 1977

311. Henderson T M and Johnson R R Appl Phys Letts 31 18 (1977)

312. Campbell P M, Johnston R R, Mayer F J, Powers L V and Slater DC Phys Rev Letts 39 274 (1977)

313. Malone R C, McCrory R L and Morse R L Phys Rev Letts 34 721 (1975)

314. Yaakobi B and Bristow T C Phys Rev Letts 38 350 (1977)

315. Mitchell K B and Godwin R P, Inner-shell excitation from 10 μm laser-produced plasmas. Paper 4 A-9, 18th Annual meeting of the Division of Plasma Physics of the American Physical Society 15 - 19 November 1976

316. Morse R L and Nielson C W Phys Fluids 16 909 (1973)

317. Winsor N K and Tidman D A Phys Rev Letts 31 1044 (1973)

318. Craxton R S and Haines M G Phys Rev Letts 35 1336 (1975)

319. Manheimer W M Phys Fluids 20 265 (1977)

320. Mitchell R W, Forshund D W, Kindell J M et al Bull Am Phys Soc 20 1377 (1975)

321. Laser Fusion Studies at NRL, NRL Report No 7838, October 1974, P105

322. Donaldson T P, Hutcheon R J, Key M H and Urquhart R J J Phys B:Atom Molec Phys 9 1645 (1977)

323. Haas R A et al Phys Rev Letts 39 1553 (1977)

324. Haas R A et al J Appl Phys 47 1318 (1976)

325. Avrov A I et al Pisma Zh Eksp Teor Fiz 24 293 (1976)

326. Rosenbluth M N Phys Rev Letts 29 565 (1972)

327. Krokhin O N et al JETP Lett 22 21 (1975)

328. Garban C Thesis. Etude Experimentale des Mechanisms d'interaction laser plasma a haute intensite a partir de l'analyse spectrale du rayonnement laser reflechi. L'University de Paris VI March 1977

329. Wickens L and Allen J E, submitted to J Plasma Phys

330. Storm E K, Ahlstrom H G and Holzrichter J F Exploding pusher targets illuminated using f/1 lenses. Presented at the 10th European Conference on laser interaction with matter, Palaiseau, France October 1976

331. Nikolaev V S et al Sov Phys JETP 13 695 (1961)

332. Allison S K Rev Mod Phys 30 1137 (1958)

333. Christiansen J P, Ashby D E F F and Roberts K V CLM-P374 MEDUSA: A 1-D laser fusion code

334. Mosher D NRL Memorandum Report 2563 The coronal equilibrium of high atomic number plasmas

335. Christiansen J P and Magill J Computational Methods in Classical and Quantum Physics Ed. Hooper M B (Advance Publications) A time-dependent atomic physics model applied to laser-plasmas

336. Hansen J P, Pollock E L, McDonald I R, Vieillefosse P Phys Rev A8 3096 (1973), Phys Rev A8 3110 (1973) and Phys Rev A11 1025 (1975)

337. DeWitt H E and Hubbard W B UCRL-76948 Report

338. Geiger W, Hornberg H, Schramm KH, Eneg des exakt Naturwix Ed G Höhler, Springer Tracts in Modern Physics, Springer, Berlin 1968

339. Brueckner K A and Jorna S Rev of Mod Phys 46 326 (1974)

340. Pert G J J Comp Phys (in press)

341. Carlson B G Los Alamos Reports LA 2260 (1959)

342. Kershaw D S J Comp Phys (in press)

343. Pert G J J Plasma Phys 18 227 (1977)

344. Pokrant M A Phys Rev A16 413 (1977)

345. Galam S and Hansen J P Phys Rev A14 816 (1976)
See also references 336

346. Lee R W J Phys B 11 L167 (1978)

347. Lee R W 'Ion dynamic effects on Lyman and Balmer lines'
(submitted to J Phys B, 1978)

348. Lee R W 'Plasma broadening of spectral lines of hydrogenic ions'
(submitted to J Phys B, 1978)

349. Lee R W 'Non thermal effects in the plasma broadening of
spectral lines' (1978) (preprint available)

350. Burgess D D, Kolbe G, Ward J M 'Direct laser-based measurements
of the collisional depopulation rate of the n=2 level in a hydrogen
plasma' J Phys B, 1978 (in press)

TABLE I

The table below indicates the approximate amount of time in weeks allocated during the period 1 April 1977 to 31 March 1978 to the activities listed. Though the scientific group structure changed during the year (see preface) the activities are listed under the grouping effective at 31 March 1978.

GROUP AND ACTIVITY	TIME IN WEEKS
Laser Plasma Interactions	
Gas Breakdown	1
Harmonic spectroscopy (plane targets)	3½
Harmonic spectroscopy (microballoons)	2½
Transport and Particle Emission	
Magnetic Field measurements	1
Thin foil burn through	6½
Burn through layered microballoons	1
Plane layered targets	2
Shadowgraphy and M/Z Analyser	2
Atomic and Radiation Physics	
XUV auxilliary sources	1
X-ray and VUV transitions, Vanadium to Iron	2
X-ray streak spectra	½
X-ray space resolved spectra	1½
Ablative Compression	
X-ray backlit implosions	1½
X-ray streaked implosions	2
Core spectroscopy	3
DT Neutron emission	1
Pin hole imaged implosions	2
Facility Development	
Maintenance and Beam Characterisation	10
Commission Disc Amplifiers	2
Double Pass Disc Amplifiers	1
Improved pulse switch out system	1

TABLE 2

ENERGY ABSORPTION RESULTS

SHOT NUMBER	ENERGY ON TARGET J	ENERGY RECOVERED IN IONS J	% ABSORPTION INCLUDING CORRECTION FOR X-RAY AND IONIZATION ENERGY	% ABSORPTION FROM DIODES CALORIMETERS
42	20.5	2.1 ± 0.5	11.5 ± 2.5	-
65	18.6	-	-	20 ± 10
73	17.9	2.7 ± 0.7	15 ± 4	16 ± 9
75	21.2	1.9 ± 0.6	10 ± 3	8.5 ± 7
76	18.9	1.6 ± 0.5	9 ± 3	13 ± 7

TABLE 3

OPTICAL ENERGY BALANCE FOR COMPRESSION SHOTS

TYPICAL BREAKDOWN FOR ON TARGET ENERGIES $\approx$ 18 JOULES, IN A 100ps PULSE, FOCUSSED NEAR THE SPHERE CENTRE.

QUANTITY	RANGE RECORDED	MEASUREMENT ERROR
FRACTION OF LASER ENERGY RE-EMERGING THROUGH LENSES	15 TO 30%	1 TO 2%
FRACTION OF LASER ENERGY DIFFUSELY SCATTERED OUTSIDE LENS CONES	55 TO 65%	6%
FRACTION OF LASER ENERGY ABSORBED	13 TO 20%	6 TO 10%

ALL PERCENTAGES USE MAIN LASER ENERGY AS THE BASE

TABLE 4

DENSITY MEASUREMENTS

Neon

Ne IX $1^1S_o - 3^1P_1$	Stark profile gives ρ
Ne X Ly α	Optical depth yields ρR

Glass

Si XIII $1^1S_o - 3^1P_1$	Stark profile gives ρ

ABSOLUTE RECOMBINATION CONTINUA

Ne X, Si XIII	Give Ne Ni V

SPACE PROFILES (Spectra & Pinhole Pictures).

Give Source Dimensions

TABLE 5

TEMPERATURE MEASUREMENTS

Electron T_e

Recombination continuum slope Ne X, Si XIII

Line ratios, eg.

$$\frac{\text{Si Ly } \gamma}{\text{Si XIII } 1^1S_o - 4^1P_1} \sim \frac{N^{14+}}{N^{13+}} \sim T_e$$

Ions T_i

DT neutron and α yield at known density gives T_i

TABLE 6 - COMPRESSED NEON PARAMETERS

Shot 250577/28

Microballoon 70.5 μm diameter
0.96 μm wall thickness
filled with Ne at 8.5 bar

Incident laser energy 8.5 J and 9.6 J

Crystal spectrometer - TℓAP

$T_e = 500 \pm 100$ eV	Ne IX and Ne X recombination continuum slope
$\frac{n^{10+}}{n^{9+}} = 0.4 \pm 0.2$	Intensity ratio Ne X Lyβ/Ne IX $1^1S_o - 3^1P_1$
$T_e = 400 {}^{+30}_{-70}$ eV	From n^{10+}/n^{9+} above using ionisation equilibrium temperature dependence
$n_e = 6 \pm 2 \times 10^{22}$ cm^{-3}	Stark broadening of Ne IX $1^1S_o - 3^1P_1$
$n_e^2V = 3 \pm 1.3 \times 10^{36}$ cm^{-3}	Absolute intensity of Ne IX and Ne X recombination continua
$V = 2 \pm 0.7 \times 10^{-9}$ cm^3	Axial core diameter from space-resolved spectrum, ellipticity from pinhole photography
$n_e = 4 \pm 1.5 \times 10^{22}$ cm^{-3}	From n_e^2V and V above
Compression ratio = 30 Density $\rho = 0.23$ gm cm^{-3}	From Stark broadening density value above
$\rho R = 2.8 \times 10^{-4}$ gm cm^{-2}	From Stark broadening density value and axial core diameter above

TABLE 7 - COMPRESSED GLASS PARAMETERS

(X-ray Emission Zone)

Shot 250577/30

Microballoon 69.5 μm diameter
0.82 μm wall thickness
Gas fill - Neon at 8.5 bar

Incident laser energy 7.2 J and 6.4 J

Crystal Spectrometer - PET

$T_e = 450 \pm 50$ eV	Si XIII and Si XIV recombination continuum slope
$n^{14+}/n^{13+} = 0.3 \pm 0.1$	Si XIV Ly γ / Si XIII $1^1S_o - 4^1P_1$ intensity ratio
$T_e = 840 {}^{+30}_{-100}$ eV	n^{14+}/n^{13+} above plus coronal equilibrium temperature dependence (assumed)
$n_e = 9 \pm 3 \times 10^{22}$ cm^{-3}	Si XIII $1^1S_o - 3^1P_1$ Stark broadening
$n_e^2V = 1.1 \pm 0.3 \times 10^{37}$ cm^{-3}	Absolute intensity of Si XIII & Si XIV recombination continua
$r = 8 \pm 2$ μm	Outer radius of emission shell from space-resolved spectrum
$\Delta r = 2 \pm 0.7$ μm	Thickness of emission shell from n_e^2V, ne and r
$\rho = 0.32$ g cm^{-3}	Assuming $n_e = 9 \times 10^{22}$ cm^{-3}
$\rho\Delta r = 6.4 \times 10^{-5}$g cm^{-2}	From Δr and ρ above

TABLE 8 - GLASS SHELL PLASMA PARAMETERS

(X-ray Emission Zones)

Shot 250577/30 (see Table 4)

T_e = 500 ± 150 eV	From Si XIII and Si XIV recombination continuum slope
n^{14+}/n^{13+} = 0.2 ± 0.1	Si XIV Lyα/Si XIII $1^1S_o - 4^1P_1$ intensity ratio.
T_e = 800 ± 70 eV	n^{14+}/n^{13+} above plus coronal equilibrium temperature dependence (assumed)
n_e = 1 ± 0.3 x 10^{22} cm^{-3}	Stark broadening of Si XIII $1^1S_o - 3^1P_1$
n_e^2V = 1.3 ± 0.5 x 10^{37} cm^{-3}	Absolute intensity of Si XIII & Si XIV recombination continua
V = 3 ± 1 x $10^{-8}cm^3$	Axial dimension from space-resolved spectrum, transverse from pinhole photographs
n_e = 2 x 10^{22} cm^{-3}	From n_e^2V and V above

TABLE 9 - 'HOT' ELECTRON ENERGY TRANSPORT CAUSES EXPLODING PUSHER BEHAVIOUR AND REDUCES IMPLOSION DENSITY

GAS FILL	DENSITY ρ g cm^{-3}	MEDUSA DENSITY (NO HOT ELECTRONS)	MEDUSA DENSITY (HOT ELECTRONS, $T_H = 10\ T_c$)	SHOT NO
10 Bar $D_2 + T_2$	0.23	12	1.3	250577/28

TABLE 10

IMPLODED GAS DENSITY

* Calculated   ** Normalised to shot 28

Gas Fill	ρ expt ± 30% (g cm^{-3})	Compression Ratio (Expt)	Compression Ratio (Medusa)		Compression Ratio (Storm et al) $\frac{8.6}{\rho_o} \frac{\Delta r}{r}$	Δr (μm)	r (μm)	Laser Energy (J)	Shot Number
			*	**	*				
Neon 8.5 bar	0.23	30	195	30	30	0.96	70.5	18.2	250577/28
Neon 2.5 bar	0.23	100	652	100	99	0.90	68	16.2	091177/108
D_2 + 5% Ne 11 bar	0.14	60	250	38	77	0.91	84.1	16.3	091177/105
D_2 + T_2 10 bar	(0.14)	(60)	273	42	77	0.88	88	15.3	091177/102

TABLE 11 - TEMPERATURE IMPLODED GAS

Gas Fill	Expt T_e eV	Expt T_i eV	Medusa T_e eV	Medusa T_i eV	Shot
8.5 bar Neon	500	-	1000		250577/28
11 Bar D_2 + 5% Ne	500	-	1000		091177/105
10 bar $D_2 + T_2$	(450)	700	540	640	091177/102

TABLE 12 - IMPLODED GLASS

Gas Fill	ρ glass (expt) ± 30% gm cm^{-}	ρ glass (Medusa) (gm cm^{-}	Te glass (expt) ± 15% (eV)	Te glass (Medusa) eV	Δr (thickness of X-ray emission zone) (expt) μm	Shot No
Neon 8.5 bar	0.32	3.0	450	200	2	250577/30
$D_2 + T_2$ 10 bar	0.21	2.5	450	150	-	081177/102

BELFAST-ROYAL HOLLOWAY-RUTHERFORD

DOUBLE BEAM FOCUSSING

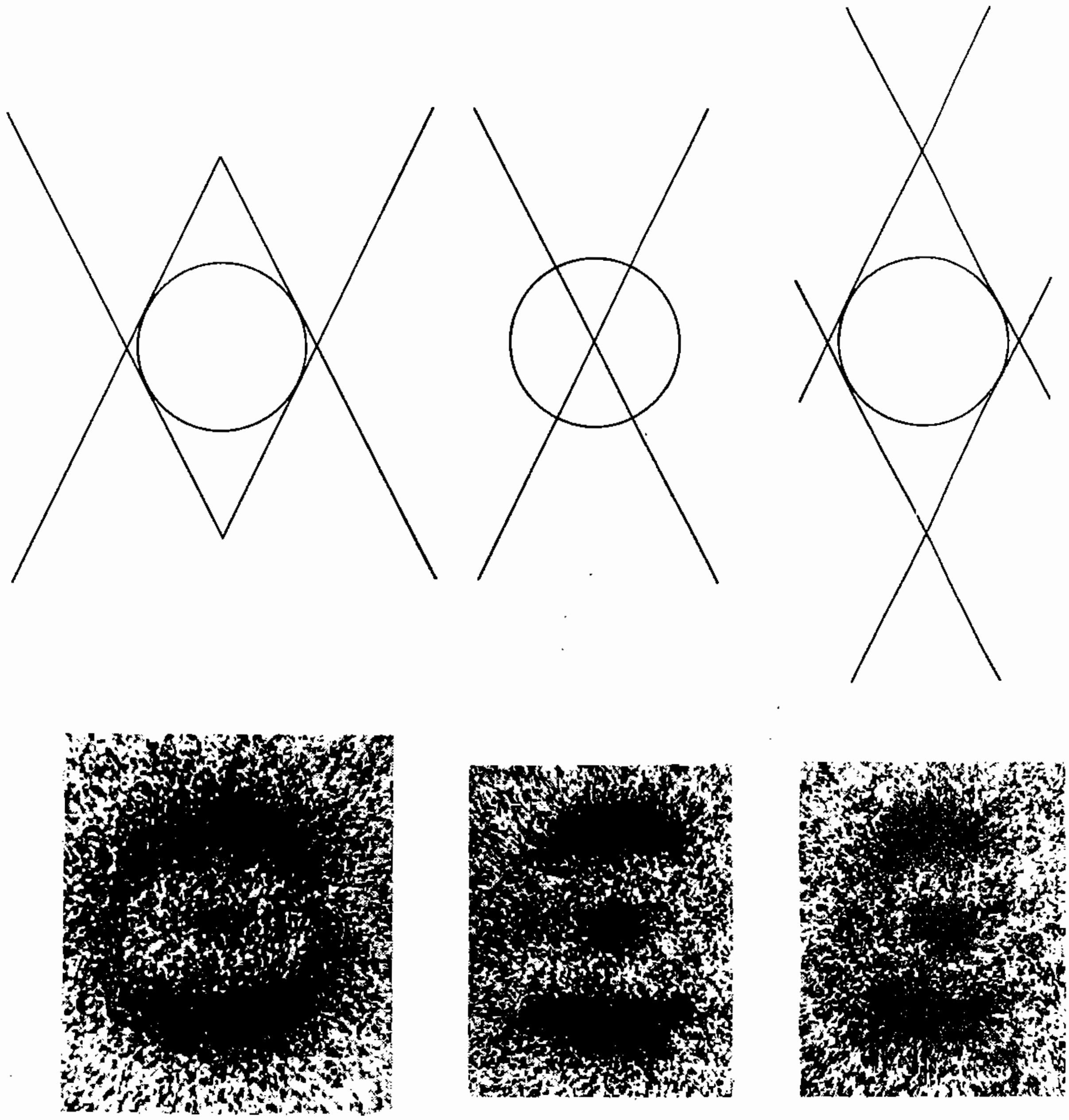

FIG. 301

RUTHERFORD

TYPICAL ION COLLECTOR PROBE DATA

SIGNALS FROM FOUR PROBES SITUATED AT 38 CM FROM A GLASS MICROSPHERE TARGET

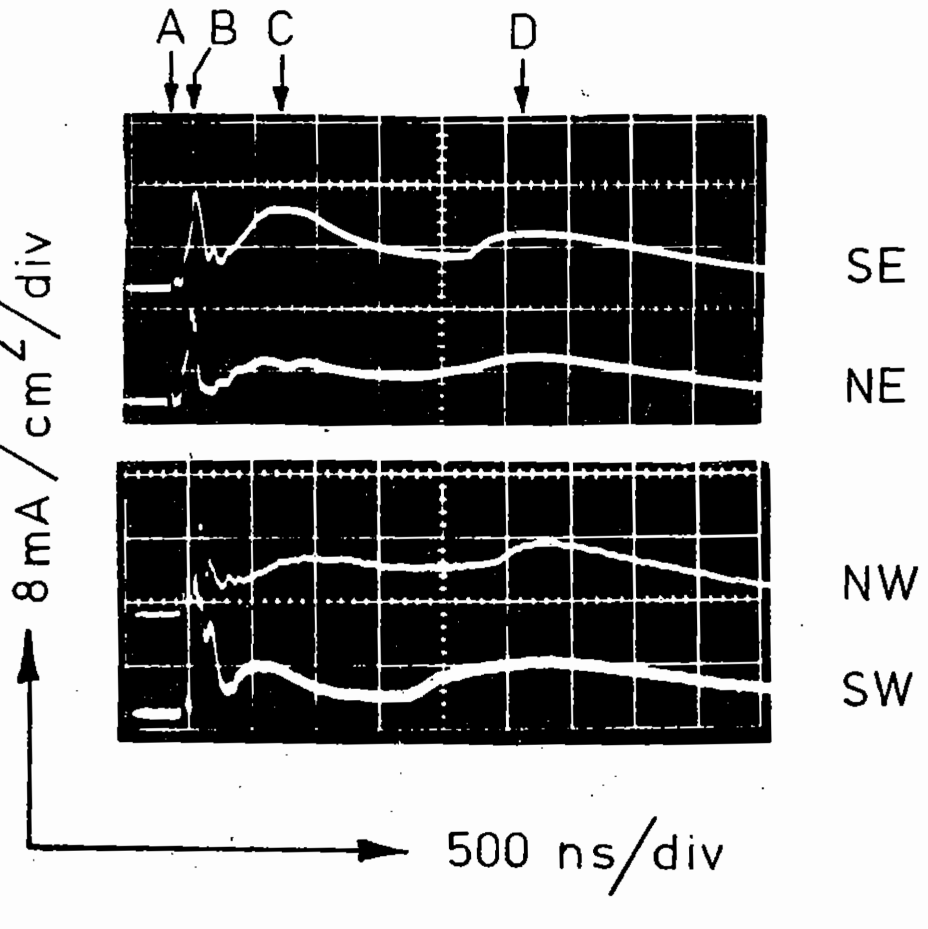

A - PHOTO EMISSION FROM PROBE GRID GIVES LASER TIME MARKER.

B - FAST ION SIGNAL ($V \sim 2.10^{8}$ CM/SEC)

C - NORMAL ION SIGNAL ($V \sim 5.10^{7}$ CM/SEC)

D - SLOW ION SIGNAL ($V \sim 10^{7}$ CM/SEC)

FIG. 302

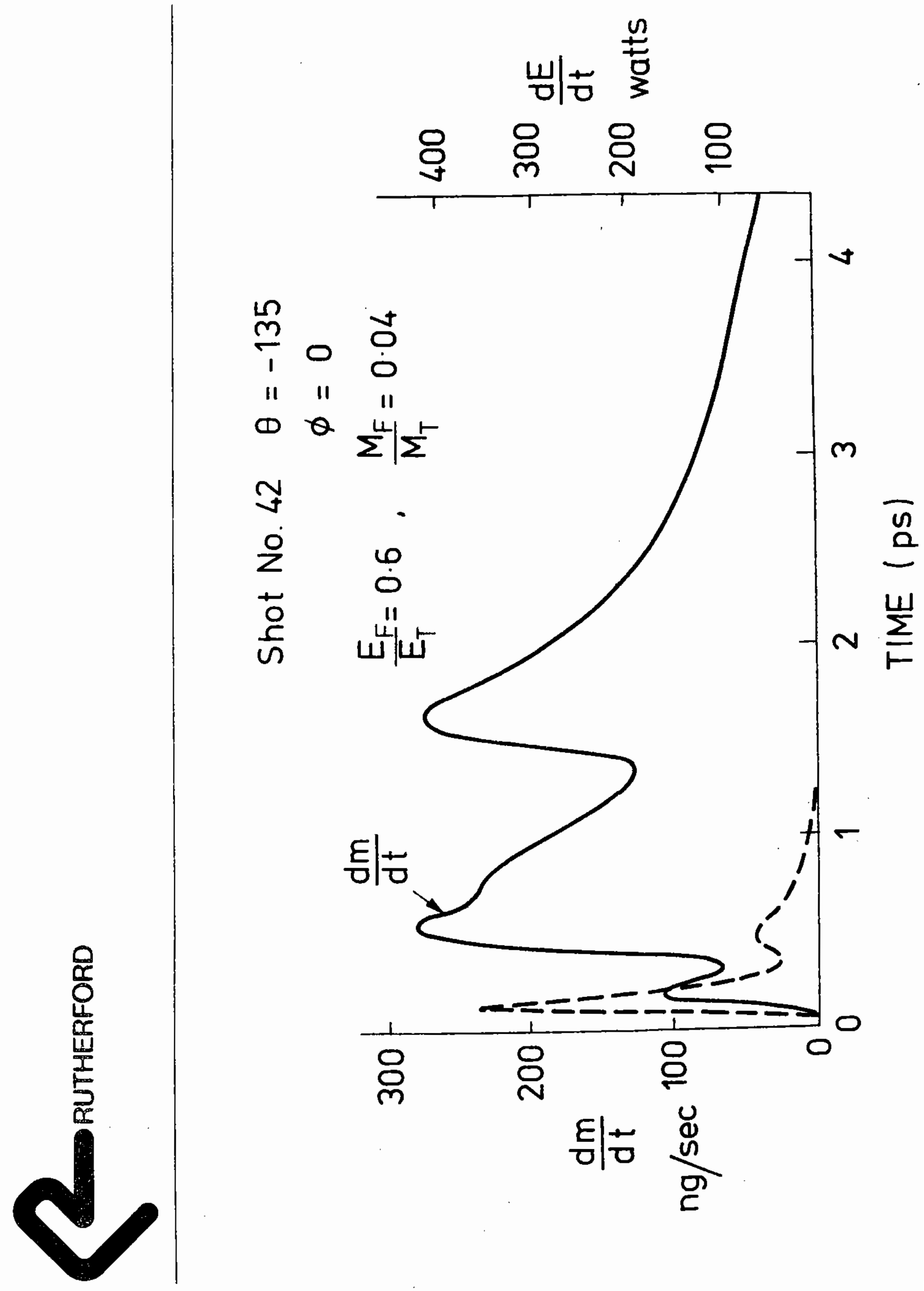
RUTHERFORD
Shot No. 42
θ = −135
φ = 0
E_F/E_T = 0·6 ,
M_F/M_T = 0·04
dm/dt
dm/dt ng/sec
300
200
100
0
dE/dt watts
400
300
200
100
0
1
2
3
4
TIME (ps)

FIG. 303

RUTHERFORD

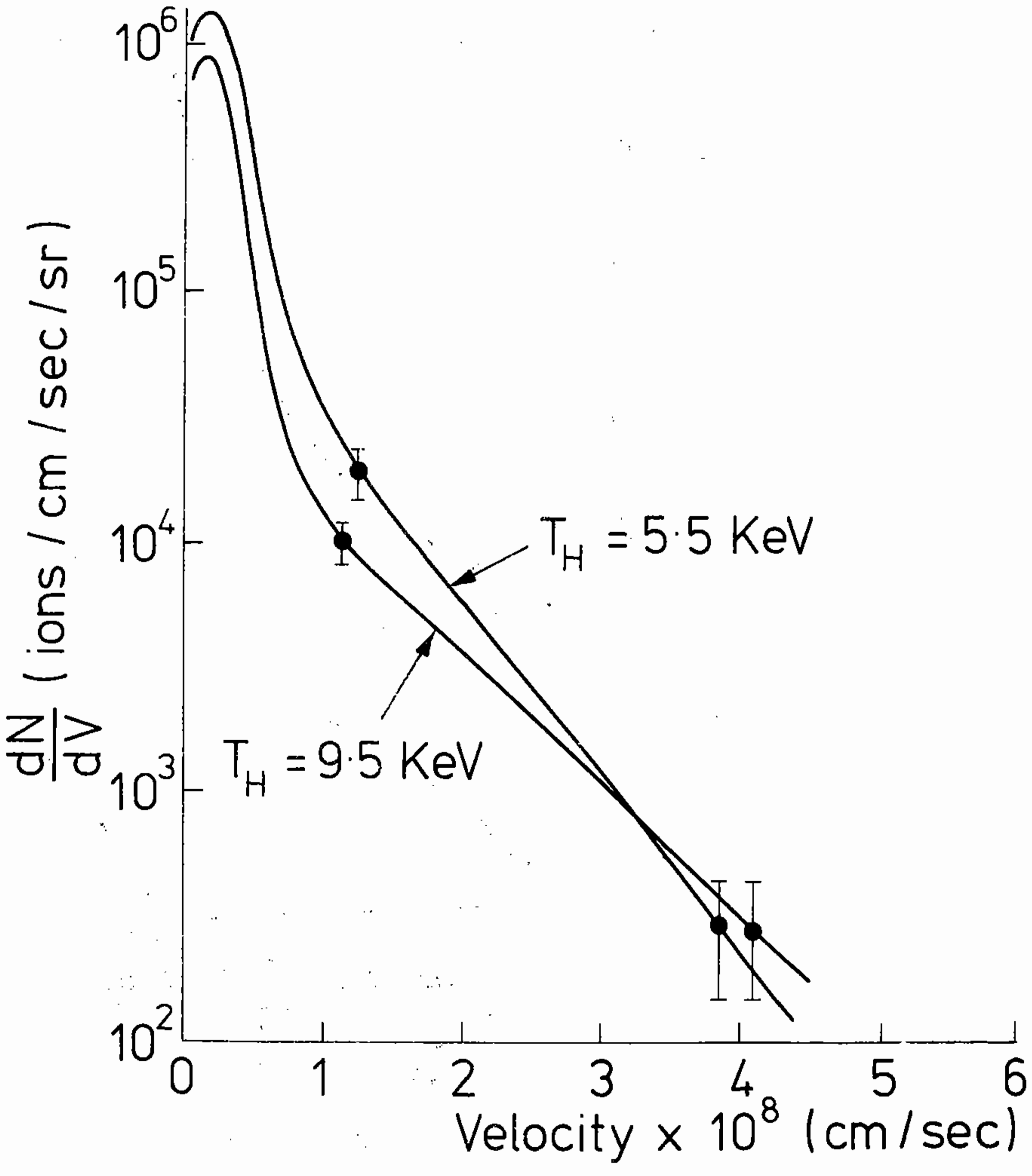

ION ENERGY SPECTRA

For two different detectors on shot 76

FIG. 304

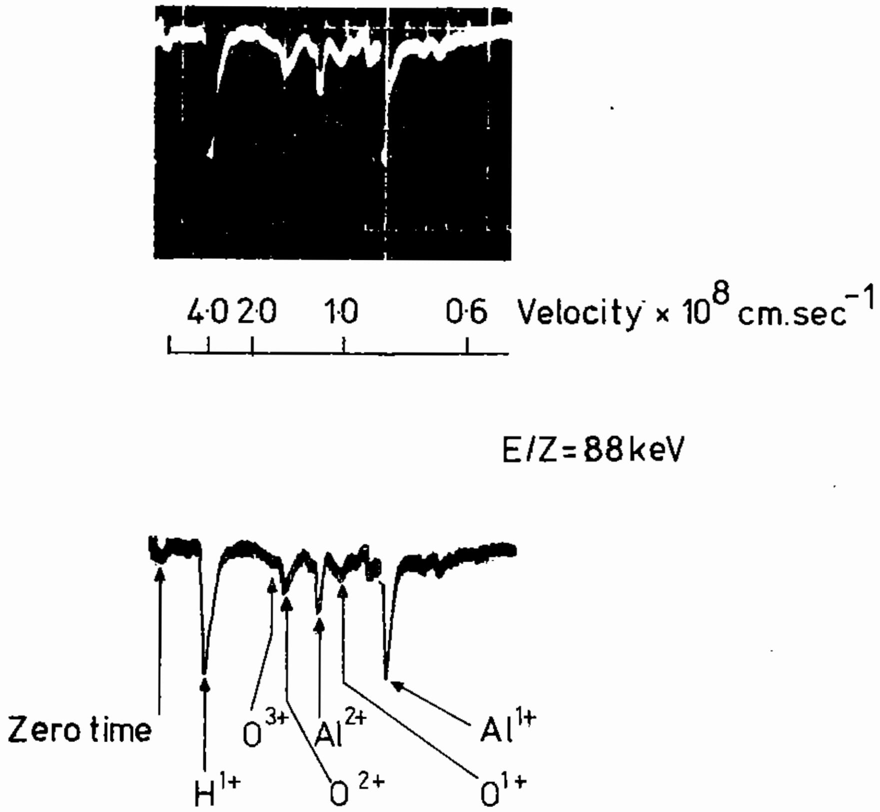

90^0 ELECTROSTATIC M/Z ANALYSER OUTPUT FOR TYPICAL MICROBALLOON SHOT, SHOWING PRESENCE OF PROTONS THAT ORIGINATE FROM IMPURITIES ON THE WALL.

FIG. 305

RUTHERFORD

From compression shot 73
energy = 17·9 Joules on target
absorption fraction 16 ± 9 %

X-ray pinhole photograph in plane (1)

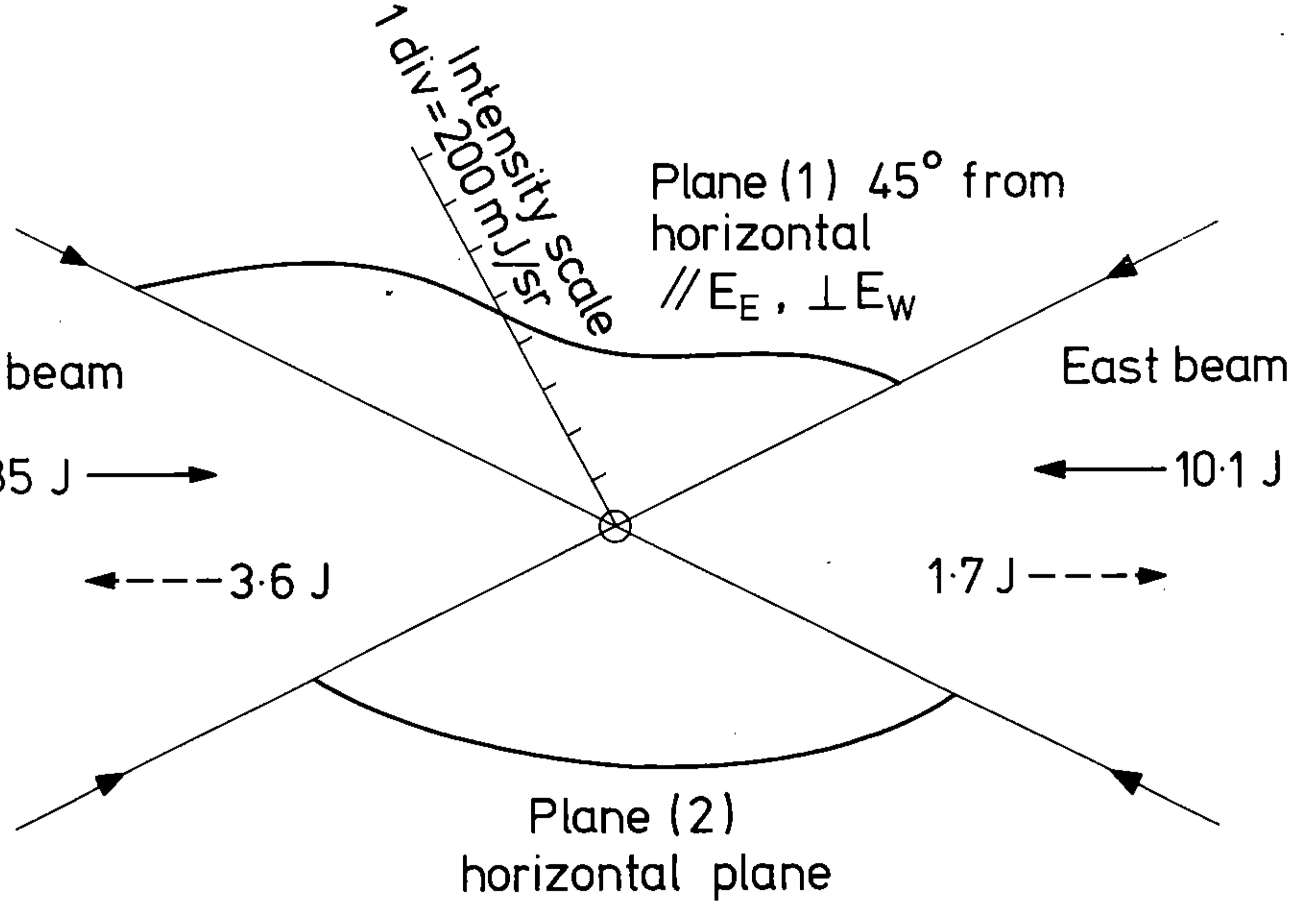

REPRESENTATIVE POLAR PLOT OF SCATTERED ENERGY AT 1·06 μm

FIG. 306

BELFAST - ESSEX

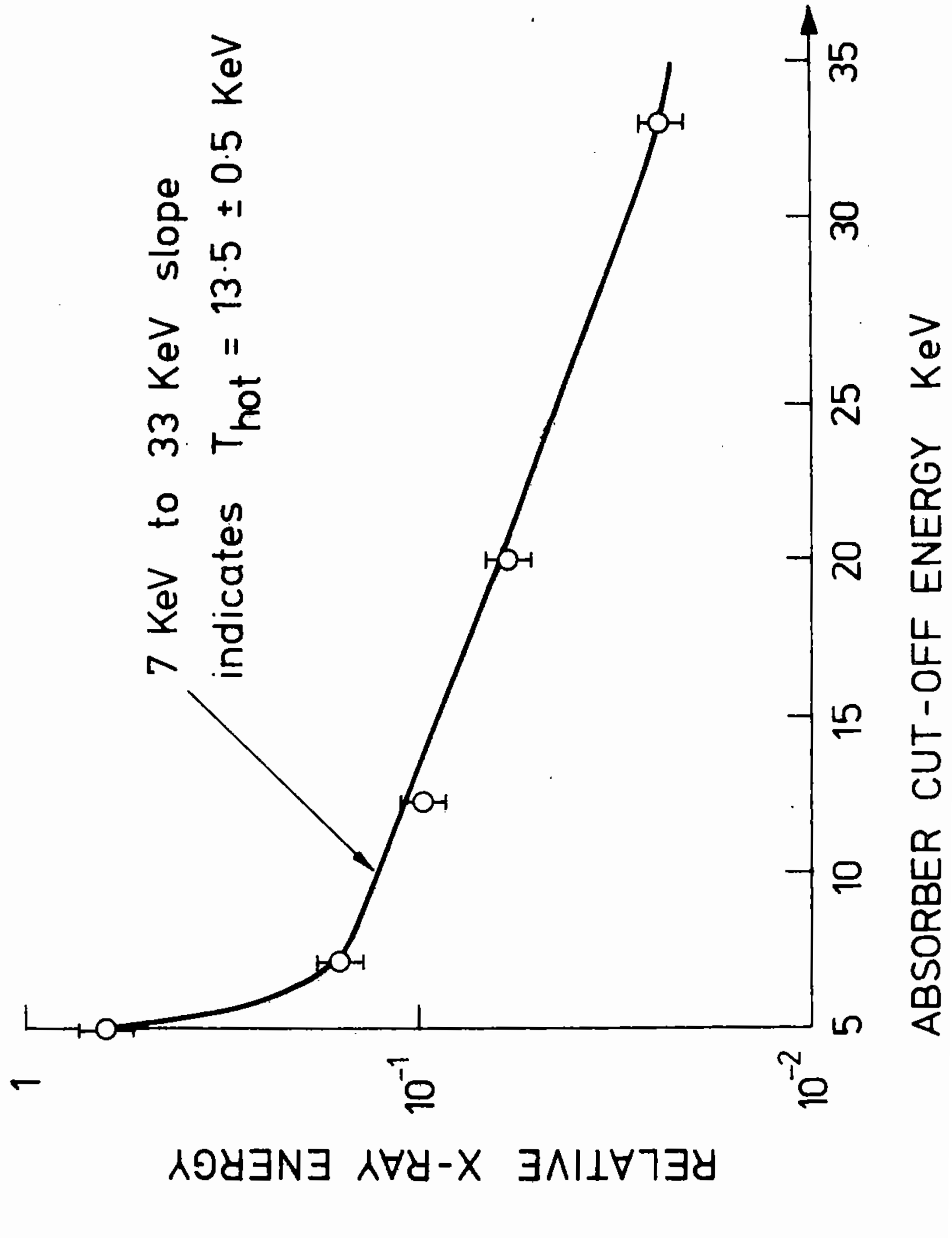

FIG. 307

ESSEX

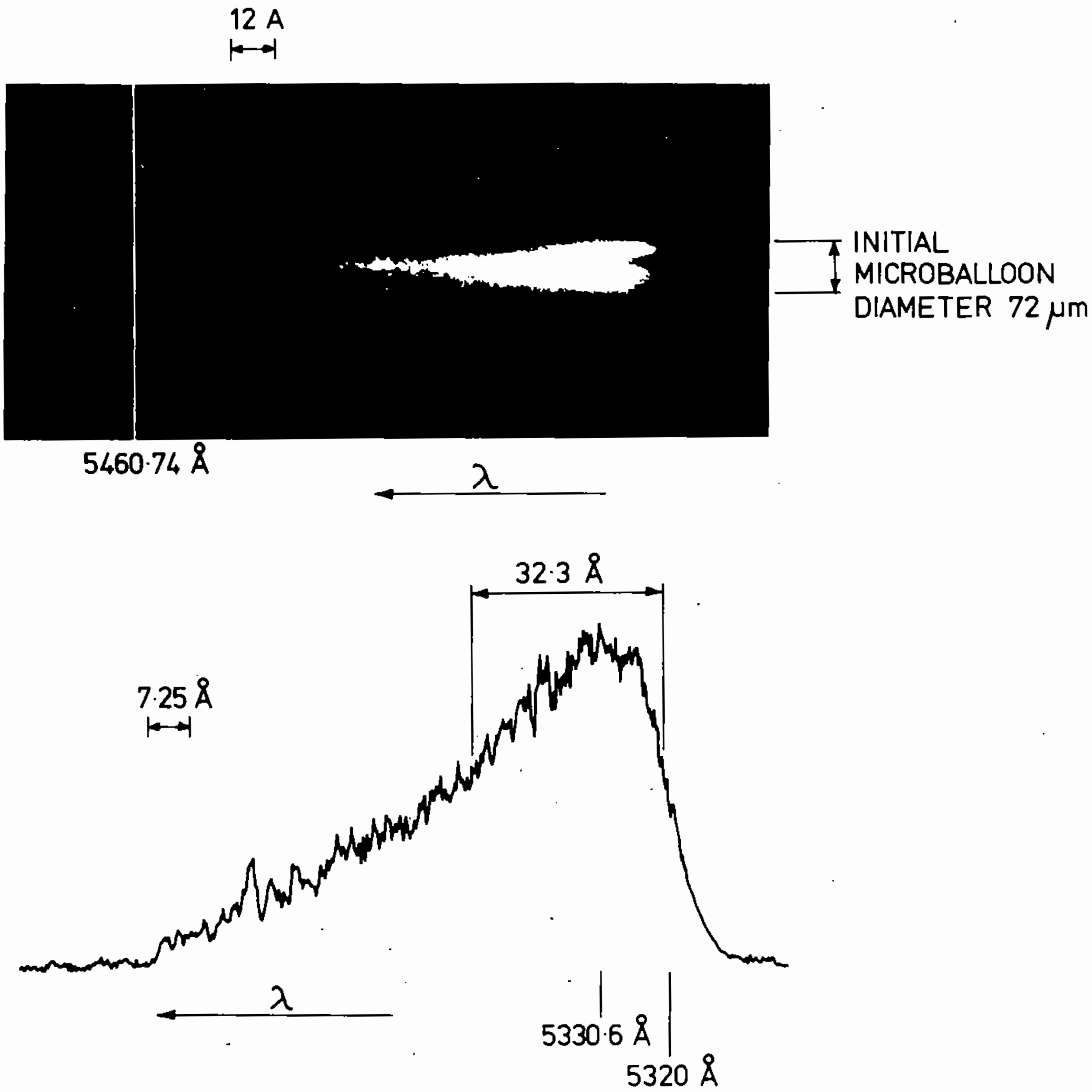

Shot 16

SPACE RESOLVED $2\omega_o$ SPECTRUM

FIG. 308

ESSEX - ROYAL HOLLOWAY

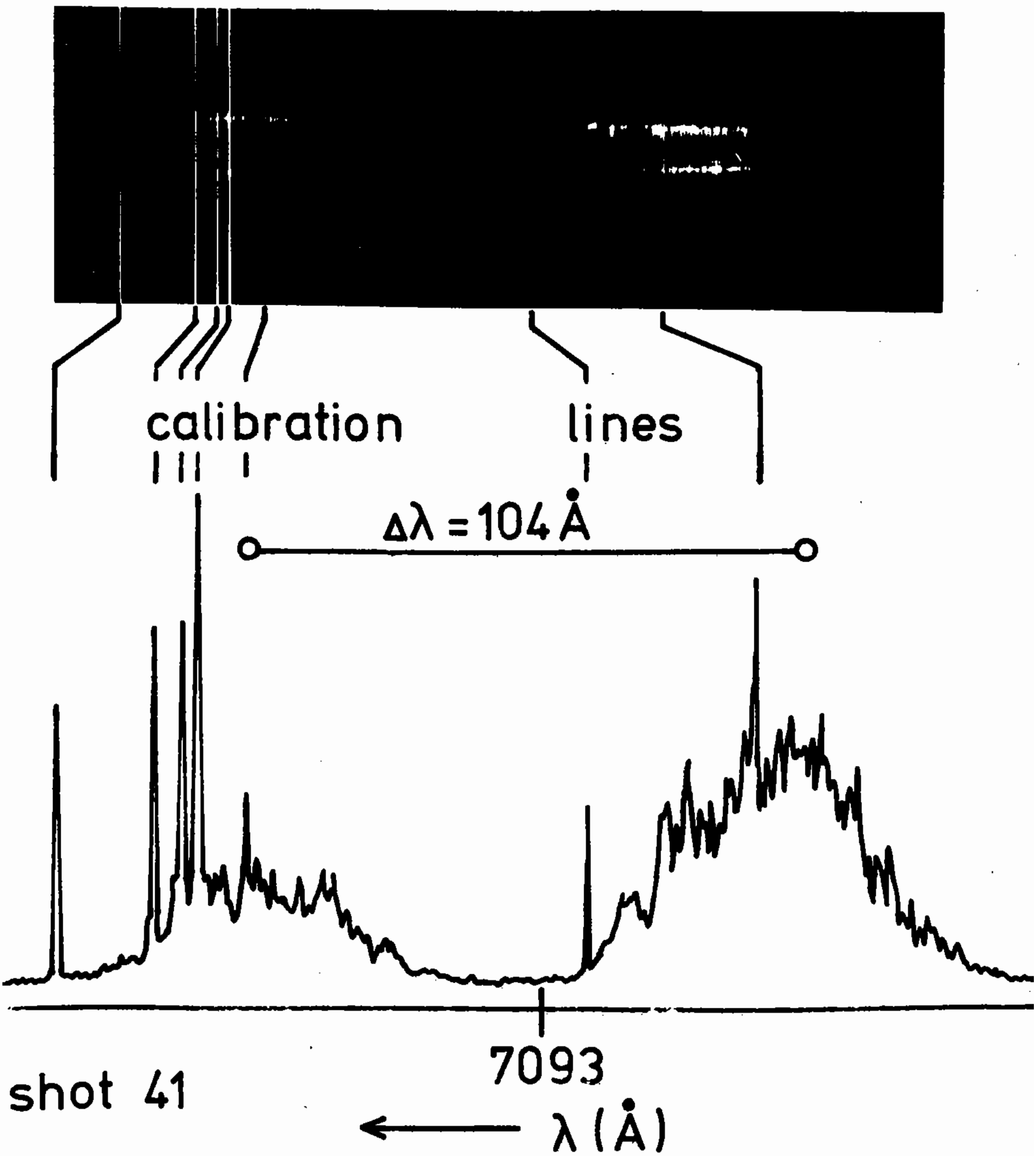

FIG. 309

RUTHERFORD - OXFORD

HARMONIC PHOTOGRAPHY

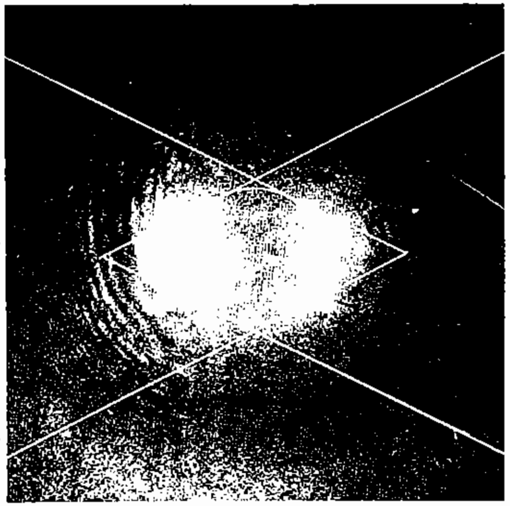

$2\omega_o$ $\frac{3}{2}\omega_o$

horizontally polarized emission

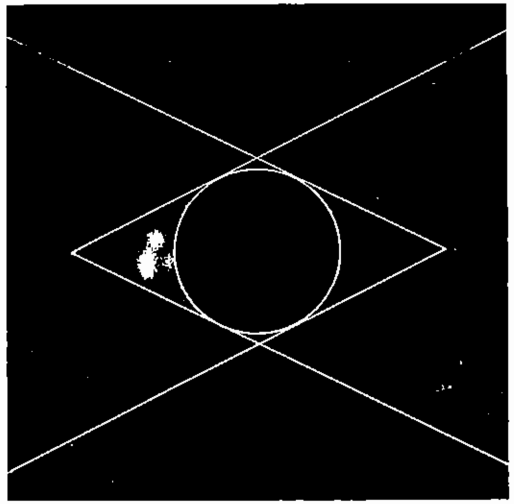

East Beam 8·5 J

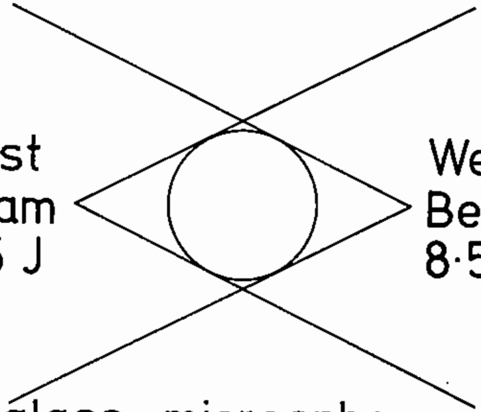

West Beam 8·5 J

glass microsphere
75 μm dia, 1·1 μm wall

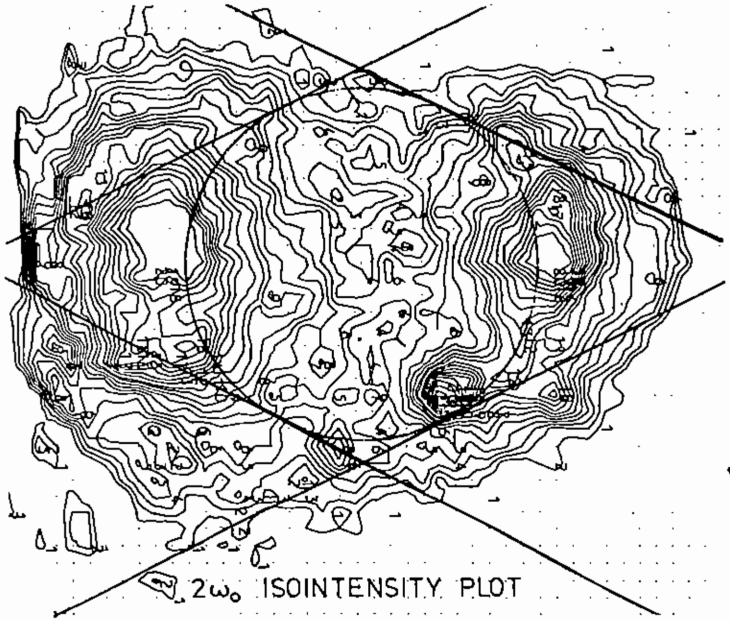

$2\omega_o$ $\frac{3}{2}\omega_o$

vertically polarized emissior

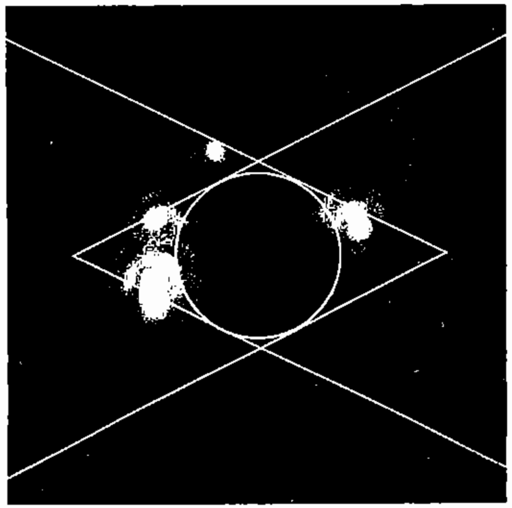

SIMULTANEOUS SIDE-ON PHOTOGRAPHS OF TARGET TAKEN IN EMITTED GREEN ($2\omega_o \equiv 530$ nm) AND RED ($\frac{3}{2}\omega_o \equiv 710$ nm) LIGHT

FIG. 310

RUTHERFORD - BELFAST

SPACE RESOLVED X-RAY SPECTRUM

8·5 bar NEON filled microballoon

Initial microballoon diameter 70·5 μm wall thickness 0·82 μm

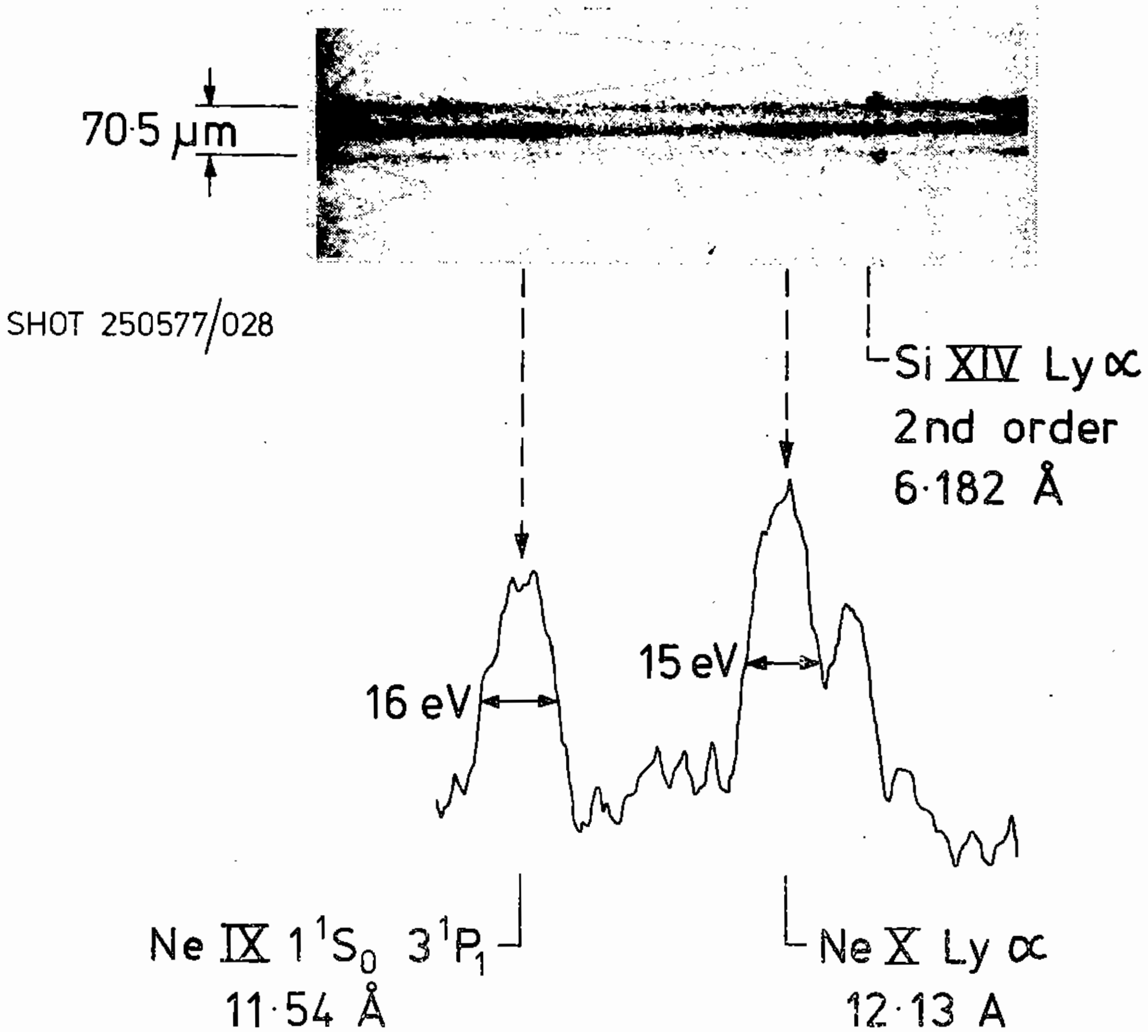

IMPLOSION CORE SPECTRUM

FIG. 311

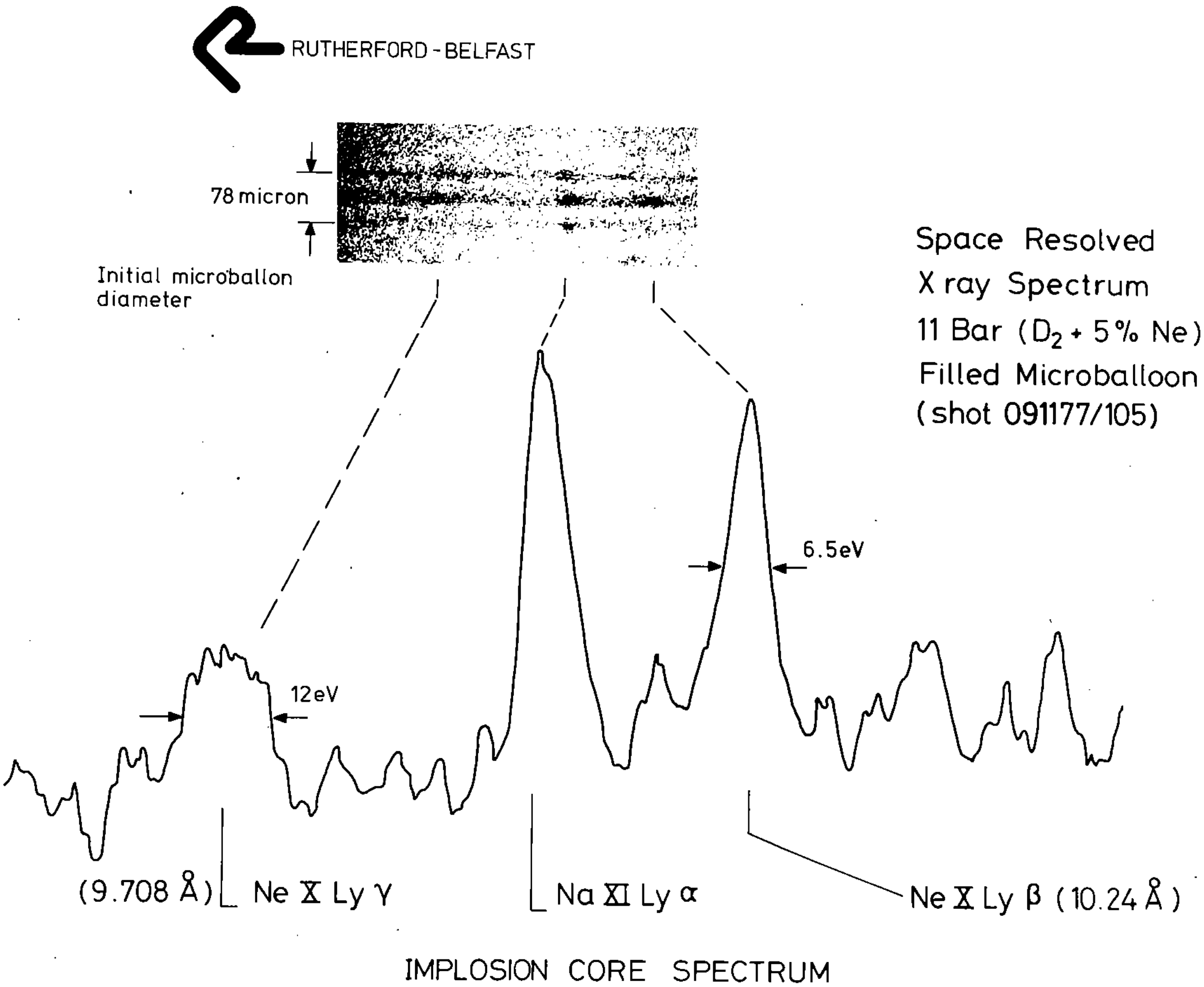
RUTHERFORD - BELFAST
78 micron
Initial microballon diameter
Space Resolved
X ray Spectrum
11 Bar (D_2 + 5 % Ne)
Filled Microballoon
(shot 091177/105)
12eV
6.5eV
(9.708 Å) Ne X Ly γ
Na XI Ly α
Ne X Ly β (10.24 Å)
IMPLOSION CORE SPECTRUM

FIG. 312

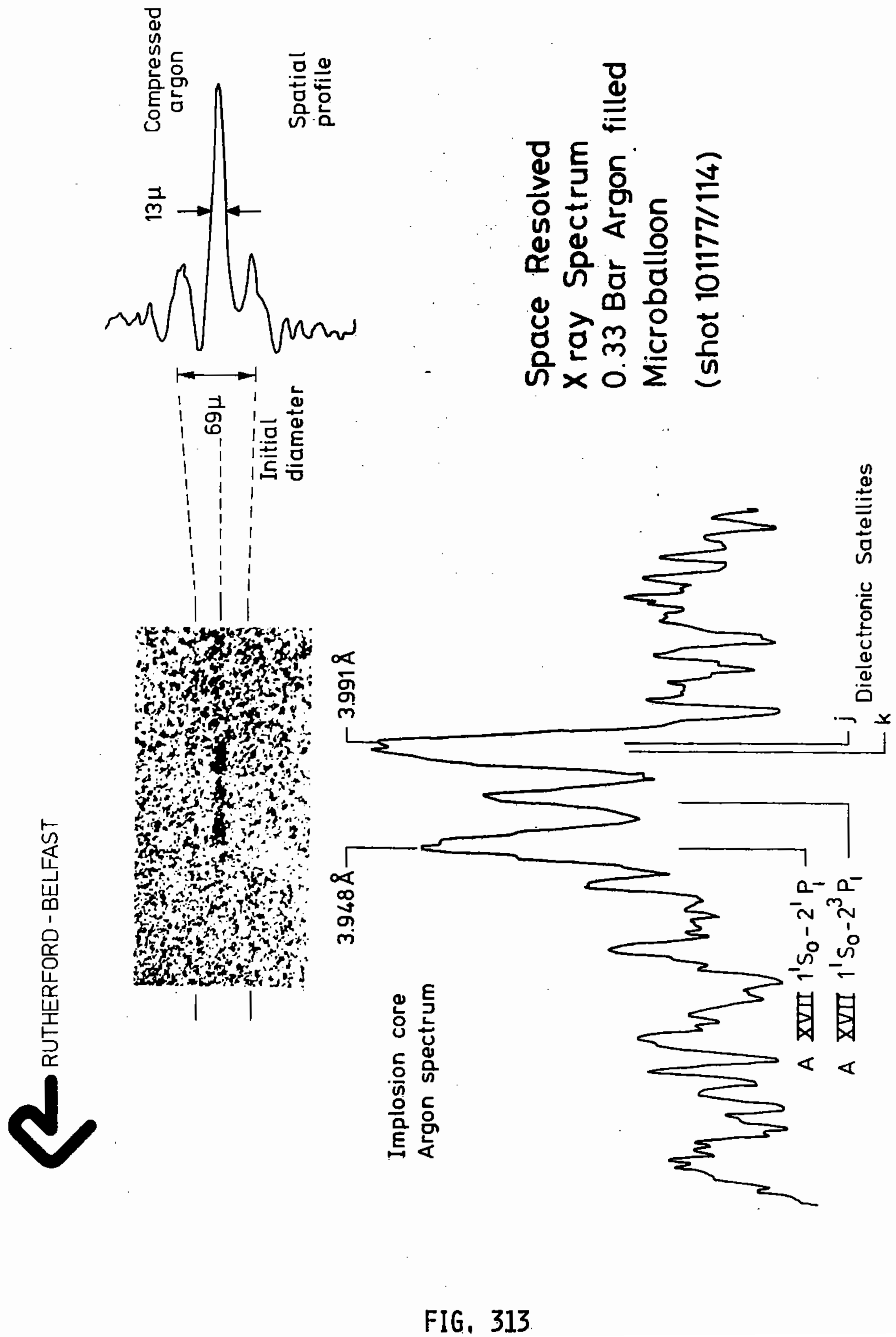

RUTHERFORD-BELFAST
Compressed argon
Spatial profile
13μ
69μ
Initial diameter
Space Resolved
X ray Spectrum
0.33 Bar Argon filled
Microballoon
(shot 101177/114)
3.948 Å
3.991 Å
Implosion core
Argon spectrum
A XVII $1^1S_0-2^1P_1$
A XVII $1^1S_0-2^3P_1$
j
k
Dielectronic Satellites

FIG. 313

RUTHERFORD

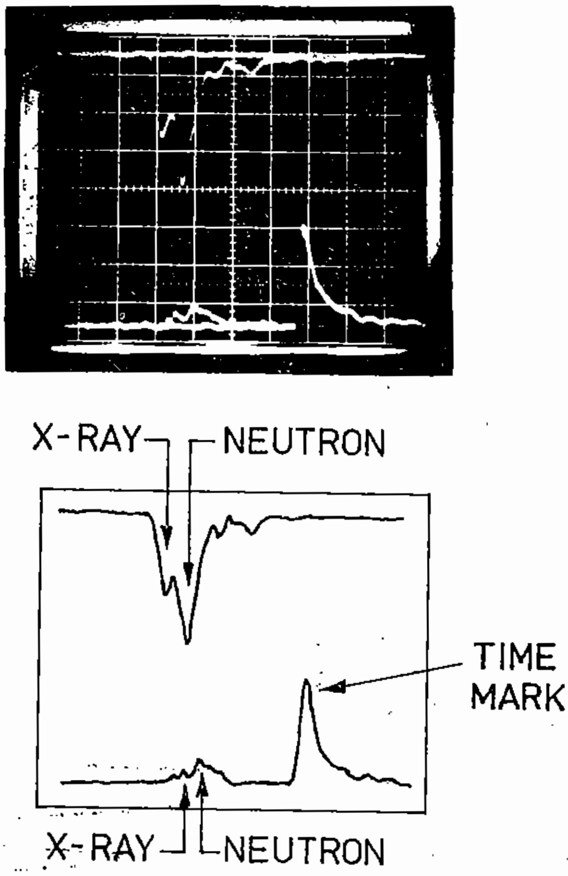

DT TARGET

FIG. 314

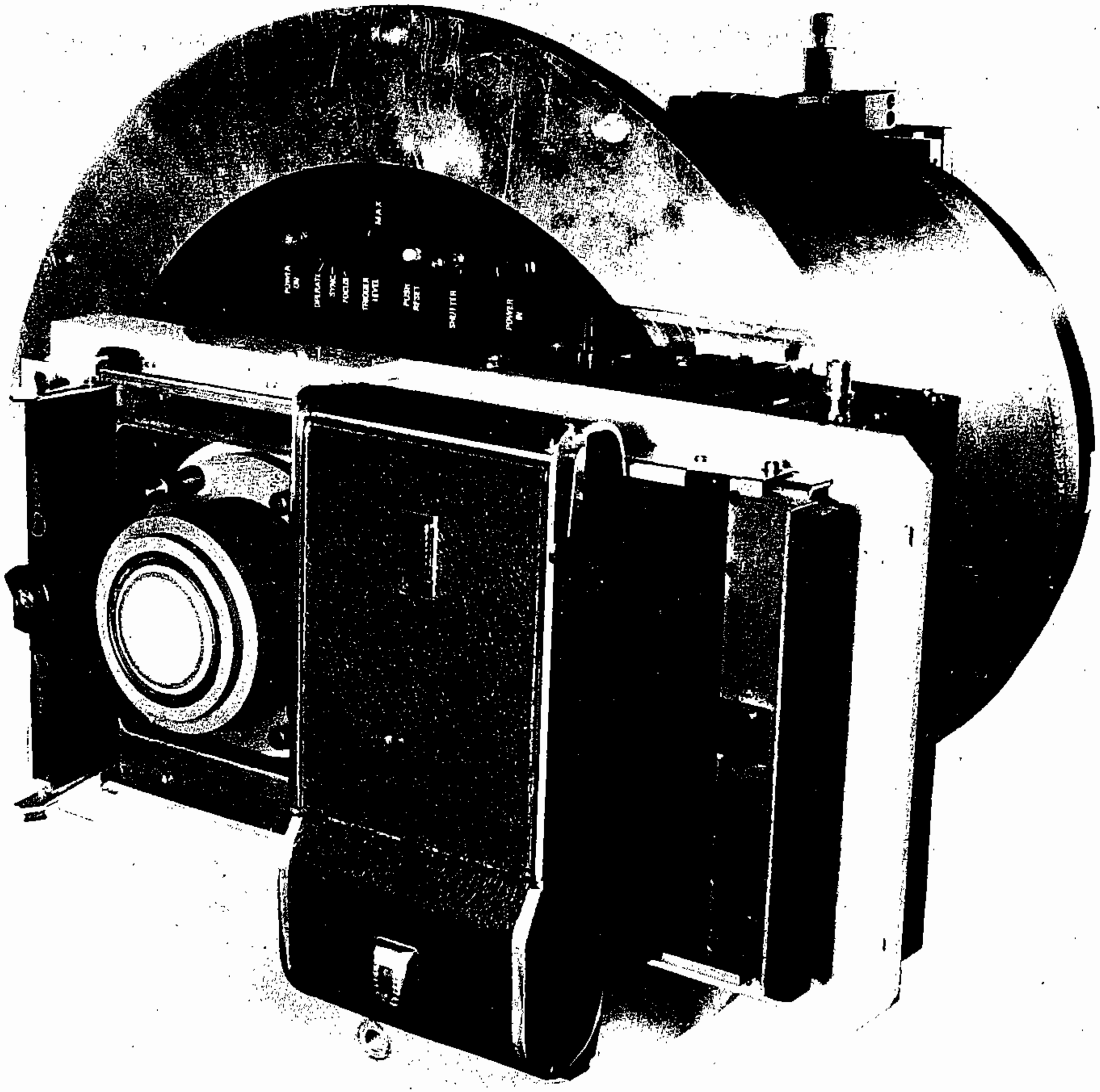

<u>X-ray streak camera</u> assembled in re-entrant vacuum flange. View from the output end showing fibre optic coupled image intensifier camera. Pinhole imaging apparatus is seen at the input end.

[Camera manufactured by Hadland Photonics Ltd.]

FIG. 315

RUTHERFORD-BELFAST-IMPERIAL COLLEGE

a) 8.4 JOULES PER BEAM IN 100 Psec PULSE ON EMPTY GLASS MICRO BALLOON OF DIAMETER 70 MICRONS AND WALL THICKNESS 1.28 MICRONS

b) 7.6 JOULES PER BEAM IN 100 Psec PULSE ON $D_2 + T_2$ FILLED GLASS MICRO BALLOON OF DIAMETER 88 MICRONS AND WALL THICKNESS 0.88 MICRONS

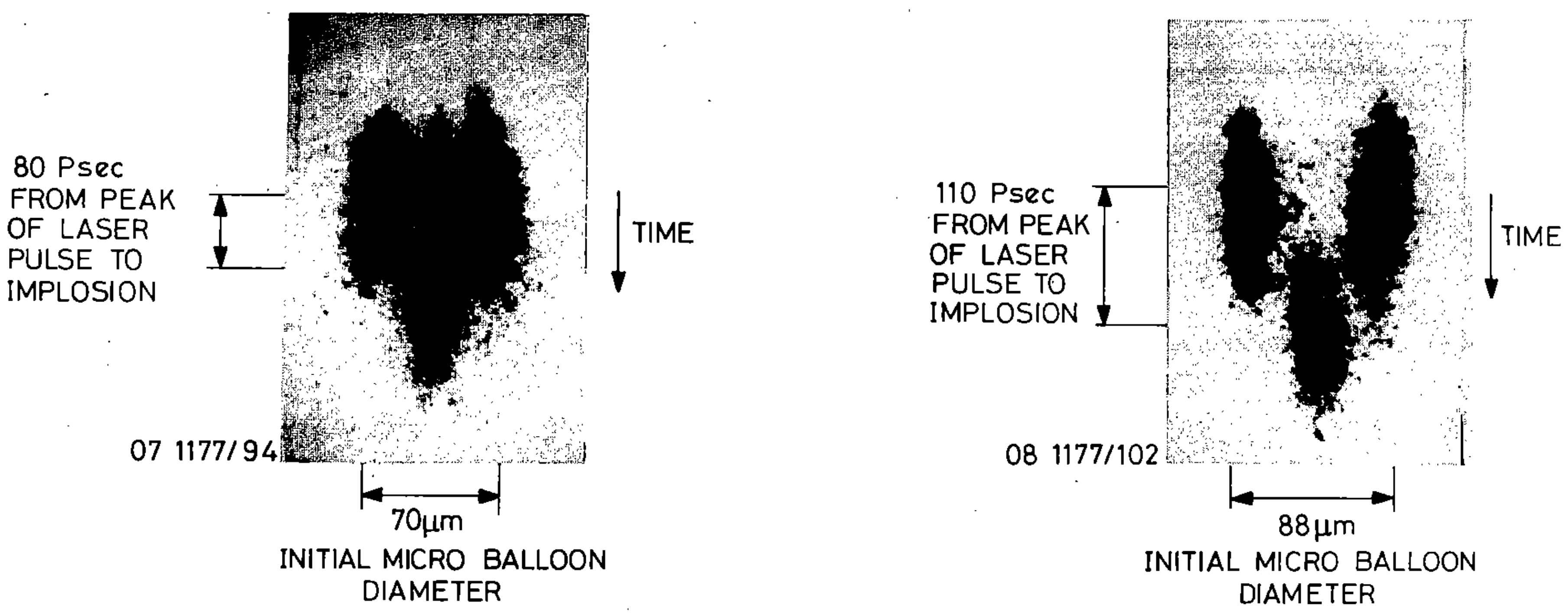

TIME AND SPACE RESOLVED X-RAY EMISSION FROM IMPLOSION OF (a) EMPTY AND (b) 10 BAR $D_2 + T_2$ FILLED GLASS MICRO BALLOONS

FIG. 316

RUTHERFORD-IMPERIAL COLLEGE

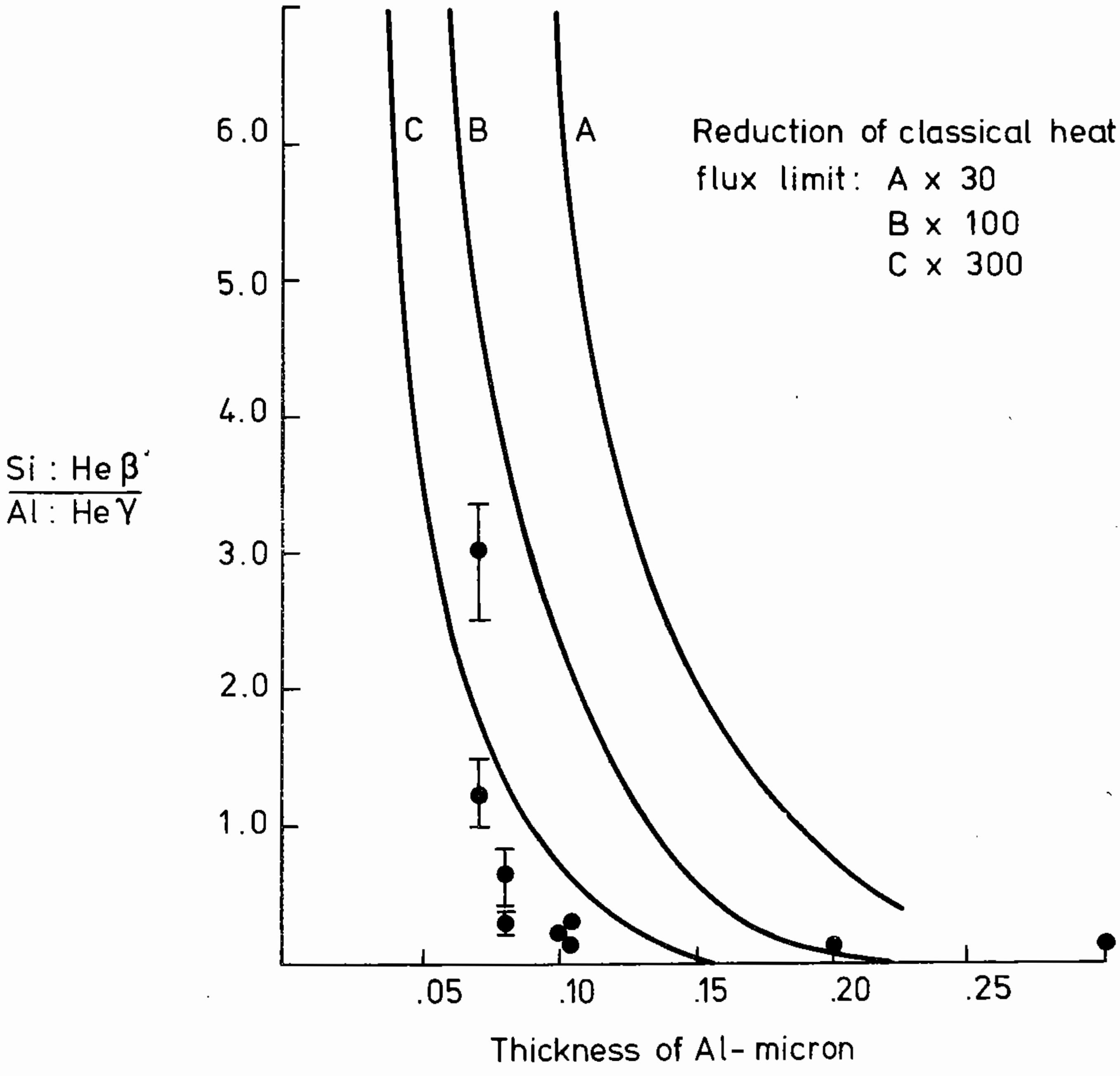

Relative Si XIII and Al XII emission from Al coated microballoons

FIG. 317

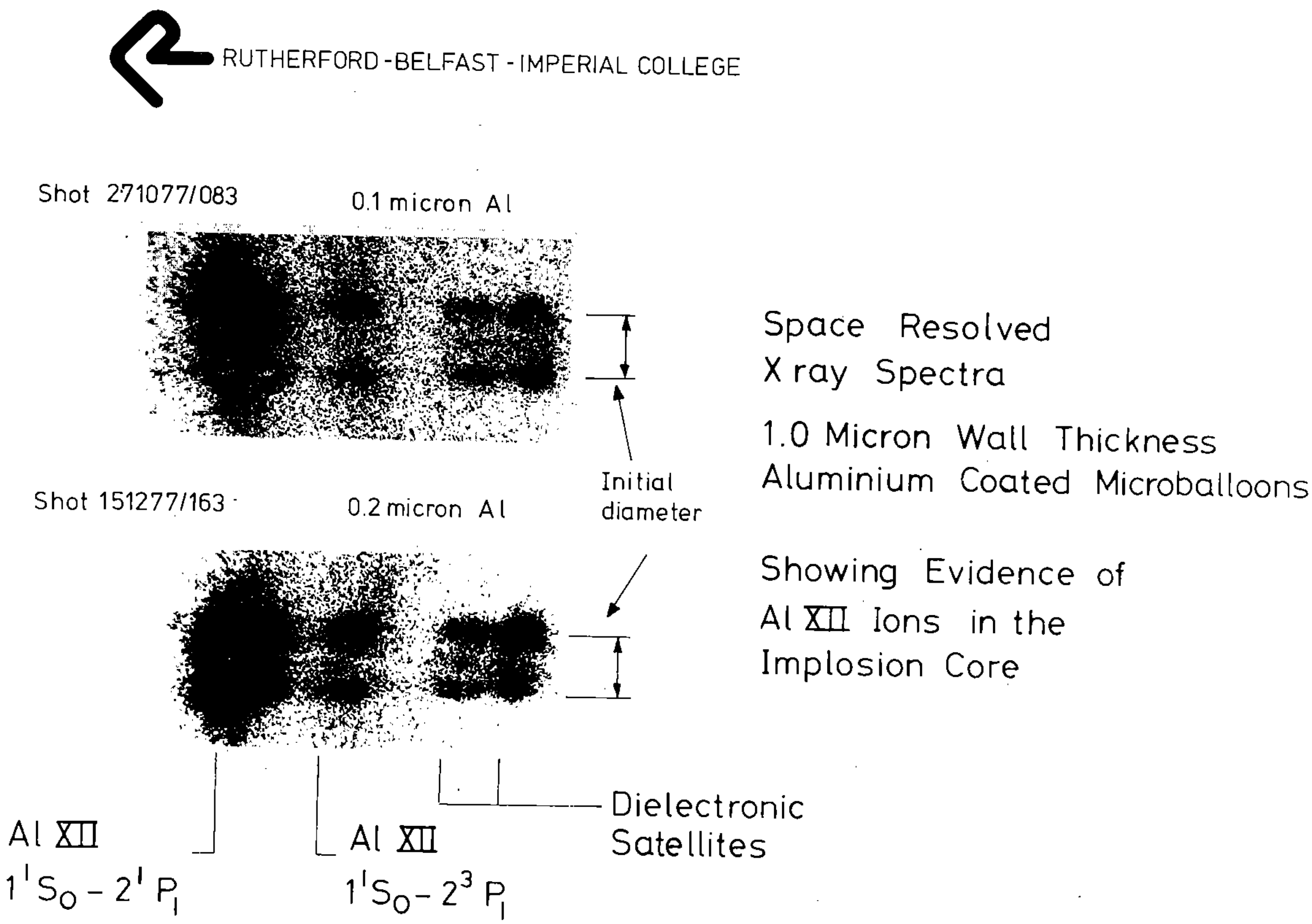

RUTHERFORD-BELFAST-IMPERIAL COLLEGE
Shot 271077/083
0.1 micron Al
Shot 151277/163
0.2 micron Al
Initial diameter
Space Resolved
X ray Spectra
1.0 Micron Wall Thickness
Aluminium Coated Microballoons
Showing Evidence of
Al XII Ions in the
Implosion Core
Dielectronic
Satellites
Al XII
1¹S₀ - 2¹P₁
Al XII
1¹S₀ - 2³P₁

FIG. 318

RUTHERFORD-BELFAST-ESSEX

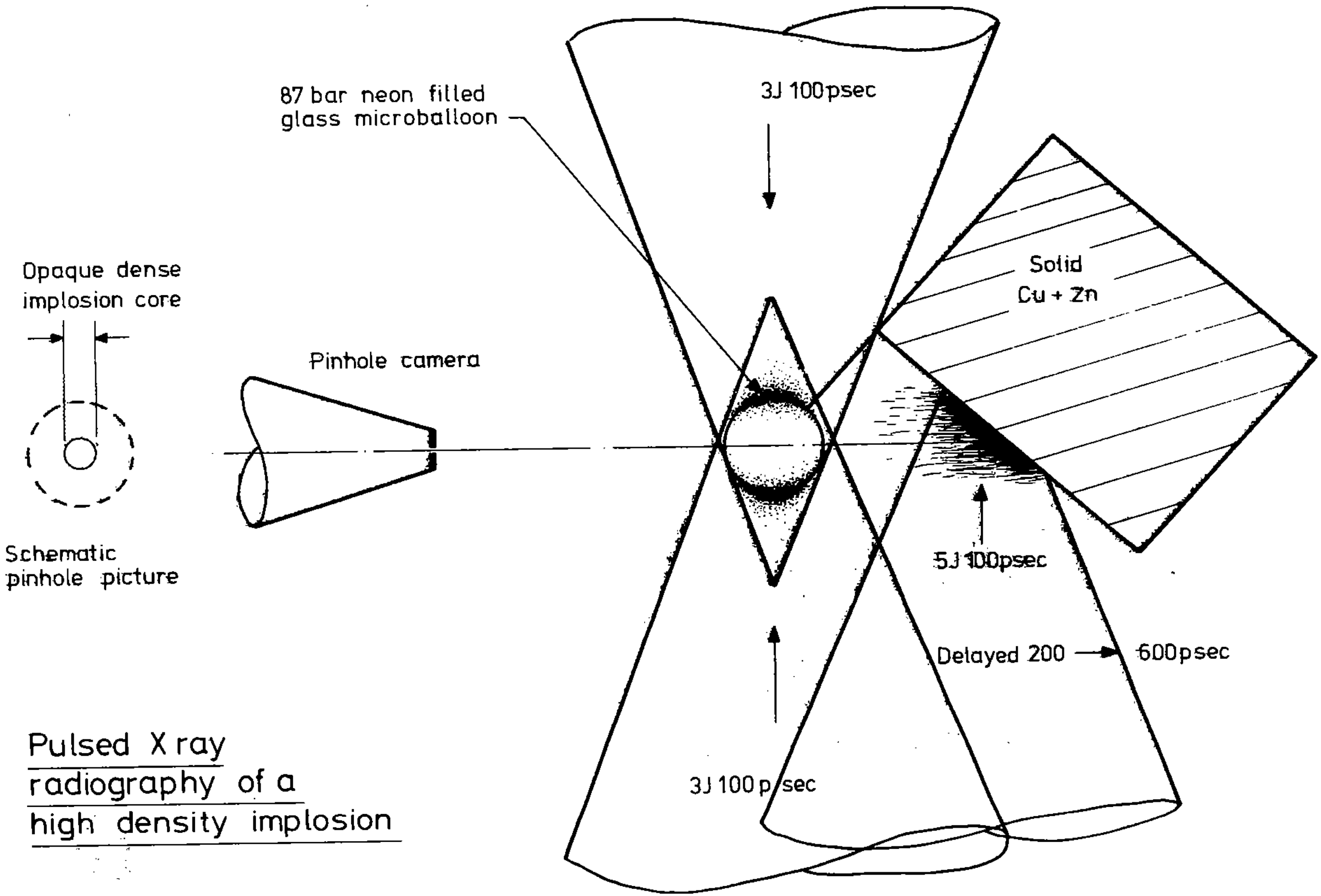

Pulsed X ray radiography of a high density implosion

FIG. 319

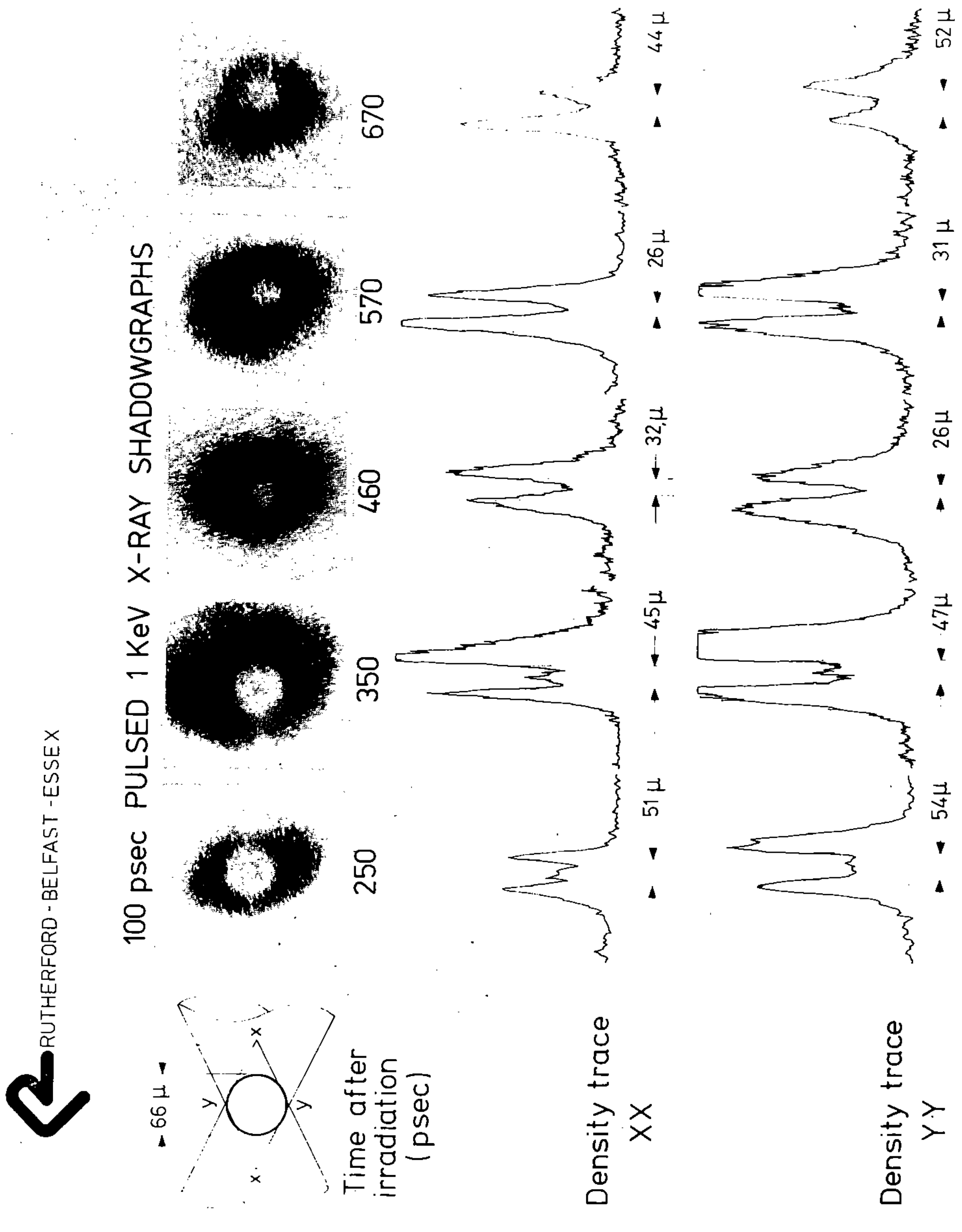

RUTHERFORD - BELFAST - ESSEX
100 psec PULSED 1 KeV X-RAY SHADOWGRAPHS
66 μ
Time after irradiation (psec)
250
350
460
570
670
Density trace XX
51 μ
45μ
32μ
26 μ
44 μ
Density trace YY
54μ
47μ
26μ
31 μ
52 μ

FIG. 320

RUTHERFORD

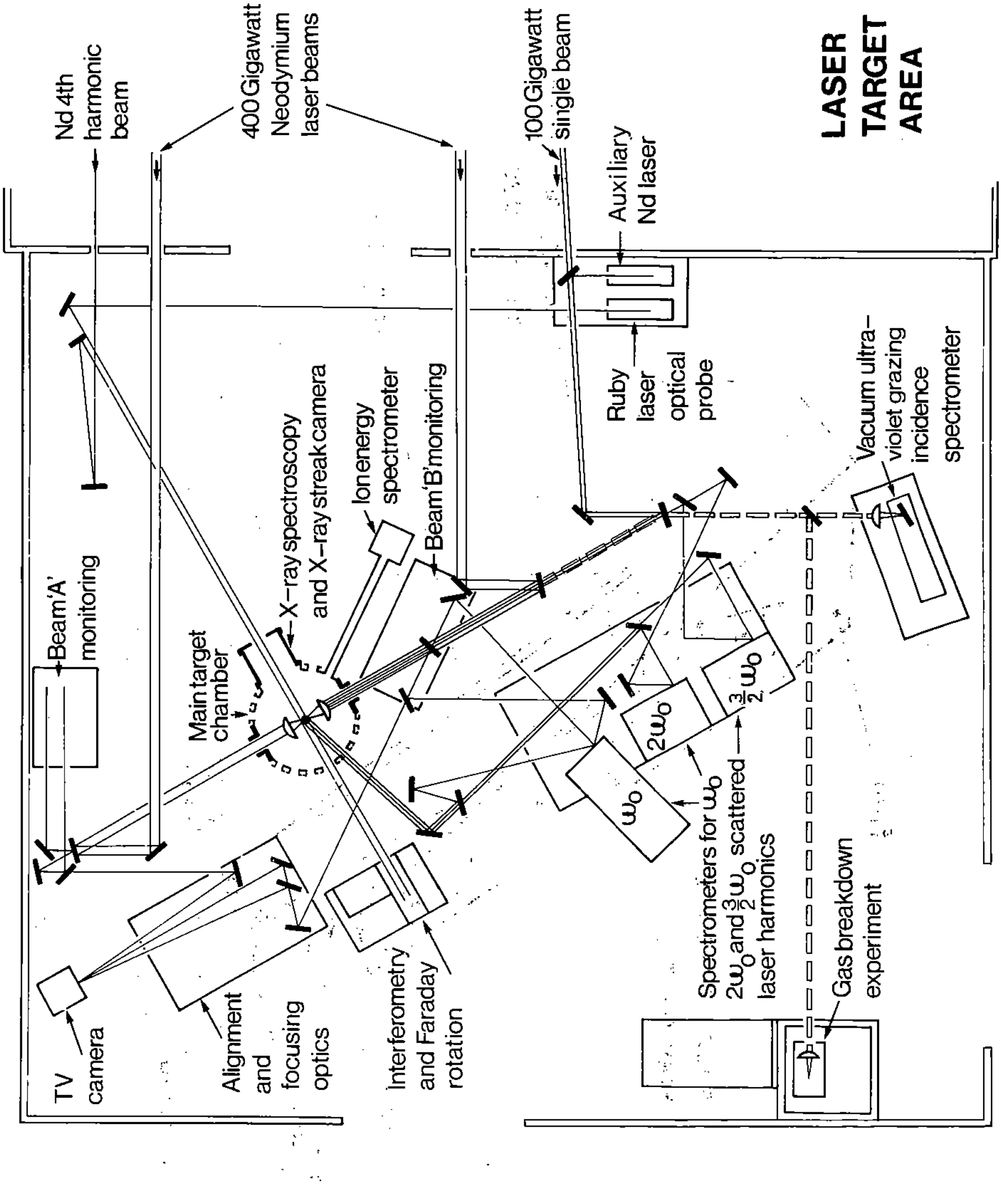

FIG. 321

BELFAST

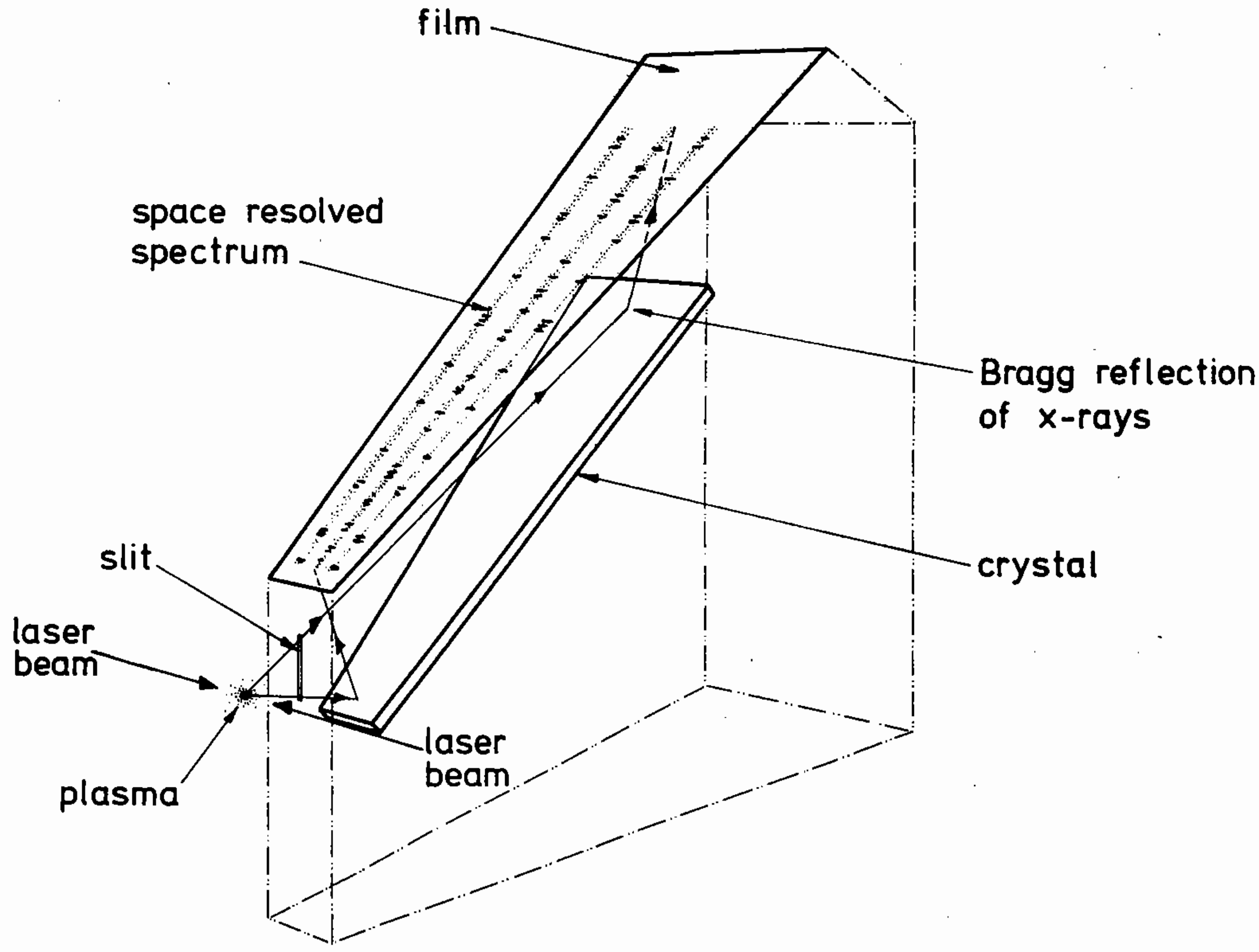

MINIATURE SPACE RESOLVING X-RAY SPECTROMETER

FIG. 322

BELFAST

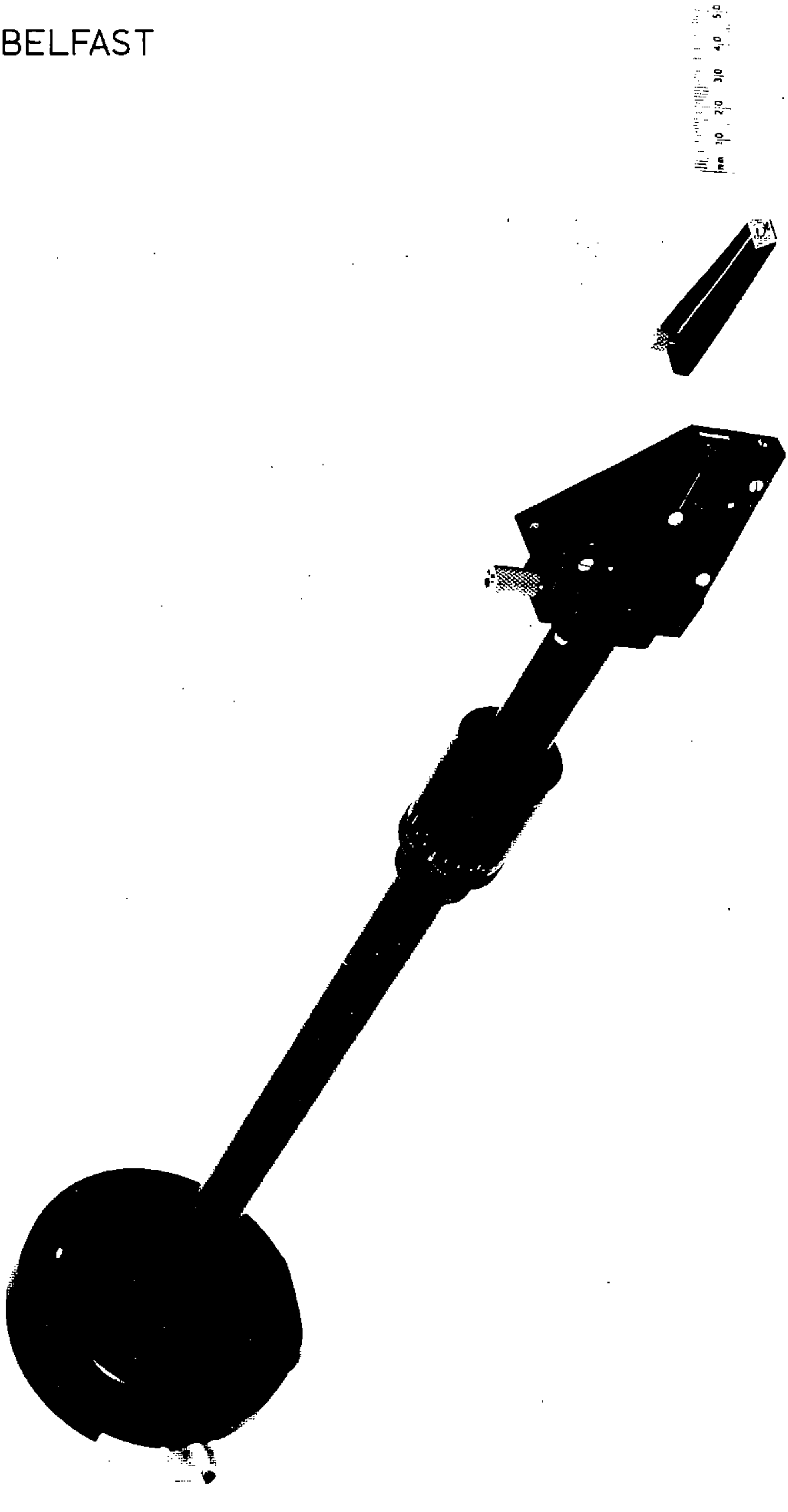

FIG. 323

BELFAST

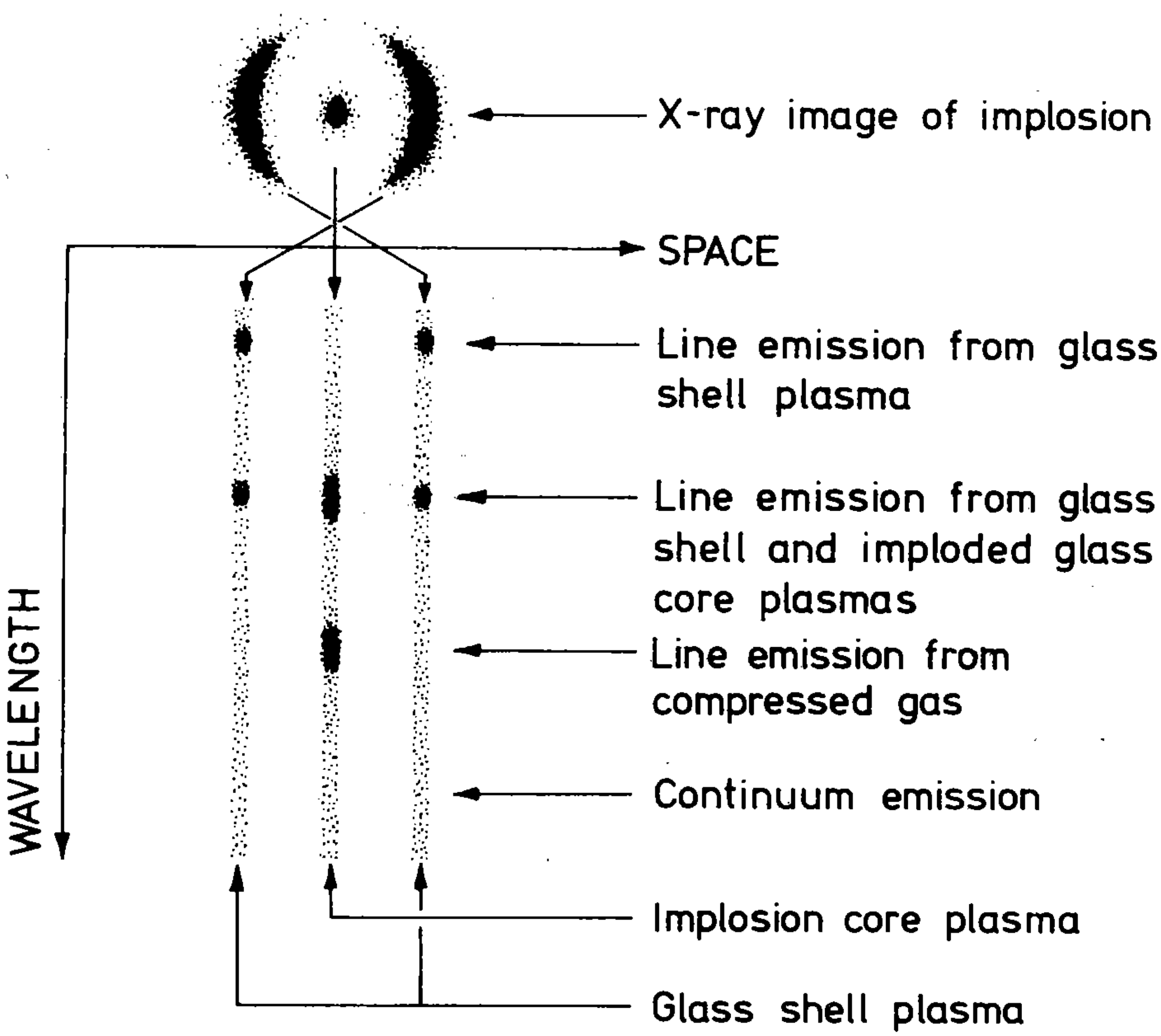

SCHEMATIC OF SPACE RESOLVED SPECTRUM

FIG. 324

RUTHERFORD - BELFAST

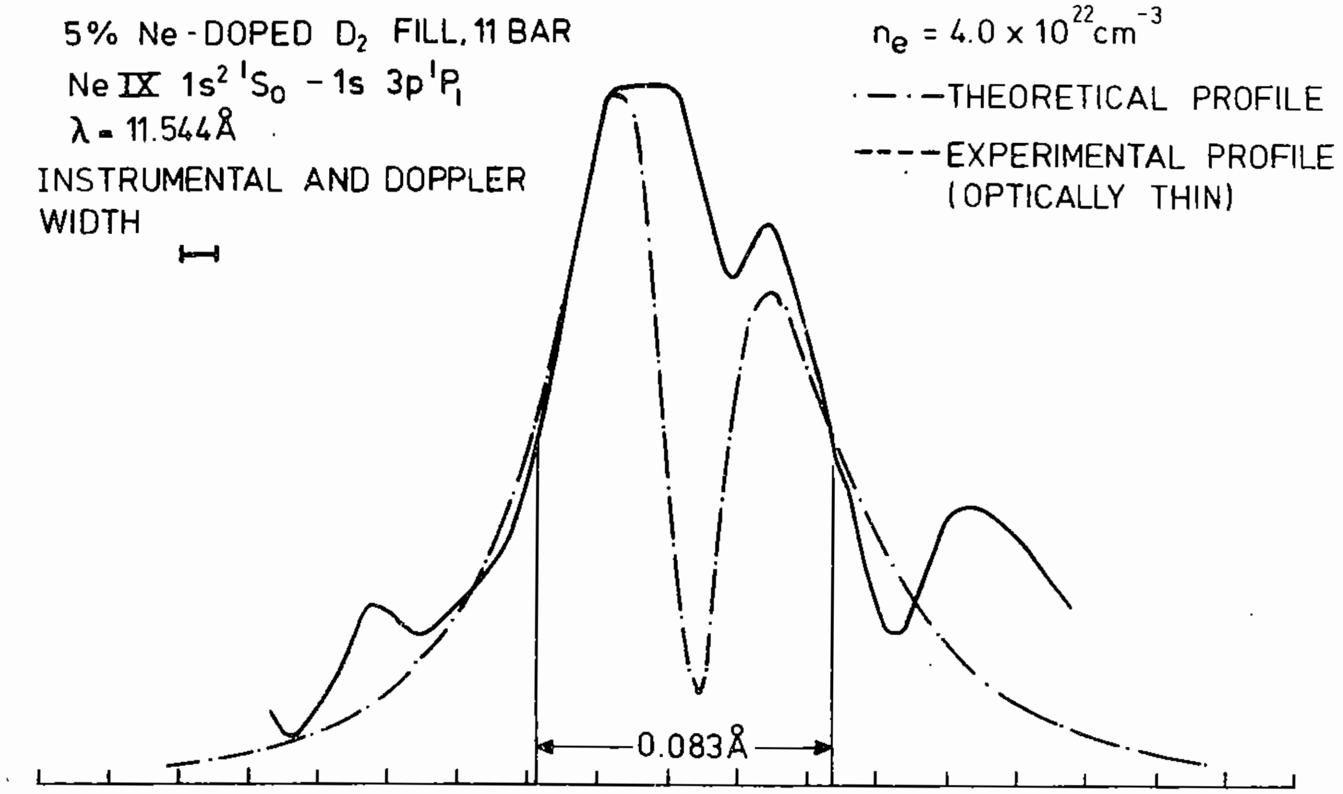

Imploded Gas Shot 091177/105

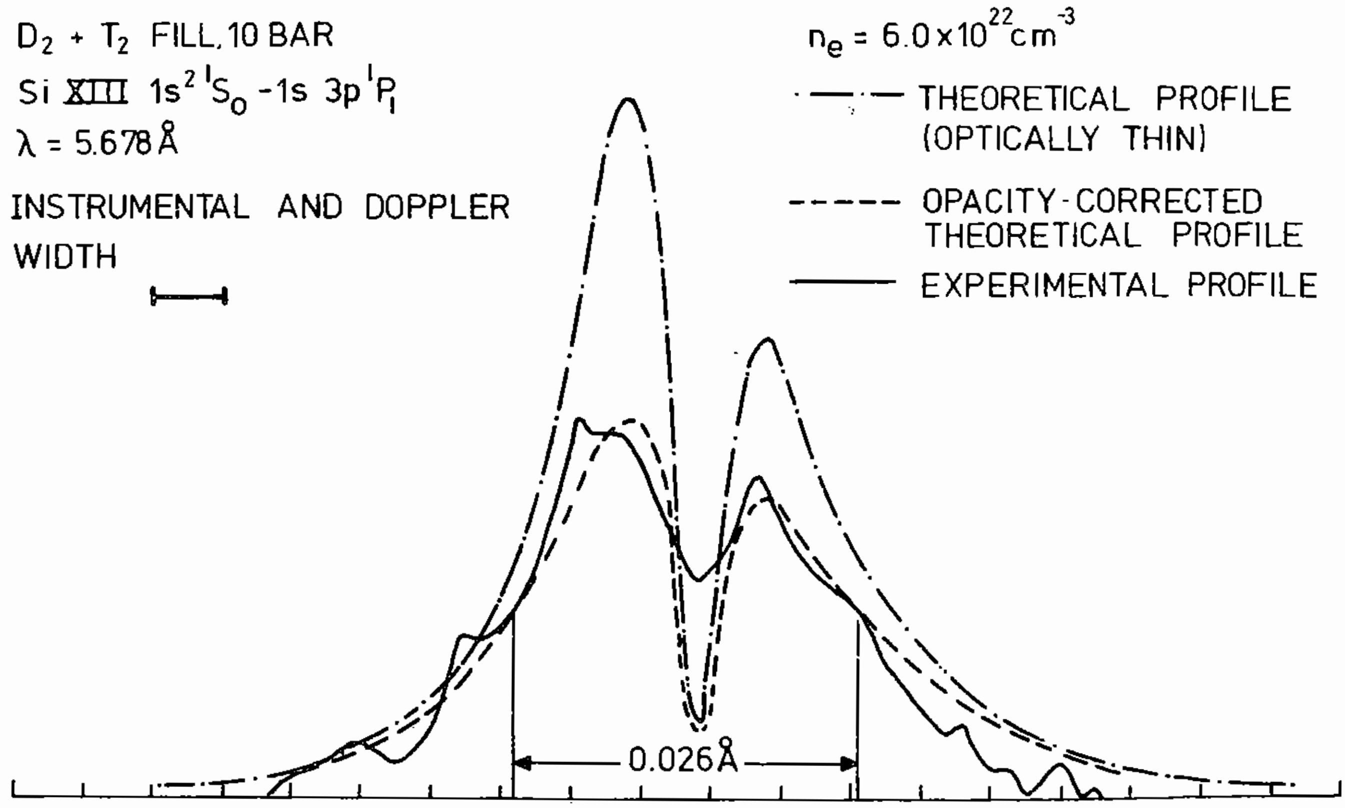

FIG. 325 Imploded Glass Shell Shot 081177/102

RUTHERFORD - BELFAST

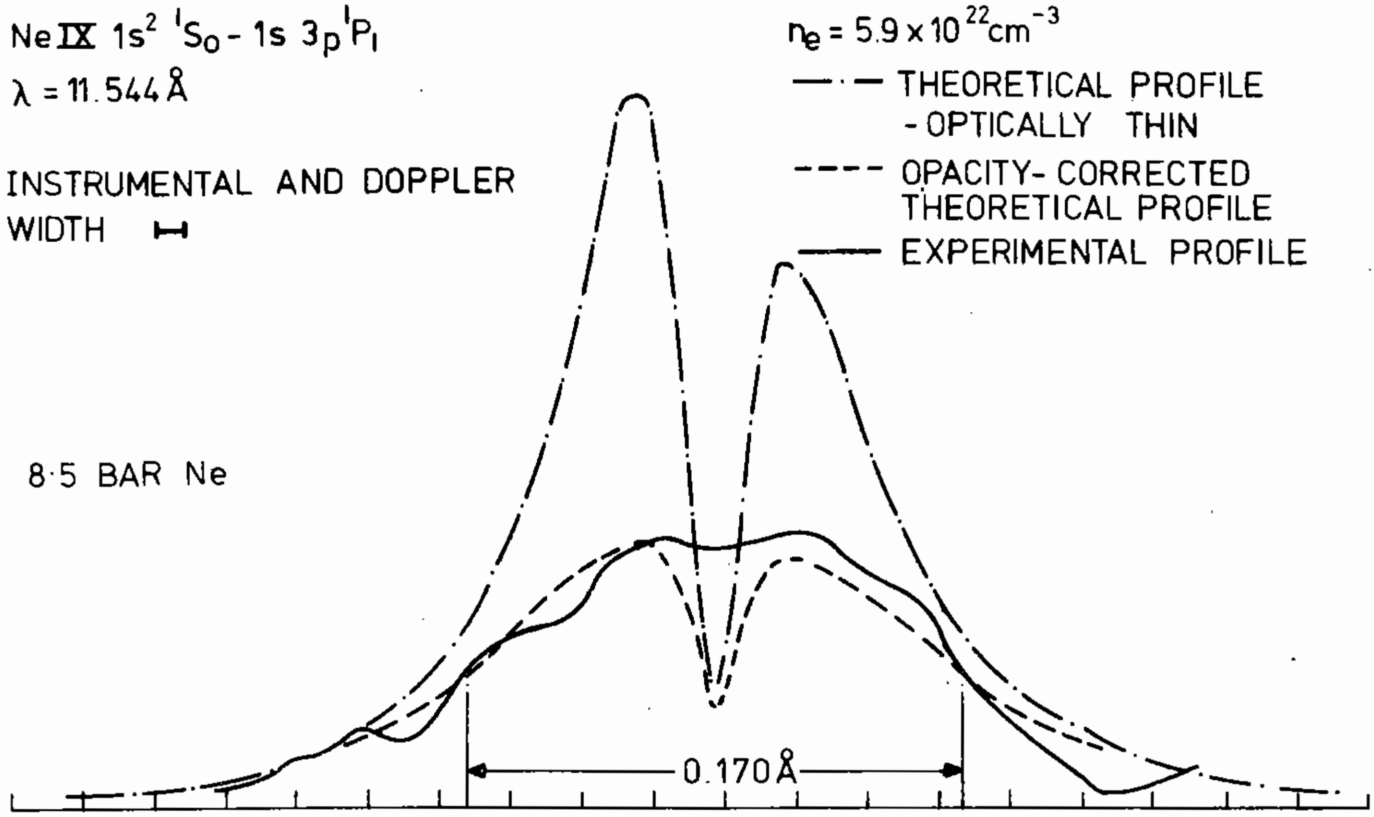

Imploded Gas Shot 250577/028

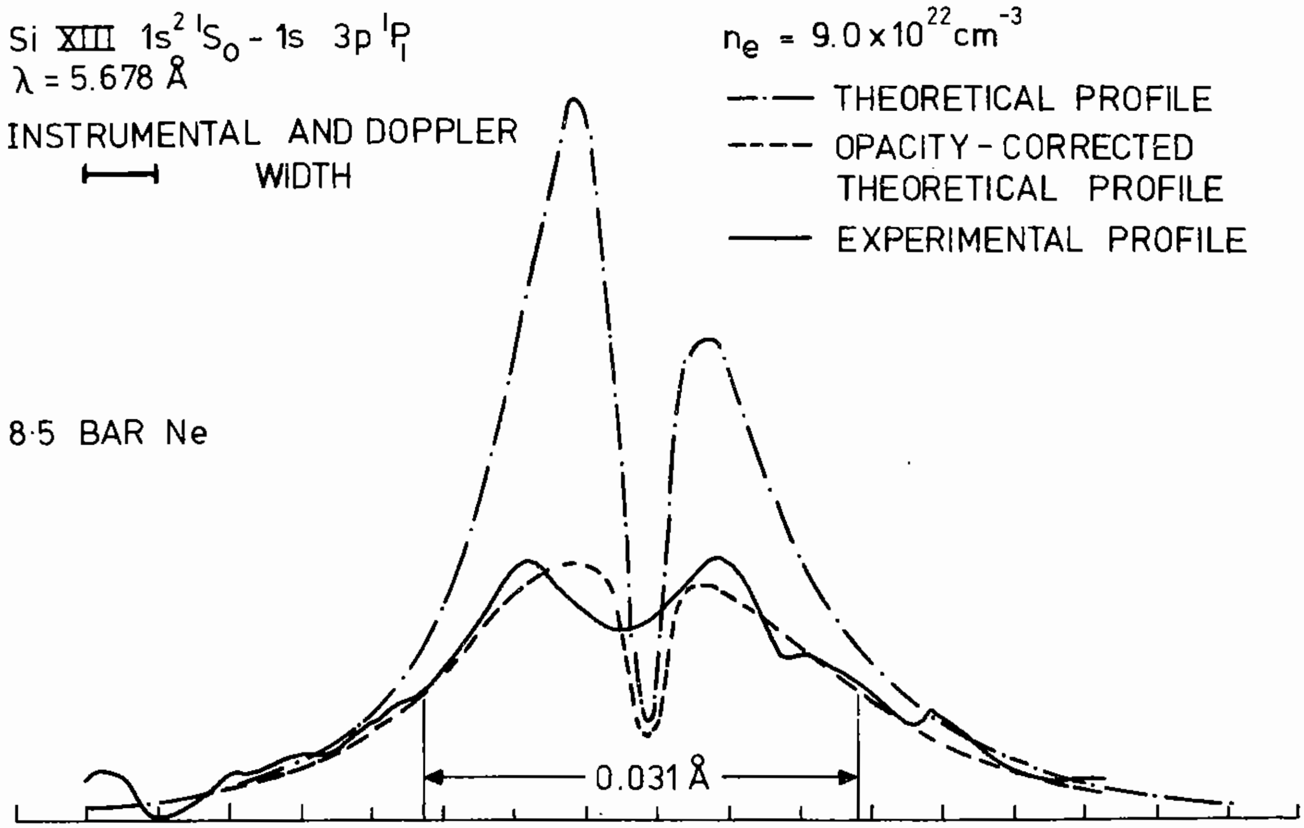

FIG. 326 Imploded Glass Shell Shot 250577/030

RUTHERFORD

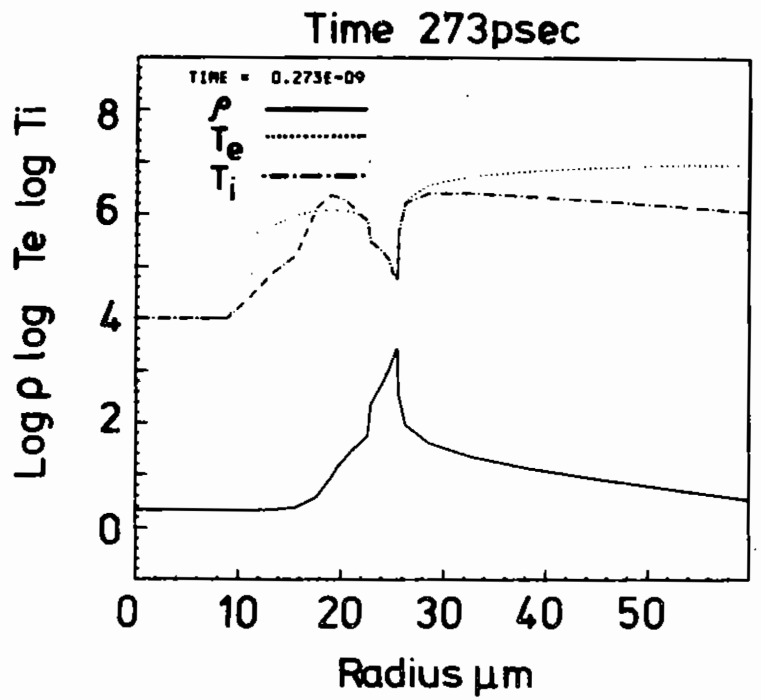

Ablative implosion:
No fast electron
energy transport

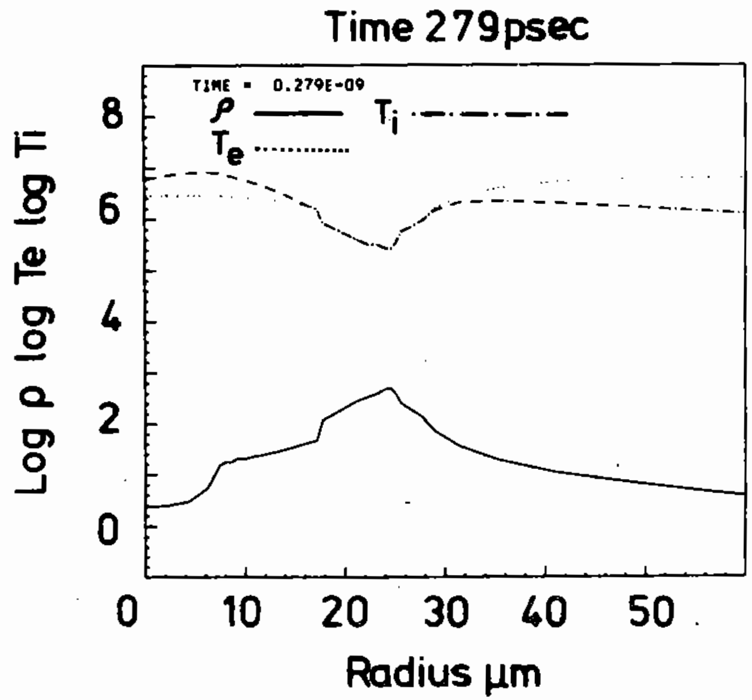

Exploding pusher:
With preheating by
fast electrons

FIG. 327

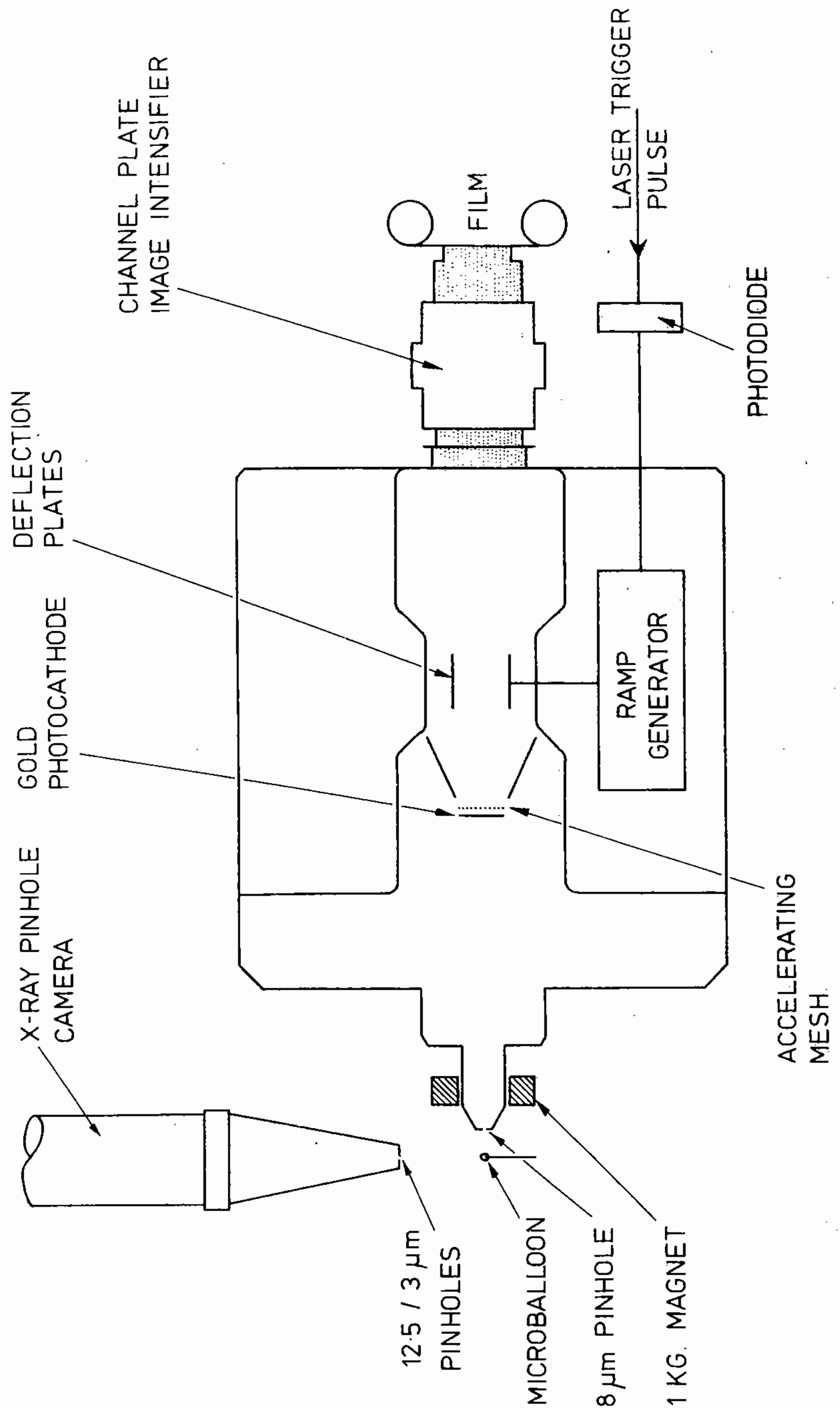
CHANNEL PLATE
IMAGE INTENSIFIER
FILM
LASER TRIGGER
PULSE
PHOTODIODE
DEFLECTION
PLATES
GOLD
PHOTOCATHODE
RAMP
GENERATOR
X-RAY PINHOLE
CAMERA
ACCELERATING
MESH
12·5 / 3 μm
PINHOLES
MICROBALLOON
8 μm PINHOLE
1 KG. MAGNET

FIG. 328

RUTHERFORD-BELFAST-IMPERIAL COLLEGE

7.6 JOULES PER BEAM IN 100 Psec PULSE ON 10 BAR $D_2 + T_2$ FILLED GLASS MICRO BALLOON OF 88 MICRON DIAMETER AND 0.88 MICRON WALL THICKNESS, YIELDING 2×10^4 NEUTRONS

88µm
INITIAL MICRO BALLOON
DIAMETER

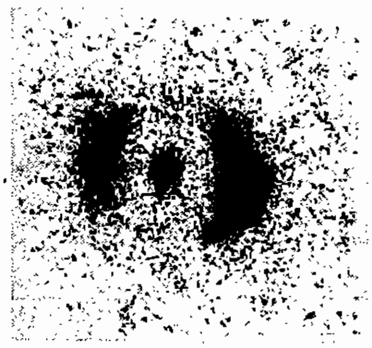

X-RAY PINHOLE IMAGE

110 Psec FROM PEAK OF LASER PULSE TO IMPLOSION

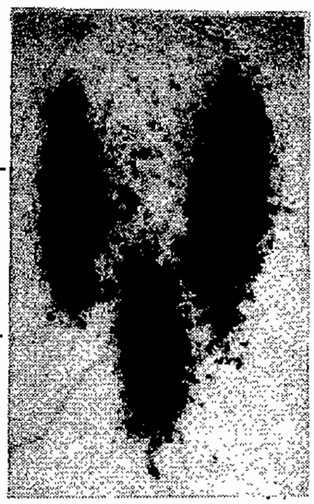

TIME

X-RAY STREAK IMAGE

08 1177/102

TIME AND SPACE RESOLVED X-RAY EMISSION FROM IMPLOSION OF 10 BAR $D_2 + T_2$ FILLED GLASS MICRO BALLOON

FIG. 329

RUTHERFORD - BELFAST

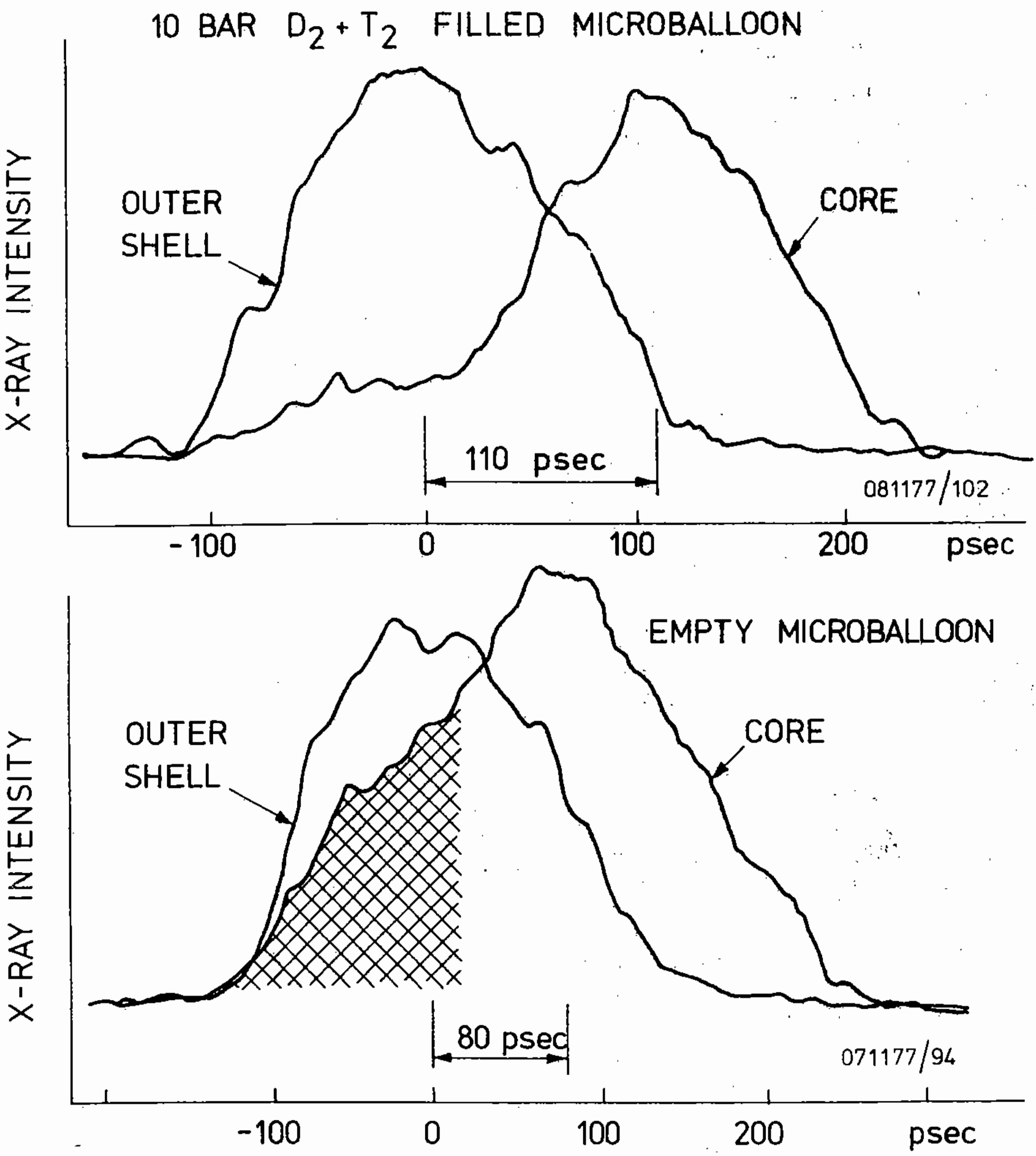

SPACE AND TIME RESOLVED X-RAY EMISSION FROM MICROBALLOON IMPLOSIONS

FIG. 330

BELFAST

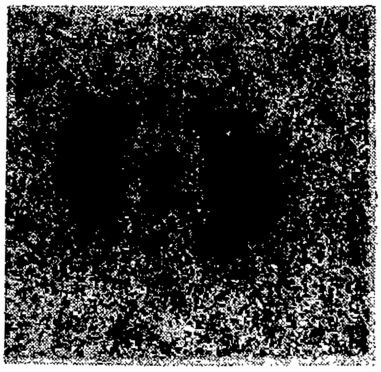

STATIC
X-RAY IMAGE

74 micron
initial microballoon diameter

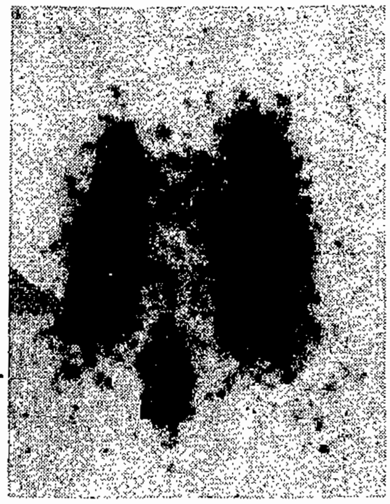

120 psec
time from laser power
peak to implosion

STREAKED
X-RAY IMAGE

Shot No. 021177 / 087

50 psec LASER PULSES. ENERGY ON TARGET 7·4 J
IN TWO BEAMS.

FIG. 331

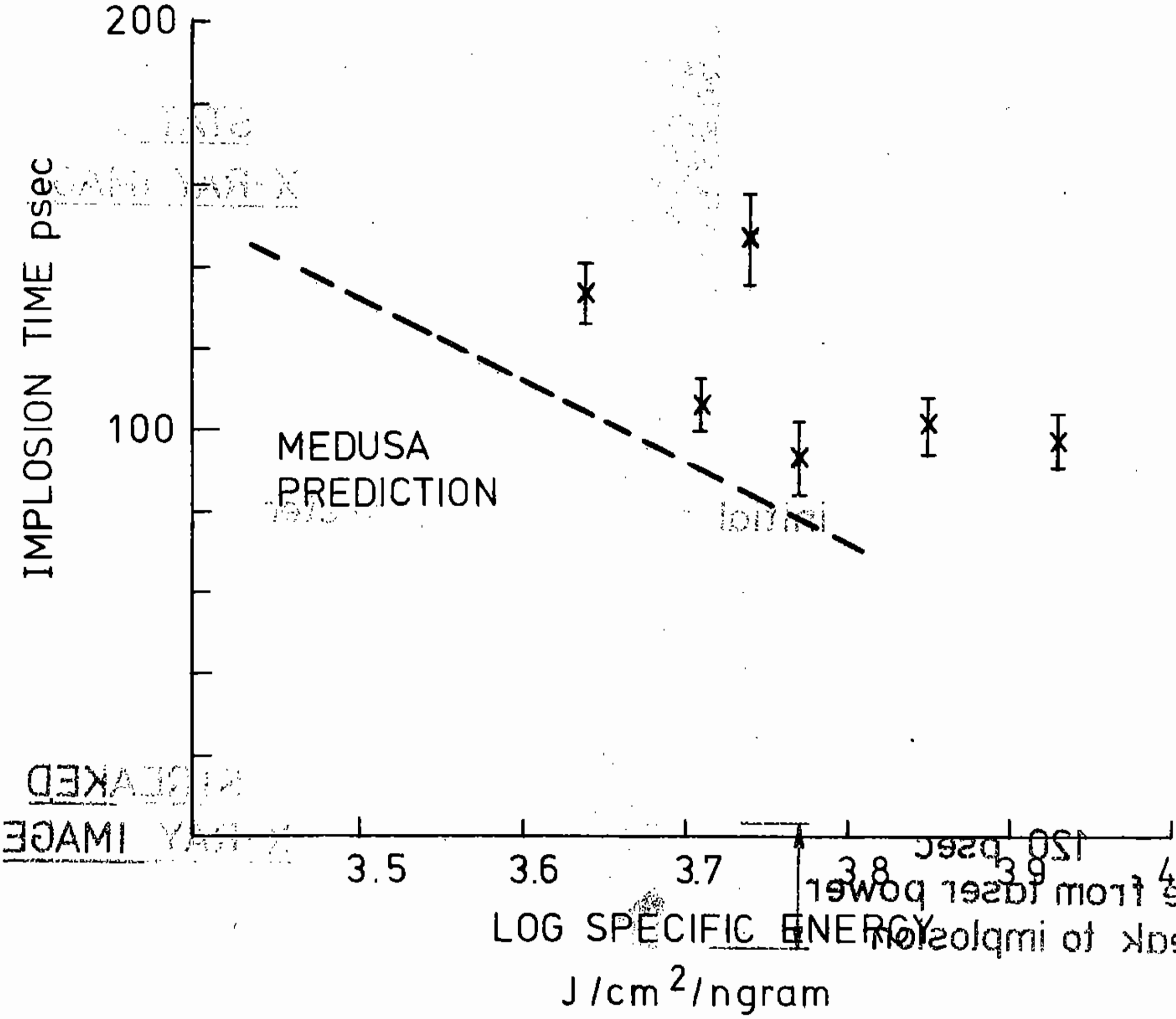

Variation of Implosion Time with
Laser Energy

FIG. 332

RUTHERFORD

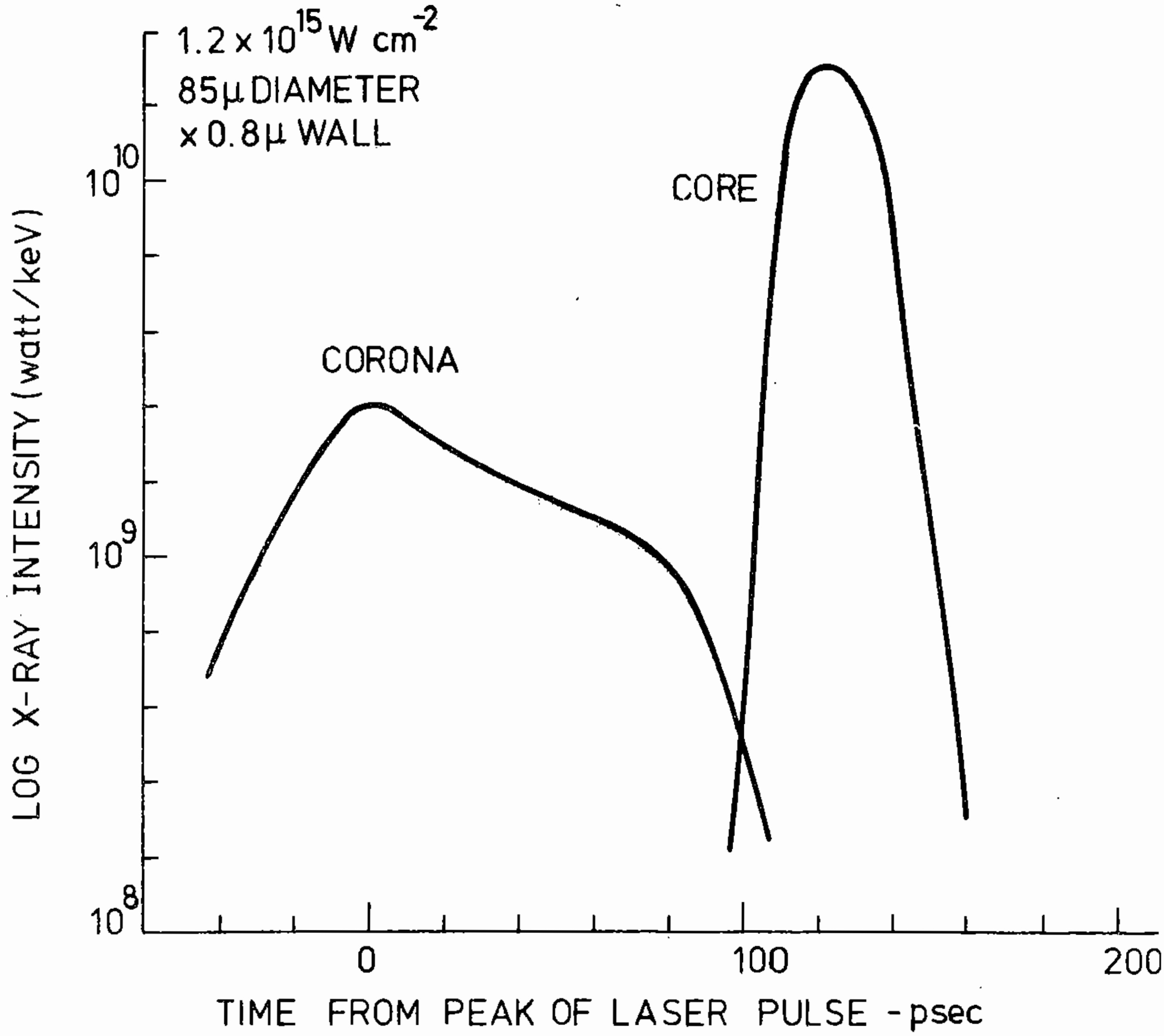

Medusa Simulation of 1keV X-Ray Emission from D-T Filled Microballoon

FIG. 333

RUTHERFORD-BELFAST-IMPERIAL COLLEGE

Aluminium Coated Glass Microballoon 'Burn through' Observations from Relative Intensity of Isolated Al XII and Si XIII X ray Transitions

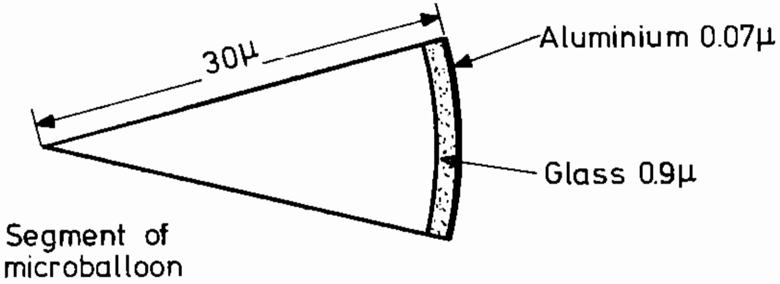

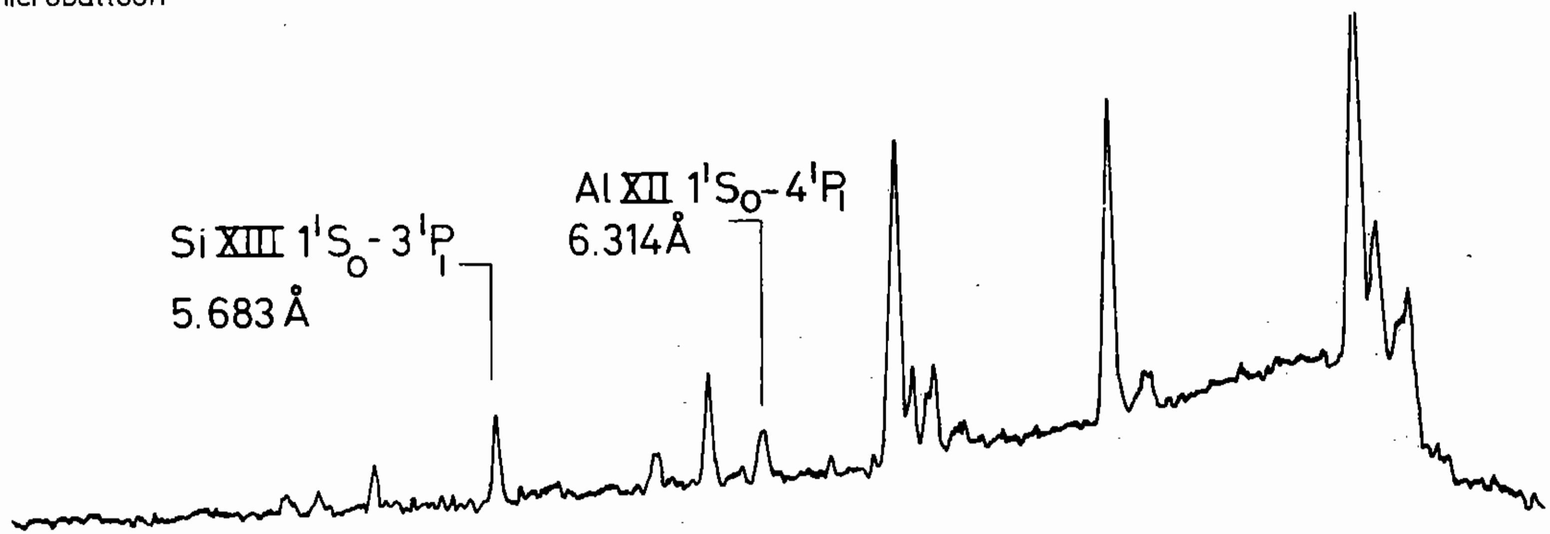

DENSITOMETER TRACING OF SPACE RESOLVED X RAY SPECTRUM

Shot 130178/180

FIG. 334

RUTHERFORD

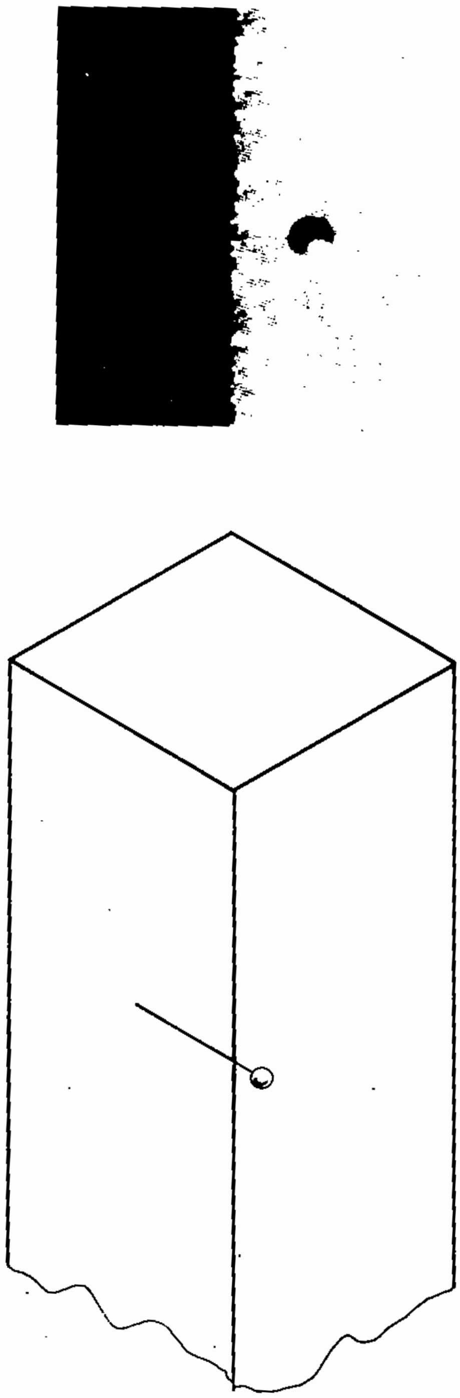

MICROBALLOON TARGET MOUNTED FOR X-RAY SHADOWGRAPHY ON A SOLID Cu + Zn ROD

FIG. 335

X-RAY SPECTRUM OF BRASS (Cu + Zn) BACKLIGHTING SOURCE. (normal transmission through 25 um Be foil.)

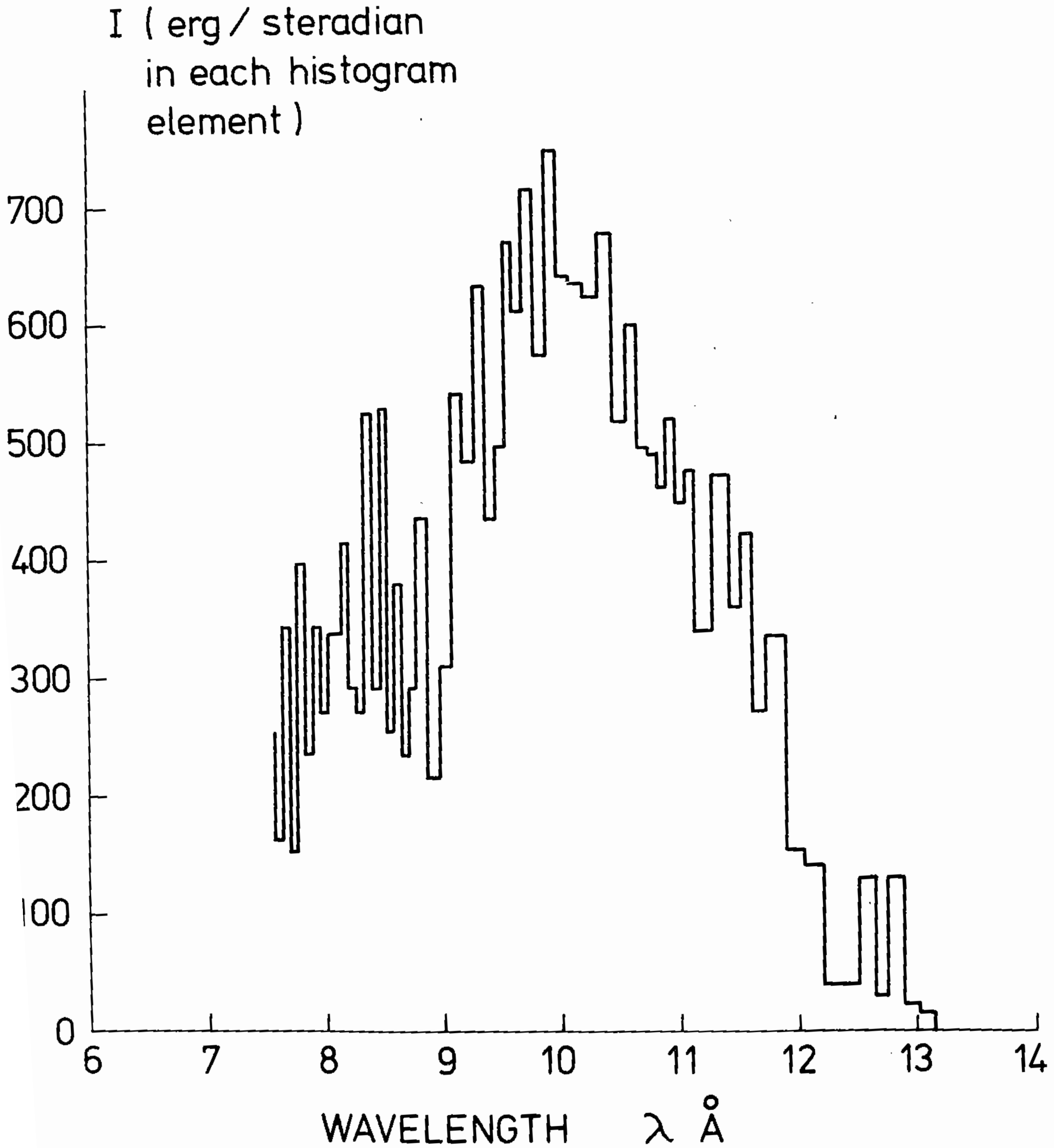

FIG. 336

RUTHERFORD - BELFAST - ESSEX

100psec Pulsed
1keV X ray
Shadowgraph

87 Bar NEON
filled Glass
Microballoon

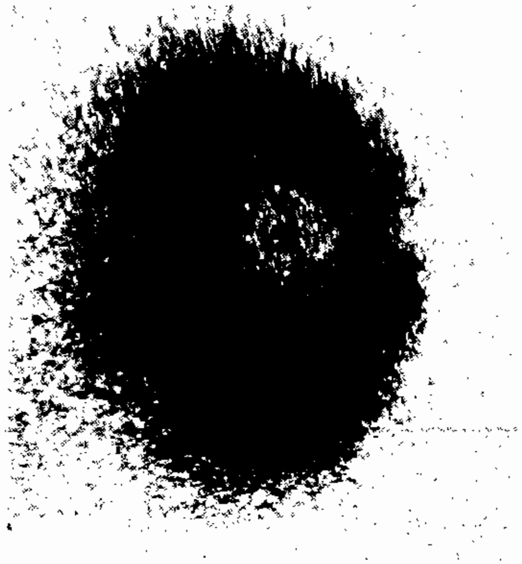

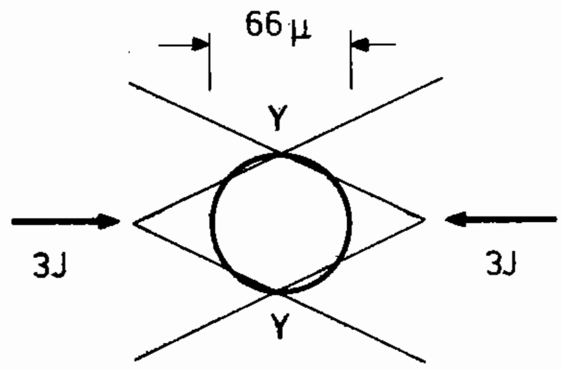

Initial
target

Time after
Irradiation

350psec

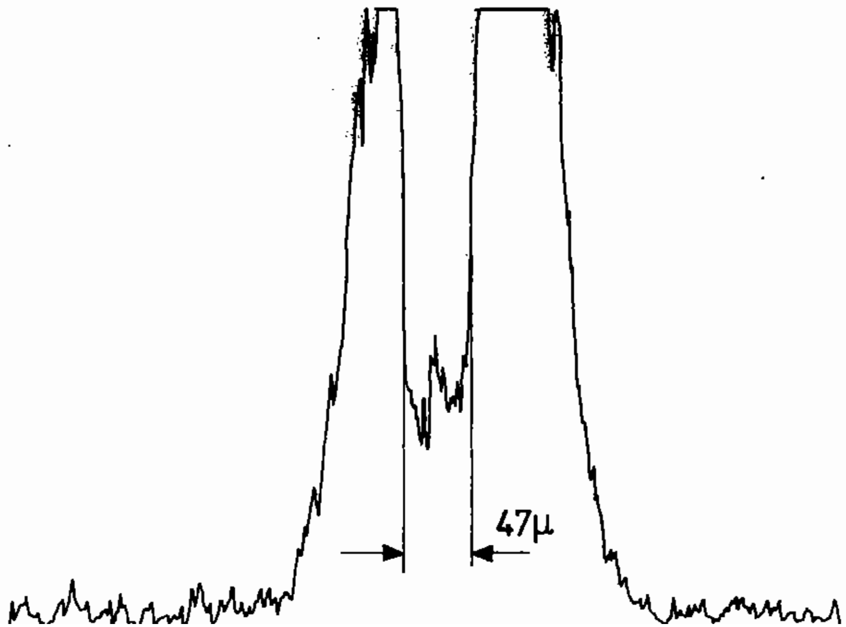

Densitometer Trace
of the Absorption
Zone Along YY

FIG. 337

RUTHERFORD - BELFAST - ESSEX

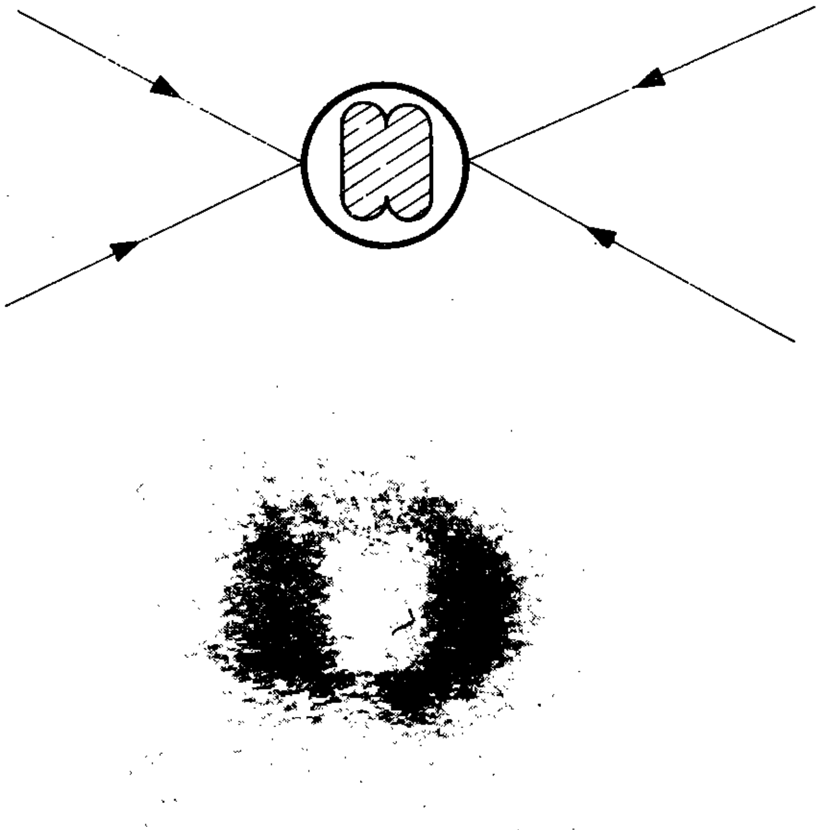

Polar focus

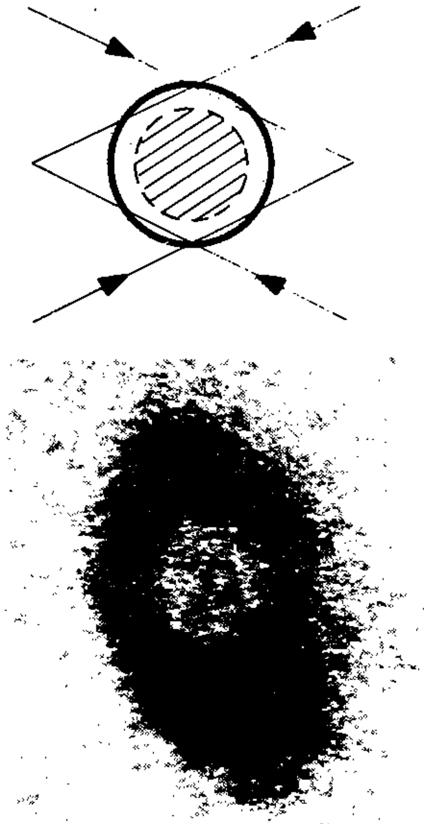

Equatorial focus

X ray shadowgraphs (250 psec delay)

FIG. 338

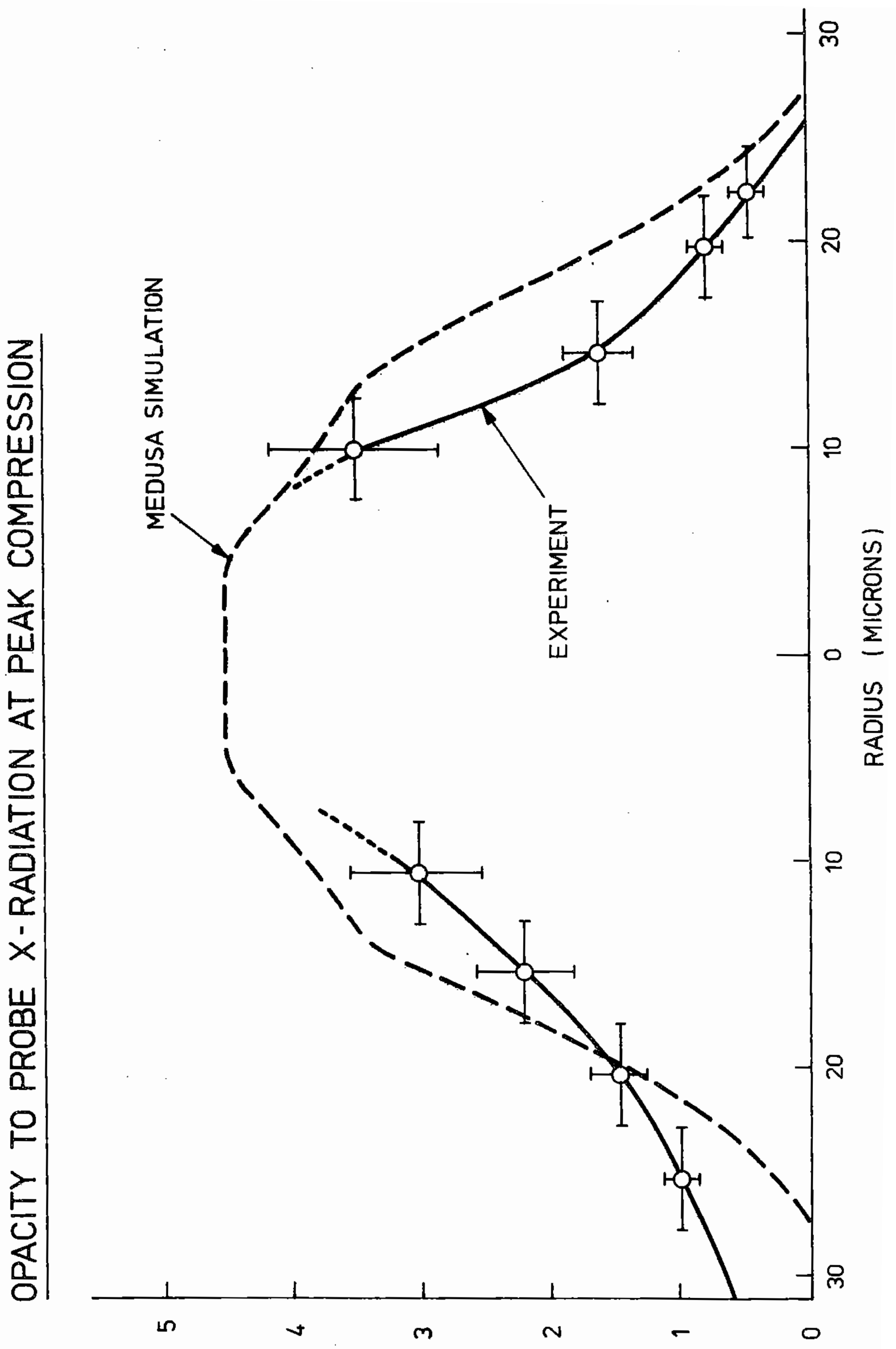

OPACITY TO PROBE X-RADIATION AT PEAK COMPRESSION
MEDUSA SIMULATION
EXPERIMENT
$Ln\left(\frac{1}{T}\right)$
0
1
2
3
4
5
30
20
10
0
10
20
30
RADIUS (MICRONS)

FIG. 339

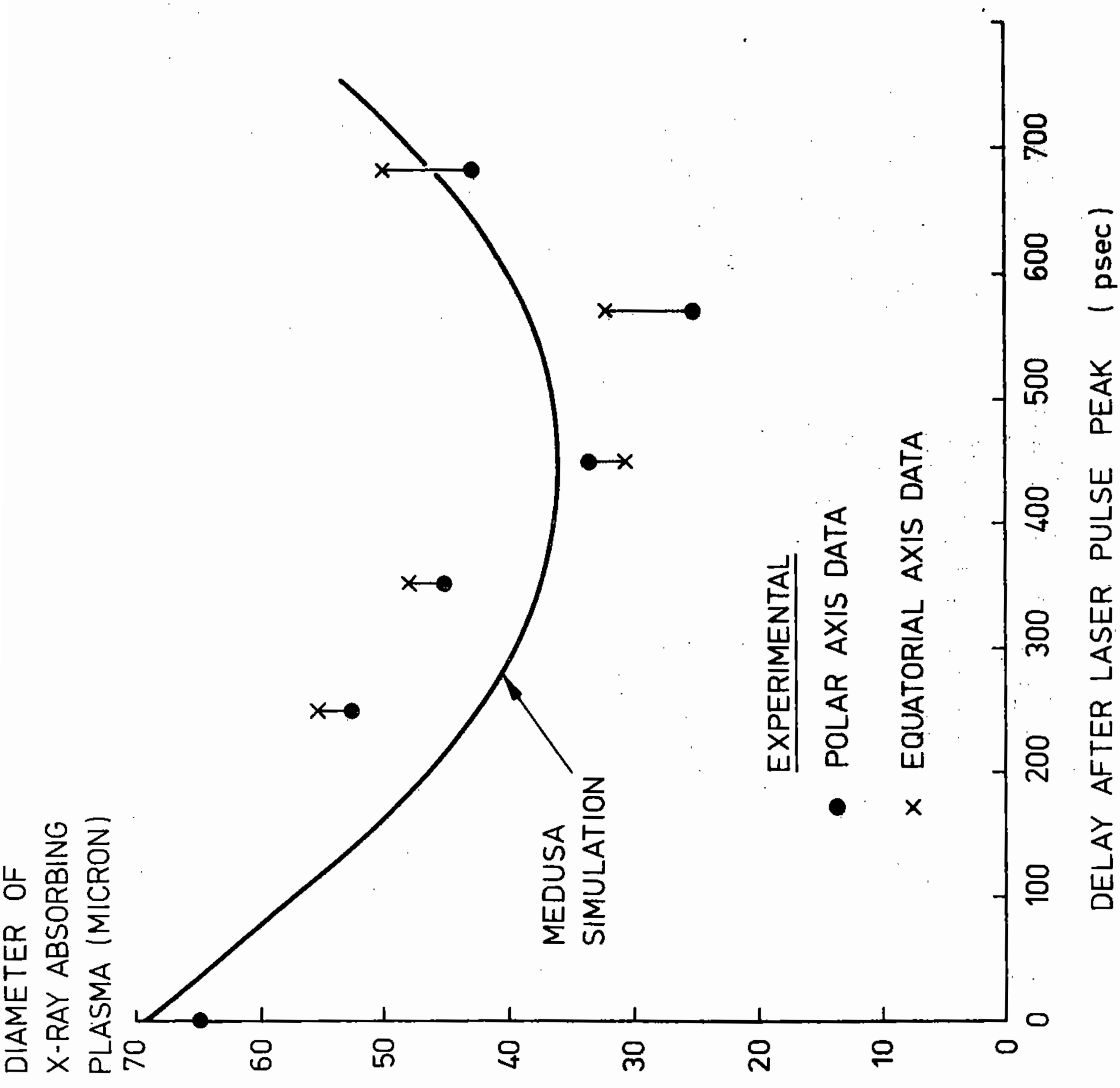

DIAMETER OF
X-RAY ABSORBING
PLASMA (MICRON)
70
60
50
40
30
20
10
0
0
100
200
300
400
500
600
700
DELAY AFTER LASER PULSE PEAK (psec)
MEDUSA
SIMULATION
EXPERIMENTAL
● POLAR AXIS DATA
× EQUATORIAL AXIS DATA

FIG. 340

RUTHERFORD·OXFORD

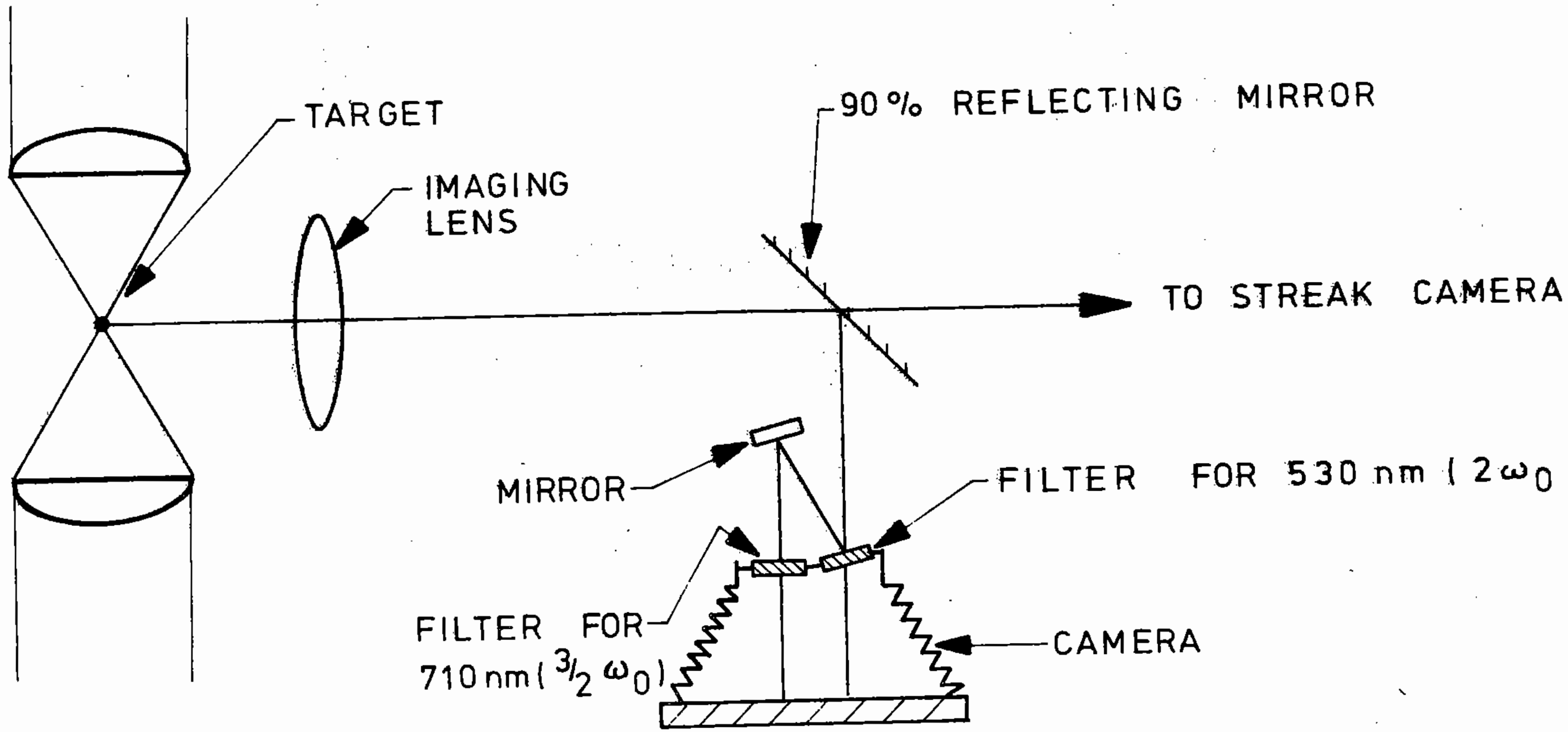

SIMULTANEOUS PHOTOGRAPHY AT $2\omega_0$ AND $3/2\ \omega_0$

FIG. 341

IMPERIAL COLLEGE - RUTHERFORD

SHOT 39: harmonic (2ω) emission

target diameter:
72·5 µm

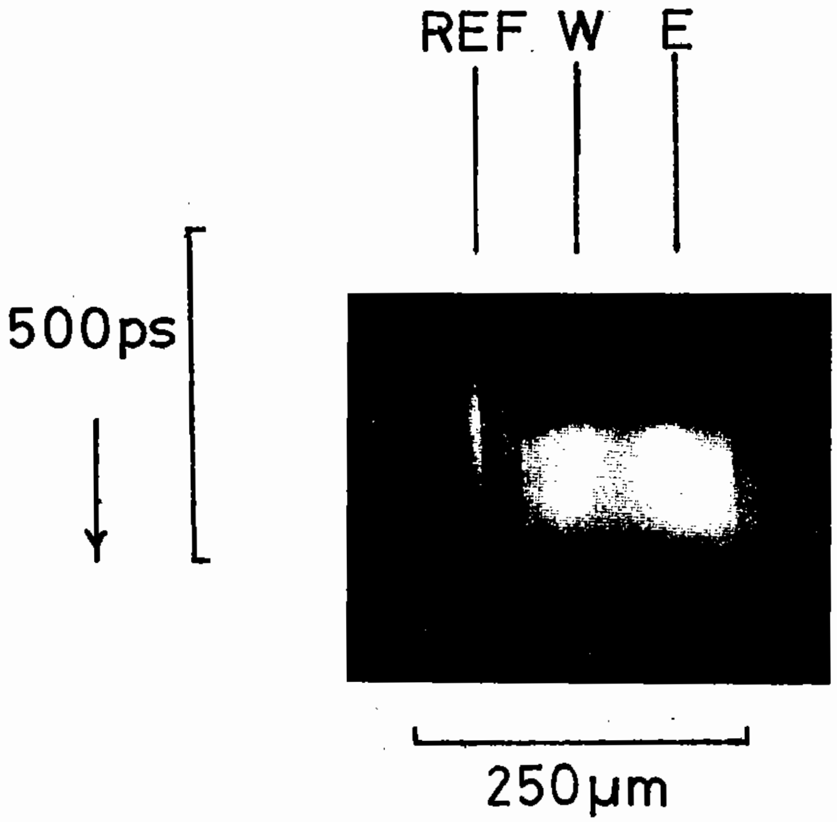

[R/I.C.]

FIG. 342

Ruby side illumination of
microshell implosion
SHOT 081277/154

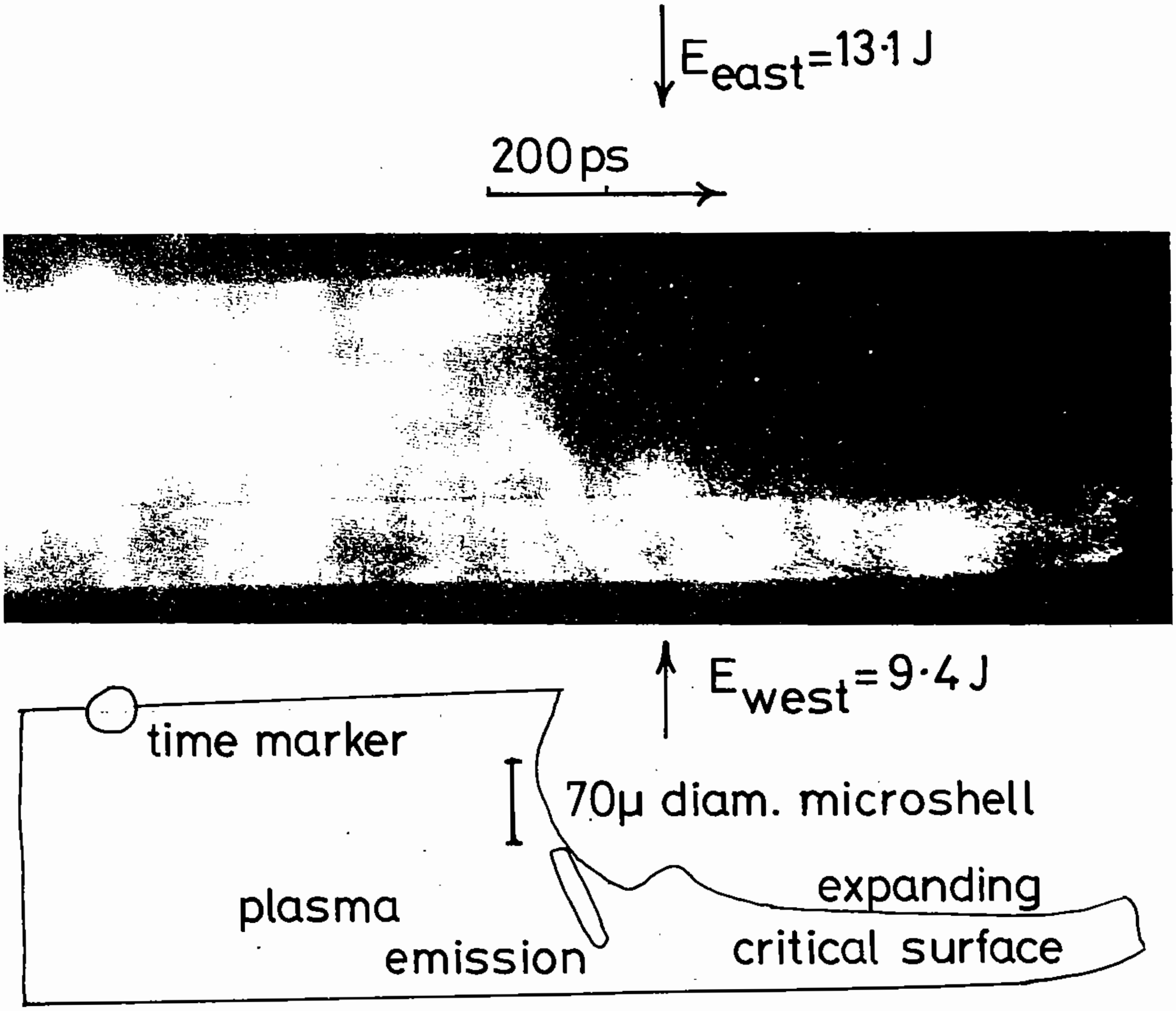

[R/IC]

FIG. 343

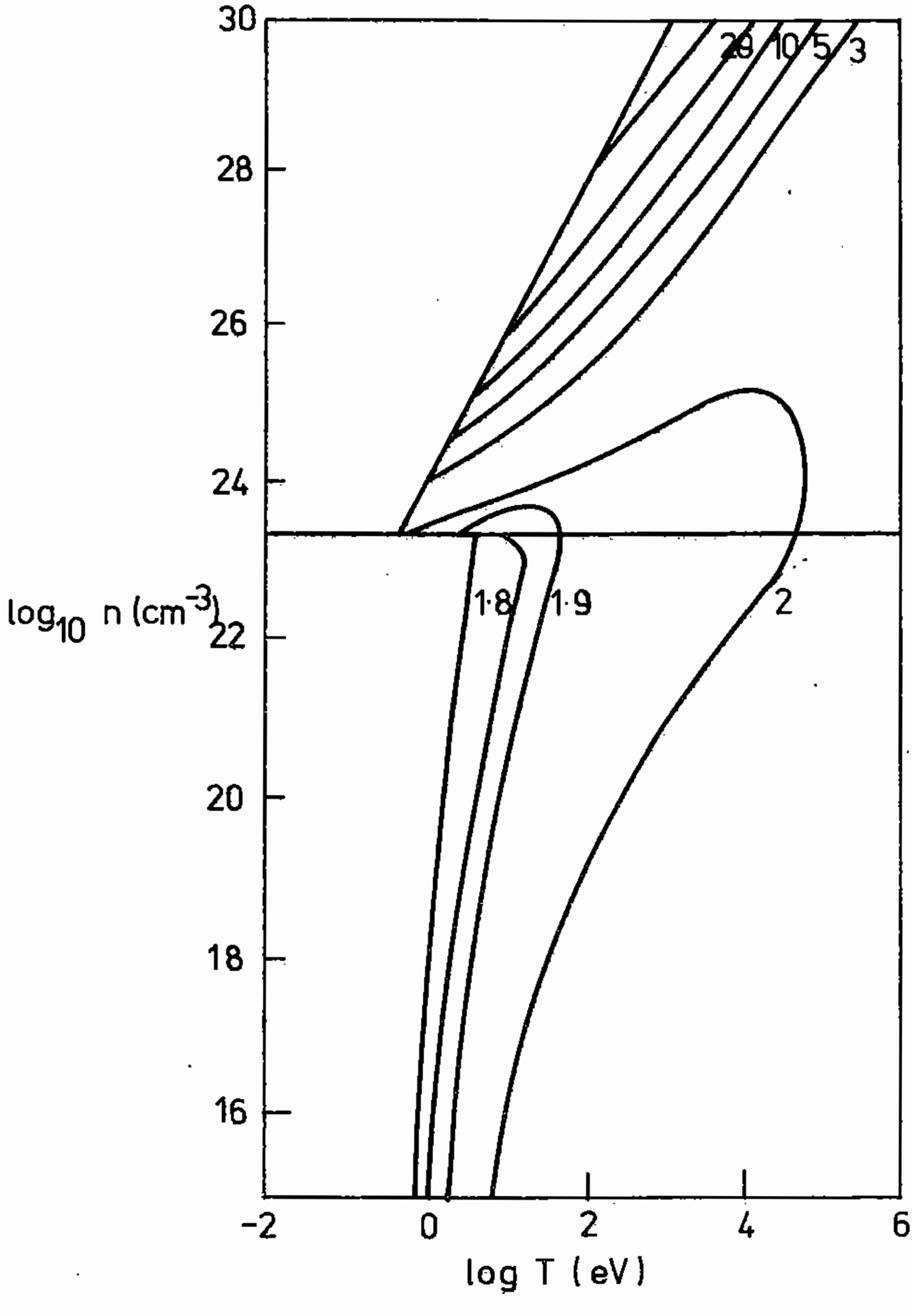

DEPARTURE OF THE 'QUASI-ATOM' MODEL FROM AN IDEAL GAS. THE PARAMETER OF THE CURVES IS $\frac{u}{nkT}$

FIG. 344

PLANE GEOMETRY

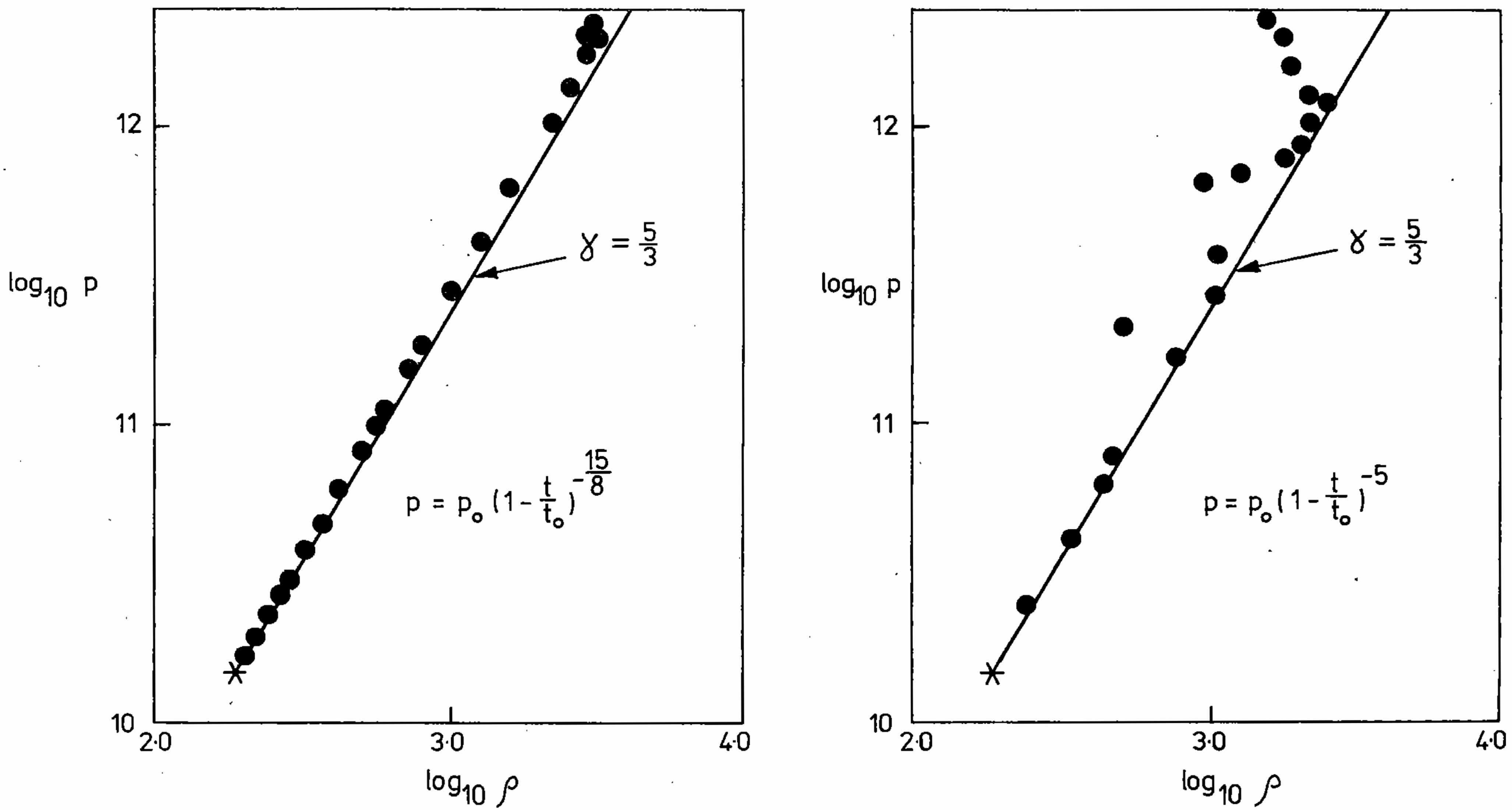

FIG. 345 MEDUSA CALCULATIONS OF PRESSURE AND DENSITY IN THE COMPRESSION OF A PLANE TARGET BY AN APPLIED BOUNDARY PRESSURE.

APPENDIX

MEMBERS OF THE GLASS LASER SCIENTIFIC PROGRAMME AND SCHEDULING COMMITTEE

Dr J Allen (Oxford)

Dr T D Beynon (Birmingham)

Mr J E Boon (RL)

Prof T J M Boyd (Bangor)

Prof D J Bradley FRS (Imp Coll)

Dr D A Brown (Royal Holloway)

Dr D D Burgess (Imp Coll)

Dr R A Cairns (St Andrews)

Dr A E Dangor (Imp Coll)

Dr R G Evans (RL)

Dr B Fawcett (ARD Appleton)

Dr L Gardner (Bangor)

Dr A F Gibson (RL) (Chairman)

Prof C Grey Morgan (Swansea)

Prof M G Haines (Imp Coll)

Dr T A Hall (Essex)

Mr T P Hughes (Essex)

Dr R Hutcheon (Leicester)

Dr H Hutchinson (Imp Coll)

Dr R Illingworth (Strathclyde)

Dr M H Key (RL) (Programme Co-ordinator)

Dr J Kilkenny (Imp Coll)

Dr E Laing (Glasgow)

Dr C L S Lewis (Queen's)

Dr H T Miles (Swansea)

Prof H Motz (Oxford)

Dr D J Nicholas (RL)

Dr N J Peacock (Culham)

Dr G Pert (Hull)

Prof S A Ramsden (Hull)

Dr I N Ross (RL)

Dr P T Rumsby (RL)

Dr W Sibbett (Imp Coll)

Mr W Toner (RL)

Dr C J Webb (RL)

Prof W T Welford (Imp Coll)

Dr M S White (RL)(Secretary)

Dr P R Williams (RL)

Dr E Wooding (Royal Holloway)

ATOMIC AND RADIATION PHYSICS GROUP

Prof T J M Boyd	Bangor	
Dr D Burgess	Imperial College	
Mr L Cooke	Queen's	
Dr R G Evans	Rutherford	(Secretary)
Dr K Evans	Leicester	
Dr B Fawcett	ARD Culham	(Convenor)
Dr A F Gibson	Rutherford	
Dr T A Hall	Essex	
Mr T P Hughes	Essex	
Dr R Hutcheon	Leicester	
Dr M H Key	Rutherford	
Dr E W Laing	Glasgow	
Mr R Lee	Imperial College	
Dr C L S Lewis	Queen's	
Mr J G Lunney	Queen's	
Mr A Moore	Queen's	
Dr N J Peacock	Culham	
Mr A G Richards	ARD Culham	
Dr A Ridgeley	ARD Culham	
Dr R J Speer	Imperial College	
Mr N A Tahir	Glasgow	
Dr R K Thareja	Strathclyde	
Mr J M Ward	Imperial College	

FACILITY DEVELOPMENT GROUP

Mr J E Boon	(Rutherford)	(Secretary)
Prof T J M Boyd	(Bangor)	
Dr A F Gibson	(Rutherford)	
Mr P Gottfeldt	(Rutherford)	
Dr T A Hall	(Essex)	
Dr D C Hanna	(Southampton)	
Mr T P Hughes	(Essex)	
Dr M H Key	(Rutherford)	
Dr E W Laing	(Glasgow)	
Dr I N Ross	(Rutherford)	
Dr P T Rumsby	(Rutherford)	
Prof W Welford	(Imperial College)	
Dr M S White	(Rutherford)	
Dr P R Williams	(Rutherford)	(Convenor)

THEORY AND COMPUTATIONAL MODELLING GROUP

Dr S Abas (Bangor)

Dr J Allen (Oxford)

Dr H C Barr (Bangor)

Dr T D Beynon (Birmingham)

Prof T J M Boyd (Bangor)

Prof R K Bullough (UMIST)

Dr D Burgess (Imp Coll)

Dr R A Cairns (St Andrews)

Dr C J Evans (Swansea)

Dr R G Evans (RL)

Dr G Gardner (Bangor)

Dr L Gardner (Bangor)

Prof M G Haines (Imp Coll(Convenor)

Mr W T Hewitt (Bangor)

Mr M Hooper (Strathclyde)

Mr G Humphreys-Jones (Bangor)

Prof J Irving (Strathclyde)

Dr M H Key (RL)

Dr J Kilkenny (Imp Coll)

Dr E Laing (Glasgow)

Prof H Motz (Oxford)

Dr D J Nicholas (RL)

Dr G J Pert (Hull)

Mr A Raven (RL)

Mr N A Tahir (Glasgow)

Dr W P S Tan (Glasgow)

Dr C Webb (RL)(Secretary)

Dr E Wooding (Royal Holloway)